NEUTRON TRANSPORT STUDY OF DYNAMIC NEUTRON RADIOGRAPHY

NEUTRON TRANSPORT STUDY OF A BEAM PORT BASED DYNAMIC NEUTRON RADIOGRAPHY FACILITY

By

ANAS M. KHAIAL, B.SC, M.SC.

A Thesis

Submitted to the School of Graduate Studies

in Partial Fulfilment of the Requirements

for the Degree

Doctor of Philosophy

McMaster University

DOCTOR OF PHILOSOPHY (2008) McMaster University

(Engineering Physics) Hamilton, Ontario

TITLE: Neutron Transport Study of A Beam Port Based Dynamic Neutron Radiography Facility

AUTHOR: Anas Mahmoud Khaial, B.Sc., M.Sc. (Alexandria University, Egypt)

SUPERVISORS: Dr. Glenn D. Harvel and Dr. Jen-Shih Chang

NUMBER OF PAGES: xxiii, 221

Summary

Neutron radiography has the ability to differentiate between gas and liquid in two-phase flow due both to the density difference and the high neutron scattering probability of hydrogen. Previous studies have used dynamic neutron radiography – in both real-time and high-speed – for air-water, steam-water and gas-liquid metal two-phase flow measurements. Radiography with thermal neutrons is straightforward and efficient as thermal neutrons are easier to detect with relatively higher efficiency and can be easily extracted from nuclear reactor beam ports.

The quality of images obtained using neutron radiography and the imaging speed depend on the neutron beam intensity at the imaging plane. A high quality neutron beam, with thermal neutron intensity greater than 3.0×10^{6} n/cm^{2}-s and a collimation ratio greater than 100 at the imaging plane, is required for effective dynamic neutron radiography up to 2000 frames per second.

The primary objectives of this work are: (1) to optimize a neutron radiography facility for dynamic neutron radiography applications and (2) to investigate a new technique for three-dimensional neutron radiography using information obtained from neutron scattering.

In this work, neutron transport analysis and experimental validation of a dynamic neutron radiography facility is studied with consideration of real-time and high-speed neutron radiography requirements. A beam port based dynamic neutron radiography facility, for a target thermal neutron flux of 1.0×10^{7} n/cm^{2}-s, has been analyzed, constructed and experimentally verified at the McMaster Nuclear Reactor.

The neutron source strength at the beam tube entrance is evaluated experimentally by measuring the thermal and fast neutron fluxes using copper activation flux-mapping technique. The development of different facility components, such as beam tube liner, gamma ray filter, beam shutter and biological shield, is achieved analytically using neutron attenuation and divergence theories. Monte-Carlo simulations (using MCNP-4B code) are conducted to confirm the neutron parameters along the beam path and at the imaging plane. Good agreement between the analytical and the numerical values for the thermal neutron flux at the imaging plane to within 5% has been achieved. The MCNP simulations show that neutron back scattering, due to the presence of the back-wall biological shielding and the beam catcher, have an insignificant effect on the thermal neutron flux at the imaging plane, however, the epithermal and fast neutron fluxes have increased by 4-11%.

Experimental results show that the thermal neutron flux is nearly uniform over an imaging area of 20.0-cm diameter. The thermal neutron flux ranges from 1.0×10^7 – 1.26×10^7 n/cm^2-s at a reactor operating power of 3.0 MW. The measured value for the neutron-to-gamma ratio is 6.0×10^5 n/cm^2-μSv and the Cadmium-ratio is observed to be 1.22. These values promote real-time neutron radiography with relatively high neutron attenuating materials such as light water and high-speed neutron radiography with relatively low neutron attenuating materials such as heavy water and Freon type fluids with a minimal contrast degradation resulting from non-thermal neutron content of the beam.

A dynamic neutron radiography system has been developed and modified to obtain less neutron damage to the low-light level video camera. The system is used to visualize air-water two-phase flow in a natural-circulation loop to examine the dynamic capabilities of the radiography facility. Measurements of bubble velocity, void fraction, and phase distribution are successfully made. Single frames (~33 ms) of neutron images were captured using the dynamic neutron radiography system for air-water two-phase flow. The system was able to resolve single bubbles interfaces with an image spatial resolution of approximately 0.44 mm.

Thermal neutron detectors are placed at the periphery of the neutron beam to detect neutrons scattered by a non-flowing two-phase object placed on a turntable to simulate motion of the gas phase. The results show the potential ability to use neutron scattering technique to provide two-dimension neutron radiography with additional information to the third dimension.

Acknowledgements

A scientific research conducted for more than five years cannot be attributed to a single person. Above all, I am indebted to GOD for guiding me to the right path and always directing me to what is beneficial.

This work has been sponsored in part by National Science and Engineering Research Council (NSERC) of Canada, Canada Foundation of Innovation (CFI), Ontario Technology Institute (OTI) and Centre for Earth and Environmental Technologies (OCE Inc. E-tech.)

My supervisors Prof. Glenn D. Harvel and Prof. Jen-Shih Chang extended their help to me. Their comments and advices helped me a lot to complete working on this thesis and their efforts will always be remembered. I am especially indebted to Prof. Glenn D. Harvel for his continuous encouragement, dedication and vision.

I would like to thank Prof. C. Y. Ching, Dr. V.S. Krishnan, Mr. Mike Butler, Mr. Dave Tucker and Mr. Robert Pasuta for their valuable discussion and comments.

I acknowledge the assistance provided by the technical staff of the McMaster Nuclear Reactor, the technical staff of the Thermalhydraulic and Electromagnetic Hydrodynamics Laboratory, and the technical staff of the Health Physics Department in completing the facility construction and experiments.

My colleagues in the Thermalhydraulic and Electromagnetic Hydrodynamics Laboratory provided assistance, comments, and humour at all times. Special recognition for Mr. Behrooz Komeili, Mr. Emanuel Delacruz and Mr. Jon Markel.

The dedication, continuous support and above all prayers of my family made my success a reality. My wife and my two children (Maalik and Muaaz) deserve recognition.

I apologize for the meagre expression of thanks here and hope that all the individuals who have facilitated my work will understand that my gratitude reaches for deeper than words can express.

This work is dedicated to my father, Mahmoud. Although he passed away, his prayers have always protected me.

Table of Contents

List of Figures

List of Tables

1 INTRODUCTION

This chapter discusses the background of the dynamic neutron radiography (imaging) technique, introduces and defines neutron radiography parameters and describes the key objectives of this thesis.

1.1 Background

Neutron radiography is an imaging technique based on the difference in the attenuation characteristics of neutrons in various materials [1]. Unlike X-rays which interact with the atomic electron cloud, thermal neutrons are not characterized by a dependence on the atomic number of the object, and the relationship between the two is quite random. No generalization can be made to relate the neutron attenuation characteristics to the atomic mass and/or the atomic number [1].

Applications of neutron radiography have been proposed for many non-destructive examination applications since the attenuation characteristics of neutrons in materials are much different from those of X-rays and γ-rays, i.e., objects difficult to be visualized by X-rays and γ-rays can possibly be visualized by neutrons. Thermal neutrons can easily penetrate most dense metals, where they are attenuated by such materials as hydrogen, boron, gadolinium, and cadmium [2].

Neutron radiography and X-ray radiography are considered as complementary techniques but in some special cases neutron radiography shows superiority [3]. Neutron radiography has important advantages in many specifications where large thicknesses of most dense metals can be penetrated, high sensitivity can be obtained for small details containing hydrogen and certain other light elements, and materials of similar density and isotopes of the same element can be contrasted [4].

Non-destructive testing with neutrons can yield important information that is not obtainable by other traditional non-destructive testing methods. The neutron radiography technique has versatile applications in non-destructive testing and multi-phase flow studies in energy and environmental engineering applications.

Industrial applications of neutron radiography usually involve the detection of a particular material, or lack thereof, in an assembly containing two or more materials [5]. Absence of material is usually determined by soaking and rinsing the component of interest in a neutron absorbing material such as gadolinium. Residual gadolinium remains in cracks and crevices and identifies the location where material loss has occurred. In addition, neutron radiography offers advantages in testing and inspecting nuclear materials because different isotopes of the same element, in most cases, can be differentiated, and clear images can be obtained even if the inspection objects are highly radioactive.

The neutron radiography technique has been extensively applied in thermalhydraulic studies for visualization and measurement of multiphase fluid flow that are difficult to be observed by other methods [6].

Neutron radiography using a steady neutron beam is classified according to image detection into three methods [2]; static neutron radiography or film radiography, dynamic neutron radiography (with the recording speed of 25-30 frames/s) which is generally called "real-time" neutron radiography (RTNR), and high-frame rate dynamic neutron radiography (HFRNR) also called high-speed neutron radiography (HSNR).

Most industrial neutron radiography is still performed today with film radiography. Although film techniques provide excellent resolution, they can be time consuming. Real-time neutron radiography has been used for a relatively long time but only applied as a research tool. Research on neutron radiography has advanced to a new phase since a steady high flux thermal neutron beam, of the order 10^8 n/cm^2-s was achieved in the JRR-3M Research Reactor [7].

1.2 Main Neutron Radiography Variables

The extent to which neutrons can be utilized for practical radiography is dependent on several neutron source parameters such as; neutron energy, neutron beam intensity, neutron beam collimation, and background radiation. Other parameters – that should be considered – include size, cost, and portability of the assembly.

1.2.1 Neutron Energy

Most neutron radiography has been done with thermal neutrons, i.e., neutrons in the energy range (0.01 eV – 0.5 eV), since neutrons in this energy region exhibit higher attenuation characteristics. Also, thermal neutrons are easier to detect and hence imaging is straightforward and efficient. Other neutron energies are usually used to satisfy special test requirements or for some specialized inspections. Epithermal neutrons (0.5 eV – 10 keV) are usually used in applications where thermal neutrons do not penetrate the inspection object sufficiently to produce useful images. Radiography with cold neutrons (< 0.01 eV) involves taking advantage of the high absorption cross-sections, which allows taking images of small material concentrations. Fast neutrons (1.0 keV – 1.0 MeV) are rarely used in radiographic techniques because the attenuation characteristics of most materials are similar and their detection efficiencies are relatively low.

1.2.2 Neutron Beam Intensity

The fundamental figure of merit for a radiography source is the maximum neutron flux available for beam extraction. This available source is then apportioned to beam collimation or intensity and hence beam intensity can be increased only by sacrificing collimation and vice versa [5].

From the statistical analysis of the detected number of neutrons, Mishima and Hibiki [2] obtained a relationship between the frame exposure time and the incident neutron beam intensity as follows;

$$1/\Delta t = I\exp(-\Sigma\delta)R^2\xi^2 \qquad (1.1)$$

where Δt is the frame exposure time [s], I is the neutron intensity [n/cm^2-s], Σ is the neutron macroscopic cross-section [cm^{-1}], δ is the object thickness [cm], R^2 is the image spatial resolution [cm^2] and ξ is the allowable statistical detection error.

The above relation shows that the beam intensity at the imaging plane affects both the speed of exposure and image resolution. Very few practical applications of neutron radiography can tolerate a detector exposure of neutron intensity less than 10^5 n/cm^2-s. Neutron intensities lower than this level will require long exposure times. High-resolution neutron radiography may require neutron intensity higher than 10^6 n/cm^2-s at the imaging plane [5]. It should be noted that Equation 1.1 is based upon an ideal system where the effects of background radiation, neutron detection efficiency and signal noise are not considered.

1.2.3 Collimation Ratio

The collimation ratio is a measure of resolution capability of a neutron radiographic system. The collimation *(L/D)* ratio is the ratio between the total length *(L)* from the collimator inlet aperture to the detector and the effective dimension of the collimator inlet aperture *(D)*. The *L/D* ratio determines to a large extent the neutron intensity at the imaging plane and the image geometric sharpness and hence resolution. Neglecting the neutron flux gradient at the inner face of the collimator assembly, an estimate of the neutron beam intensity at the imaging plane [1] is given by;

$$I = \frac{\phi_i}{16\,(L/D)^2} \tag{1.2}$$

where ϕ_i is the neutron flux at the inner face of the collimator assembly [n/cm^2-s].

Many types of neutron collimators have been proposed and used. The principle of a point neutron source (collimation is not required), parallel-wall collimator, and the divergent collimator are shown in Figure 1.1. The divergent collimator is widely used since it resembles the point source.

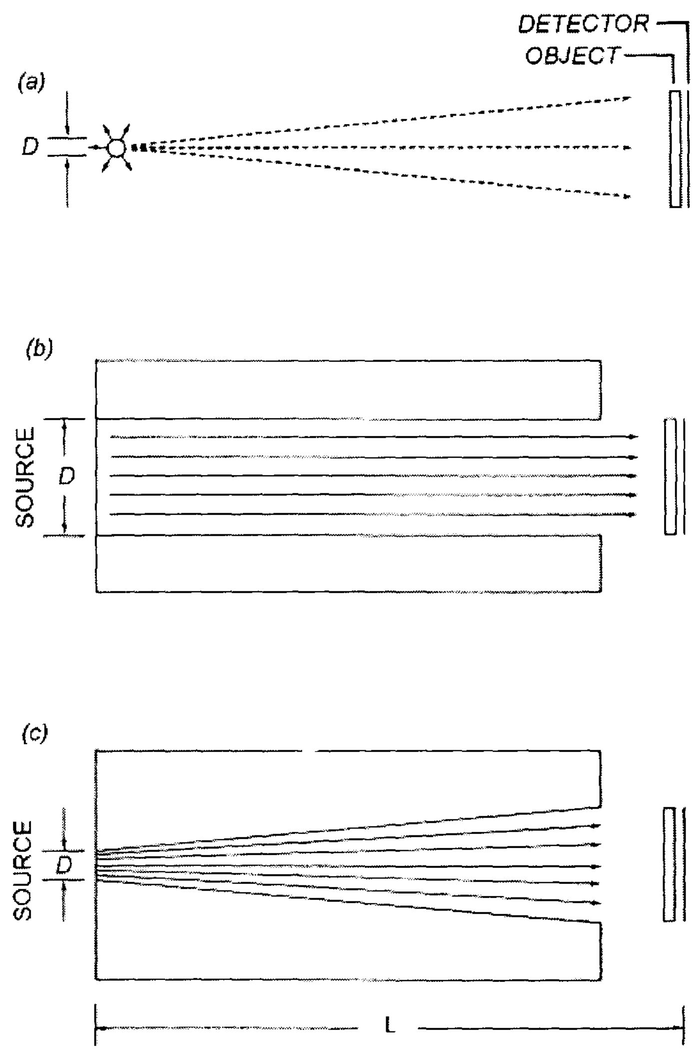

Figure 1.1. Neutron collimators: (a) Point neutron source (No collimator); (b) Parallel-wall collimator; (c) Divergent collimator [5].

The geometric unsharpness (U_g) in a neutron radiograph or image can be determined [1] as follows;

$$U_g = D\left(\frac{L_f}{L - L_f}\right) \cong \frac{L_f}{(L/D)} \qquad (1.3)$$

where L_f is the object to image distance in cm.

When $L >> L_f$, the geometric unsharpness depends linearly on the inverse of the collimation ratio, hence a relatively large collimation ratio is required to maximize image geometric sharpness [9]. This requirement leads to a direct conflict with the desire to achieve maximum neutron flux. Figure 1.2 shows the relation between source geometry and geometric sharpness.

1.2.4 Background Radiation in the Beam

The neutron image contrast and hence resolution is affected by the amount of gamma ray contamination in the neutron beam. To obtain a good quality neutron beam, the gamma ray content must be reduced below the gamma sensitivity limits of the neutron detector. Direct metal-screen image detectors (commonly used in static radiography) require a n/γ ratio of about 10^5 n/cm^2-μSv, while scintillators (commonly used in dynamic radiography) require a ratio of about 10^4 n/cm^2-μSv to produce neutron images with negligible gamma-radiation interference [8]. The most commonly used materials for gamma filtration are bismuth and lead since they have higher gamma attenuation and relatively lower neutron attenuation.

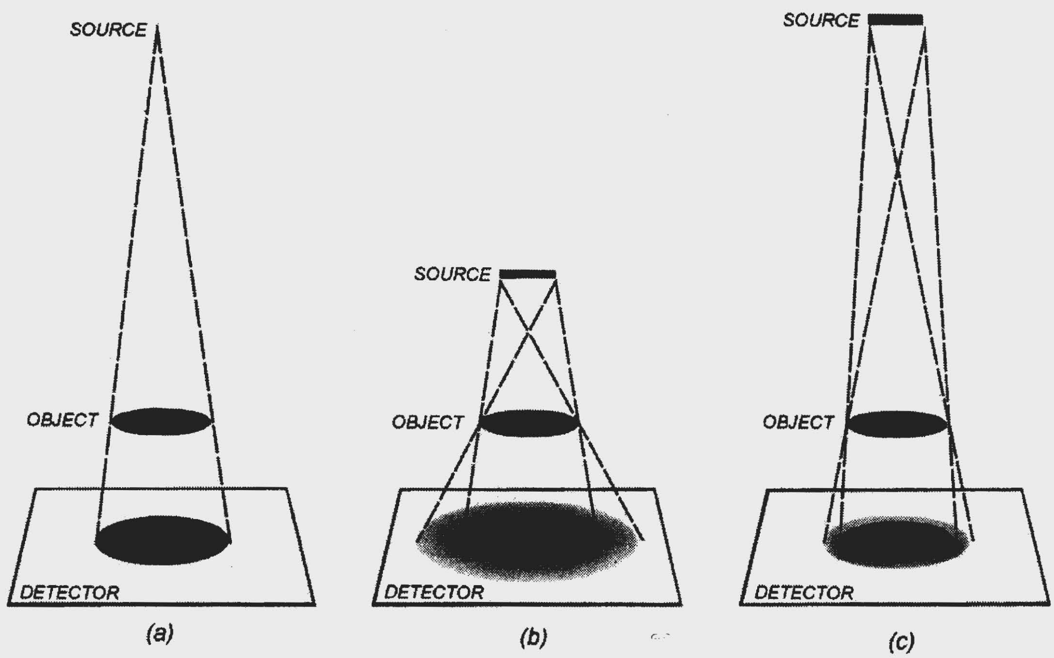

Figure 1.2. Illustration of geometric unsharpness for (a) Point neutron source (b) Small collimation ratio and (c) Large collimation ratio [9].

The neutron-to-gamma *(n/γ)* ratio at the imaging plane can be estimated by;

$$n/\gamma = [n/\gamma]_{Source} \times \frac{\exp[-(\Sigma X)_{Filter}]}{\exp[-(\mu X)_{Filter}] \times B[(\mu X)_{Filter}]} \tag{1.4}$$

where X is the thickness [*cm*], μ is the gamma rays attenuation coefficient [cm^{-1}] and $B[(\mu X)]$ is the gamma rays dose build-up factor.

Neglecting the neutron build-up in the filter material, Equation 1.2 is modified to include the neutron attenuation associated with the filter material and hence the neutron beam intensity at the imaging plane is estimated by;

$$I = \frac{\phi_i \exp[-(\Sigma X)_{Filter}]}{16\,(L/D)^2} \tag{1.5}$$

Similar to the case with a collimation ratio, increasing the n/γ ratio conflicts with the neutron flux requirement as shown by Equation 1.5. Therefore, requirements of large neutron flux, large collimation ratio and large n/γ ratio should be compromised based on the required image geometric sharpness.

In radiography applications with thermal neutrons, another measure of the background radiation interference is defined by the Cadmium ratio, i.e., the ratio of the activity of a bare gold foil induced by the neutron beam to that of a gold foil covered with cadmium. The presence of neutrons with higher energies reduces the contrast of the neutron images, and a high Cadmium ratio is required to preserve contrast. Most thermal neutron detectors have a negligible response to energetic neutrons and neutron energy filtration may not be necessary.

1.3 Third Dimension in Neutron Radiography

Conventional neutron radiography is a planar projection method that produces two-dimensional images. It provides average attenuation characteristics of the test object along the beam path (third dimension) that is not sufficient to obtain the spatial distribution of attenuating materials along the beam path. Hence, full three-dimensional capability using dynamic neutron radiography has not been demonstrated.

Computed tomography has been applied to neutron radiography to reconstruct three-dimensional details from all two-dimensional radiographic projections taken over 180° by calculating the three-dimensional array of attenuation values [10]. This technique is currently restricted to three-dimensional imaging of static objects.

Additional information about the spatial distribution of attenuating materials along the beam path can be obtained using a neutron scattering technique. Figure 1.3 shows a schematic of a potential three-dimensional dynamic neutron imaging technique based on neutron radiography, where the information represented by neutrons scattered from the test section can be integrated with the two-and-half-dimensional information (x, y and half z from the neutron beam attenuation in the z-direction) to obtain three-dimensional information of the test object.

1.4 The Objectives of This Work

The quality of images obtained using neutron radiography depends greatly on the neutron beam intensity at the imaging plane. The previously developed neutron

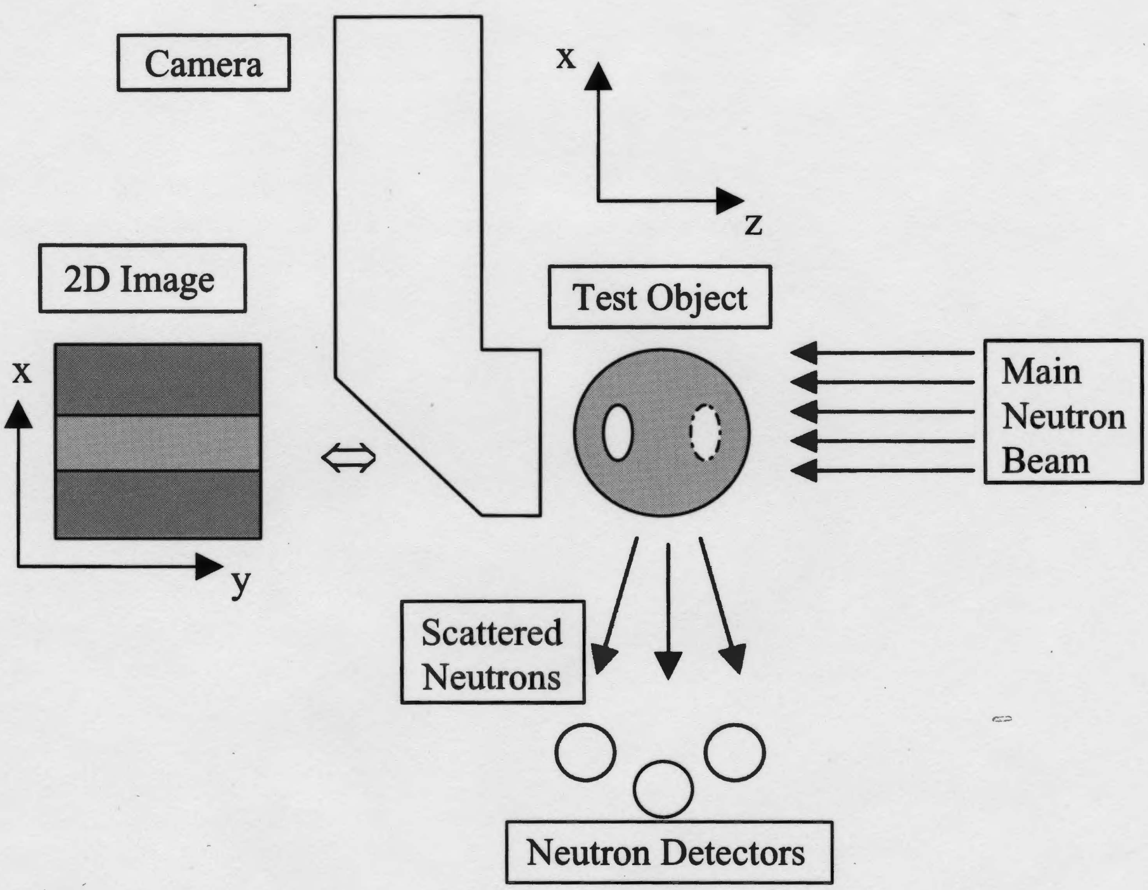

Figure 1.3. Principle of potential three-dimensional dynamic neutron imaging technique.

radiography facility at the McMaster Nuclear Reactor (Beam Port #2) has relatively low neutron intensity and is limited for static film radiography or low quality real-time radiography.

The objectives of the current work are:

- to analyze the neutronics of a beam tube and imaging plane to optimize a neutron radiography facility for dynamic neutron imaging including both real-time and high speed applications. Beam Port #3 at the McMaster Nuclear Reactor is chosen for the development of the new dynamic neutron facility.
- to investigate the practicality of enhancing real time neutron radiography for three dimensional imaging by including neutron scattering information.

Chapter 2 reviews the existing neutron based measurement techniques. Chapter 3 describes the neutron transport analysis based on source measurements (flux mapping) using conventional neutron attenuation and divergence models and dynamic neutron radiography variables. Chapter 4 includes numerical simulations using the Monte-Carlo method. Chapter 5 describes the experimental characterization of the developed dynamic neutron facility, beam tube liner, beam shutter, and biological shielding. Chapter 6 describes the experimental measurements using the developed real-time neutron radiography system and the experimental examination of the potential neutron scattering technique. Concluding remarks and recommendations for future work are summarized in Chapter 7.

2 REVIEW OF NEUTRON BASED MEASURING TECHNIQUES

Non-destructive testing with neutrons can yield important information not obtainable by other traditional non-destructive testing techniques. This chapter reviews different neutron based imaging techniques including; static neutron radiography, real-time neutron radiography, high-speed neutron radiography and other neutron based measuring techniques as well.

2.1 Neutron Radiography

Radiography with neutrons can be traced to the mid 1930's, shortly after Chadwick discovered the neutron [5]. Research work in this field has been carried through to the present time, with a significant increase in development activity since 1960. The majority of research work involving neutron radiography has been done with thermal neutrons. The reason is that useful and interesting attenuation characteristics are found in the thermal region. Another advantage is that thermal neutrons are easy to detect with relatively high efficiencies. In addition, thermal neutron beams can be relatively easily extracted from nuclear reactors.

Neutron energy ranges, available for potential use in radiography, include thermal, epithermal, cold, fast and resonance [5]. The different imaging techniques using thermal neutron radiography and their applications will be discussed later in this chapter.

In some applications, thermal neutrons do not penetrate the object sufficiently for meaningful neutron radiography. Epithermal neutrons are used to satisfy test requirements for these applications. The most extensive use of epithermal neutrons has been the inspection of highly enriched nuclear reactor fuel specimens. For example, Bordo et al. [11] examined irradiated Liquid Metal Fast Breeder Reactor (LMFBR) fuel specimens using epithermal neutron radiography.

Cold neutrons show advantages in some specialized inspections; the penetration power of neutrons can be greatly enhanced for some crystalline materials [12] by taking advantage of the reduced scattering at neutron energies below the Bragg cutoff (where neutron wavelength is sufficiently long, compared to the specimen's atomic spacing, to prohibit diffraction). Another advantage of cold neutrons, when compared to thermal neutrons, is the higher absorption cross-sections in many materials such as boron and lithium. This may allow contrasting small concentrations of these materials that are too small to be imaged by thermal neutrons. Kamata et al. applied cold neutron radiography to visualize lithium ion movement in lithium based conductors [13] and lithium distribution in lithium batteries before and after discharge [14] and confirmed the mobility of 50% of lithium ions (interstitial) and measured a lithium ion transport number that is coincident with electromagnetic field measurements.

The primary advantages of fast neutrons for radiography are their excellent penetration powers and their availability in point sources. Lower detection efficiency and interference from scattering limit the practical applications of fast neutron radiography. Also, the similarity of fast neutron attenuation characteristics for most materials places a significant restriction on contrast ability. Recently, Takenaka et al. [15] applied fast neutron radiography to visualize low void fraction distribution of air-water two-phase flow near a stainless steel spacer in simulated 4x4 aluminium rod bundle. The fast neutron attenuation coefficient of water is higher than those of metals hence fast neutrons can be used to visualize two-phase flow in thick metallic walls. Lehmann et al. [16] investigated the feasibility of fast neutron radiography with 14.0 MeV neutrons from a generator using hydrogen loaded neutron conversion screen.

Very high sensitivities to a particular element or isotope can be obtained if neutron radiography is accomplished at the resonance energy of a neutron cross-section [5], by using a detector with a resonance reaction or a time-of-flight energy separation technique. Schrack [17] examined the suitability of using resonance neutron radiography as a mean to monitor the amount of ^{235}U in waste materials. ^{235}U concentrations ranging from 4.8×10^{-4} to 4.6×10^{-3} g/cm^3 were observed with uncertainty from 16% to 2.5% using a position sensitive ^3He detector. Neutron resonance transmission analysis was carried out by Overley [18] and obtained two-dimensional elemental-density projection of some light elements (H, C, N and O) with 10% uncertainty by measuring the energy spectra of transmitted fast neutrons using time-of-flight techniques.

Neutron radiography using thermal neutron beam is classified according to the temporal resolution of the image detector into three methods; static or film neutron radiography, real-time neutron radiography (RTNR) (with the recording speed of 25-30 frames/s), and high-speed neutron radiography (HSNR) or high-frame rate neutron radiography (HFRNR).

2.1.1 Static Neutron Radiography

The exposure times involved in static neutron radiography techniques are usually greater than one second so they are essentially a static technique [1]. After the neutron beam has penetrated the object a conversion screen is used to absorb neutrons to produce an α, β, γ-ray, or electron beam that exposes an image recorder either directly or indirectly. Static neutron radiography image recorders are categorized into photographic film and track-etch recorders.

No special films are available for neutron radiography, and standard X-ray and photographic films are normally used. These films consist of a base material with a gelatin coating in which fine grains (0.1 – 3.0 μm) of silver halides are dispersed. When photons or electrons (resulting from neutron conversion) fall on the film, an emulsion occurs and silver ions are reduced to metallic silver to form a latent image. When developed with suitable agents the unaffected grains are dissolved away by the fixing solution, leaving a black metallic-silver image where the density of silver increases almost uniformly with exposure.

Film radiographic techniques involve two different approaches [5]; the direct exposure method and the transfer (indirect) method. In the direct exposure method, the film is actually present in the neutron beam during the exposure. In the transfer method, the film needs not to be exposed to the neutrons; the film exposure is made by "autoradiography" using a radioactive, image-carrying metal screen.

For the direct exposure method, neutron conversion screens are chosen to increase the detector (film) response by emitting radiation to which the adjacent film is sensitive [5]. As the conversion processes are continuous reactions, this method can be used with low neutron fluxes and long integration exposures. The direct method provides faster results and yields better spatial resolution.

The transfer method has the advantage that the film is not present in the imaging beam. Therefore, the film will not be exposed to gamma radiation from a radioactive object, from reactions between neutrons and objects in the beam path, or gamma rays in the radiation beam itself. The most common materials for transfer neutron radiography are indium ($T_{1/2}$ = 54 min) and dysprosium ($T_{1/2}$ = 140 min). The transfer technique has been widely used to inspect radioactive materials such as irradiated reactor fuels.

In the track-etch recording techniques, the tracks caused by radiation damage in a dielectric can be chemically etched so these tracks become visible, and the collection of many tracks can form a visual image [5]. For neutron radiography, most track-etch applications have involved plastics and neutron converters that emit alpha particles (such as boron or lithium.) Alpha particles cause surface-damage pits and take short, relatively straight, paths giving good spatial resolution [1]. When compared to photographic film/foil techniques, the track-etch technique has the advantage of being insensitive to gamma rays thus a gamma filter is unnecessary, which lead to a flux gain for the same neutron source. On the other hand, longer irradiation times are required due to lower neutron absorption of boron and lithium.

Examples of static neutron radiography applications include the detection of residual ceramic cores in an investment-cast turbine blade [19], detection of corrosion in a metallic assembly [20], detection of explosives in metallic assemblies [21] and inspection of rubber O-rings in a valve [22]. A recent application of neutron radiography as a non-destructive testing tool has been applied to automobile exhaust studies where it has been used to measure thickness of particulate matter deposit in various components of diesel exhaust systems as part of pollution control studies [23].

2.1.2 Real-Time Neutron Radiography (RTNR)

For many years, the commonly used neutron radiography technique was the film (static) method. Although a good spatial resolution has been obtained with this technique, there are many drawbacks demanding new detection systems with more flexible performance, especially with respect to time resolution, dynamic range and quantitative information from the images [24].

Real-time neutron radiography systems quickly followed the introduction of the image intensifiers and a television imaging system sensitive to neutrons has been demonstrated in 1966 by Berger [25]. Real-time neutron radiography systems depend on the fact that neutron-to-light converters (scintillators) yield light when irradiated with thermal neutrons. The resultant light can be amplified by image intensifiers and/or detected by television cameras.

Early camera systems made use of Silicon-Intensifier Target (SIT) video cameras [26] giving way to the use of wide dynamic range charged coupled device (CCD) cameras [27,28]. The CCD cameras showed good sensitivity, linearity and high signal-to-noise ratio (SNR) [29] but images often suffered from the display of random white spots, caused by scattered radiation in the system electronics.

Due to the strong scattering and absorption of thermal neutrons by hydrogen nuclei, dynamic neutron radiography is extremely efficient in investigations of the spatial distribution of hydrogenous liquids [30].

Most of the dynamic neutron radiography applications, known so far, consist in visualisation of fluids moving through metallic containers. In fact, the hydrogen content in such fluids is detected. The main fields where dynamic neutron imaging has been applied are; multi-phase flow and thermal hydraulics, transfer and migration of fluids into porous media, fuel behaviour. Other research fields using RTNR include; agricultural [31], electrochemical [32] and petrophysical [33] applications.

Real-time neutron radiography has been applied extensively for the visualization and measurements of multiphase flow and thermal hydraulic phenomena. Cimbala et al. [34] visualized streak lines of injected gadolinium oxide in a relatively transparent ($\Sigma_t = 0.254\,\mathrm{cm}^{-1}$) fluorinert liquid flowing around 6.35 mm cylinder in 25.4 mm aluminium pipe. Mishima et al. [35] and Harvel et al. [36] demonstrated the ability to use RTNR for air-water flow visualization and flow regime identification in simple and complex structures. Bubbly, slug, churn and annular flow regimes were identified in narrow rectangular ducts [35] and MAPLE-type research reactor fuel channel [36]. Image processing has been applied to measure void fraction by Takenaka et al [37] and Glickstein et al. [38]. Uchimura et al. [39] were able to measure bubble rise velocity and interfacial area concentration by frame isolation. Iwamura et al. [40] used RTNR technique to visualize boiling flow inside a stainless steel shroud just before and after the onset of critical heat flux (CHF). Tsuji et al. [41] visualized water behaviour in a bent stainless steel thermosyphon.

Jasti et al. [42] applied neutron radiography to visualization of dye penetration in porous media. Nemec et al. [43] studied the intrusion and transport of moisture in porous clay samples of building materials. Milczarek et al. [30] observed of water migration in porous building media.

RTNR has not been limited to the visualization of water only but other fluids have been used such as; oil, refrigerants, plastic, etc. Jones et al. [44] examined the flow of oil inside an internal combustion engine. Takenaka et al. [45] visualized cavitation phenomenon in a diesel engine fuel injection nozzle. Asano et al. [46,47] applied RTNR for the visualization and measurement of refrigerants (R-22) and (H-134a) flow in compression-type refrigerator. Kramer et al. [29] studied the behaviour of direct methanol fuel cell. Weissenberger et al. [48] visualized plastic jet-injection mold filling operations.

A few researchers have applied RTNR to liquid metal (lead-bismuth eutectic) flow visualization and measurements [49,50]. The applicability of RTNR was limited by the fact that the large density difference between the gas and liquid phase results in fast transients.

Although real-time neutron radiography with a recording speed of 30 frames/s is mainly employed as a dynamic method, this fact does not mean that this technique meets most needs for visualization of moving objects. The technique has been restricted to the visualization of relatively slow phenomena and measurements of time-averaged quantities [2].

2.1.3 High-Speed Neutron Radiography (HSNR)

A recording speed faster than 1000 frames/s is required to visualize phenomena in which objects move rapidly. This restriction could be a fatal shortcoming in applying dynamic neutron radiography to various scientific fields. High-speed neutron radiography with pulsed neutron was invented to overcome this limitation [2,34,51]. A high-intensity pulse (or flash) of neutrons lasting a few milliseconds can be achieved by removing part of the fuel in the reactor core to make the reactor sub-critical, then the missing fuel is passed rapidly through the core causing the reactor to become super-critical for a short time period thus producing a pulse of neutrons with a very large amplitude.

Although a very large amplitude thermal neutron flux in the range of 10^{11} n/cm^2-s is achieved [51], which allows for a recording speed higher than 10000 frames/s, the very short pulse duration (7-35 ms) was only sufficient to obtain a few images (5-10 frames). This method has other limitations such as the need of a triggering signal and rapidly changing neutron flux with time in addition to that most pulse reactors can only produce a few pulses per day.

When both high-speed and long recording time are required, high-speed neutron radiography with a steady (non-pulsed) neutron beam is required. The purpose of using high-speed neutron radiography with a steady neutron beam is to visualize rapid phenomena, in which object particles have a speed greater than 1.0 m/s, for a long time period. Therefore, a high-speed camera with a relatively long recording time (> 30.0 s) should be used. Otherwise, the capability of high-speed neutron radiography with a steady neutron beam is consequently similar to that with a pulsed neutron beam. Most of high-speed cameras developed recently adopt an electronic memory as a recording device and so the images manipulation, such as image post-processing, data extraction, archiving and data transfer, is much easier.

Hibiki and Mishima [52] succeeded in performing high-speed neutron radiography with a steady thermal neutron beam of 1.2×10^6 n/cm^2-s, but it was limited for small thickness object (2.4 mm of light water) and a recording speed of 500 frames/s.

The achievement of high flux thermal neutron beam, of the order 10^8 n/cm^2-s at the JRR-3M Research Reactor [7], has opened up the way to apply dynamic neutron radiography to visualization and measurements of rapid transient phenomena.

Table 2.1 shows the performance characteristics of research reactors based facilities used for high-speed neutron radiography.

The application of high-speed neutron radiography as a research tool was concentrated in Japan at the JRR-3M Research Reactor (1.5×10^8 n/cm^2-s) for the visualization and measurement of air-water two-phase flow in narrow metallic ducts [53,54], steam explosion and molten metal-water interaction [55,56], gas-molten metal flow with large density difference [57,58] and vapour generation in sub-cooled boiling [59,60].

2.2 Other Neutron Based Measuring Techniques

Neutron techniques are of particular interest due to their ability to provide isotopic and elemental information. A neutron, as a neutral particle, is not affected by the electromagnetic forces of the atom and therefore interacts with all nuclei. Neutron

Table 2.1. Performance characteristics of developed high-speed neutron radiography facilities.

	Bossi et al. 1982	Cimbala et al. 1988	Mishima and Hibiki 1996	Hibiki et al. 1994	Hibiki and Mishima 1996
Reactor	OSUR	PSBR	NSSR	JRR-3M	KUR
Source Type	Pulsed	Pulsed	Pulsed	Steady	Steady
Power (MWth)	3000 (pulse)	2000 (pulse)	23000 (pulse)	20	5
Neutron flux (n/cm^2sec)	$4.2x10^{11}$	N/A	$1.0x10^{10}$	$1.5x10^8$	$1.2x10^6$
Cd ratio	2.24	56	8.7	130	400
L/D ratio	30 horizontal 41 vertical	55	67	176 horizontal 153 vertical	100
n/γ ratio (n/cm^2-μSv)	N/A	$3.6x10^4$	$5.0x10^3$	$6.25x10^5$	$1.0x10^5$
Frame rate (frames/s)	10000	2000	500	10000	1000
Reference	[51]	[34]	[2]	[2,7]	[2]

techniques include neutron radiography, neutron gauging (transmission, scattering and/or moderation), and neutron activation.

In both neutron radiography and gauging, the penetration nature of neutron radiation is used to obtain information about the internal structure of an object [4]. Neutron gauging, the older of the two fields, consists in its basic form of a neutron source and one or more detectors used in either transmission geometry or scattering geometry. Radiography, on the other hand, consists of a set of radiation sources and a two-dimensional detector and the output is a two dimensional image. Gauging melds into radiography when the detectors in a gauging system are used in a special scanning mode [61].

Although neutron gauging is more sensitive than neutron radiography, it is less commonly used than radiography. Neutron radiography is widely used as a non-destructive tool for evaluation of materials, while neutron gauging, however, is still used in some particular fields.

Neutron activation is perhaps the most powerful and definite elemental identifier, as it results in the production of gamma rays that are characteristics of the neutron absorbing element or isotope [62]. Thermal neutron activation is the preferred mode of interaction, since the activation cross-section is usually highest in the thermal neutron energy region. Fast neutron activation is a more practical approach for a portable device, since fast neutrons are readily emitted from isotopic sources and neutron generators. The gamma rays emitted in fast neutron activation are mostly produced by the inelastic scattering of fast neutrons.

In principle, with respect to the time of measurement, neutron activation analysis falls into two categories: prompt neutron activation analysis and delayed neutron activation analysis [63]. In the prompt neutron activation, the emitted gamma ray occurs instantaneously. Delayed gamma emissions occur when the target nucleus is transmuted to a radioactive nucleus that decays later through gamma decay.

2.2.1 Neutron Transmission (Attenuation) Techniques

Early developers of radiation techniques concentrated on utilizing transmitted (uncollided) thermal neutrons [64,65]. These techniques require, however, the availability of an intense thermal neutron beam. The beam can be extracted from either a nuclear reactor or a bulky thermalization assembly containing an isotopic source. The transmission of fast neutrons can overcome the need for a strong source, since fast neutrons have lower attenuation coefficients.

Another transmission technique depends on the presence of strong resonances in the neutron cross-sections. By measuring the energy spectra of transmitted neutrons, elemental information can be obtained providing that the cross-sections for these elements exhibit resonances at some energies. Neutron resonance transmission analysis with slow neutrons was used by Behrens et al. [66] to measure the isotopic content of fresh and spent nuclear fuel pellet samples. While Overley [67] used the technique with fast neutrons to obtain elemental content of bulk organic materials. Accelerators were used in the above work. Gokhale and Hussein [68] examined the feasibility of a similar approach, employing a ^{252}Cf neutron isotopic source, for bulk detection of explosives.

2.2.2 Neutron Scattering Techniques

Small Angle neutron scattering (SANS) refers to the coherent scattering of neutrons at small angles (~ 5°) [69]. The coherent scattering of neutrons is a consequence of the interaction of neutrons with all nuclei throughout the material. SANS has been a well-established technique for microstructure studies of alloys, ceramics, polymers where information is required over distances of the order of tens of Angstroms [70]. This method is sensitive to any density fluctuations and/or composition fluctuations such as; precipitates, voids, cavities, etc [70].

Techniques based on epithermal/fast neutron scattering have been developed [71-73] to determine the average void fraction and/or steam quality in gas-liquid two-phase flow in pipes. These techniques rely on measuring the amount of thermal neutrons produced as a result of the combined slowing down and attenuation of fast neutrons by the liquid phase. The number of thermal (slow) neutrons scattered depends strongly on the density of available scattering material, and consequently can provide an estimate of the volume (void) fraction [74]. Epi-thermal and fast neutron scattering techniques are less sensitive to the spatial phase-distribution and the magnitude of the signal produced is proportional to the amount of liquid present in the pipe.

2.3 Neutron Tomography

Traditional radiography has limits since it only provides information on the total attenuation integrated over the path of the radiation through the material [75]. Details of internal structure are easily hidden in this effective averaging. Tomography using the method of image reconstruction from projections allows two- and three-dimensional details to be obtained and the object to be visualized in cross-sectional views, retaining the spatial distribution of radiation attenuation characteristics and thus the details of the object's internal structure [76].

The advantages of neutron tomography over radiography were realized in the late 1970's and prototype systems assembled and tested [77]. Later, resolution on the order of 1 mm was obtained using film radiography [78,79] and a neutron television system utilizing a neutron scintillator and video camera [80]. The advances of cooled slow-scan CCD cameras and computer technology during the last decade have made three dimensional neutron computed tomography feasible in a reasonable scan time [10]. Although the applicability of neutron radiographic techniques for computed tomography are limited to static objects, some researchers applied the technique to obtain time averaged three dimensional distributions [15, 81].

Another neutron tomography technique (scatterometer) that is based on fast neutron scattering has been developed [82]. In this technique, the elastic scattering of neutrons at a particular angle and the energies of these scattered neutrons are dependant on the energy of incident neutrons as well as the mass number of the scattering nucleus. This technique can be used for dynamic tomography, however, its applicability is limited by the low probability of neutron scattering to a certain angle and the poor detection efficiency of fast neutrons and therefore, a large incident neutron flux is required.

3 ADVANCED DYNAMIC NEUTRON RADIOGRAPHY FACILITY

This Chapter describes the design and construction of the components of the dynamic neutron radiography facility at the McMaster Nuclear Reactor. The first section describes the selection and experimental evaluation of the neutron source for the facility including determining the source strength based on dynamic radiography requirements. Section three describes the analysis and characteristics of the different facility components such as: the beam tube liner, gamma ray filter and biological shielding. The last section describes the characteristics of the neutron radiography system components (camera, neutron conversion screen and image recording and processing systems).

3.1 McMaster Nuclear Reactor and Source Flux Mapping

Many neutron sources have been used for neutron radiography. These include accelerators, radioisotopes, sub-critical assemblies or nuclear reactors [4]. Nuclear reactors provide the most intense neutron beams and therefore higher quality neutron radiographs. The disadvantages of nuclear reactors are their lack of mobility and high capital cost, while their advantages are their intense neutron intensity and their low operating cost per neutron [1]. Most of the reactors in use for neutron radiography are principally research reactors and their high utilization justifies the capital cost.

The McMaster Nuclear Reactor (MNR) is a 5.0 MW light-water moderated/cooled pool-type research reactor. The reactor is normally operated in a range from 2.0 – 3.0 MW. Six perpendicular and one tangential beam tubes are installed in the reactor pool as shown in Figure 3.1. Beam Port #3 (BP3) has been selected for the advanced dynamic neutron radiography facility [83]. Being a perpendicular beam tube, BP3 has the advantage of streaming a higher thermal neutron intensity.

An operating reactor is a powerful source of radiation, since fission process and subsequent radioactive decay of fission products produce neutrons and gamma rays with various energies, which are highly penetrating radiations. Fission neutrons are born at about 2.0 MeV and are slowed down by moderation to the thermal energy region of approximately 0.3 eV. Thus a nuclear reactor produces fast neutrons, thermal neutrons and gamma rays in prolific quantities. Therefore, an evaluation of the source strength is required in order to determine the amount of thermal neutrons available for beam extraction and the amount of biological shielding necessary to attenuate the fast neutrons and gamma rays.

A neutron flux mapping experiment has been conducted to evaluate BP3 source strength where copper foils have been irradiated approximately 1.0 mm from BP3 tube entrance. Two different measurements were conducted, one with bare copper foils and the second with copper foils enclosed in cadmium. As such, the activity produced in the bare copper foils is due to absorption of thermal and epi-thermal neutrons and the activity produced in the Cd-enclosed foils is due primarily to the absorption of epi-thermal (with energies higher than cadmium cut-off) neutrons only. Figure 3.2 shows a top-view of the MNR core arrangement installed during experimental flux measurements at the beam port entrance including the location where the copper foils have been irradiated.

Copper has two naturally occurring isotopes, ^{63}Cu (60.09%) and ^{65}Cu (30.91%).

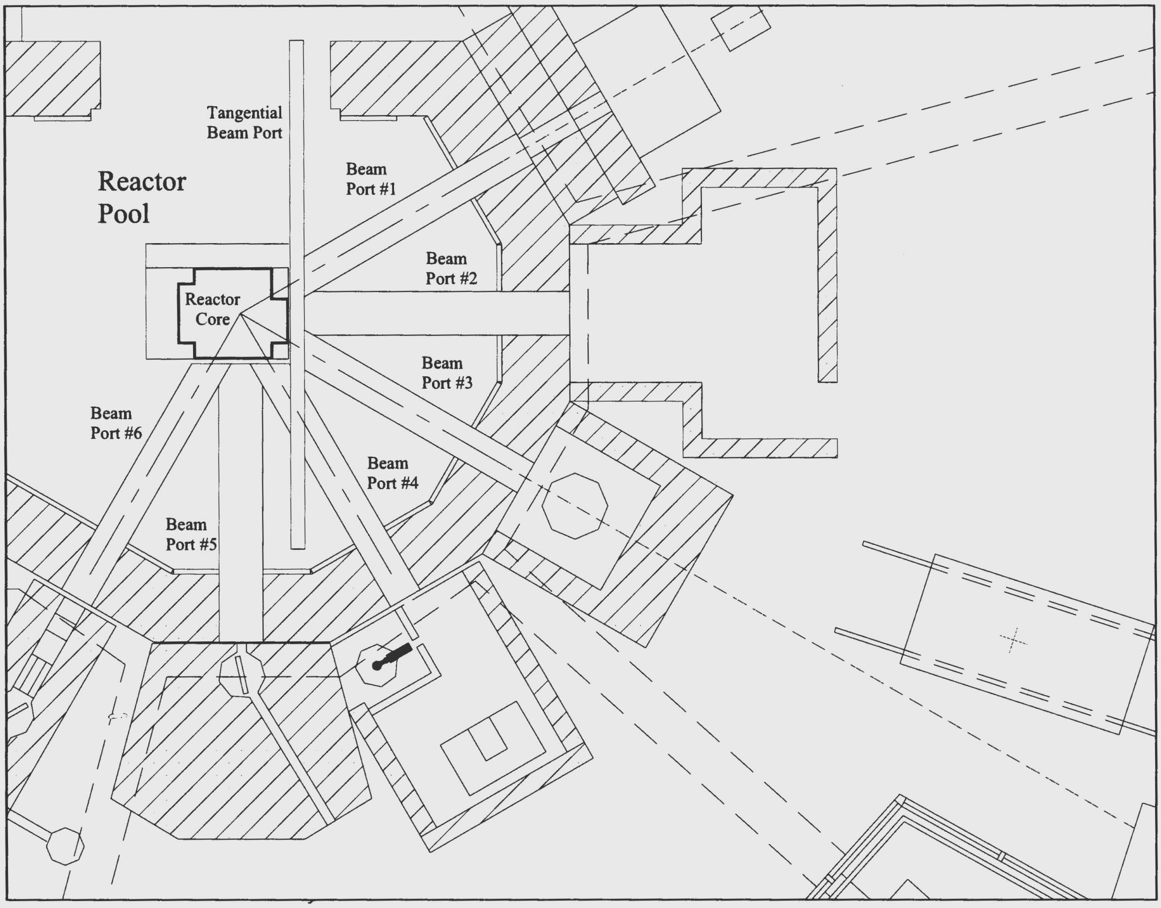

Figure 3.1. Schematic of MNR core and beam ports arrangement (Top view) as of January 2002 (Before Facility Construction).

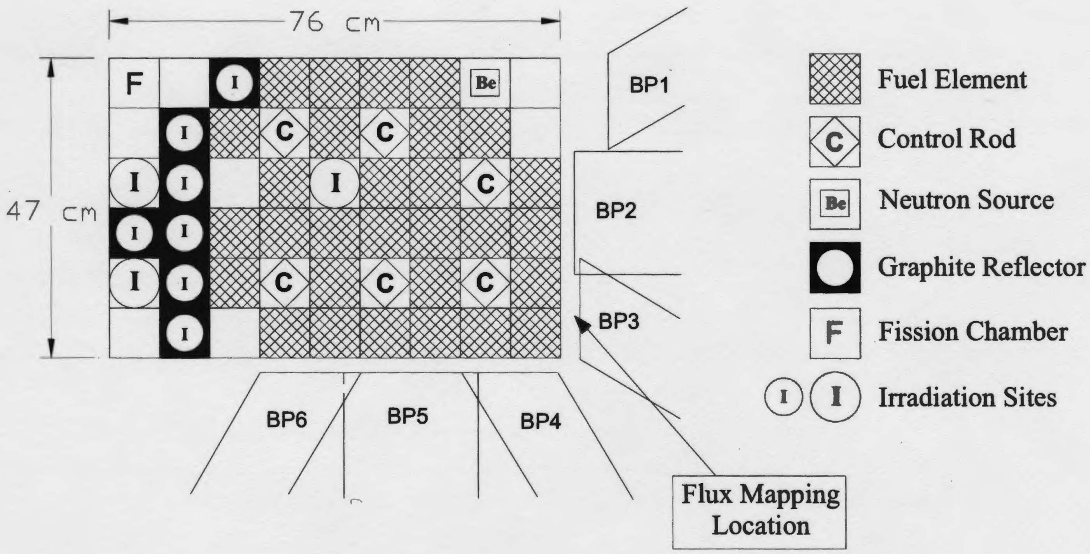

Figure 3.2. MNR core arrangement and flux mapping measurement location.

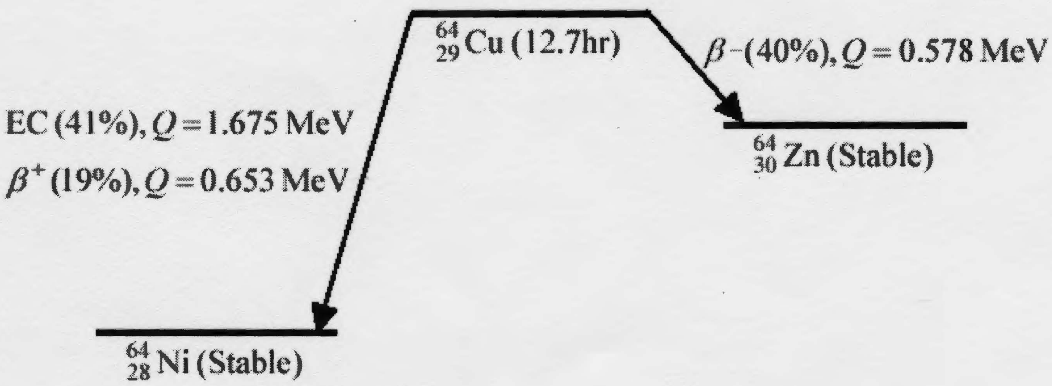

Figure 3.3. Decay scheme for ^{64}Cu [84].

When a ^{65}Cu nucleus captures a neutron, the product nucleus, ^{66}Cu ($T_{1/2}$ = 5.1 min), is unstable and it undergoes β^--decay (Q = 2.632 MeV) to produce the stable nucleus ^{66}Zn [84]. When a ^{63}Cu nucleus captures a neutron, the product nucleus, ^{64}Cu ($T_{1/2}$ = 12.7 hr), is unstable and it decays through three different decay modes as shown in Figure 3.3. The neutron flux mapping measurements are based on detecting the β^+-decay mode of ^{64}Cu nuclei. The positron emitted in the primary decay process, at the end of its travel, combines with a normal negative electron where both disappears (annihilate) and replaced by two oppositely directed 0.511 MeV gamma ray photons.

The net count rate of the 0.511 MeV gamma rays at the end of irradiation time, Δt, in a bare copper foil is given by;

$$A_{Bare} = C_F \times I_{Cu} \times \eta\, V(1 - e^{-\lambda\Delta t}) + \sigma_{Cu} \times \phi_o \times \eta\, V(1 - e^{-\lambda\Delta t}) \qquad (3.1)$$

and hence

$$A_{Bare} = (C_F \times I_{Cu} + \sigma_{Cu} \times \phi_o) \times \eta\, V(1 - e^{-\lambda\Delta t}) \qquad (3.2)$$

All foils have the same volume, V, same detection efficiency, η, and same irradiation time; hence, Equation 3.2 can be simplified to

$$A_{Bare} = \alpha\, (C_F \times I_{Cu} + \sigma_{Cu} \times \phi_o) \qquad (3.3)$$

Similarly, the activity produced in cadmium enclosed foil is given by:

$$A_{Cd} = \alpha\, (C_F \times I_{Cu}) \qquad (3.4)$$

where A_{Bare} is the net count rate of a bare copper foil at the end of irradiation time, A_{Cd} is the the net count rate of a Cd-enclosed foil at the end of irradiation time, α is the net counts per neutron absorbed, C_F is the 1/E epi-thermal neutron flux constant, ϕ_o is the

2200 m/s (E_o = 0.0253 eV) neutron pseudo-flux, I_{Cu} is the ^{63}Cu resonance integral and σ_{Cu} is the ^{63}Cu 2200 m/s neutron capture cross-section.

To omit the effects of detection efficiency, foil weight, etc., the value of the net counts per neutron absorbed, α, was obtained by calibrating the net 0.511 MeV gamma rays counts of two copper foils (one bare and one shielded in Cd) irradiated at position 8D in the MNR core to the neutron flux measured at this location using a self-powered neutron detector (SPND).

Self-powered neutron detectors are unique devices widely applied for in-core neutron flux measurements. These devices incorporate a material (such as rhodium or vanadium) with relatively high neutron capture cross-section leading to subsequent beta decay. The detector operates on the basis of directly measuring the beta decay current following the capture of the neutrons with no external voltage applied. This current is proportional to the rate at which neutrons are captured and hence the neutron flux [85]. The neutron sensitivity of the self-powered neutron detector (Reuter-Stokes Canada Ltd, Model M-3 Rhodium) used to measure the neutron flux at position 8D is 1.2×10^{-21} A/(n/cm^2-s)-cm [86].

The value of neutron flux measured by the SPND, ϕ_{SPND}, can be related to the thermal and epithermal neutron fluxes using the following relation;

$$\phi_{SPND} = \phi_o + C_F \times I_{Rh} / \sigma_{Rh} \qquad (3.5)$$

where I_{Rh} is the rhodium resonance integral and σ_{Rh} is the rhodium 2200 m/s neutron capture cross-section.

The above equations are subject to the following assumptions;

- activity due to neutron capture in ^{63}Cu only (actual activity measurements were taken after at least 28.0 hrs so that any ^{66}Cu activity has been reduced to negligible levels),
- the SPND measures total (thermal and epi-thermal) flux,
- Cadmium foils will attenuate all thermal neutrons and has negligible attenuation for the epi-thermal flux.

Figure 3.4 shows thermal and epithermal neutron fluxes profiles along the beam tube horizontal centre-line at the core-side obtained from flux mapping measurements using copper foils irradiation. The average thermal flux and the average 1/E flux constant, C_F, obtained (per MW operation) were 3.0×10^{12} and 1.28×10^{11} n/cm^2-s respectively. The neutron flux profiles shown in Figure 3.4 are not symmetric since Beam port #3 is located to the side of the reactor core vertical centre line. As such the neutron fluxes decrease as the distance from the core centre line increases. Table 3.1 lists the neutron parameters of different materials used in calculating neutron flux values at the beam tube entrance.

Figure 3.5 shows the estimated neutron spectrum at the beam port entrance based on the experimental flux measurements. In this figure, the neutron spectrum is normalized to a maximum of 100 (arbitrary units), and a neutron temperature of 32 °C is used for the thermal neutron Maxwellian spectrum based on the average temperature of the moderator around beam tube entrance [88].

The gamma ray strength at BP3 entrance was estimated from the value of neutron-to-gamma ratio reported for BP2 and the thermal neutron strength at BP3 evaluated by the

Table 3.1. Neutron parameters used in flux mapping measurements [87].

	^{63}Cu	Rhodium	Cadmium
2200 m/s Capture Cross-section (barn), σ	4.5 ± 0.02	155 ± 3	2570 ± 50
Resonance Integral (barn), I	4.97 ± 0.08	1175 ± 55	70 ± 10

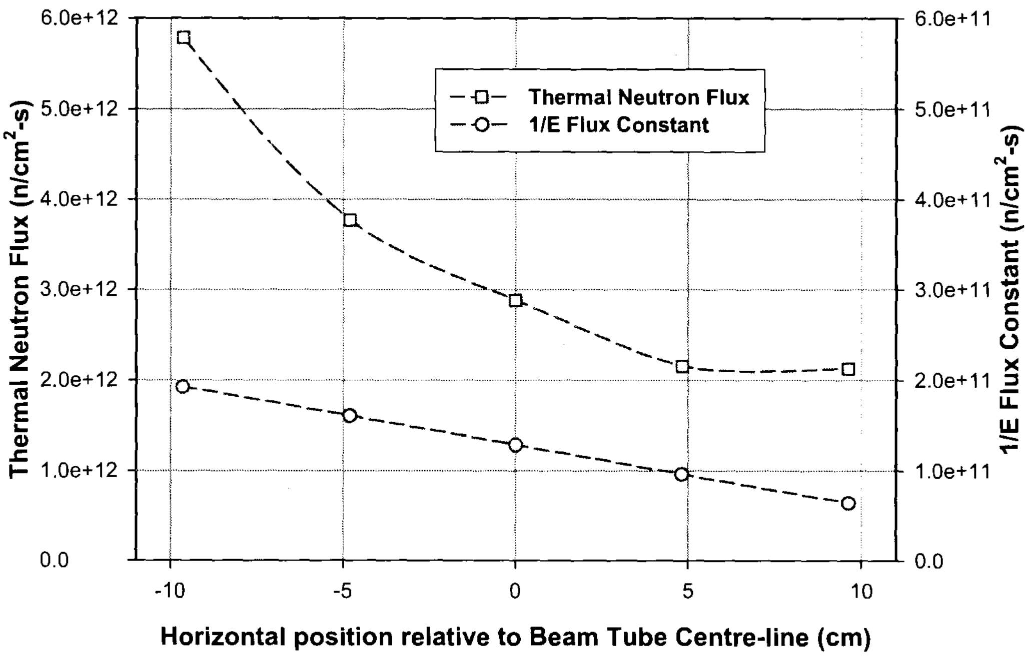

Figure 3.4. Thermal and epithermal neutron fluxes profiles along beam tube horizontal centre-line at core-side face calculated from the activity of irradiated copper foils.

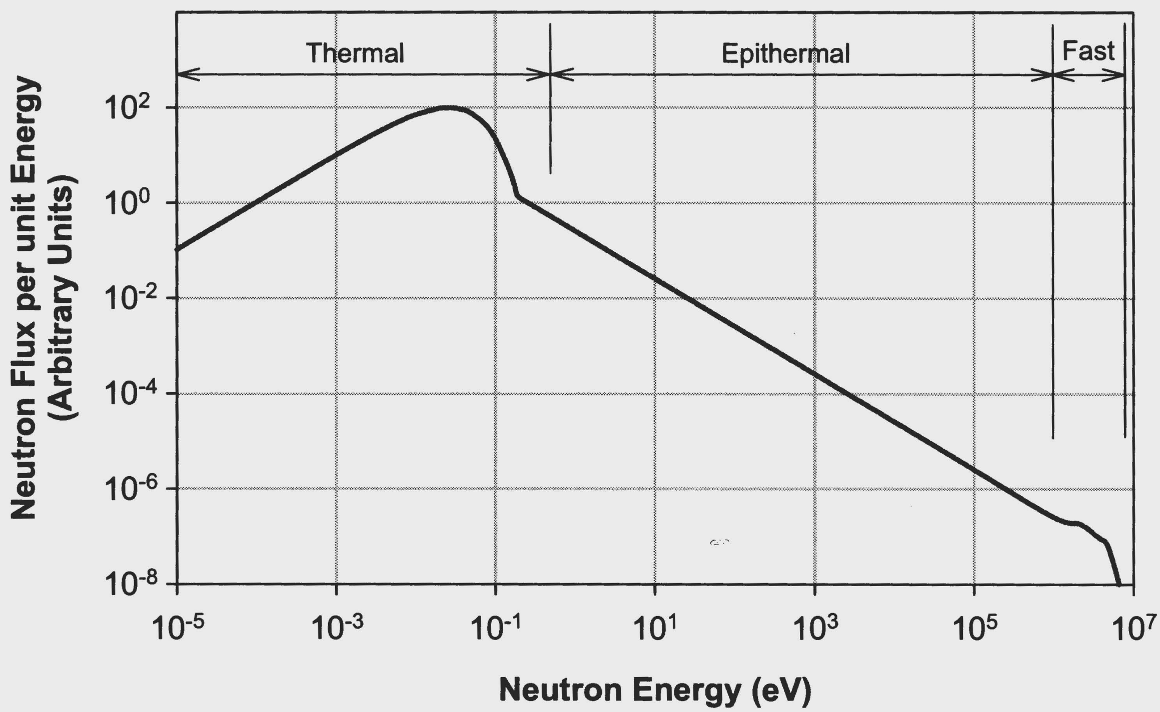

Figure 3.5. Normalized neutron energy spectrum at beam port entrance estimated experimentally by flux mapping in reactor pool location shown in Figure 3.2.

flux mapping experiment. A 15.24 cm (6") bismuth filter is installed in BP2 such that the neutron-to-gamma ratio, $[n/\gamma]$, is 6.0×10^{6} n/cm^2-μSv [88]. Using Equation 1.4 the neutron-to-gamma ratio at the beam entrance, $[n/\gamma]_{Source}$, is 8.724×10^{4} n/cm^2-μSv. Accordingly the gamma dose rate at the BP3 entrance, H_o, is estimated to be 1.24×10^{11} μSv/hr (per MW operation).

3.2 Neutron Intensity Requirement for Dynamic Neutron Radiography

The recording speed as a function of the thermal neutron intensity based on Equation 1.1 is shown in Figure 3.6 for various working fluids. Figure 3.6 shows that thermal neutron intensity greater than 3.0×10^{6} n/cm^2-s is required for high-speed imaging to obtain a wide application field with acceptable spatial resolution and image contrast.

Although higher thermal neutron intensity at the imaging plane is required, as it produces higher quality neutron images and promotes higher speed imaging, increasing the thermal neutron intensity is constrained by other limiting factors. A nuclear reactor produces both thermal and fast neutrons, and since fast neutrons have more penetration power than thermal neutrons, increasing the thermal neutron intensity will in turn increase the fast neutron intensity and larger volumes of biological shielding will be necessary resulting in reducing experimental space and hence limiting the application field of the facility. Figure 3.6 also shows that thermal neutron intensity required for high-speed imaging decreases when the working fluid has a lower macroscopic cross-section such as Freon, liquid metal or heavy water. Table 3.2 lists the thermal neutron parameters of

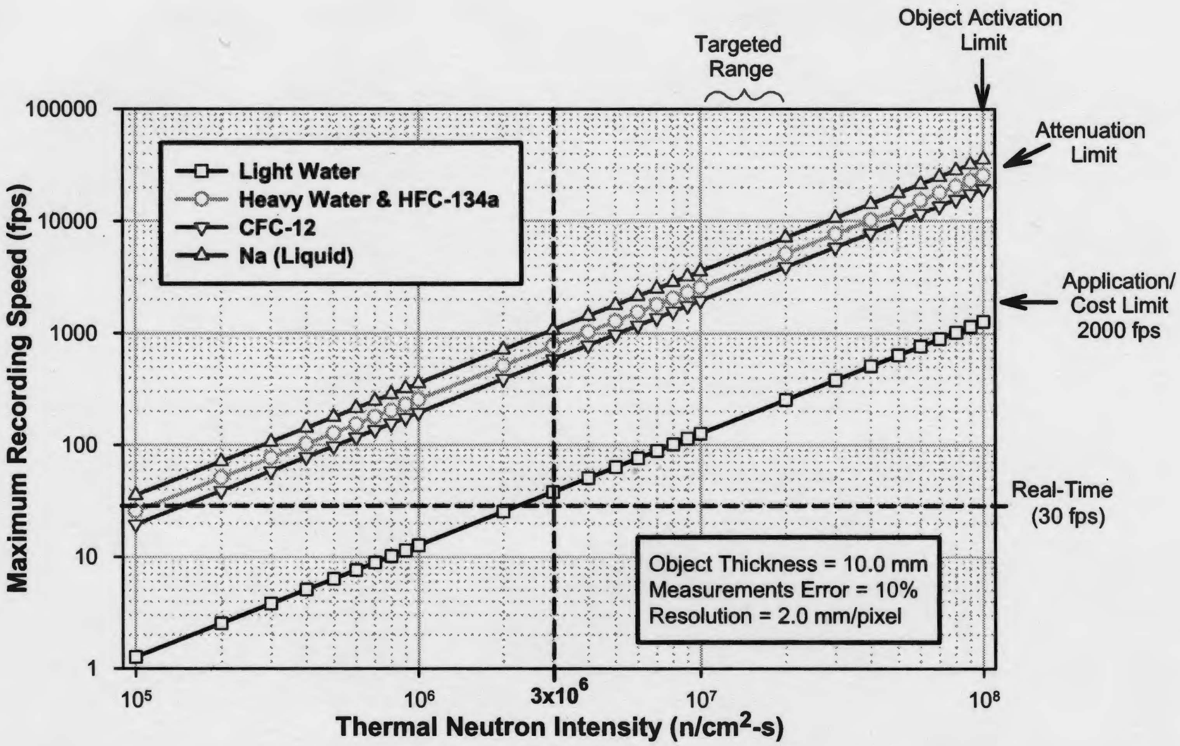

Figure 3.6. Recording speed as a function of thermal neutron flux for various working fluids based on Equation 1.1.

Table 3.2. Thermal neutron parameters of different working fluids [89].

Working Fluid	Total 2200 m/s Macroscopic Cross-section (cm^{-1})	Mean Free Path (cm)
Light water	3.45	0.29
Heavy water	0.449	2.23
Liquid Sodium	0.115	8.70
Chlorofluorocarbon (CFC 12)	0.72	1.39
Hydrofluorocarbon (HFC 134a)	0.47	2.13

different working fluids used in Figure 3.6 calculations. It should be noted that the analysis used to obtain Equation 1.1 was performed based upon an ideal system where the effects of background radiations, neutron detection efficiency and signal noise are not considered.

3.3 Facility Components

3.3.1 Beam Tube Liner

Neutrons move about the moderator in a random manner and cannot be focused. The function of beam tube liner is to shield source neutrons and allows some of the neutrons to stream down a hole in this shield.

Thermal neutrons can be attenuated very easily, hence a higher targeted centre-value of thermal neutron intensity at the imaging plane has been selected to provide adequate margin to contain any errors resulting from experimental measurements, component fabrication and installation.

Table 3.3 summarizes the targeted centre-values of beam characteristics that form the guidelines for the beam tube liner design.

3.3.1.1 Beam Tube Liner Geometry

From the geometrical representation of the beam tube, collimator and imaging plane as shown in Figure 3.7, the following equation can be derived which relates the required *L/D* ratio and the collimator aperture and position;

Table 3.3. Summary of targeted beam characteristics at the imaging plane (at 3.0 MW).

	Targeted centre-value	Acceptable range
Thermal neutron intensity [I], n/cm^2-s	1.5×10^7	$3\times10^6 - 10^8$
Collimation ratio [L/D]	120	> 100
Neutron-to-gamma ratio [n/γ], n/cm^2-μSv	10^5	$> 3\times10^4$
Imaging area diameter, cm	20.0	> 15.0*

* Smaller dimensions are acceptable but limit application.

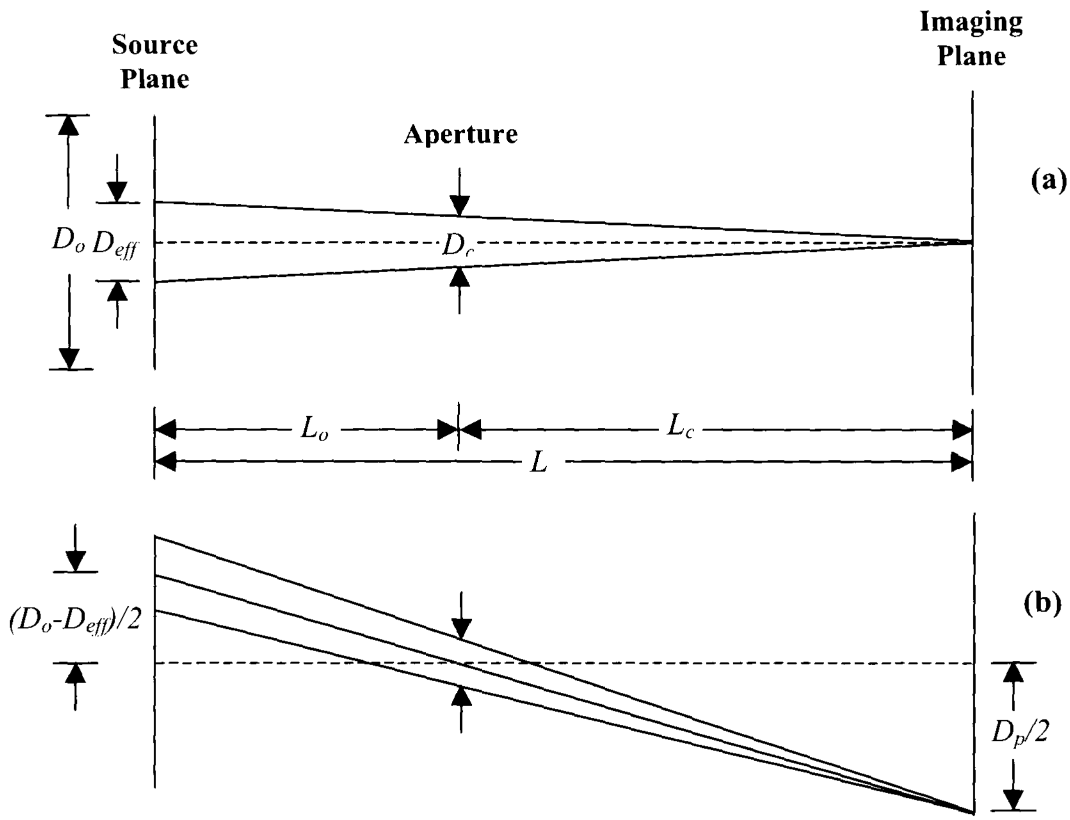

Figure 3.7. Beam tube geometrical representation. **(a)** Source projection to a point at the centre of the imaging plane, **(b)** Source projection to a point at the edge of the imaging plane.

$$\frac{L_c}{D_c} = \frac{L}{D_{eff}} > (\frac{L}{D})_{\mathrm{Re}quired} \tag{3.6}$$

Hence the effective source diameter is given by

$$D_{eff} = L/(L/D)_{Required} \tag{3.7}$$

where D_c is the collimator-aperture diameter, L_c is the distance between the collimator aperture and the imaging plane.

The position of the collimator aperture is to permit the projection of each point in the imaging plane onto the source area with a projection diameter equal to D_{eff}. This criterion leads to the following relation (See Figure 3.7 b);

$$L_c = L/(1 + \frac{D_o - D_{eff}}{D_p}) \tag{3.8}$$

where D_o is the source diameter, D_p is the image diameter. Accordingly, by inserting Equation 3.6 into Equation 1.5, the thermal neutron intensity at the imaging plane, I, is given by;

$$I = \frac{\phi_i \exp[-(\Sigma X)_{Filter}]}{16\,(L/D_{eff})^2} \times \cos 30 \tag{3.9}$$

where the angle of the source plane (30°) is taken into consideration

Table 3.4 gives the position of the collimator aperture, L_c, and its diameter, D_c, as a function of the required L/D value for different image diameters, D_p, and source diameter, D_o.

3.3.1.2 Gamma Filtration

Table 3.4. Collimator parameters and maximum achievable thermal neutron intensity calculated for different collimation ratios, image diameter and source diameter.

$(L/D)_{Required}$	D_{eff} (cm)	D_p = 30 cm, D_o = 10 cm.		D_p = 20 cm, D_o = 10 cm.		Maximum I without Filter (n/cm^2-s)
		L_c (cm)	D_c (cm)	L_c (cm)	D_c (cm)	
80	7.50	553.8	6.92	533.3	6.67	8.8×10^7
90	6.67	540	6.0	514.4	5.72	6.9×10^7
100	6.00	529.4	5.29	500.0	5.00	5.6×10^7
120	**5.00**	514.3	4.29	**480**	**4.00**	$\mathbf{3.9\times10^7}$
150	4.00	500	3.33	461.5	3.08	2.5×10^7

$(L/D)_{Required}$	D_{eff} (cm)	D_p = 30 cm, D_o = 12 cm.		D_p = 20 cm, D_o = 12 cm.		Maximum I without Filter (n/cm^2-s)
		L_c (cm)	D_c (cm)	L_c (cm)	D_c (cm)	
80	7.50	521.7	6.52	489.8	6.12	8.8×10^7
90	6.67	509.5	5.66	473.7	5.26	6.9×10^7
100	6.00	500	5.00	461.5	4.62	5.6×10^7
120	5.00	486.5	4.05	444.4	3.70	3.9×10^7
150	4.00	473.7	3.16	428.6	2.86	2.5×10^7

The neutron image contrast and hence resolution is affected by the amount of gamma ray contamination in the neutron beam. To obtain a good quality neutron beam, the gamma ray content must be reduced sufficiently below the gamma sensitivity limits of the neutron detector. The gamma ray sensitivity for most neutron phosphorus scintillator screens – commonly used in dynamic neutron imaging – is such that 1000 ^{137}Cs gamma-ray photons (662 keV) give the same light output as 1.0 neutron [90]. In other words, for a thermal neutron beam with a neutron-to-gamma [n/γ] ratio of 2.772×10^{2} n/cm^2-μSv, 50% of the scintillator screen light output will be due to gamma rays. In order to minimize the errors due to neutron conversion screen sensitivity to gamma rays, the required n/γ ratio has been chosen to be greater than 3×10^{4} n/cm^2- μSv (i.e., less than 1.0% of the screen light output is due to gamma interactions.) Bismuth is commonly used since it has a relatively higher gamma attenuation [μ] and a relatively lower neutron attenuation [Σ].

As discussed previously, increasing the n/γ ratio conflicts with the neutron intensity requirement as shown by Equation 1.5. Therefore increasing the n/γ ratio will require in turn decreasing the *L/D* ratio in order to maintain the value of the thermal neutron intensity at the imaging plane. From a shielding point of view, a higher n/γ ratio and a higher *L/D* ratio are preferred, since thicker filters will attenuate more radiation and higher *L/D* ratio will stream down less radiation.

Material attenuation (filtering) is preferred for gamma rays while geometrical attenuation (tailoring) is preferred for fast neutrons where increasing filter thickness increases the gamma attenuation power but decreases the fast neutron attenuation power as a result of the necessary decrease in L/D ratio to maintain the value of the thermal neutron flux at the imaging plane according to Equation 1.5. The fast neutron dose rate at the source is higher than the gamma rays dose rate, therefore geometrical attenuation (tailoring) gives a higher reduction in the total dose rate at the imaging plane, as shown in Figure 3.8, where increasing the bismuth filter thickness increases the total dose rate, which is mainly due to fast neutrons, streaming out from the beam tube. Thus, in order to achieve the required thermal neutron intensity at the imaging plane, the thickness of the gamma ray filter should be minimized, according to the n/γ ratio required by the application, therefore the L/D ratio can be maximized resulting in lower dose rates at the imaging plane.

Using Equation 1.4, a 4.0-cm bismuth filter will produce a neutron-to-gamma ratio of 1.14×10^{5} n/cm^{2}-μSv. And using Equation 3.9 the thermal neutron intensity at the imaging plane is 1.56×10^{7} n/cm^{2}-s.

3.3.1.3 Beam Tube Liner Description

The beam tube liner is a converging-diverging collimator as shown in Figure 3.9. The collimator is divided into six lead segments with two Boral disks, each 3.2-mm in thickness, between every two segments. A 0.5-mm thick gadolinium foil, with a hole 4.0-cm in diameter, is placed between the collimator converging and diverging parts to provide aperture definition. A 4.0-cm bismuth plug is used as a gamma-ray filter just before the converging part of the collimator.

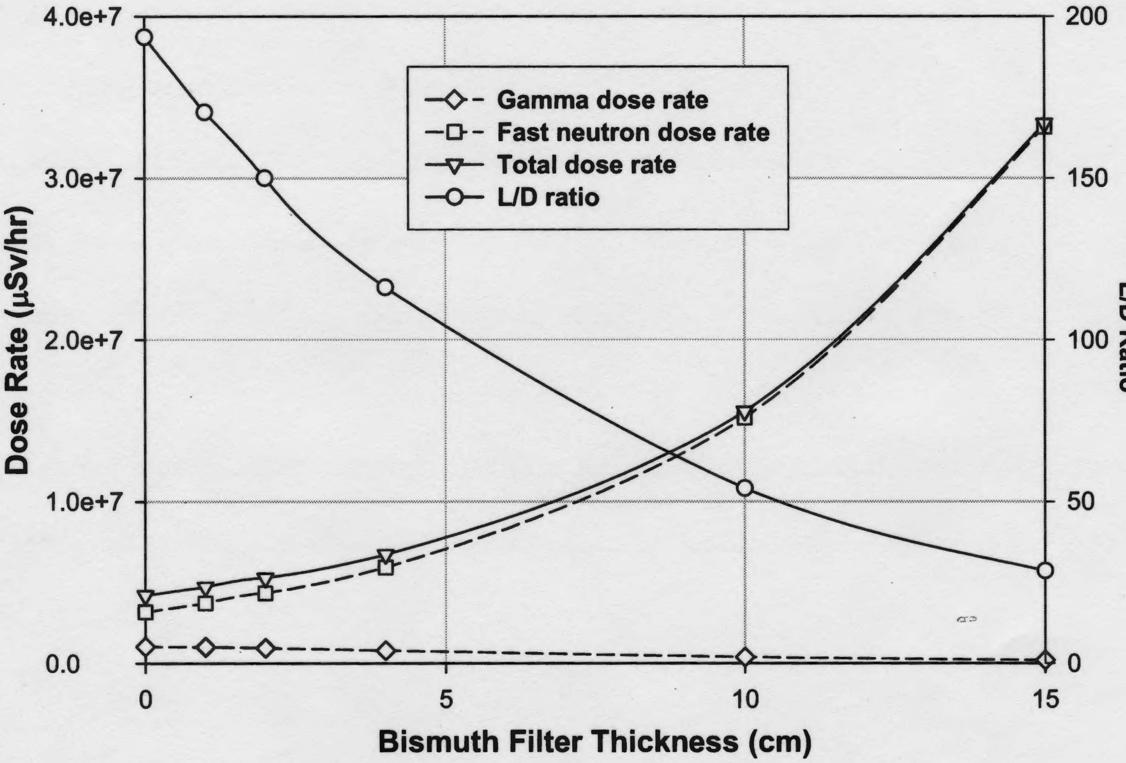

Figure 3.8. Collimation ratio and radiation doses at the end of beam tube as a function of bismuth filter thickness.

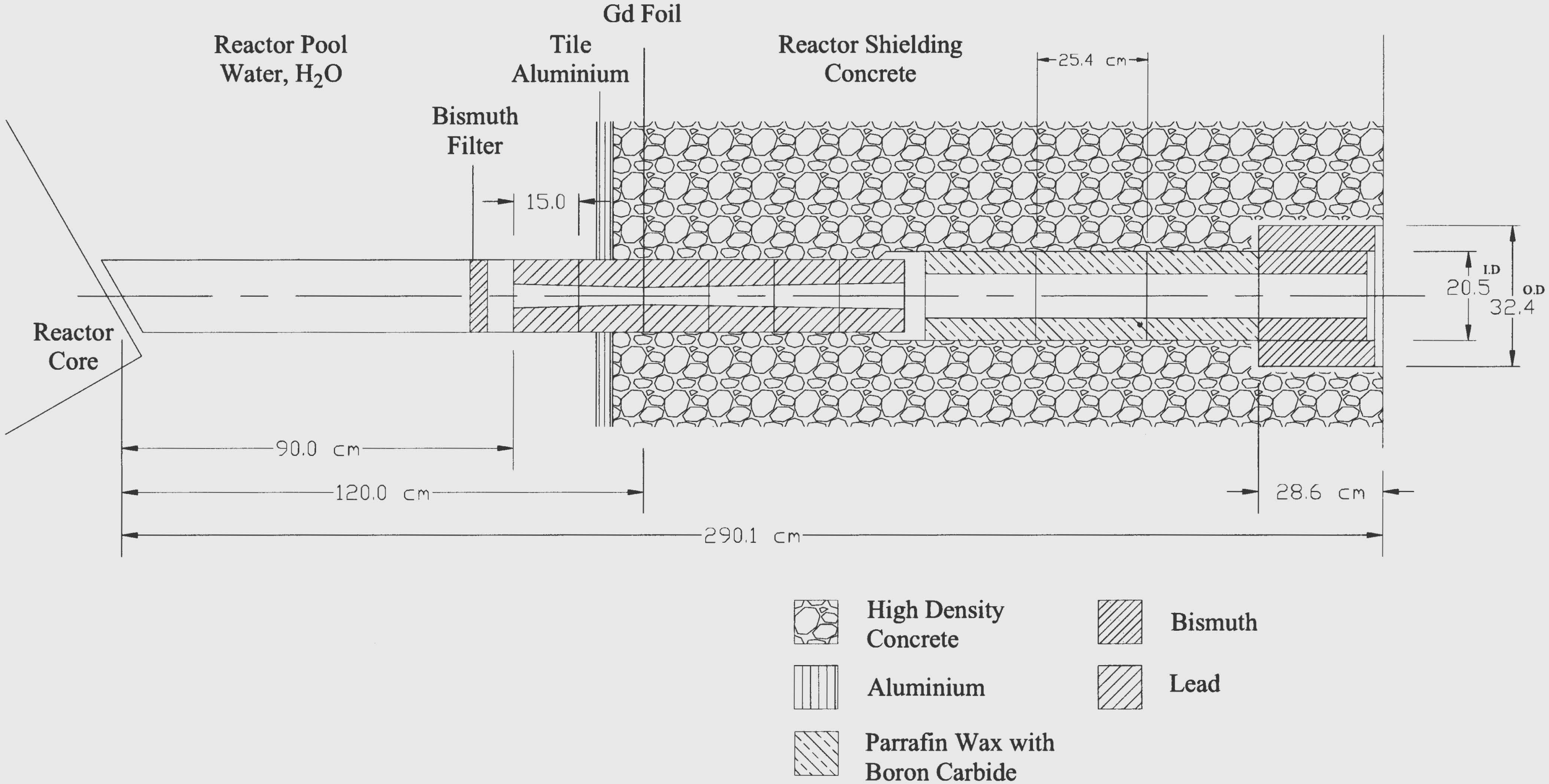

Figure 3.9. Schematic representation of beam tube and its components.

[All dimensions are in cm.]

The converging part of the collimator is divided into two segments each 15.0 cm thick. This part is to provide shielding for the Gd-foil and to minimize interference from radiation fluxes at the beam tube side.

The divergent part of the collimator is divided into four segments. Each segment is 15 cm thick (60.0 cm in total). This part is to provide beam collimation. The neutron intensity does not vanish outside the specified imaging area, D_p, but it decreases rapidly within the area surrounding it. The beam tube gap after the collimator is filled with hollow Aluminium containers filled with a mixture of Paraffin wax and boron carbide followed by a hollow lead plug at the end. These containers are to provide extra shielding and to minimize the beam shadow surrounding the effective image area. The inner diameters of these plugs are to clear the main beam. Table 3.5 summarizes the specifications of different collimator segments.

3.3.2 Beam Shutter

The Canadian Nuclear Safety Commission (CNSC) regulations and limits, followed by the McMaster Nuclear Reactor [91], state that the effective dose received by and committed to a Nuclear Energy Workers (NEW's) shall not exceed:

i- 100 mSv in a 5-year dosimetry period (equivalent to an average dose rate of 10 μSv/hr)

ii- 50 mSv in one-year dosimetry period (equivalent to an average dose rate of 25 μSv/hr)

The McMaster Nuclear Reactor Radioactive Safety Program [91] divides radiation areas based on total effective dose rate into:

i- Generally Accessible Radiation Area (Dose rate < 25 μSv/hr),

Table 3.5. Specification of collimator parts.

		Specifications					
		Outer diameter (cm)	Inner diameters (cm)		Thickness (cm)	Material	Weight (kg)
Filter		16.0	0.0		4.0	Bi	7.88
Convergent Part	Seg. 1	16.0	4.0	4.75	15.0	Pb+Boral	29.59
	Seg. 2	16.0	4.75	5.5	15.0	Pb+Boral	31.96
Aperture Definition		10.0 (Square)	4.0		0.05	Gd	0.05
Divergent Part	Seg. 1	16.0	4.0	4.5	15.0	Pb+Boral	29.74
	Seg. 2	16.0	4.5	5.0	15.0	Pb+Boral	29.17
	Seg. 3	16.0	5.0	5.5	15.0	Pb+Boral	30.41
	Seg. 4	16.0	5.5	6.0	15.0	Pb+Boral	29.68

ii- Designated Radiation Areas with Limited Access (25 μSv/hr < Dose rate <1000 μSv/hr) and,

iii- Restricted Radiation Area (Dose rate > 1000 μSv/hr).

As such there is no clear definition of required dose rate. As a factor of safety, the shielding calculation will assume a dose rate target of 10 μSv/hr.

A beam shutter is to be placed between the beam tube and the neutron imaging room (cave) such that when it is closed, the radiation beam contents are attenuated to below the allowable radiation dose limits to permit access to inside the imaging room for safe loading and unloading of experimental setups.

3.3.2.1 Material Selection and Attenuation Calculation

In order to have an efficient shutter with a lower achievable weight; a shutter made of composite materials is used. Each material is one of the most safe and efficient attenuators for a specific type of radiation (fast neutrons, thermal neutrons and gamma rays) encountered in the beam tube.

The total distance between the source and the end of the shutter, L_s, is 436 cm (beam tube length 286 cm). Recalling the geometrical design of the beam tube collimator, the apparent source diameter for both fast neutrons and gamma ray will be;

$$D_{App} = \frac{L_S}{L_S - L_o} \times D_{C1} \tag{3.10}$$

and the geometric factor is;

$$G = \frac{\pi}{4} \times \frac{D_{App}^2}{\cos 30} / 4\pi L_S^2 = \frac{D_{App}^2}{16 L_S^2 \cos 30} \qquad (3.11)$$

where L_o is the distance between the source and collimator start, D_{c1} is the diameter at the beginning of the collimator from core side (D_{c1} = 5.5 cm, the maximum diameter of the convergent part.)

Using 100.0 cm of Paraffin wax in addition to 30.0 cm of lead and 10.0 cm of Boroflex sheets will reduce the total dose rate (at 5.0 MW) to 4.4 μSv/hr. The details of the shutter design are provided in Appendix A.

3.3.2.2 Beam Shutter Description

The shutter consists of two steel cylinders, each 70.0 cm in length and 23.0 cm in diameter, and is filled with layers of Paraffin wax, lead and Boroflex sheets. The shutter total length is 140.0 cm while the thickness of lead layers is 30.0 cm and the thickness of Paraffin wax layers is 100.0 cm. The materials are layered repeatedly, to provide near homogeneous composition, starting with Boroflex sheets to minimize thermal neutron captured in Paraffin wax and lead. Layers of Boroflex separate the lead and wax to increase absorption of thermalized neutrons in boron before being captured in wax and/or lead. The shutter is driven by a compressed air cylinder to ensure that the shutter will close under its own weight in case of electric power loss. The shutter mechanism is enclosed in a concrete room where the surrounding gaps are filled with Paraffin wax and Boroflex to attenuate the radiation scattered from the side of the shutter cylinders. Figure 3.10 illustrates a schematic of the shutter mechanism.

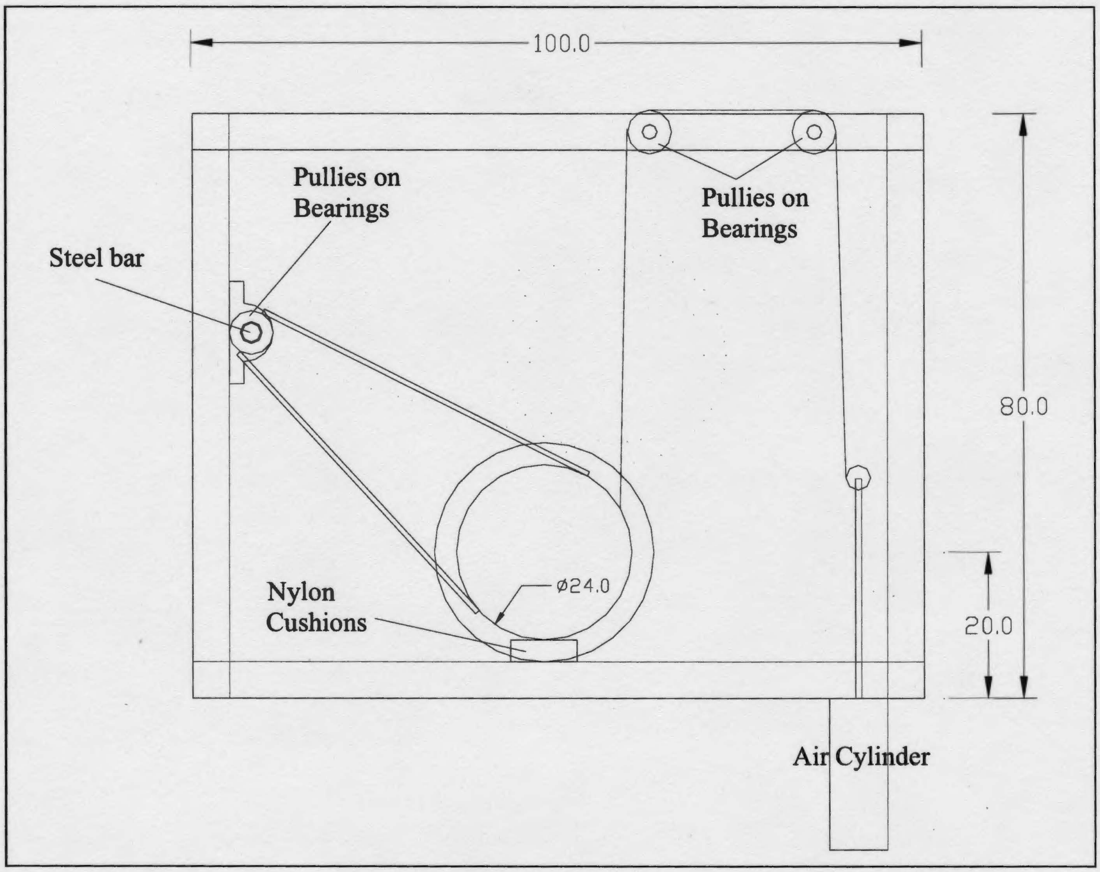

Figure 3.10. Schematic of shutter mechanism (Front view).

3.3.3 Beam Catcher and Biological Shielding

The cave shielding is to reduce the radiation fluxes outside the cave to acceptable limits to protects persons working around Beam Port #3 and to prevent interference to/from the prompt neutron activation facility (Beam Port #4) and the static neutron radiography facility (Beam Port #2). Additional shielding materials will be added inside the cave such that the dose rates meet the maximum annual allowable dose for an Atomic Radiation Worker [91]. To minimize the shielding wall thickness, high-density concrete (with Hematite aggregate) is used.

Thermal neutrons are not considered in shielding calculations since; thermal neutron cross-sections are much larger than fast neutron cross-sections, and a thermal neutron flux of 260 n/cm^2-s is to produce the same dose effect (10 μSv/hr) that is produced by a fast neutron flux of 7.0 n/cm^2-s [92]. In order to account for thermal neutron diffusion and subsequent capture, shielding materials are loaded with layers of Boroflex (borated rubber) sheets.

3.3.3.1 Shielding Approach and Calculations

The differential neutron scattering cross section for fast neutrons assuming isotropic scattering in the CMS (Center-of-Mass System) is given by:

$$\sigma(\theta) = \frac{\sigma}{\pi}\cos(\theta), \qquad 0 \le \theta \le \frac{\pi}{2} \tag{3.12}$$

for hydrogen [93]; and by:

$$\sigma(\theta) = \frac{\sigma}{9\pi(1-\alpha)} \frac{[\cos(\theta) + \sqrt{4-\sin^2(\theta)}]^2}{\sqrt{4-\sin^2(\theta)}}, \quad 0 \le \theta \le \pi \tag{3.13}$$

for deuterium [93], where

$$\alpha = (A-1)^2/(A+1)^2 \tag{3.14}$$

and the differential Compton scattering coefficient for gamma rays is given by [85]:

$$\sigma(\theta) = [\frac{r_o^2}{1+a(1-\cos\theta)}]^2 [\frac{1+\cos^2\theta}{2}][1 + \frac{a^2(1-\cos\theta)^2}{(1+\cos^2\theta)(1+a(1-\cos\theta)}],$$

$$0 \le \theta \le \pi \tag{3.15}$$

where

$$a = E_{\gamma o}/m_e c^2 \tag{3.16}$$

and r_o is the classical electron radius.

Thus, the scattered radiation dose rate at any location is given by:

$$H_p = \Sigma V \phi_o \times \frac{\sigma(\theta) \times d\Omega(\theta)}{\sigma \times dA} = \Sigma V H_o \times \frac{\sigma(\theta)}{\sigma \times R^2} \tag{3.17}$$

where Σ is the scattering macroscopic cross section of the test object, V is the scattering object volume subject to radiation, H_o is the radiation dose at the scattering object location, $d\Omega(\theta)$ is the differential solid angle around the scattering direction, dA is the differential element of area around the shielding location, R is the distance from the scattering object to the shielding location and θ is the angle between the scattering direction and the beam direction. The scattering object is taken to be a 5.0 cm diameter pipe with 18.0 cm length (Beam diameter at the object location.)

Shielding calculations – details are provided in Appendix A – show that 35.56 cm of Concrete and 20.32 cm of Paraffin wax are required for the back wall (does not include shielding non-scattered incident beam), 17.78 cm of Concrete for the right hand side wall (BP2/BP3). The ceiling is 17.78 cm of Concrete covered with 30.48 cm of Paraffin wax.

In addition to the 35.56 cm of Concrete and 20.32 cm of Paraffin wax back wall, 15.24 cm of lead, 50.8 cm of Paraffin wax are used as a beam catcher to attenuate the radiation levels when the shutter is open.

Civil structure stress analysis has been performed to ensure structural integrity during transportation and after installation, details are provided in Appendix A.

3.3.3.2 Beam Catcher and Biological Shielding Description

To minimize the thickness of cave shielding walls, high-density concrete (with Hematite aggregate) is used. In addition to the back wall (35.6 cm high-density concrete and 20.3 cm Paraffin wax), 15.2 cm of lead and 61.0 cm of Paraffin wax loaded with boron carbide are used as a beam catcher to attenuate the radiation levels while the shutter is open. The thicknesses of the cave side shielding walls are to be validated experimentally during the commissioning phase of the facility.

A plan-layout of the MNR with a schematic of the facility cave is shown in Figure 3.11. No modifications regarding Beam Port #4 are required. On the other hand, Beam Port #2 walls have been partially modified. It should be noted that the shielding calculation is based on 5.0 MW reactor operation and hence some of the shielding blocks

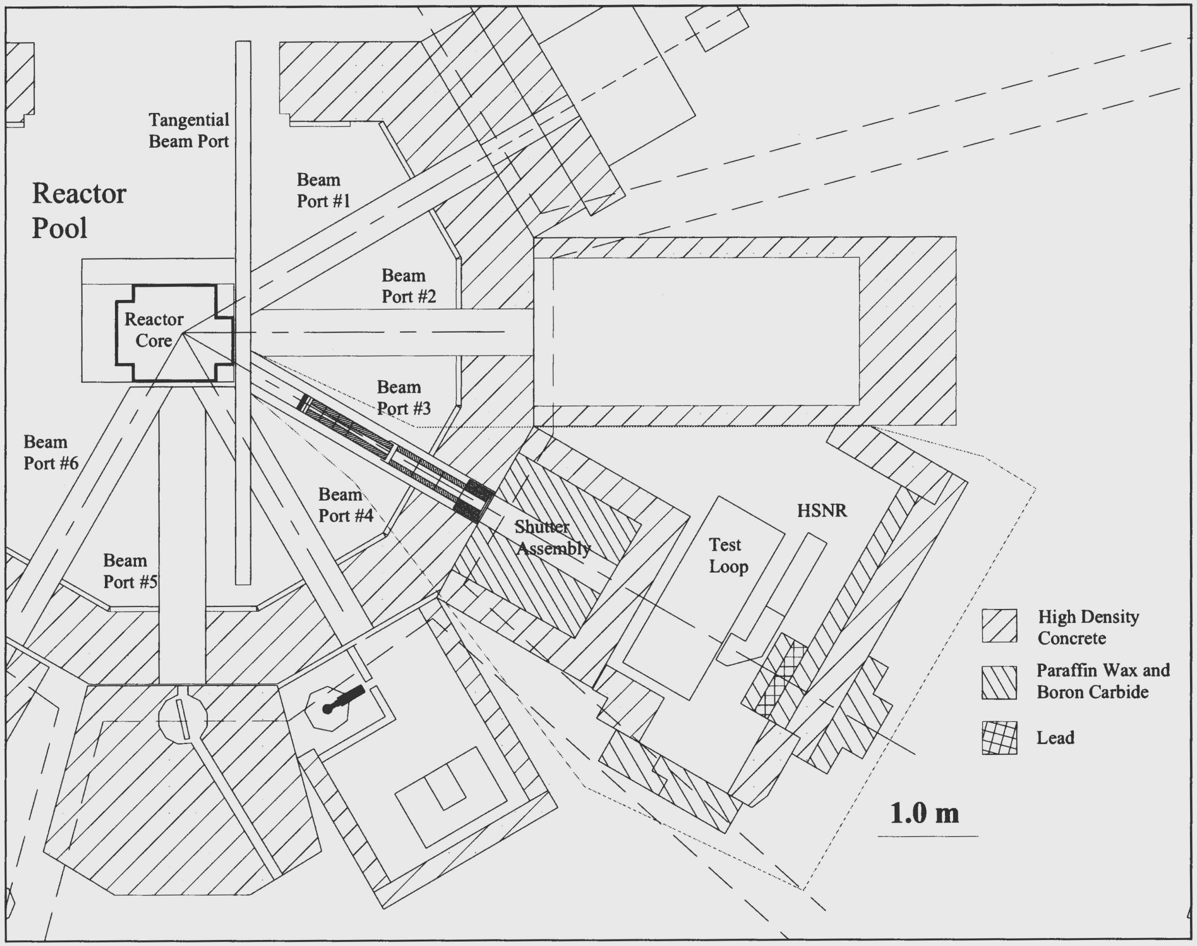

Figure 3.11. Schematic of MNR experimental floor and final facility components (Top View).

(such as the extra wax cap outside the concrete cave) will be used (if necessary) at such reactor power.

Table 3.6 lists the fast neutrons (E > 1.0 MeV) and gamma dose rates analytically calculated at different locations at 5.0 MW operation along the beam path based on neutron flux values obtained from experimental measurements at beam port entrance for both shutter closed and open cases.

3.4 Dynamic Neutron Radiography System

The main component of the dynamic neutron radiography system used in these measurements is a high-sensitivity CCD camera (COHU-4910.) The other components include a time code generator (Telecom Research Model T5010) for frame encoding, a JVC (Model HR-S2911U) videocassette recorder (VCR), a Panasonic (Model DMR-E85H) digital video recorder (DVR), an image processing board (Data Translation DT2853), and a personal computer (IBM Intellistation Z Pro.)

The CCD camera outputs a standard RS-330 video signal to a video recorder and the video can be acquired by the image processing board for enhancement and analysis. Figure 3.12 shows a schematic of the neutron radiography system.

3.4.1 Real Time Video Camera

Due to the low light yield from the neutron conversion process in neutron-to-light conversion screens, high sensitivity video cameras are most suitable for neutron imaging applications. The 4910 Series High Performance Monochrome "½-inch" CCD camera

Table 3.6. Summary of fast neutron and gamma dose rates calculated along beam path (at 5.0 MW).

	Distance from Beam Tube Entrance	Dose Rate with Shutter Closed (μSv/hr)		Dose Rate with Shutter Open (μSv/hr)	
		Fast Neutrons	Gamma Rays	Fast Neutrons	Gamma Rays
Beam Tube Entrance*	0.0 cm	1.9×10^{12}	6.2×10^{11}	1.9×10^{12}	6.2×10^{11}
End of Beam Tube	290.1 cm	7.0×10^{7}	9.2×10^{6}	7.0×10^{7}	9.2×10^{6}
End of Shutter	440.0 cm	4.2	0.2	2.4×10^{7}	3.1×10^{6}
Imaging Plane	600.0 cm	1.9	0.1	1.1×10^{7}	1.4×10^{6}
End of Beam Catcher	755.0 cm	~0.0	~0.0	5.8	2.9

* *Based on experimental flux measurements.*

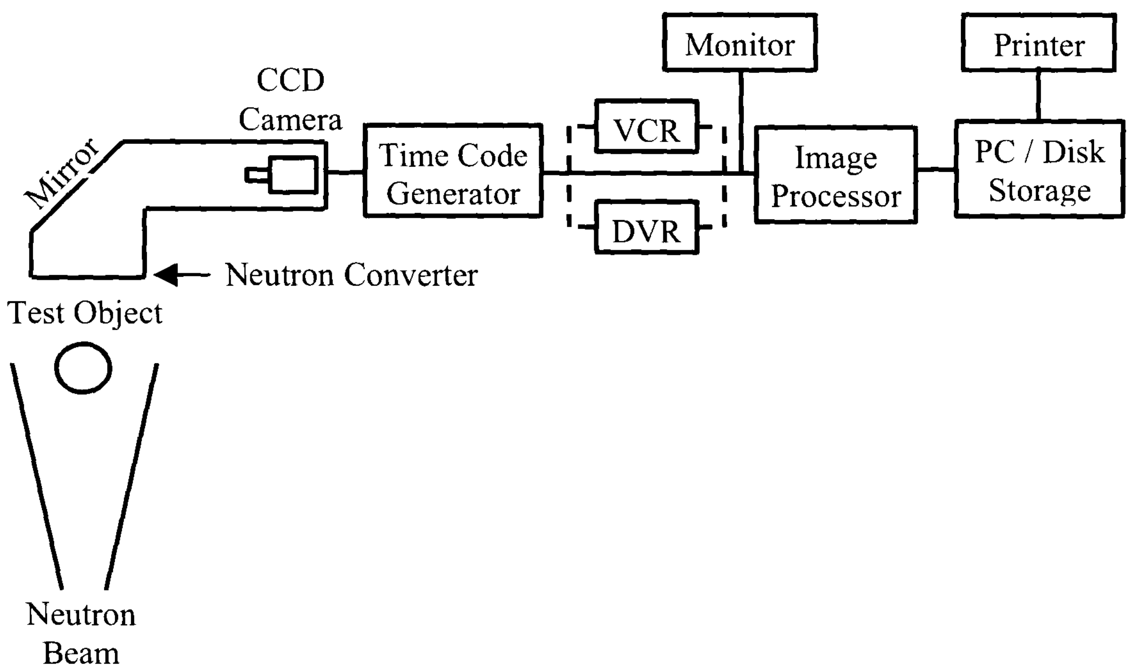

Figure 3.12. Schematic of the real-time neutron radiography system.

VCR: Video Cassette Recorder, DVR: Digital Video Recorder, PC: Personal Computer.

from Cohu is used. It offers high sensitivity and high resolution for use in a broad range of security/surveillance, scientific, and industrial video applicants. The sensitivity quoted by the manufacturer is 0.65-lux full video (AGC off) and 0.02 lux at 80% video (AGC on) and 0.004 lux at 30% video at the standard video rate. The Cohu 4910 camera uses a "½-inch" format interline transfer sensor with on-chip micro-lenses, which reduces dark current, lag, and blooming, while improving dynamic range and spectral characteristics. The 4910 Series design also incorporates a removable trim plate for side panel access to controls such as gamma, electronic shuttering, gain and sharpness.

3.4.2 Neutron Conversion Screens

The neutron conversion screen is a critical component in the high-speed neutron radiography system (HSNR). In order to be used in HSNR, a neutron converter should have a relatively short light-decay time, in addition to high neutron sensitivity (or light yield) and high spatial resolution.

Although rare earth metal converters of gadolinium compounds such as gadolinium oxysulphide (Gd_2O_2S) and gadolinium oxybromide (GdOBr) can provide an image with high spatial resolution, their light decay constant is about 400 ms, which does not allow high-speed imaging. Glass scintillators have rapid decay constant on the order of 40 to 60 ns, but their light yield is very poor. Only zinc sulphide (ZnS) scintillators mixed with Lithium Fluoride (ZnS/LiF) meet HSNR requirements. These scintillators have decay characteristics of scintillation consisting of two components: a fast component having a decay constant on the order of 100 ns and a slow component on the order of 40 to 100 μs. The slower component limits the temporal resolution because of the afterglow on the converter. The sensitivity of ZnS/LiF scintillators is 100 times greater than those of gadolinium metal, and their spatial resolution is on the order of 100 μm [51].

Three different scintillator-type neutron conversion screens are available for experimental use in addition to the screen originally available from the LTV RTNR system. Table 3.7 lists the different properties of the commercially available scintillator screens.

3.4.3 Video Recorders / Time Code Generator

A Video Cassette Recorder (VCR), JVC Model HR-S2911U, and a Digital Video Recorder (DVR), Panasonic Model DMR-E85H, have been used to record the video signal output from the camera for storage and/or further image processing.

The time code generator, Telecom Research Model T5010, is used to mark each video frame with time and experiment codes to simplify temporal analysis where detailed information regarding frame number, time of acquisition and the experiment code identify each experimental condition.

3.5 Image Processing System

The image processing system allows for some key manipulation such as frame averaging, filtering, image subtractions and contrast imaging. The ability to average many

Table 3.7. Characteristics of different types of LiF/ZnS scintillator screens used in current work.

	BC 704	**ND**	**NDG**
Manufacturer	Saint-Gobain	Applied Scintillation Technologies	Applied Scintillation Technologies
Thickness	0.25 mm	0.42 mm	0.42 mm
Blend (LiF:ZnS)	3:1	4:1	4:1
Activator	Ag	Ag	Cu, Al and Au
Peak Emission	450 nm (Blue)	450 nm (Blue)	540 nm (Green)
Particle size	1.5-5.0 μm	1.5-7.0 μm	NA

frames and to pass the images through various filters greatly reduces the noise associated with the radiographs. Image subtraction can then be applied to remove the image details according to the neutron beam and the test geometry. Contrast imaging allows the enhancement of the image to aid in visualizing either very weak or very strong attenuating materials.

3.5.1 Image Capture Boards

Two image capture boards (frame grabbers) are available for use in this work. The DT3152 and I-50 HSN boards have high accuracy, are programmable and are monochrome Peripheral Component Interface (PCI) bus frame-grabbers ideal for both image analysis and machine vision. These frame-grabbers are bus masters on the PCI bus allowing very high-speed image acquisition via DMA (Direct Memory Access) directly to system memory. The host system's memory and display controller are utilized to store and display images. Table 3.8 summarizes the technical characteristics of the two image capture boards used in the current work.

The DT3152 can acquire many different monochrome and variable scan video formats (RS-170, NTSC, CCIR and PAL) and transfer the image to memory or display in real-time. The I-50 HSN stores the 8 or 10 most significant of 12 bits. The I-50 HSN can acquire RS-343, RS-330, RS-170 and non-standard video signals.

The I-50 HSN delivers extreme image quality with very low pixel jitter of ±1.0 ns, superior analog design, and a 62 dB S/N ratio due to the use of a precision 12 bit Analog-

Table 3.8. Technical characteristics of image capture boards available for the current work.

	DT3152	**I-50 HSN**
Manufacture	Data Translation	Foresight Imaging
Acquisition Speed	20 MHz max	50 MHz max
Resolution RS-170	4kx4k, 4Mpixel max	2kx2k
Pixel Jitter	4.0 ns	1 ns
Pixel Level	8 bit (256 Grey levels)	8 or 10 bit out of 12
Look-Up Tables (LUT)	2	1
On-board Memory	No	8 Mega-pixels
Signal-to-Noise Ratio (SNR)	--	62 dB

to-digital (A/D) converter. This superior S/N ratio enables highly sensitive imaging applications to deliver the best in signal integrity on a per pixel basis.

3.5.2 Image Processing Software

Image processing is needed for improving the visual appearance of images and preparing images for analysis and information extraction. Two commercial software packages are available for manipulating images captured by image capture boards. HLImage++ and ImagePro Plus are standalone applications, which support custom made tools. Image analysis operations such as, histogram, line profiles, filtration and contrast enhancement are included.

The HLImage++ supports the DT3152 frame grabber. The I-50 HSN frame grabber is supported with the IDEA software development kit, which allows video signal streaming and recording in digital AVI format.

The Adobe Premiere Elements software package manipulate digital video format from recorded DVD disks through frame isolation into still images.

It is important to emphasize that image enhancement is applied after the image has been digitized and stored, and therefore will be unable to deliver the highest quality result that could have been achieved by optimizing the acquisition process in the beginning.

3.6 Neutron Scattering System

The system includes three Saint-Gobain BC-702 thermal neutron detectors. The BC-702 is a highly efficient scintillator detector of thermal neutron, and provides excellent discrimination against gamma background. The detector is a disk 0.25" (6.35 mm) thick and 1.5" (38.1 mm) in diameter that can be mounted directly to a photomultiplier tube. The detector incorporates a matrix of a lithium compound enriched to 95% ^{6}Li dispersed in a fine ZnS(Ag) phosphor powder. The detection process employs the nuclear reaction ^{6}Li(n,a)^{3}H with a Q-value of 4.78 MeV. The lithium content is 11 mg/cm^{3} and the intrinsic detection efficiency for thermal neutrons (0.0253 eV) is 55%.

One Saint-Gobain BC-720 fast neutron detector and one Saint-Gobain NaI(Tl) gamma detector are included in the system too. The BC-720 is a scintillator designed specifically for detecting fast neutrons. It consists of ZnS(Ag) phosphor embedded in a clear hydrogenous plastic and functions by means of the proton recoil interaction in the plastic.

The signal processing and power supplies accessories include, Four ORTEC Model 590A amplifiers and timing single-channel analyzers, an ORTEC 4001A/4002D NIM Bin with 160-W NIM Bin Power Supply and an ORTEC Model 556 high-voltage power supply that can provide up to 3000V and 10 mA.

The ORTEC Model 920E is a multichannel buffer that can accommodate up to 16 simultaneous inputs, with independent start, stop and preset controls. It employs a 4k-channel Analog-to-digital converter (ADC) with15-μs fixed conversion time (dead time). The ORTEC CONNECTIONS-32 toolkit applications software simplify the task of making a user-written application communicate with the Model 920E.

4 MONTE-CARLO NEUTRON TRANSPORT SIMULATIONS

Monte-Carlo simulations are conducted to simulate neutron transport through facility components to estimate the neutron beam parameters. Several cases were simulated to obtain the characteristics of different components.

4.1 Monte-Carlo Method and MCNP Code

A definition of a Monte-Carlo method would be one that involves deliberate use of random numbers in a calculation that has the structure of a stochastic process. A stochastic process means a sequence of states whose evolution is determined by random events.

One feature of the Monte-Carlo method is the simple structure of the computational algorithm [94]. This algorithm consists, in general, of a process for producing random events. The process is repeated N times, each trial being independent of the rest, and the results of all the trials are averaged together. Because of its similarity to the process of performing a scientific experiment, the Monte-Carlo method is sometimes called the method of statistical trials. A second feature of the method is that, among all numerical methods that rely on N-point evaluations in M-dimensional space to produce an approximate solution, the Monte-Carlo method has an absolute error of estimation that decreases as $N^{-1/2}$ whereas, in the absence of exploitable special structure, all other methods have errors that decreases as $N^{-1/M}$ at best [95]. This property gives

Monte-Carlo method an edge in computational time efficiency as M, the size of the problem, increases.

Areas of physics in which Monte-Carlo simulations are often employed are radiation transport, radiation heat transfer and nuclear reactor theory [96]. The transport of radiation is a natural stochastic process that is amenable to Monte-Carlo modeling. To do so it is not necessary to write down the equations that are actually being solved. The Monte-Carlo method provides approximate solutions to a variety of mathematical problems by performing statistical sampling experiments on a computer. Remarkably, the method applies to problems with absolutely no probabilistic content as well as those with inherent probabilistic structure. The Monte-Carlo method can be considered as an experiment involving the transport of particles through a medium that is performed by a computer.

Two features of the thermal energy range distinguish it from the rest of the energy spectrum [97]. One is upscattering – if a slow neutron strikes a nucleus in thermal motion, the neutron's energy may increase. On the other hand, if the neutron energy is much higher than kT, almost every scattering collision will slow it down. Thus, while the upscattering of fast neutrons may be ignored, the upscattering of thermal neutrons cannot be ignored.

Although transport of low energy neutrons and scattering laws are extremely complicated, it is possible, sometimes, to calculate the neutron flux by a deterministic method [97], but usually with significant inaccuracy. When the geometric structure is complicated, one is usually forced to rely on numerical techniques. Despite the advances in discrete ordinates and finite element methods, Monte-Carlo is still the most efficient way of solving difficult problems in the field of neutron and photon linear transport [98]. The analytical methods used to obtain the neutron source requirements do not account for the neutron energy spectrum, epithermal neutron doses, neutron build-up and neutron fields at the side of the beam tube and information such as the exact imaging area size, flux shadowing around the imaging area and backscatter radiation cannot be obtained.

The Monte-Carlo N-Particles (MCNP-4B) Code developed at the Los Alamos National Laboratory [99] is used in the present analysis to simulate neutron transport through facility components to estimate the neutron beam parameters at the imaging plane and the shielding capacity of the beam shutter and biological shield. Several cases were simulated to obtain the characteristics of different components.

4.2 Description of MCNP Input Cards

The MCNP input card consists of different data cards (section) that supply the input information necessary to describe the problem. This information describes the physical geometry of the problem through surfaces and cells definition, source parameters, information to be extracted from simulation process and material compositions.

MCNP-4B supplies the neutron cross-sections for different materials using combination of cross-sections and resonance parameters tabulated in the "Evaluated Nuclear Data Files" ENDF/B library produced by Brookhaven National Laboratory.

Appendix B contains the MCNP input card used to simulate fast neutron transport through a geometry that includes; the beam tube liner, beam shutter mechanism in the open position, the beam catcher and the shield wall.

4.2.1 Physical Geometry

The geometry of MCNP treats an arbitrary three-dimensional configuration of user-defined materials in geometric cells bounded by first- and second-degree surfaces and fourth-degree elliptical tori. The cells are defined by the intersections, unions and complements of the regions bounded by the surfaces. Surfaces can be defined by supplying coefficients to the analytic equations or, for certain types of surfaces, known points on the surfaces.

Using the bounding surfaces specified on cell cards, MCNP tracks particles through the geometry, calculates the intersection of a track's trajectory with each bounding surface, and finds the minimum positive distance to an intersection. If the distance to the next collision is greater than the minimum positive distance to an intersection, the particle leaves the current cell.

As a starting simulation case, the beam tube liner only was considered to estimate the required design parameters of neutron beam such as the neutron flux and the size of the imaging area. Figure 4.1 represents cross-sectional views of beam tube liner and surrounding reactor components generated by the MCNP-4B plotting tool. The problem geometry is expanded to include the shutter, in open and close positions, and its cave to

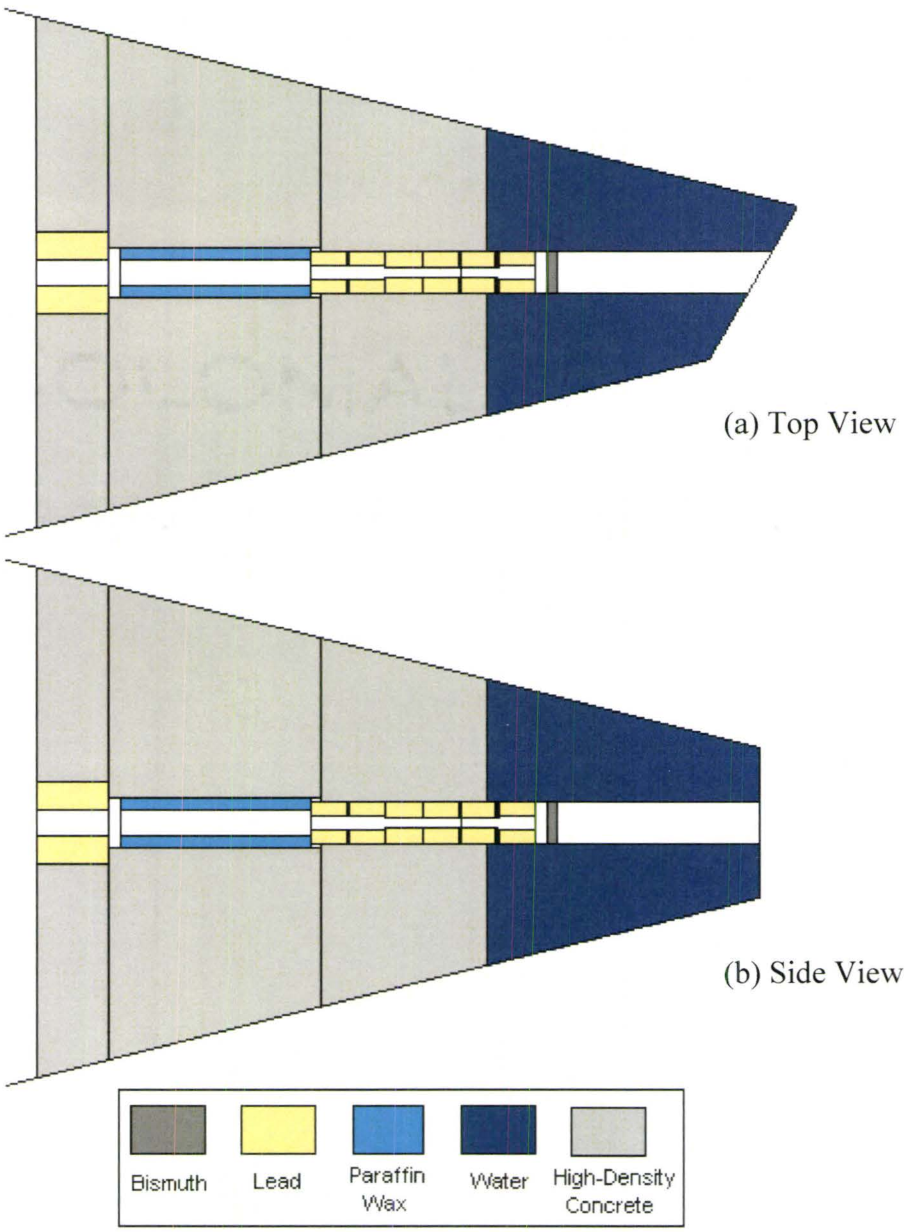

Figure 4.1. Cross-sectional views of the beam tube geometry input for MCNP (Not to scale).

assure the shielding power of the beam shutter. Then, the biological shielding, beam catcher and back-wall, were added to the problem geometry to estimate their shielding capability and obtain information about the effect of neutron backscattering on the neutron fluxes at the imaging plane. Figure 4.2 represents cross-sectional views of complete problem geometry with the beam shutter in the open position generated by MCNP-4B plotting tool. Figure 4.3 and Figure 4.4 represent zoom-in cross-sectional views of collimator structure illustrating more geometrical details.

4.2.2 Neutron Source Definition

A general source definition has been chosen to specify the source variables such as, neutron energy spectrum, position, angular distribution and area sampling. The neutron energy spectrum at the source, described in Section 3.1, was divided into 61 groups – one thermal neutron group using partial Maxwellian spectrum with energy range up to 0.2 eV, 38 groups (with equal lethargy-difference) for the energy range from 0.2 eV up to 1.0 MeV and 22 groups (with equal lethargy-difference for the energy range from 1.0 MeV up to 8.0 MeV. Figure 4.5 shows the multi-group neutron energy spectrum used as the source input for the MCNP input card.

The angular distribution of source neutrons is defined by specifying the polar and azimuthal angles defining the neutron direction. The azimuthal angle is sampled, by default, uniformly in the range from 0° to 360°. The polar angle, measured relative to a vector normal to the source surface, is specified to include only neutrons emitted from the

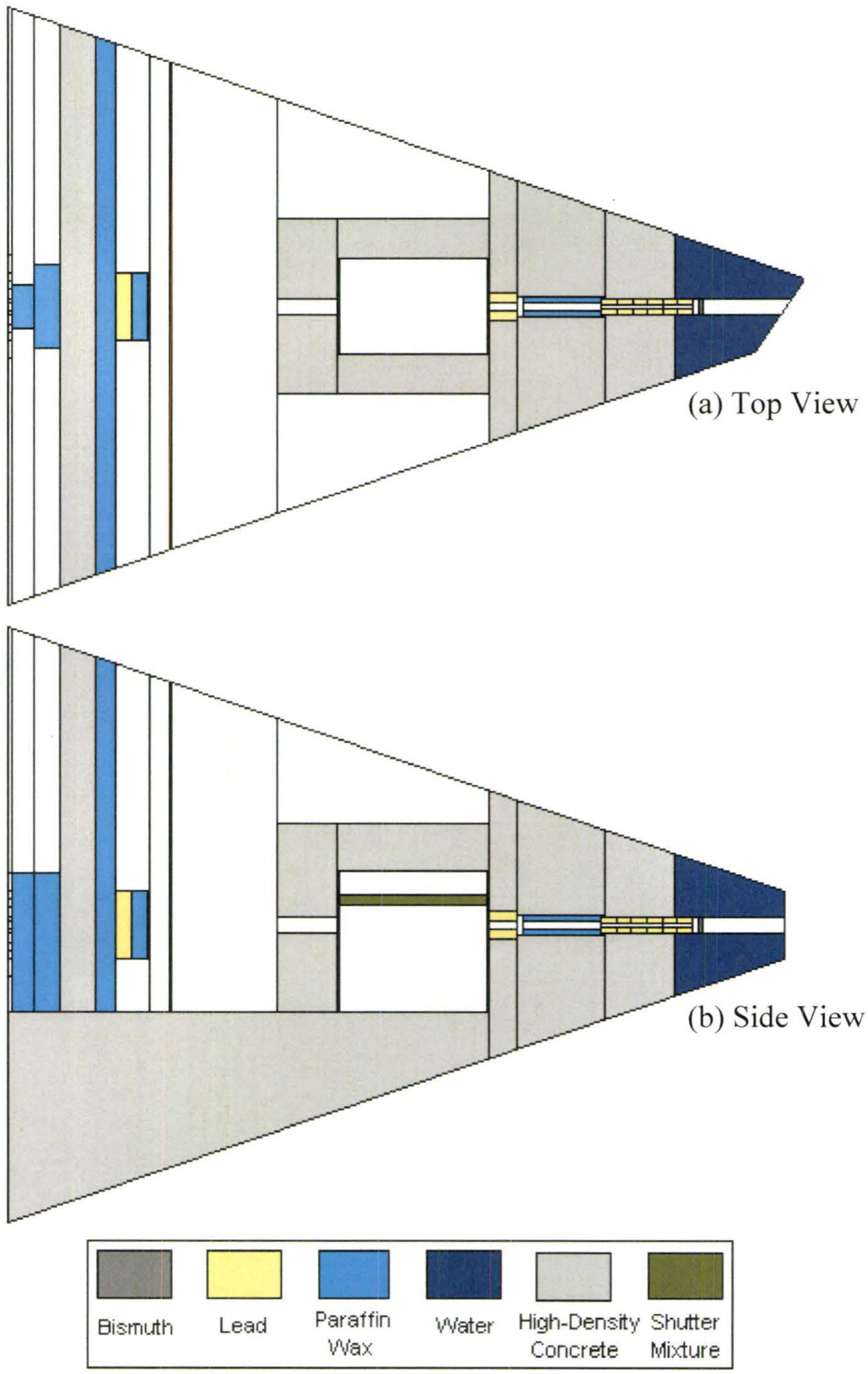

Figure 4.2. Cross-sectional views of the complete problem geometry input for MCNP (Not to scale).

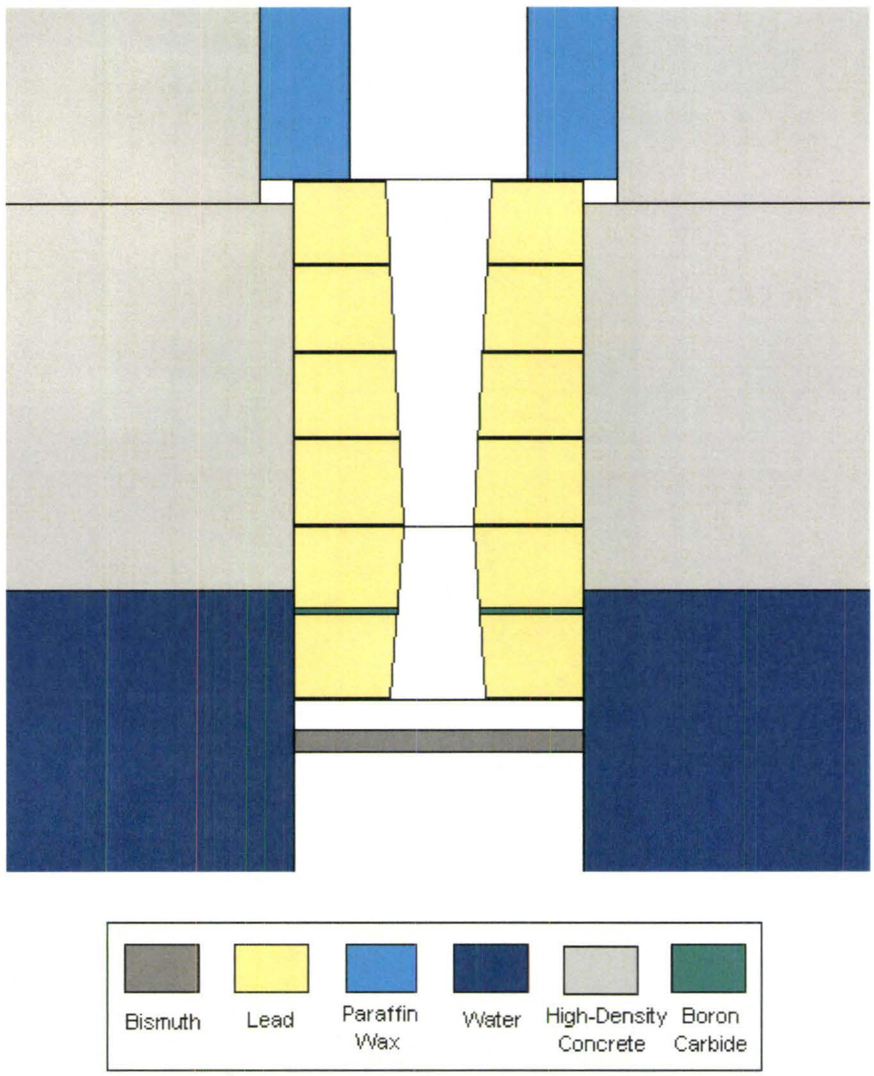

Figure 4.3. Cross-sectional view of the bismuth filter and collimator geometry input for MCNP (Not to scale).

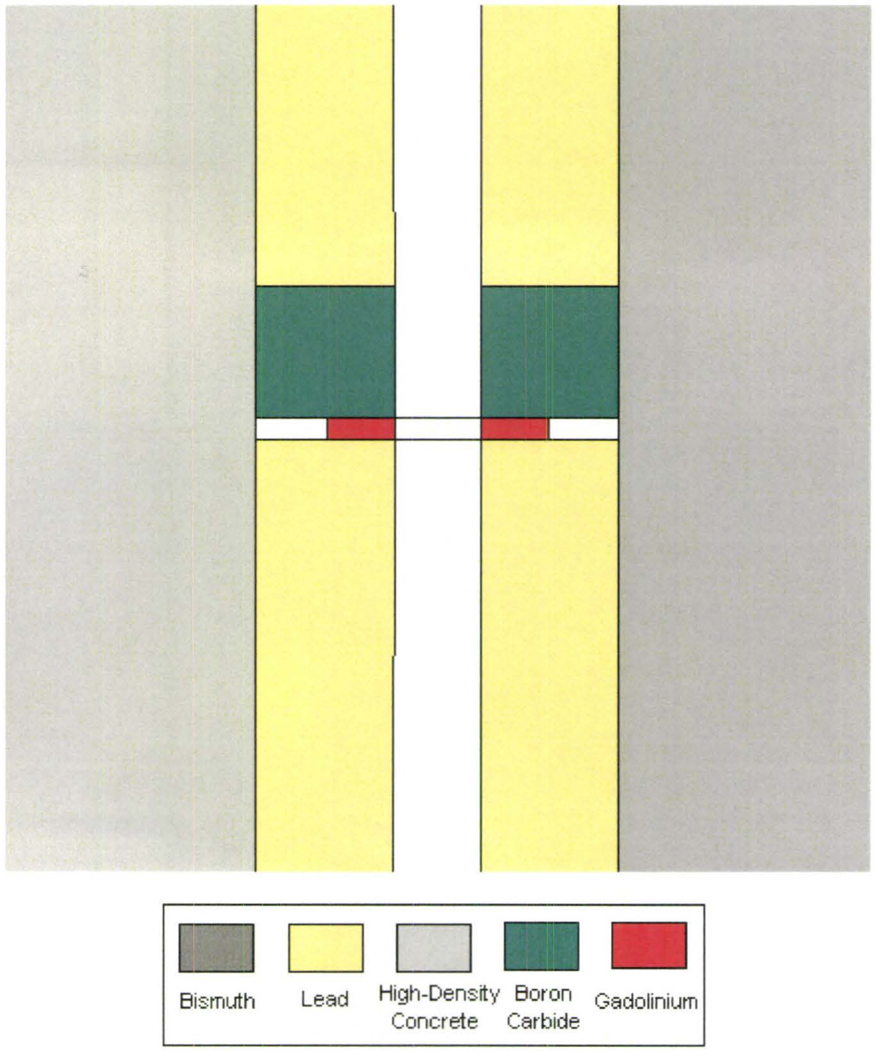

Figure 4.4. Cross-sectional view of the collimator aperture definition geometry input for MCNP (Not to scale).

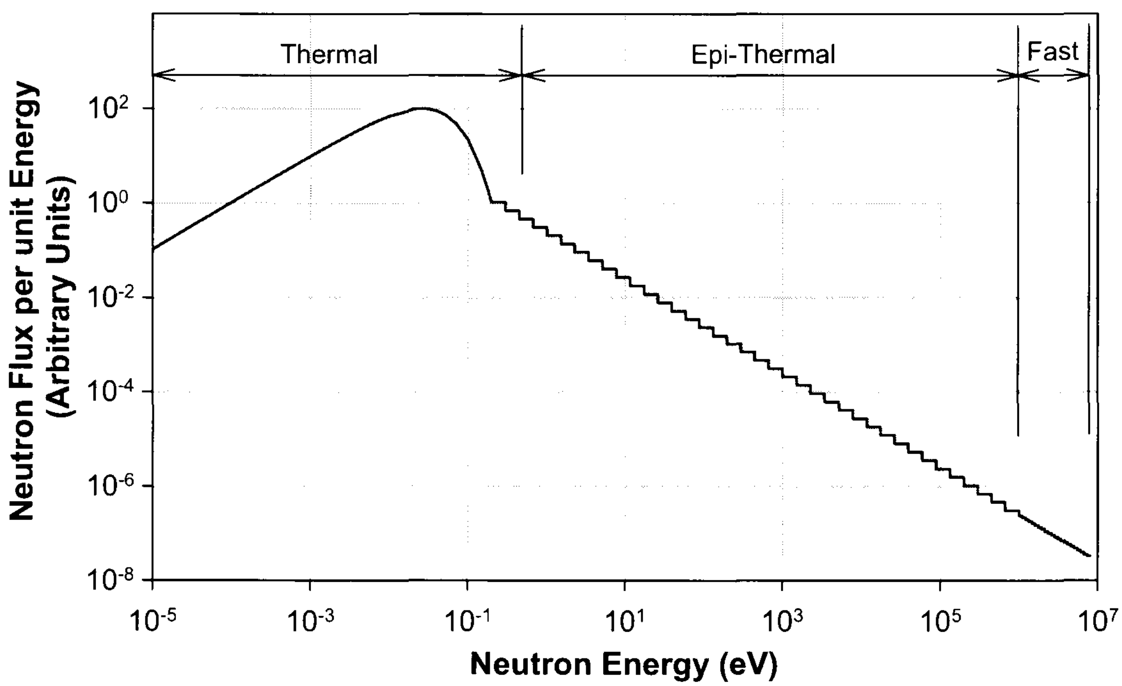

Figure 4.5. Neutron multi-group source energy spectrum input for MCNP.

surface in the forward direction (0^{o} to 90^{o}). The cosine of the polar angle is sampled using a uniform distribution.

A uniform area sampling was specified over a source radius of 15.0 cm. Sample runs were executed with a source radius of 20.0 cm and no significant changes of simulation results were observed except for longer computational times.

4.2.3 Tally Specifications

The tally card is used to specify the type of information to be extracted from the Monte-Carlo simulations. In all simulation cases, information about neutron fluxes and/or absorbed doses (using track length flux estimate "F4:N") are obtained and averaged over cells specified at the imaging plane, after the beam shutter assembly and after the back wall. The energy of neutrons tallied are divided into five energy bins between 0.0, 0.2 eV, 0.5 eV, 10 keV, 1.0 MeV and 8.0 MeV.

Table 4.1 lists the number of source neutron particles (histories) tracked in different geometrical cases to simulate the neutron transport through different facility components. As the geometry expanded, simulations of larger numbers of source neutron were needed.

4.3 Simulation Results

The track length flux estimator (F4:N) is generally quite reliable because there are frequently many tracks in a cell (compared to the number of collisions), leading to many

Table 4.1. Number of neutron particles tracked in different cases.

	Number of particles tracked		
	Thermal ($E<0.2eV$)	Epithermal ($0.2eV<E<1MeV$)	Fast ($1MeV<E<8MeV$)
Beam tube only.	5.0×10^8	3.0×10^8	10^8
Beam tube with beam shutter open.	5.0×10^8	Not simulated	Not simulated
Beam tube with beam shutter closed.	Not simulated	6.0×10^8	3.0×10^8
Back wall with beam shutter open.	5.0×10^8	6.0×10^8	5.0×10^8

contributions to this tally. Track length flux estimates of cell flux provided by MCNP are normalized to a source neutron tracked.

$$f_4 = \frac{\phi_{Cell}}{S} \tag{4.1}$$

where

f_4 is the track length flux estimate provided by MCNP for a cell,

ϕ_{Cell} is the cell flux (n/cm^2-s),

S is the total number of source particles (n/s)

Since only forward neutrons are considered, the source strength can be calculated as

$$S = \frac{\phi_o A_o}{2} \tag{4.2}$$

where

ϕ_o is the neutron flux at beam tube entrance (n/cm^2-s),

A_o is the simulated area of the beam tube entrance

and hence, the estimated cell flux is

$$\phi_{Cell} = f_4 \frac{\phi_o A_o}{2} \tag{4.3}$$

4.3.1 Beam Tube Liner

The results obtained for simulating the beam tube liner only showed that the average thermal neutron flux (E<0.5 eV) over the required 20.0 cm diameter effective imaging area (Cell #1 to Cell #3) is $1.63\times10^7 \pm 5.5\times10^5$ n/cm^2-s, which is within 4.0% of the analytical value of 1.57×10^7 n/cm^2-s. Figure 4.6 shows a comparison of thermal neutron intensity profiles obtained by analytical calculations and by MCNP simulation, the two profiles agree quantitatively and qualitatively except for small differences in the region outside the imaging area (beam penumbra) where the analytical prediction of the thermal neutron flux profile is calculated from only thermal neutron ($E < 0.5$ eV) contribution due to the reduction of the effective source area, while MCNP prediction is based on full neutron energy spectrum.

The MCNP simulation results also showed that the neutron fluxes regardless of energy spectrum decreases significantly outside the imaging area (Cell #4 to Cell #6) from the centre of the imaging area. Table 4.2 lists the neutron fluxes at the imaging plane and statistical errors estimated, at 3.0 MW, from the MCNP simulations for the beam tube liner without the other components.

The beam shutter assembly in the open position and its concrete cave has no significant effects on the neutron fluxes estimated in the effective imaging area (20.0 cm in diameter). However, outside the imaging area the size of the opening in the beam shutter cave affects the neutron fluxes. Table 4.3 shows a comparison of the number of neutron tracks entering the cells of interest at the imaging plane for different opening sizes from the simulation of the same number of source particles with partial Maxwellian distribution.

The use of a smaller opening (Square with 20.0 cm side length) has negligible effect on the number of particles entering the effective imaging area (Cell #1 to Cell #3). Outside the effective imaging area, the total number of particles entering the cells is

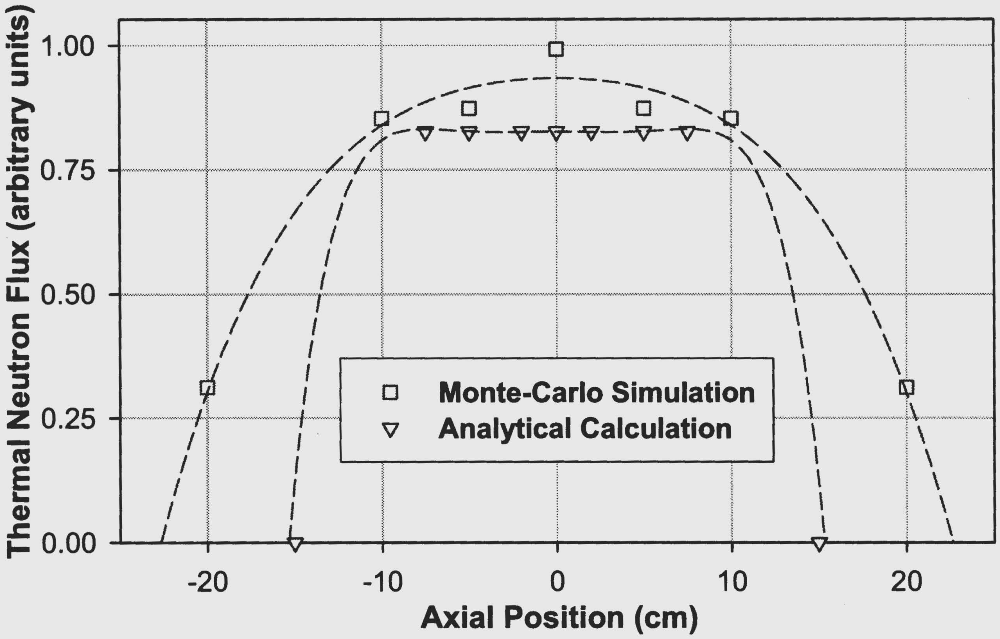

Figure 4.6. Comparison of thermal neutron intensity profiles obtained by MCNP simulation and analytical calculations.

Table 4.2. Neutron fluxes estimated at the imaging plane from MCNP simulation of beam tube liner without the other components.

Cell	Location (cm)	Neutron Flux (n/cm^2-s)					
		Thermal, E<0.5 eV		Epithermal		Fast, E>1.0 MeV	
		Flux	Error	Flux	Error	Flux	Error
1	r < 2.0	1.88×10^{7}	3.04×10^{6}	7.11×10^{6}	1.98×10^{6}	2.23×10^{6}	7.05×10^{5}
2	2.0 < r < 5.0	1.66×10^{7}	1.24×10^{6}	1.02×10^{7}	1.03×10^{6}	1.89×10^{6}	2.84×10^{5}
3	5.0 < r < 10.0	1.62×10^{7}	6.48×10^{5}	1.03×10^{7}	5.49×10^{5}	1.95×10^{6}	1.53×10^{5}
4	10.0 < r < 20.0	5.93×10^{6}	1.96×10^{5}	3.4×10^{6}	1.59×10^{5}	7.73×10^{5}	4.81×10^{4}
5	20.0 < r < 30.0	0.00	0.00	1.05×10^{4}	6.44×10^{3}	0.00	0.00
6	30.0 < r < 40.0	3.20×10^{3}	3.20×10^{3}	3.20×10^{3}	3.2×10^{3}	1.29×10^{3}	1.29×10^{3}

Table 4.3. Effect of opening size of the beam shutter cave on thermal neutron intensity at the imaging plane.

Cell	Location (cm)	Number of neutron tracks entering the cell					
		Beam Tube Only		20.0 cm side length		30.0 cm side length	
		Tracks	Error	Tracks	Error	Tracks	Error
1	r < 2.0	35	17.02%	35	17.02%	35	17.02%
2	2.0 < r < 5.0	171	7.69%	171	7.69%	171	7.69%
3	5.0 < r < 10.0	596	4.10%	597	4.10%	596	4.10%
4	10.0 < r < 20.0	860	3.41%	668	3.87%	860	3.41%
5	20.0 < r < 30.0	0	0	3	57.75%	0	0
6	30.0 < r < 40.0	0	0	4	51.87%	0	0

reduced. When a larger opening (Square with 30.0 cm side length) has been simulated, no effect on the number of particles entering all cells at the imaging plane has been detected. The use of a large opening will require increasing the beam shutter diameter to prevent radiations from streaming through the gap between the shutter and surrounding shields. Larger shutter diameter is not preferred due to the limited space available to move the shutter and also the shutter weight will become heavy.

4.3.2 Beam Catcher and Back wall

The results obtained for simulating the complete problem geometry (beam shutter assembly, shutter cave, beam catcher and back-wall) with the beam shutter in the open position showed that there is a negligible change (+0.6 %) in the value of the average thermal neutron flux (E<0.5 eV) over the required 20.0 cm diameter imaging area (Cell #1 to Cell #3) when compared to the value estimated from simulating the beam tube liner only, since the beam catcher is loaded with a high concentration of Boron Carbide which will reduce the back scattering probability of thermal neutrons and fast neutrons thermalized within the beam catcher.

The MCNP simulation results also show that there is an increase of 4% and 11% in the values of the average epithermal and fast neutron fluxes at the imaging plane respectively. This is mainly due to the backscattering of neutrons as a result of diffusion in beam catcher and back-wall.

Table 4.4 lists the neutron fluxes at the imaging plane and statistical errors

Table 4.4. Neutron fluxes estimated at imaging plane for MCNP simulation of complete problem geometry with the beam shutter in the open position.

Cell	Location (cm)	Neutron Flux (n/cm^2-s)					
		Thermal, E<0.5 eV		Epithermal		Fast, E>1.0 MeV	
		Flux	Error	Flux	Error	Flux	Error
1	r < 2.0	1.86×10^{7}	2.92×10^{6}	8.31×10^{6}	1.52×10^{6}	2.16×10^{6}	3.11×10^{5}
2	2.0 < r < 5.0	1.68×10^{7}	1.22×10^{6}	1.02×10^{7}	7.33×10^{5}	2.12×10^{6}	1.35×10^{5}
3	5.0 < r < 10.0	1.61×10^{7}	6.38×10^{5}	1.08×10^{7}	4.02×10^{5}	2.19×10^{6}	7.31×10^{4}
4	10.0 < r < 20.0	4.60×10^{6}	1.70×10^{5}	3.19×10^{6}	1.11×10^{5}	6.26×10^{5}	1.98×10^{4}
5	20.0 < r < 30.0	1.72×10^{4}	8.26×10^{3}	1.76×10^{5}	2.12×10^{4}	2.48×10^{4}	3.42×10^{3}
6	30.0 < r < 40.0	1.71×10^{4}	6.65×10^{3}	1.10×10^{5}	1.58×10^{4}	1.27×10^{4}	2.15×10^{3}

estimated, at 3.0 MW operation, from the MCNP simulations for the complete problem geometry with the beam shutter in the open position.

4.3.3 Beam Shutter and Biological Shielding

The transport of epithermal and fast neutrons through the beam shutter assembly (with the shutter in the closed position) and through the biological shielding (Beam catcher and back-wall) was simulated to assess the shielding characteristics of the beam shutter and the biological shielding.

Although 9.0×10^{8} and 1.1×10^{9} source neutron particles were simulated in the assessment of beam shutter and biological shielding respectively, no particle tracks entering the cells of interest have been detected. Larger particle numbers would require longer simulation times. On the average eight hours of execution time on the PC is required to simulate 10^{8} neutrons. Particle splitting techniques could not be applied due to the presence of many void (air) cells in the problem geometry where MCNP never splits a particle entering a void cell.

The simulation results do not provide any quantitative values for the shielding capabilities of the beam shutter and biological shielding, however, it provides qualitative measures of the beam shutter and biological shielding effectiveness. If any particle successfully entered any of the cells of interest, then that would be translated into a deficiency of the shielding capability and hence design modification would have been necessary.

5 EXPERIMENTAL CHARACTERIZATION OF THE DYNAMIC NEUTRON RADIOGRAPHY FACILITY

5.1 Characteristics of Biological Shielding and Beam Shutter

Radiation surveys were performed with the shutter closed and open at various reactor powers to assess the dose rates around the facility to ensure safe operation and to assign accessibility of different regions. A Geiger-Muller detector is used for gamma ray dose measurements and a BF_3 detector surrounded by a polyethylene sphere is used for neutron dose measurements. Also, a radiation survey with the reactor in the shut down state (zero power) has been performed with the shutter closed. All dose measurements were below detection limits, 1.0 μSv/hr for gamma and 2.5 μSv/hr for neutron.

Radiation survey measurements were performed for accessible areas inside and outside the facility biological shielding (cave) at five levels:

1- at 0.25 m from experimental floor ground level to examine if there is any radiation streams at cave walls/ground interfaces.

2- at 1.0 m from experimental floor ground level (beam level), where maximum radiation levels are expected.

3- at 2.0 m from the experimental floor ground level to examine if there is any radiation streams at cave walls/ceiling interfaces.

4- at the workstation area above the cave.

5- above the cave ceilings.

The radiation survey performed at 1.0 m from the experimental floor ground level (beam level) and at the workstation area are presented in the next section, the rest of measurements are included in Appendix C. The measurements were performed twice, first with the BP#2 shutter closed then with the BP#2 shutter open to assess the effects of BP#2 operations on measured dose rates. BP#2 shutter is located inside the BP#2 cave near the concrete wall of the reactor pool. When BP#2 shutter is open, regions near the back wall of BP#2 exhibit higher dose rates due to scattered radiation from the BP#2 back wall. On the other hand when BP#2 shutter is closed, regions close to the concrete wall of reactor pool exhibit higher dose rates due to scattered radiation from the BP#2 shutter. The effects of opening BP#4 are not studied, as BP #4 is a significantly lower strength beam port and not routinely used.

5.1.1 Closed Shutter Radiation Dose Surveys

Figures 5.1 through 5.4 show radiation dose (neutron and gamma ray) survey results measured inside and outside the facility biological shielding performed with the shutter closed at 2.0 MW and scaled to 3.0 MW (expected operating power). The dose rates outside the cave satisfy the "generally accessible area" under MNR radiation safety requirement (25.0 μSv/hr). The regions near BP#2 are affected by the higher background radiation levels due to other facilities. Inside the cave, the dose rates are around the 25.0 μSv/hr criterion except for regions near the shutter cave wall and along the beam line. The shielding power of the shutter cave wall is reduced due to the presence of gaps between the bricks used to build the wall and due to lower moisture content in these

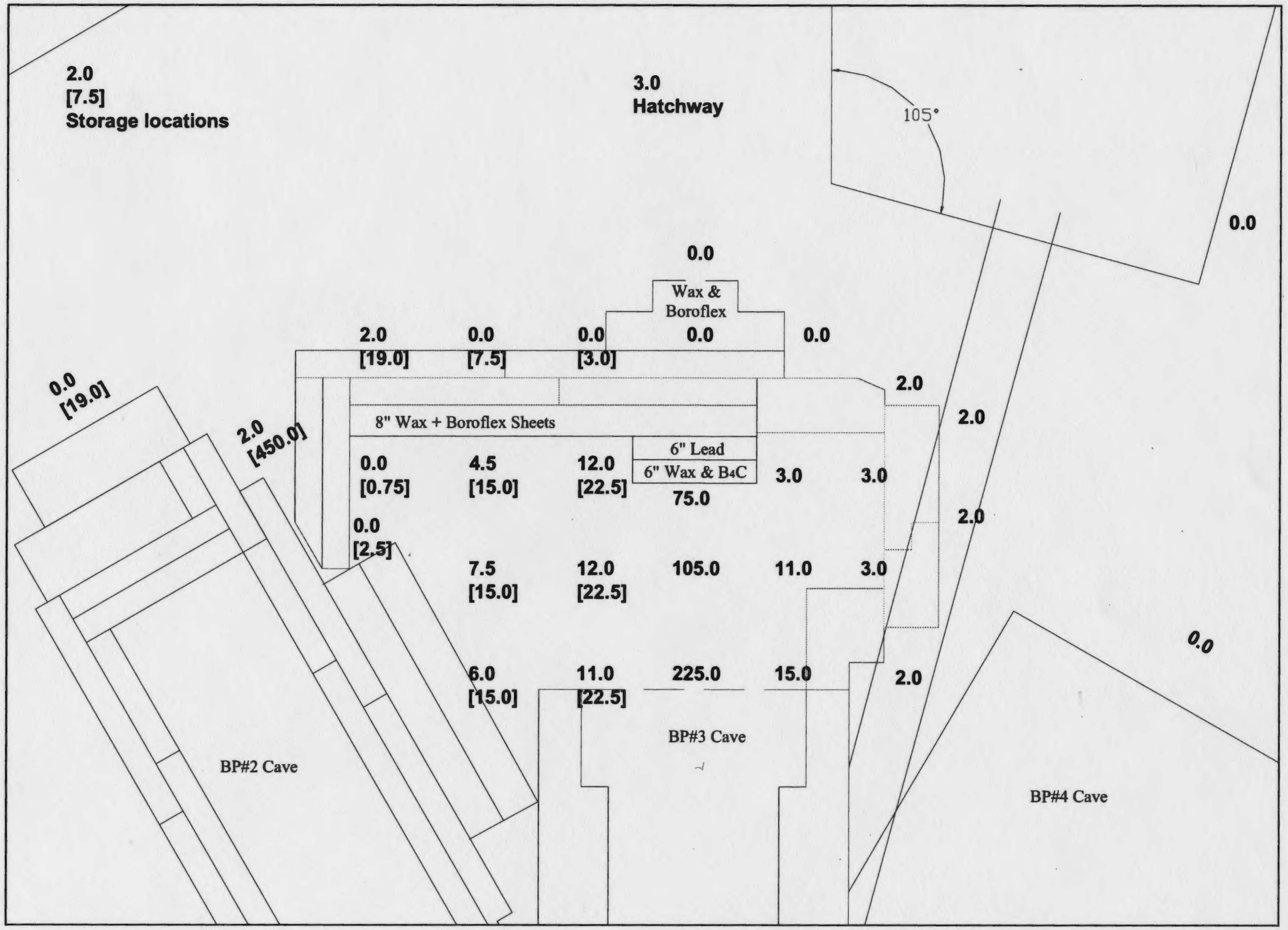

Figure 5.1. Closed Shutter Survey – Neutron dose rate (μSv/hr) at 1.0 m (Beam level) from ground level. Scaled to 3.0 MW reactor power.

[Values in square brackets are measured with BP#2 shutter open].

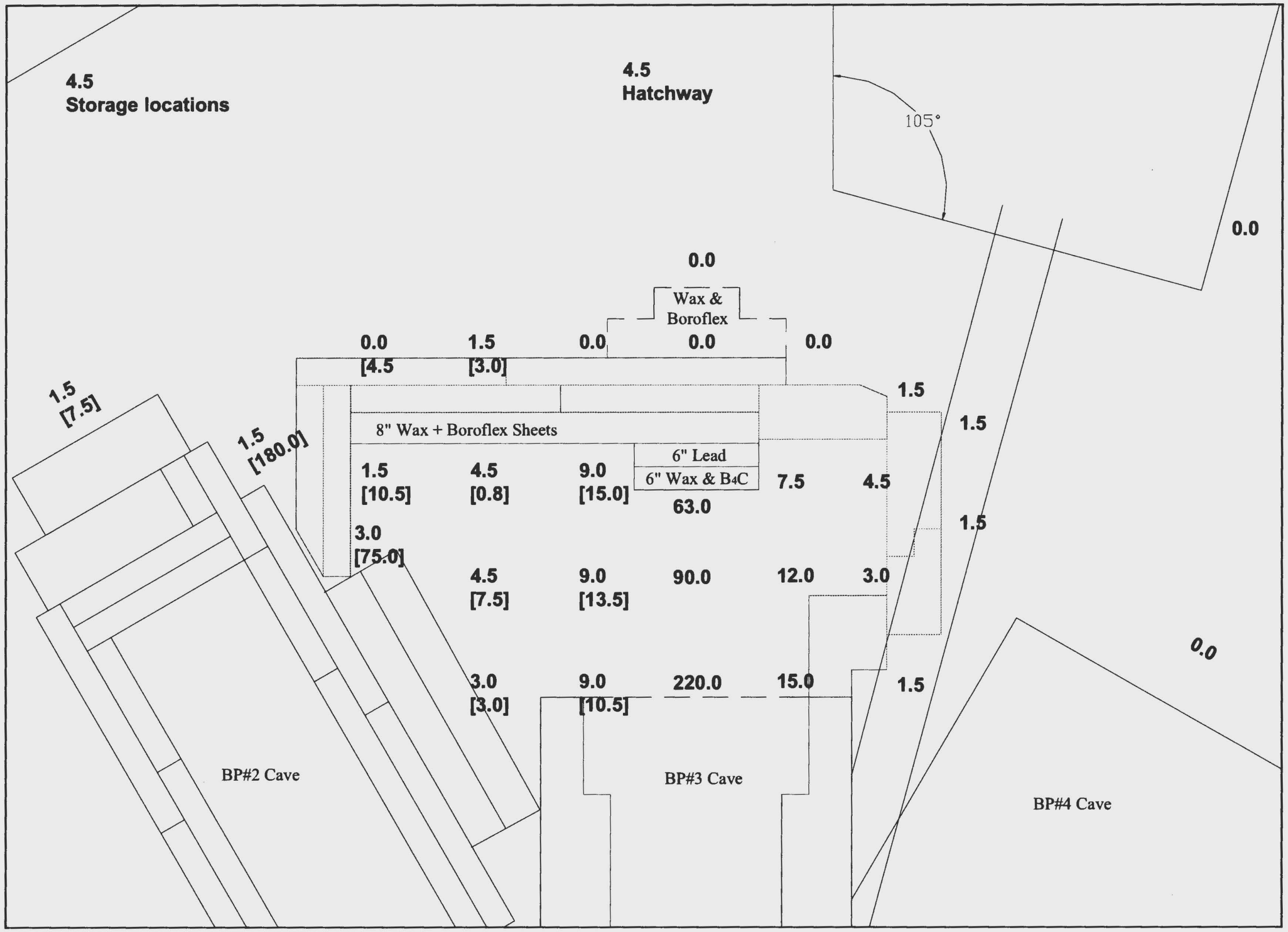

Figure 5.2. Closed Shutter Survey – Gamma dose rate (μSv/hr) at 1.0 m (Beam level) from ground level. Scaled to 3.0 MW reactor power.

[Values in square brackets are measured with BP#2 shutter open].

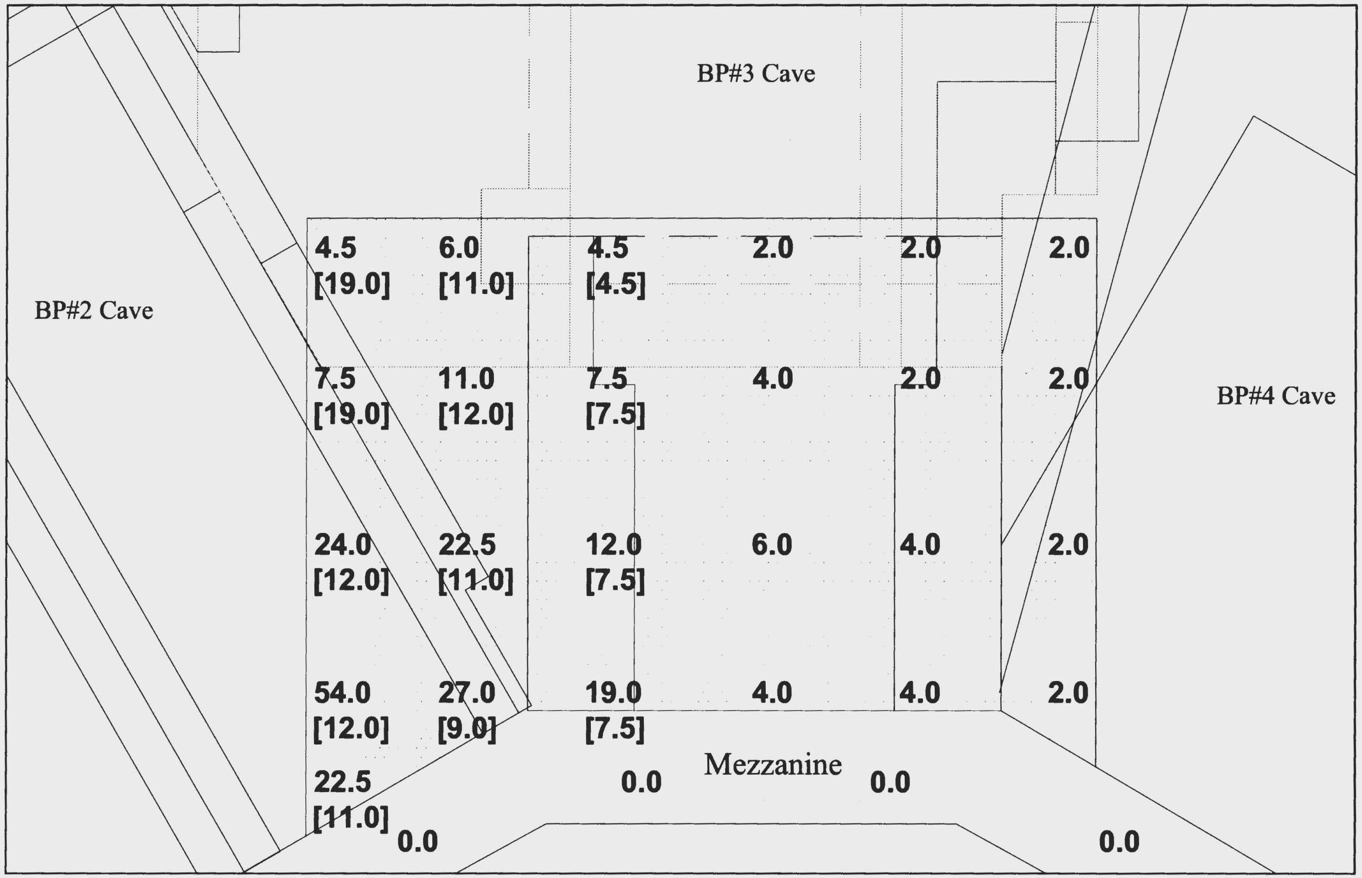

Figure 5.3. Closed Shutter Survey – Neutron dose rate (μSv/hr) above workstation. Scaled to 3.0 MW reactor power.

[Values in square brackets are measured with BP#2 shutter open].

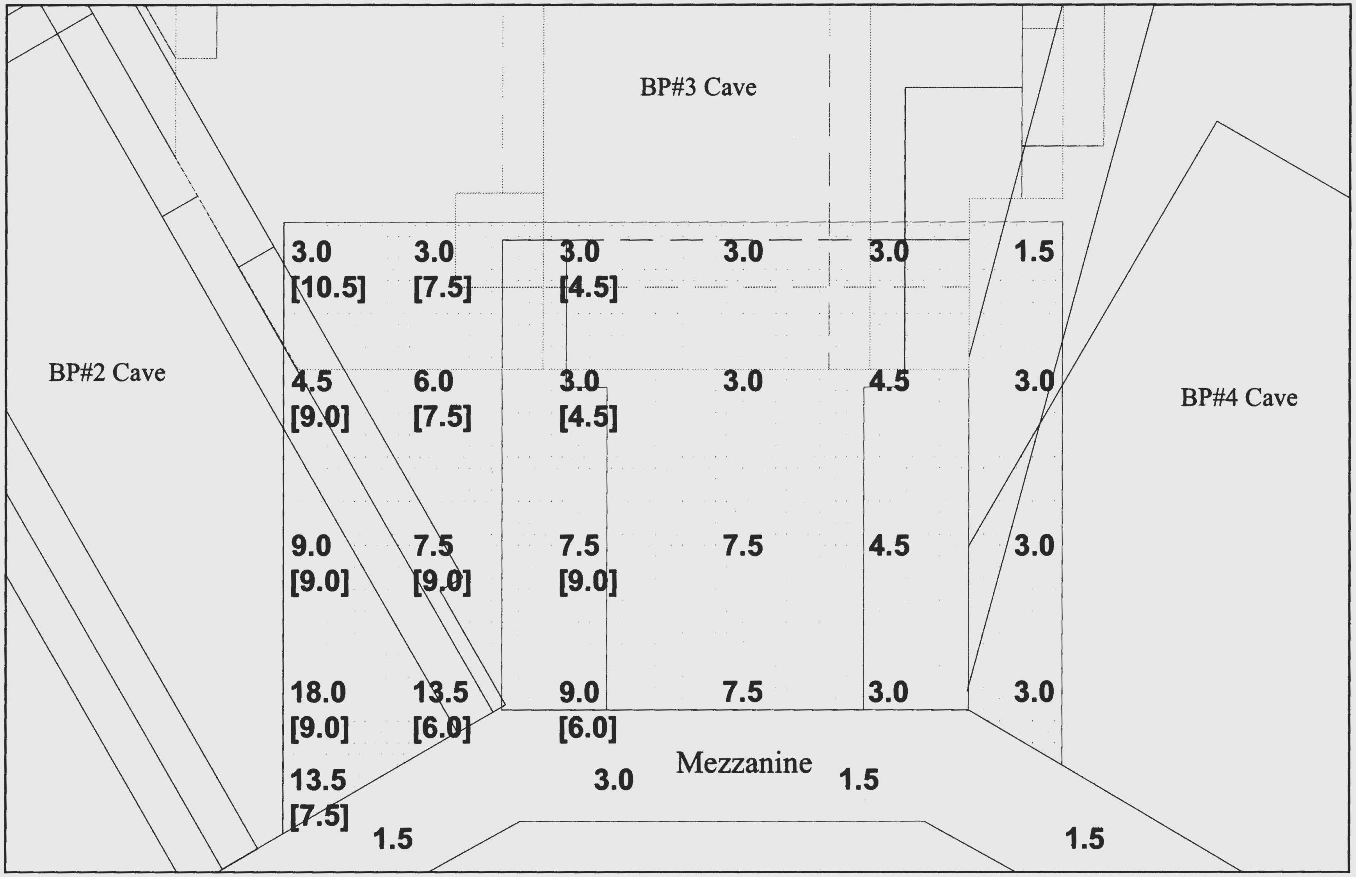

Figure 5.4. Closed Shutter Survey – Gamma dose rate (μSv/hr) above workstation. Scaled to 3.0 MW reactor power.

[Values in square brackets are measured with BP#2 shutter open].

bricks. Also, the opening in this wall is larger than what is required to clear the neutron beam and it is larger than the diameter of the shutter allowing radiation to stream from the side of shutter.

5.1.2 Open Shutter Radiation Dose Surveys

Figures 5.5 through 5.8 show radiation dose (neutron and gamma) survey results measured outside the facility biological shielding performed with the shutter open at 3.0 MW. The dose rates are around the 25.0 μSv/hr criterion except for regions near BP#2 – affected by the higher background radiation levels due to other facilities, and some regions at the side from the cave door. The door side and roof regions affected by BP#2 are considered designated radiation areas with limited access when the shutter is open.

5.2 Neutron Beam Characteristics

Several experimental measurements have been conducted to determine the characteristics of the neutron beam such as its intensity, uniformity and quality (gamma ray and fast neutron contents) at the imaging plane.

5.2.1 Beam Uniformity and Neutron Intensity

The beam uniformity (flatness) and neutron intensity have been determined using three different techniques, copper foils irradiation, scintillator-CCD camera

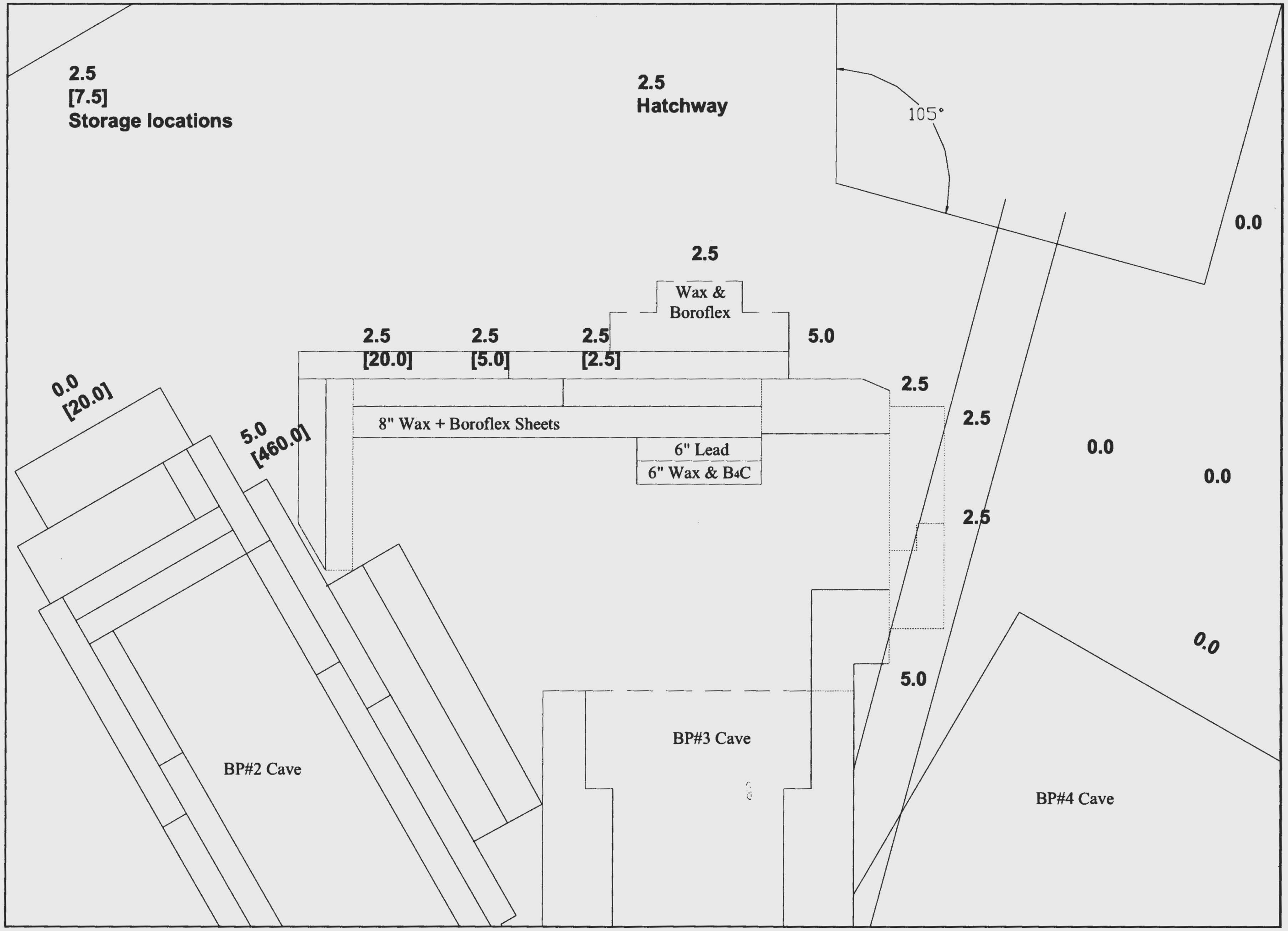

Figure 5.5. Open Shutter Survey – Neutron dose rate (μSv/hr) at 1.0 m (Beam level) from ground level.

Measured at 3.0 MW reactor power.

[Values in square brackets are measured with BP#2 shutter open].

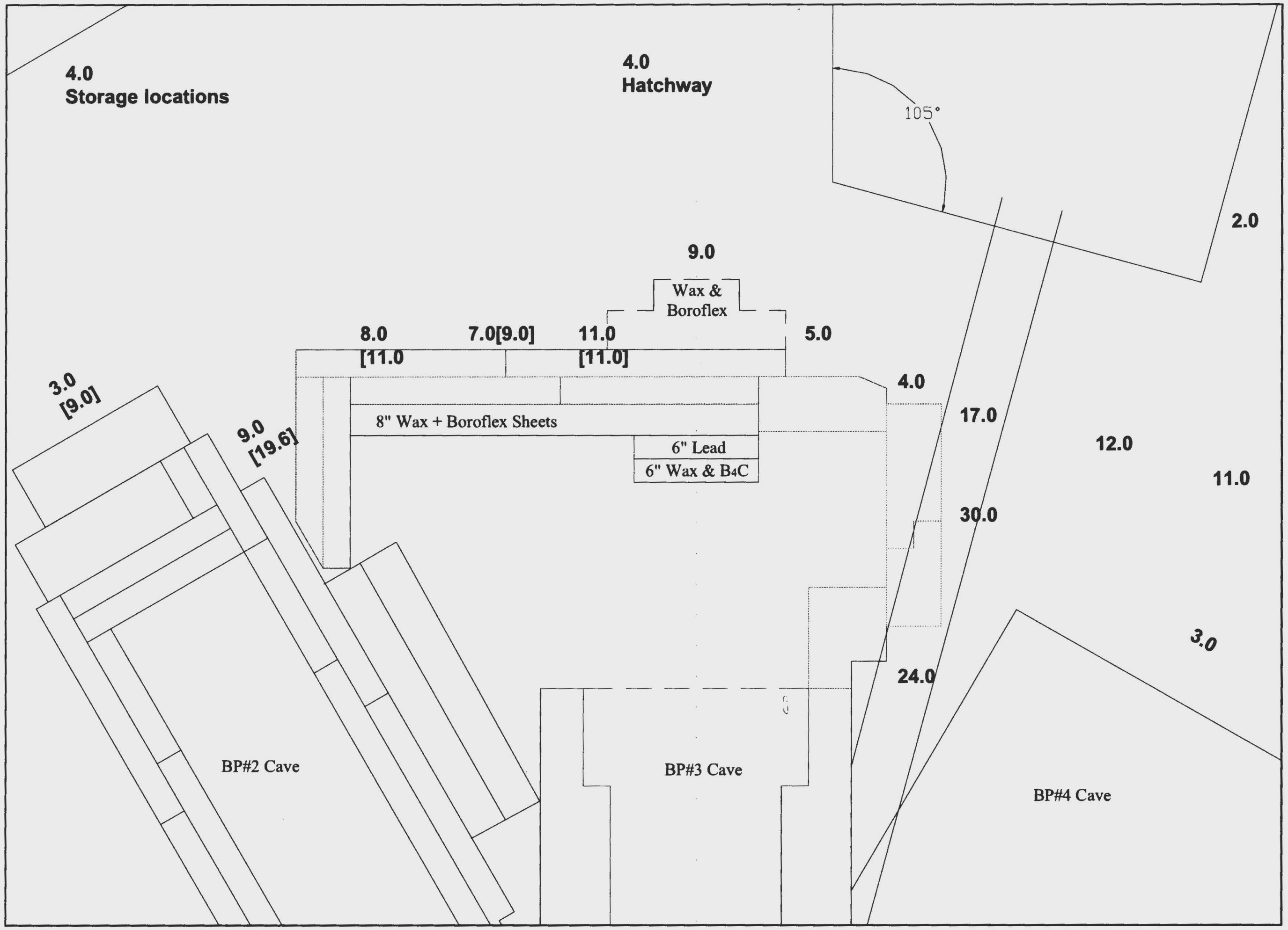

Figure 5.6. Open Shutter Survey – Gamma dose rate (μSv/hr) at 1.0 m (Beam level) from ground level. Measured at 3.0 MW reactor power.

[Values in square brackets are measured with BP#2 shutter open].

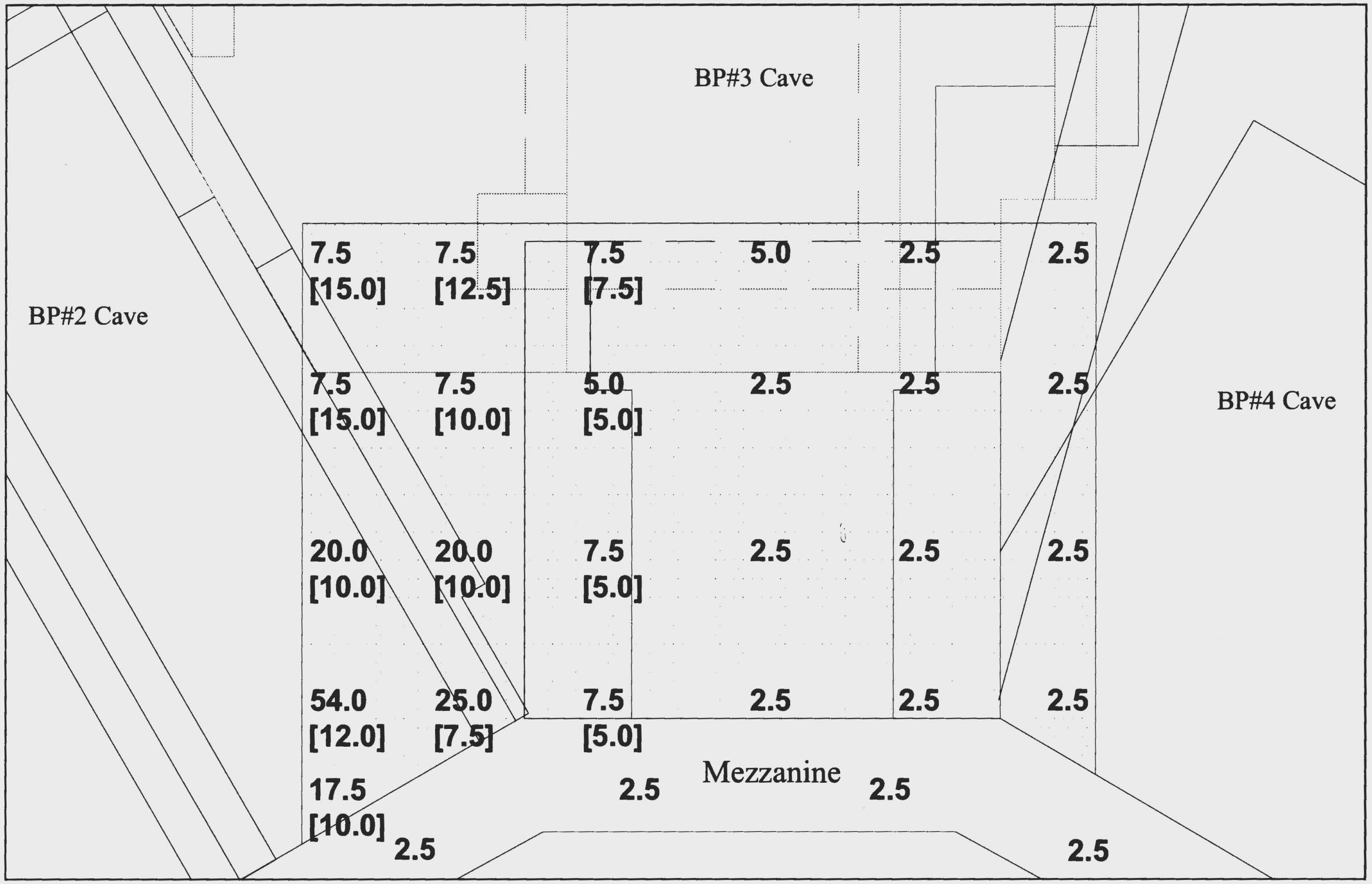

Figure 5.7. Open Shutter Survey – Neutron dose rate (μSv/hr) above workstation. Measured at 3.0 MW reactor power.

[Values in square brackets are measured with BP#2 shutter open].

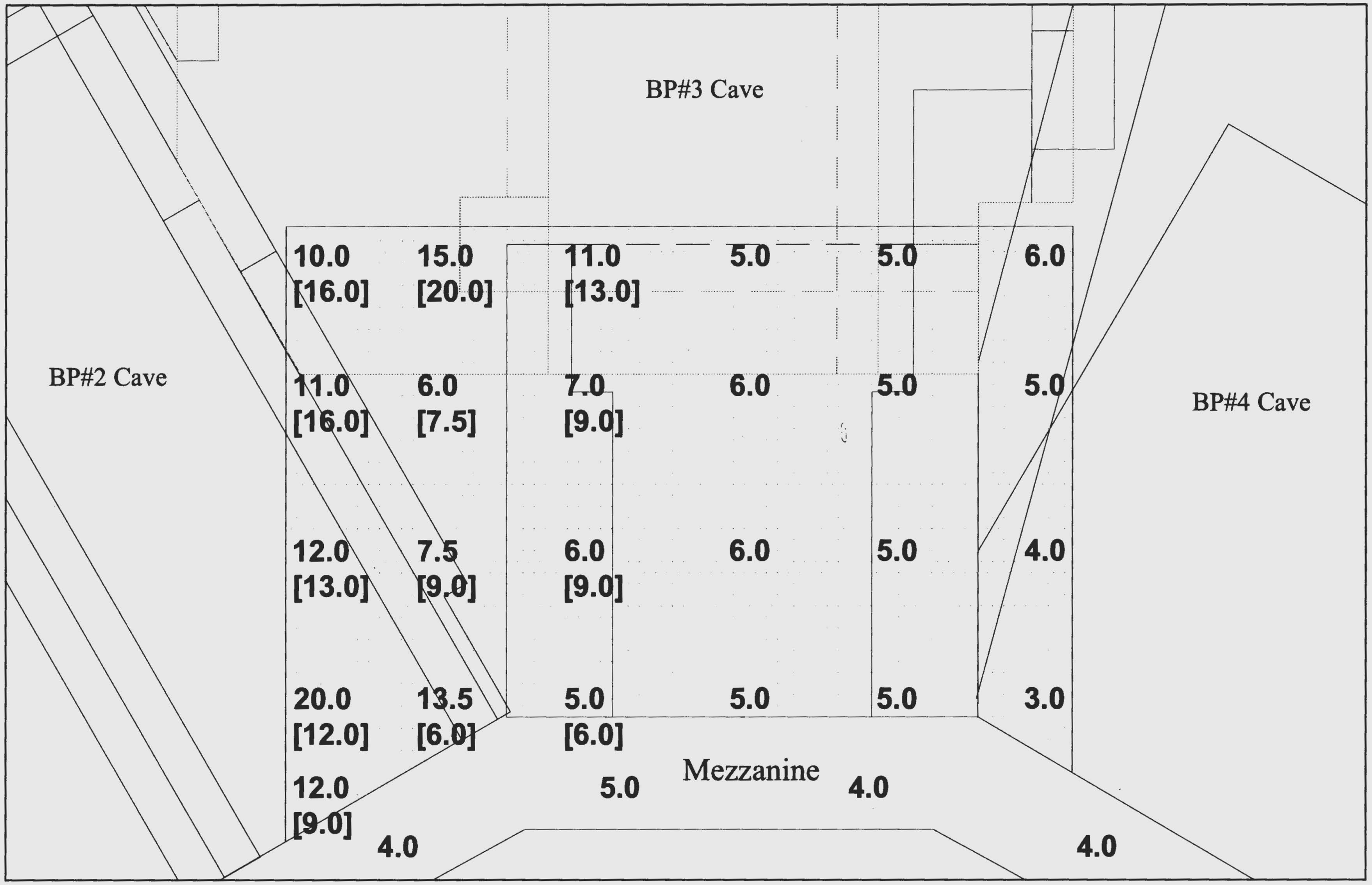

Figure 5.8. Open Shutter Survey – Gamma dose rate (μSv/hr) above workstation. Measured at 3.0 MW reactor power.

[Values in square brackets are measured with BP#2 shutter open].

radiography and standard film radiography.

A 30.0 cm × 30.0 cm two-dimensional matrix of copper foils (grid spacing is 7.5 cm) were irradiated near the imaging plane (38.0 cm away towards the back wall), using the same technique described in Section 3.1. Figure 5.9 shows a schematic of the experimental apparatus used where 30 copper foils were placed on a 0.5 mm thick 40 cm × 40 cm cadmium sheet (15 foils on each side).

Figure 5.10 shows a two-dimensional contour map representing the beam thermal neutron intensity at the imaging plane obtained from copper foils irradiation. The thermal neutron flux is nearly uniform over the 20.0 cm diameter imaging area with an average intensity ranging from 0.85×10^7–1.08×10^7 n/cm^2-s. Outside the effective area of the beam the thermal neutron intensity decreases dramatically. Considering the divergence of the beam and the difference between the irradiation location and the actual image plane location, the actual maximum calculated thermal neutron flux at the imaging plane, based on copper foil activity measurements, is interpolated to be $1.26\times10^7 \pm 0.05\times10^7$ n/cm^2-s. Figure 5.11 shows a two-dimensional contour map representing the beam fast (E>1MeV) neutron intensity at image plane, which is non-uniform with a maximum (6.5×10^6 n/cm^2-s) at the centre of the beam.

Figure 5.12 shows a neutron image of the beam with no object recorder using the developed real-time neutron radiography system; the image is an average of 128 frames captured by the frame grabber. Some white spots appear in the image due to radiation damage of some pixels in the video camera CCD chip. Also, the image shows some artifacts of increased contrast between adjacent scan lines resulting from the DVD

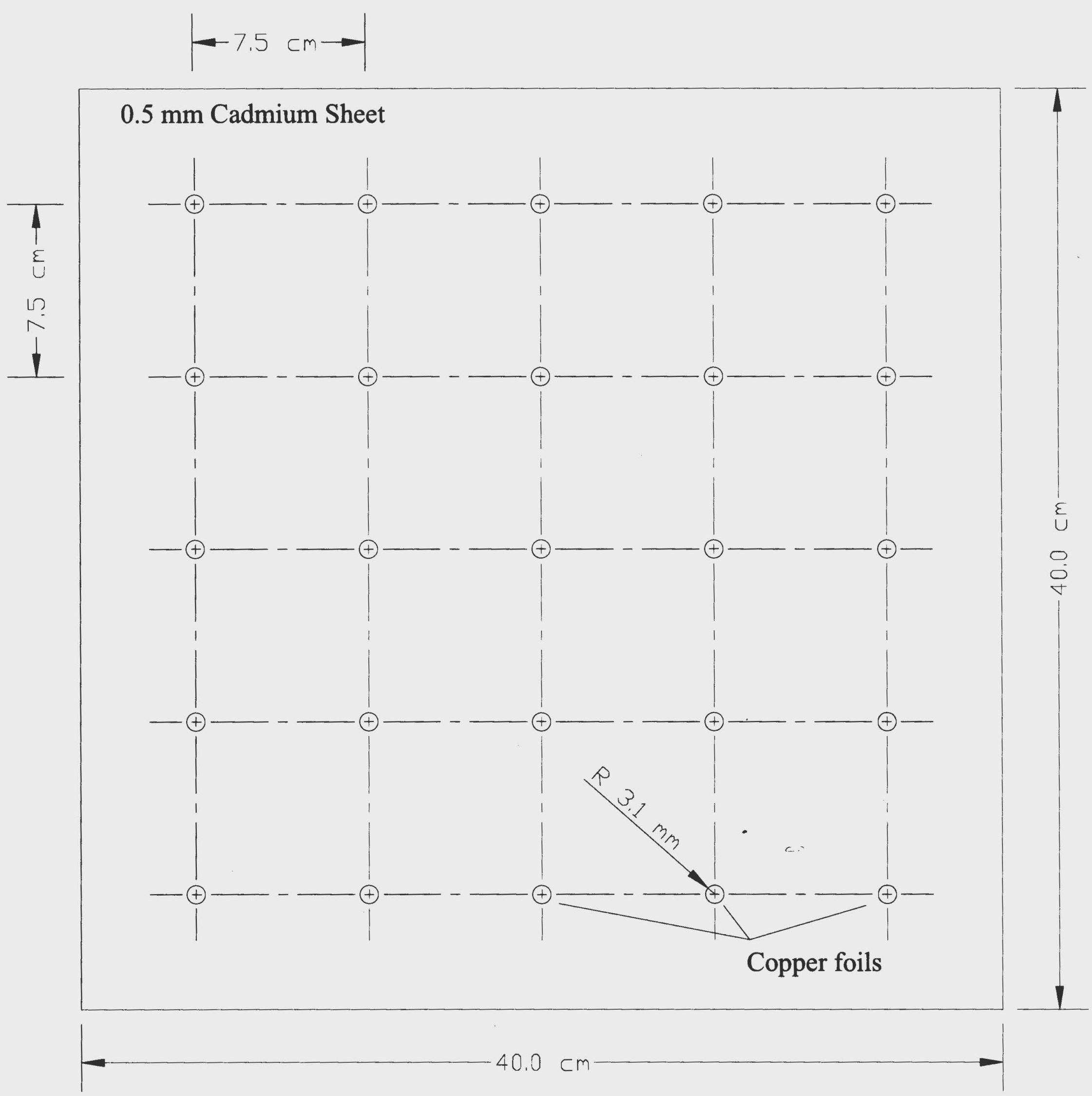

Figure 5.9. Schematic representation of the experimental apparatus used for copper-foil irradiation to evaluate beam uniformity and neutron intensity.

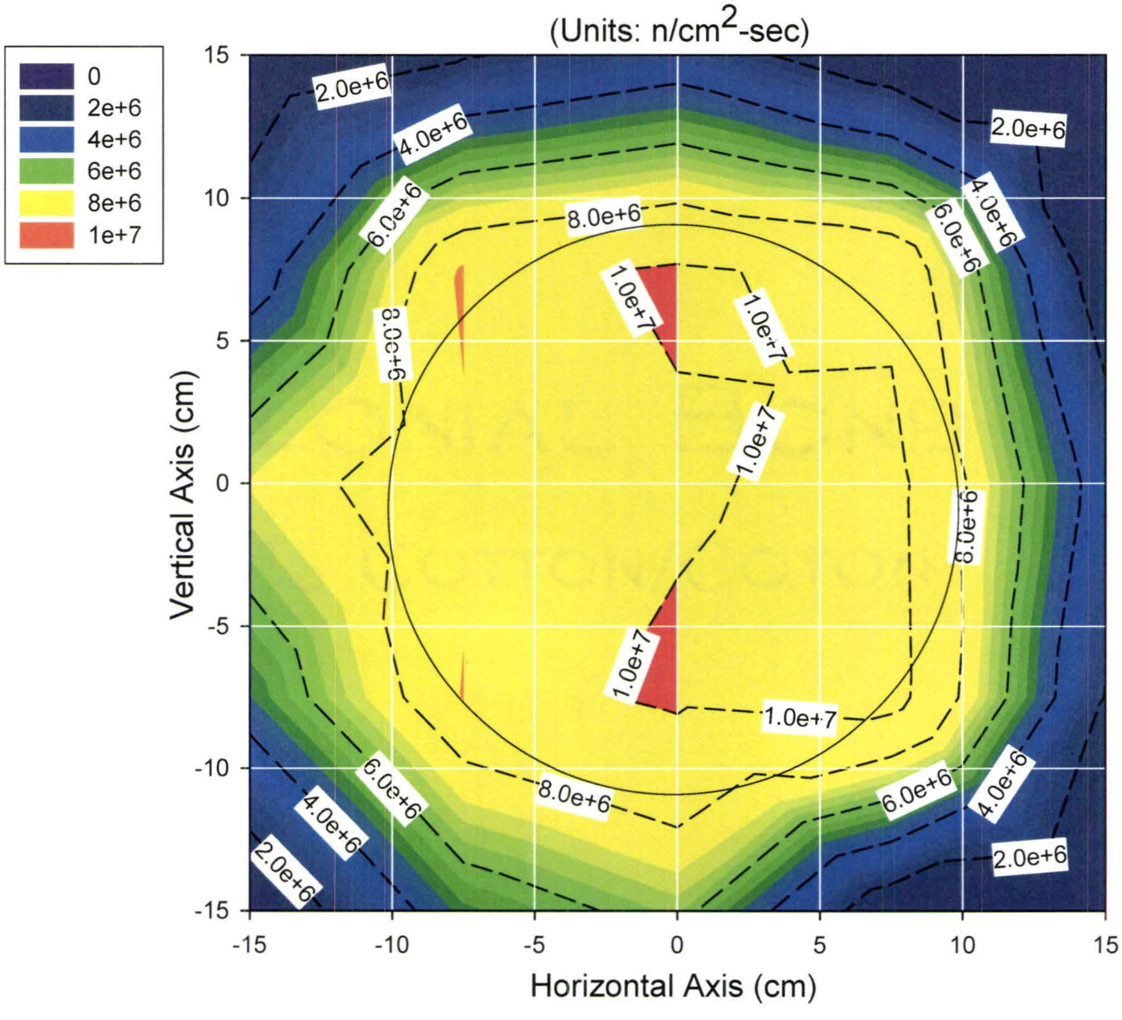

Figure 5.10. Two-Dimensional thermal neutron (E < 0.5 eV) intensity contour map near imaging plane based on copper foil irradiation experiment.

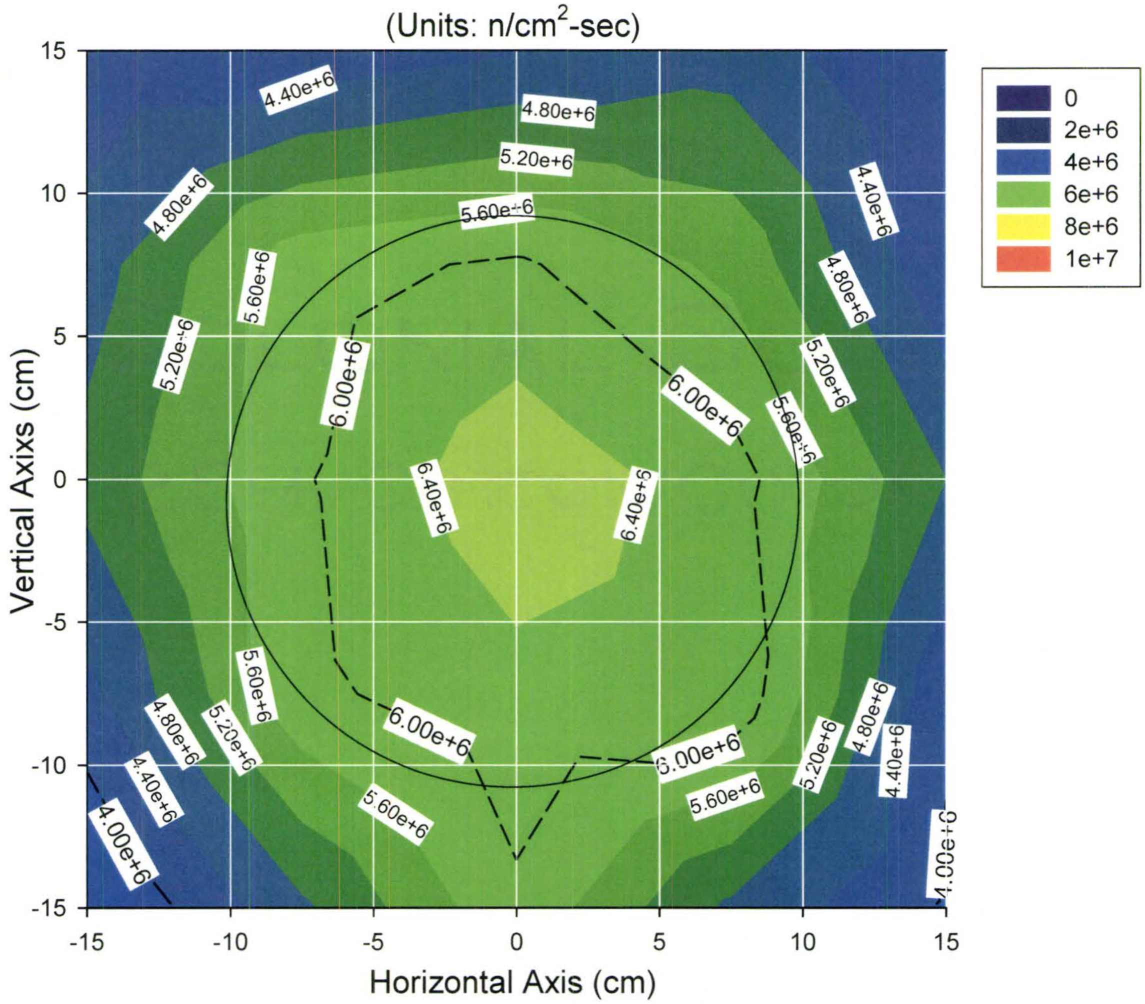

Figure 5.11. Two-Dimensional fast neutron (E > 1.0 MeV) intensity contour map near the imaging plane based on copper foil irradiation experiment.

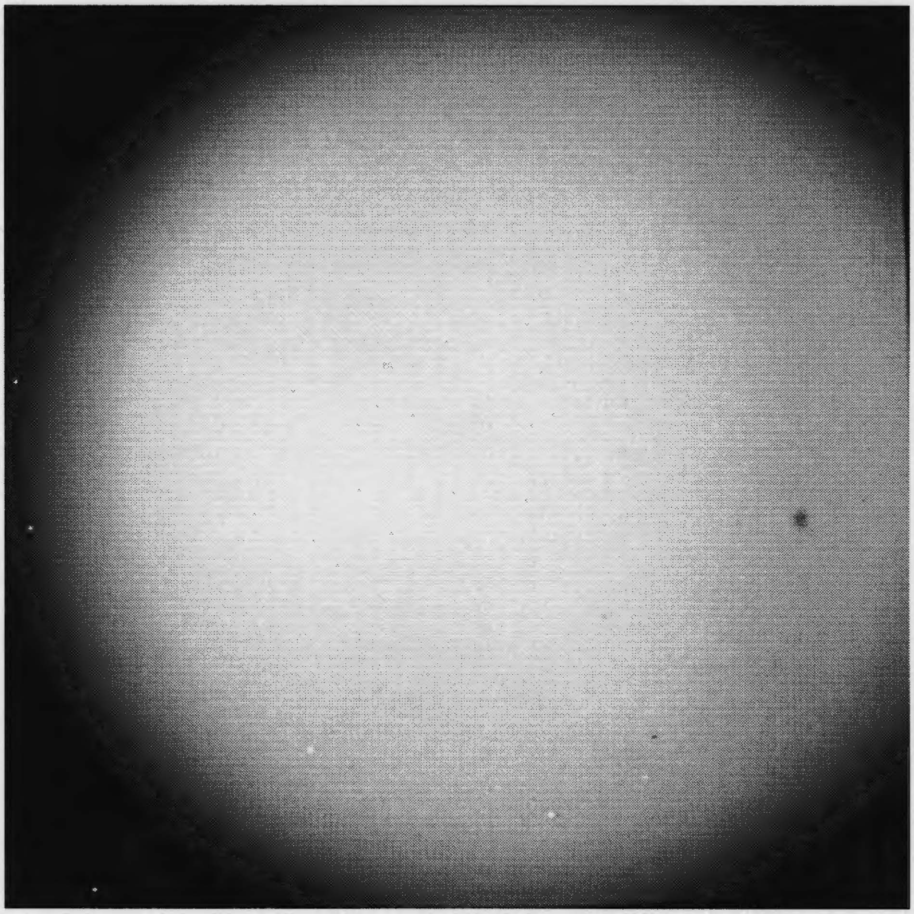

Figure 5.12. Neutron image of the beam with no object captured by the real-time neutron radiography system.

manipulation of the frames where each frame is comprised of two interlaced fields: the first field consists of all the odd lines, and the second field consists of all the even lines.

Figure 5.13 shows a scanned neutron image (with inverted Grey levels) of the beam obtained from static film radiography technique with 84.0 seconds exposure using AGFA D3-SC single coated film and a vapour-deposited Gd screen. In film radiography, using standard photographic films, increasing the neutron exposure increases the amount of Silver ions chemically reduced black metallic Silver and hence, the film darkness. The Grey levels of Figure 5.13 are inverted to resemble the Grey level scale obtained by scintillator-camera radiography. A maximum film density, dimensionless quantity, of 2.68 is measured using an optical-densitometer at the beam-centre, which is directly proportional to the thermal neutron fluence (thermal neutron flux integrated over exposure time). The following equations define the film density, D, and its relation to beam intensity and exposure time:

$$D = \log_{10}(\frac{L_o}{L}) \tag{5.1}$$

$$D = Constant \times \int_0^{\Delta t} I(t)dt = Constant \times I \times \Delta t \tag{5.2}$$

,where L_o is the measure light intensity for un-exposed film region, L is the measured light intensity for exposed film region, I is the neutron beam intensity and Δt is the exposure time.

A proportionality constant of 2.452×10^{-9} cm^2/n can be estimated from BP#2, where a thermal neutron flux of 4.0×10^{6} n/cm^2-s produces a film density of 2.55 for 260 seconds exposure time using the same film type. A maximum thermal neutron flux of

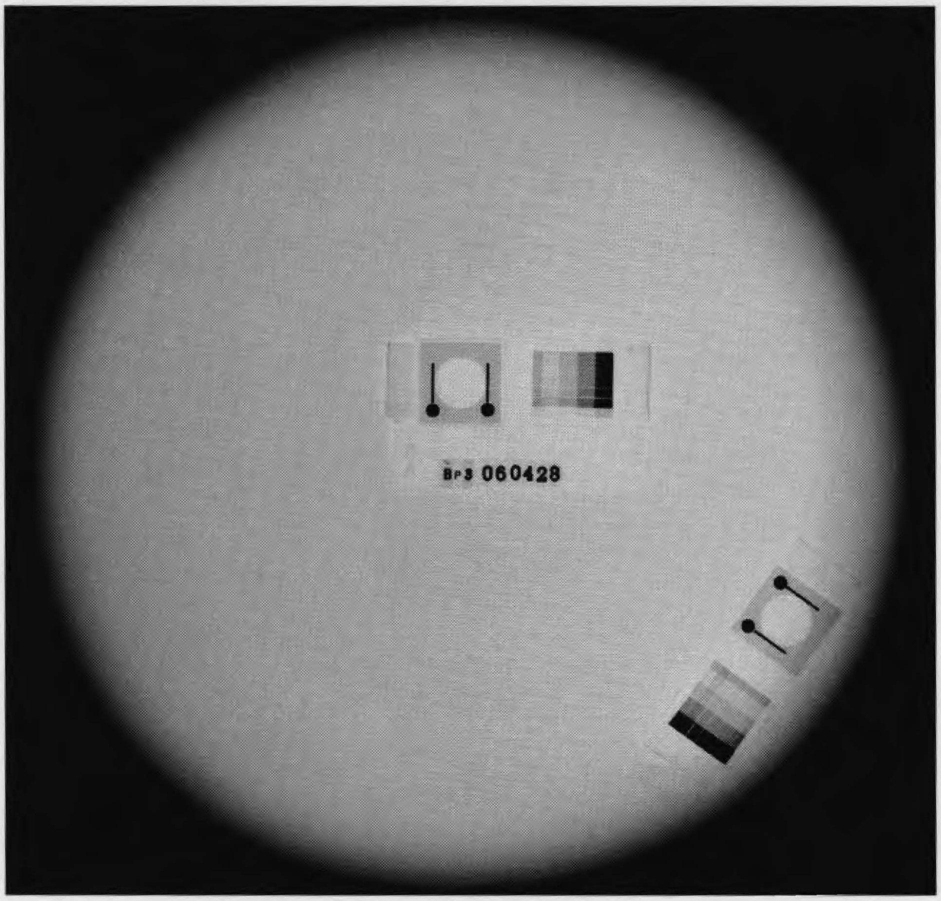

Figure 5.13. Scanned image of static film radiograph of the neutron beam. (Grey levels are inverted.)

$1.30\times10^{7} \pm 0.02\times10^{7}$ n/cm^2-s is estimated for the neutron beam based on film radiography.

Figure 5.14 shows a comparison of thermal neutron intensities obtained analytically, numerically and experimentally along beam horizontal and vertical centre-lines, where numerical values are obtained from Monte-Carlo simulations described in Section 4.3, and analytical calculations described in Section 3.3. The difference in magnitude between numerical and experimental values, both agree not only qualitatively but also quantitatively within 30%. Given the uncertainty in the measurement and analytical values, this difference is reasonable and within the acceptable range. The difference in magnitude between numerical and experimental values, both agree not only qualitatively but also quantitatively within 30%.

The differences in magnitude among the thermal neutron intensity values obtained analytically, numerically and experimentally are expected due to the uncertainty in the source flux measurements (Section 3.1), where a 1.0 mm axial displacement in copper foil position can lead to a reduction in thermal neutron flux by 3.5%. Also, analytical calculations and Monte-Carlo simulations have not accounted for the addition of ~1.0 cm of aluminium for bismuth filter container (to contain polonium gas produced from neutron absorption in bismuth) and beam tube end cover as these changes were imposed during the construction of the facility.

Figure 5.15 shows horizontal and vertical line profiles obtained from neutron images recorded by standard film radiography and real-time neutron radiography system

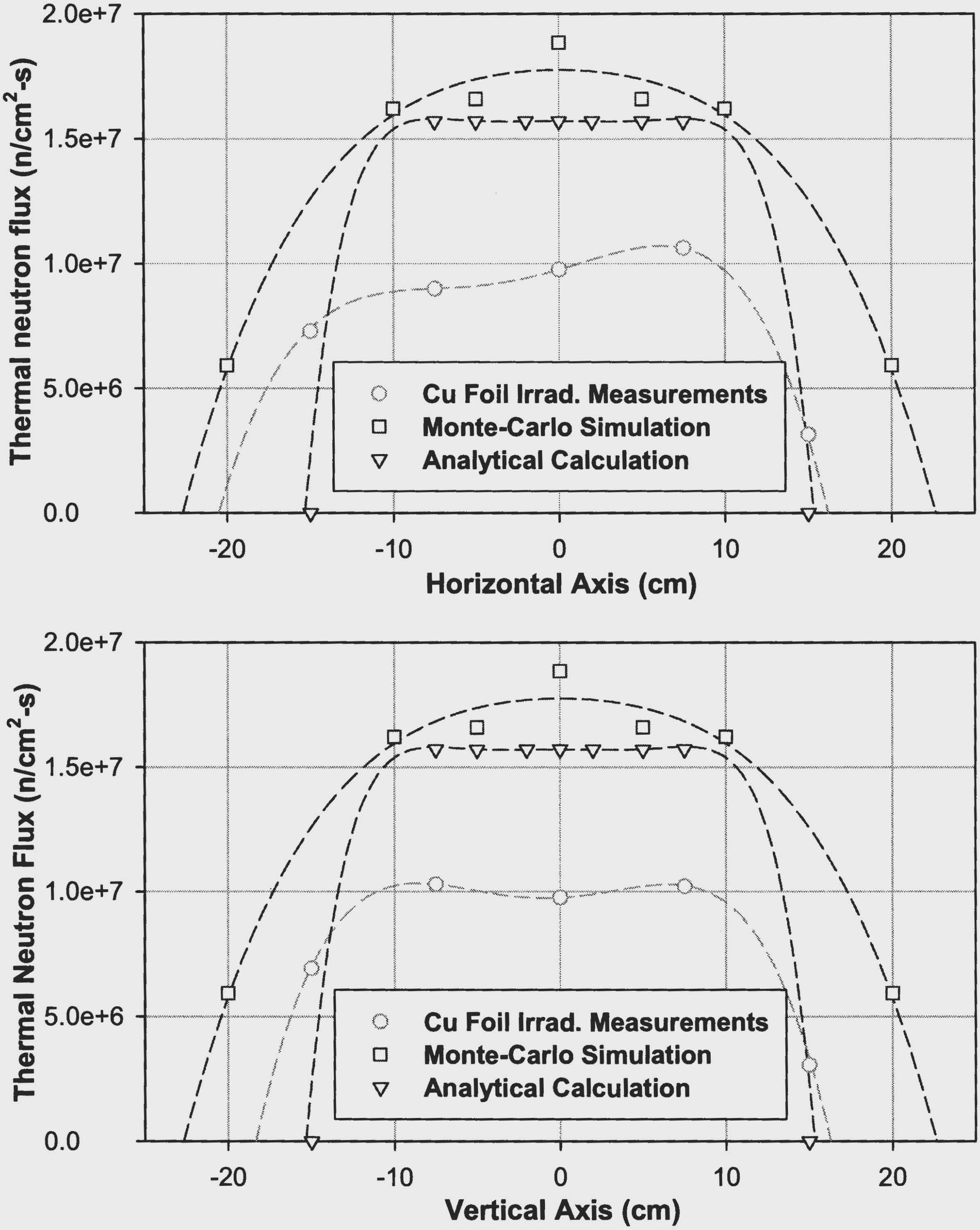

Figure 5.14. Comparison of thermal neutron intensity profiles obtained by different techniques.

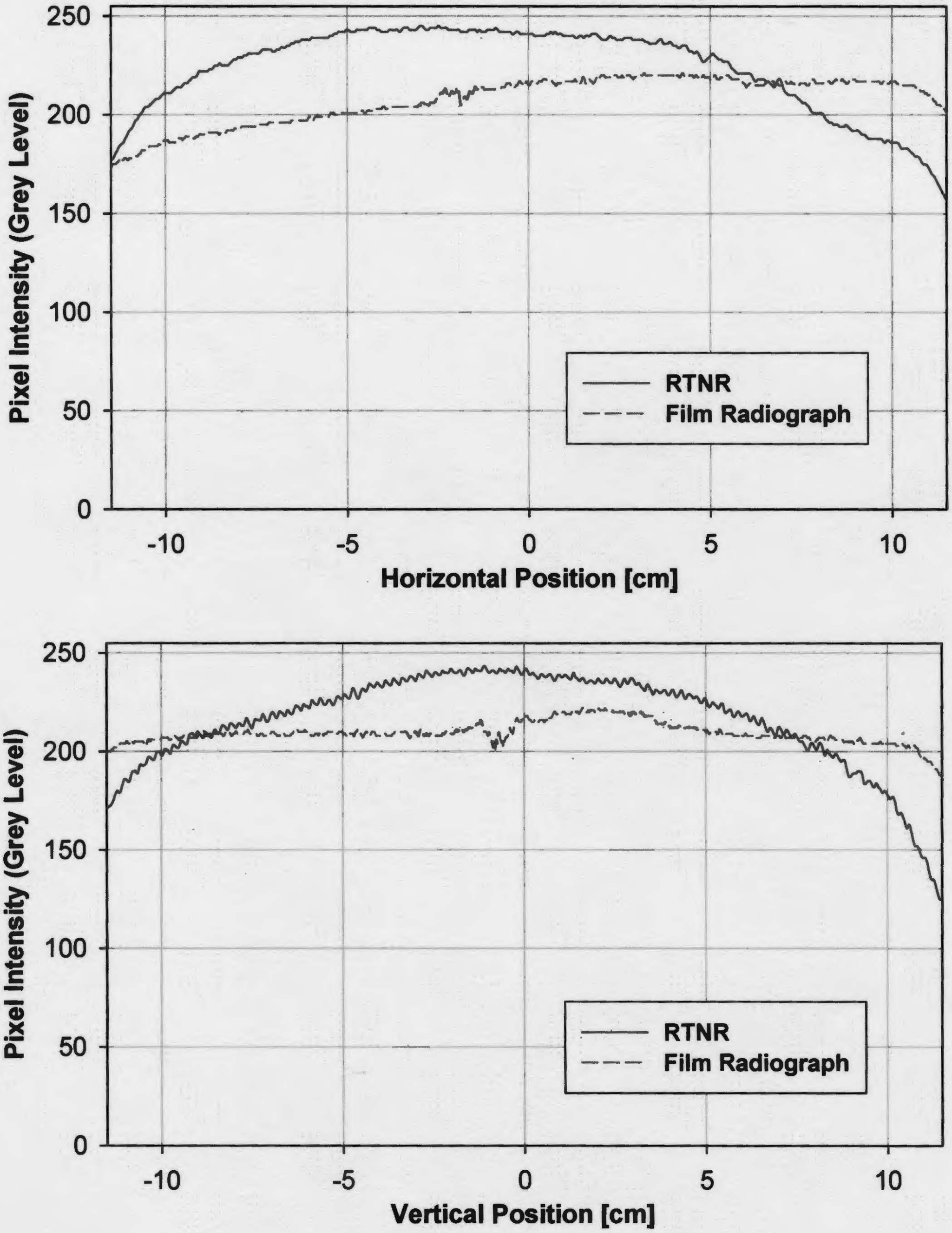

Figure 5.15. Comparison of pixel intensity profiles obtained by different techniques.

along beam centre-lines. Although the line profiles obtained by standard film radiography are quite flat and uniform, the line profiles obtained by real-time neutron radiography show larger curvature (gradient). This can be related to the fact that the light emitted from the edges of the neutron screen suffers more attenuation, as it is not incident in right angles. In addition, the light emitted from the edges of the neutron screen suffers more divergence as it travels longer distance to reach the camera aperture (inverse square law) while in the film radiography this effect is not encountered as the film is touching the neutron conversion screen.

The tilt in the horizontal line profile obtained by standard film radiography is related to the source asymmetry as discussed in section 3.1. The horizontal line profile obtained by RTNR does not show a similar trend due to non-uniformities in the neutron conversion screen.

Two sets of the American Society for Testing and Materials - ASTM E545 sensitivity and beam purity indicators are shown in the neutron image of the beam obtained from static film radiography (Figure 5.13). Figure 5.16 shows a schematic representation of the ASTM E545 sensitivity and beam purity indicators, while Figure 5.17 shows a 256-frame averaged neutron image of ASTM E545 sensitivity indicator and beam purity indicator obtained by the RTNR system.

The beam sensitivity indicator is a combined hole and gap gauge to determine the system resolution. Twelve holes are sized to be smaller than what can be seen by conventional neutron radiography and they progress up in size. Similarly, seven gaps formed by aluminium shims between sheets of acrylic resin. For sensitivity indicator

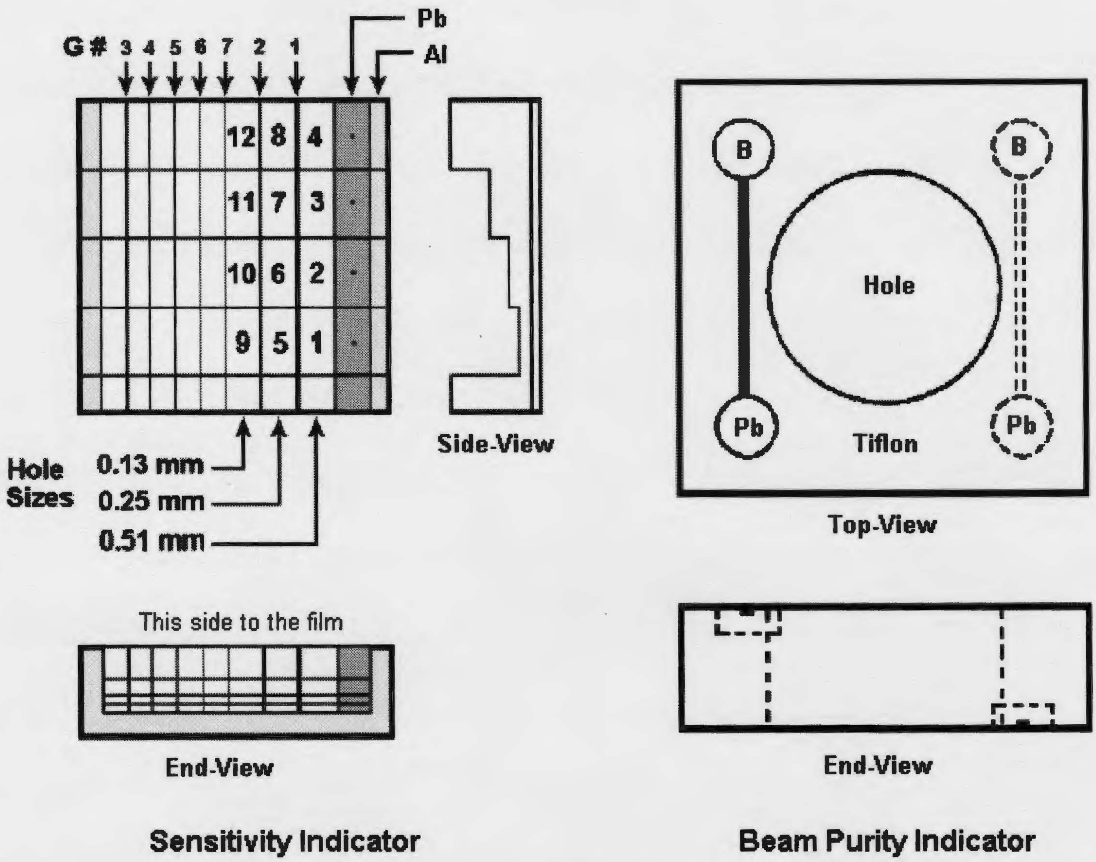

Figure 5.16. Schematics of the ASTM E545 sensitivity indicator and beam purity indicator.

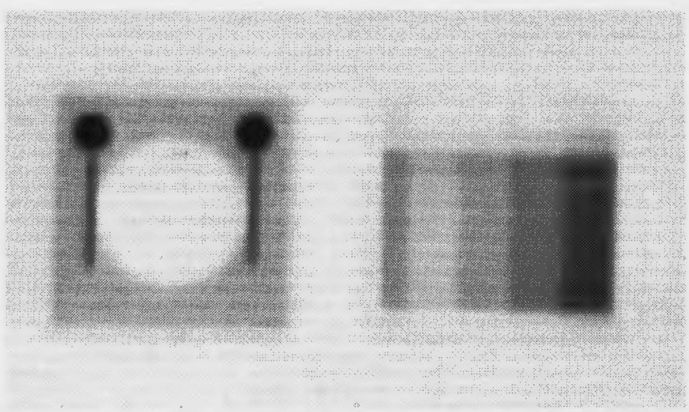

Figure 5.17. Neutron image (256-frame average) of the ASTM E545 sensitivity indicator and beam purity indicator obtained using RTNR System.

neutron image obtained by film radiography, eight holes and all the seven gaps are contrasted. Hole #8 is a 0.254 mm in diameter and covered with 5.08 mm of acrylic resin, while gap #7 is 0.0125mm aluminium shim. The largest hole size is 0.508 mm and the largest gap thickness is 0.254 mm are beyond the contrast capability of the RTNR system as the system spatial resolution is 0.444 mm as it will be discussed in Section 5.3.1.

The beam purity indicator provides quantitative measures of scattered neutrons, gamma rays and pair production contributions to the neutron image as well as the effective thermal neutron content of the beam. The indicator consists of a Teflon block with a hole in the middle. Two lead disks and two boron nitride disks are installed in the Teflon block such that each side of the block contains one desk of each material. The difference between the film densities (Grey levels) at the middle hole and at boron nitride disks provides a measure of the effective thermal neutron content of the beam. The difference in film densities (Grey levels) at the two lead disks provides a measure of the pair production, while the difference in film densities (Grey levels) at the two boron nitride disks provides a measure of the scattered neutron. Table 5.1 lists the average film densities and the Grey levels at different regions of the ASTM E545 beam purity indicator measured from the film and RTNR neutron images. The values show a good agreement between the Grey levels and film densities to within 4.0%.

5.2.2 Beam Quality

The quality of the beam is determined by how much non-thermal neutron (gamma rays and fast neutrons) content is streamed by the collimator. The gamma and fast neutron

Table 5.1. Film densities and Grey levels measured for ASTM E545 beam purity indicator.

	Film Radiograph		RTNR System	
	Film Density	Normalized film density	Grey level	Normalized Grey level
Middle Hole	2.68	1.000	243.0	1.000
Teflon	2.23	0.832	209.7	0.863
Lead (high)	2.23	0.832	208.1	0.857
Lead (low)	2.20	0.821	207.2	0.853
Boron (high)	0.89	0.332	87.3	0.359
Boron (low)	0.86	0.321	86.1	0.355

contents are determined experimentally.

5.2.2.1 Neutron-to-Gamma Ratio

The gamma content of the beam has been estimated using an available tissue-equivalent proportional counter (TEPC) filled with a Propane based tissue-equivalent plastic (FAR west Technologies Inc, Model LET-1/2). Two measurements have been conducted. The first measurement is at zero power to measure the gamma dose due to core activity while the second measurement is at low power (30.0 kW) to avoid saturating the detector. Signal processing allows isolating the gamma dose from the total (neutron and gamma) dose as the spectrum and the pulse shape of neutron events are different from those of gamma events. The TEPC gamma dose measurement was scaled to full power operation (3.0 MW) and the dose rate of beam gamma content is estimated to be 6.0×10^5 μSv/hr with a typical dose uncertainty of 10% [100]. From the thermal neutron flux measured using copper foil irradiation at the imaging plane and the gamma dose measurements, the n/γ ratio is estimated to be 6.0×10^5 n/cm^2-μSv.

5.2.2.2 Cadmium Ratio

The cadmium ratio is estimated based on the measured values of thermal and fast neutron flux obtained from copper foil irradiations. Using the 2200 m/s thermal neutron absorption cross-section and the resonance integral for gold, the cadmium ratio can be calculated as follows:

$$\text{Cd-ratio} = \frac{\sigma_{Au} \times \phi_o + I_{Au} \times C_F}{I_{Au} \times C_F} \tag{5.3}$$

where σ_{Au} is the gold 2200 m/s neutron capture cross-section, I_{Au} is the gold resonance integral, ϕ_o is the 2200 m/s (E_o = 0.0253 eV)_neutron pseudo-flux and C_F is the 1/E epi-thermal neutron flux constant.

A value of 1.22 has been estimated for the Cd-ratio at the imaging plane. This relatively small value indicates the presence of relatively large fast neutron content. Although the presence of neutrons with higher energies may reduce the contrast of the neutron images, thermal neutron scintillators have a negligible response to energetic neutrons and neutron energy filtration is not necessary.

5.3 Characteristics of the Real-Time Neutron Radiography System

5.3.1 Image Spatial Resolution

A 4.0 cm × 4.0 cm square cadmium foil (0.5 mm thick) was placed in the centre of the neutron conversion screen for a spatial calibration (conversion). Figure 5.18 shows a neutron image of the beam captured by dynamic neutron radiography system with a 4.0 cm × 4.0 cm square cadmium foil and a 3.8 cm diameter circular gadolinium foil. The cadmium and gadolinium foils are in contact with the neutron conversion screen to minimize the image unsharpness due to beam divergence. Figure 5.19 shows the image processing results, where a comparison of horizontal line profiles measured from the no object and Cd foil neutron images at the same region of interest. Figure 5.20 shows the

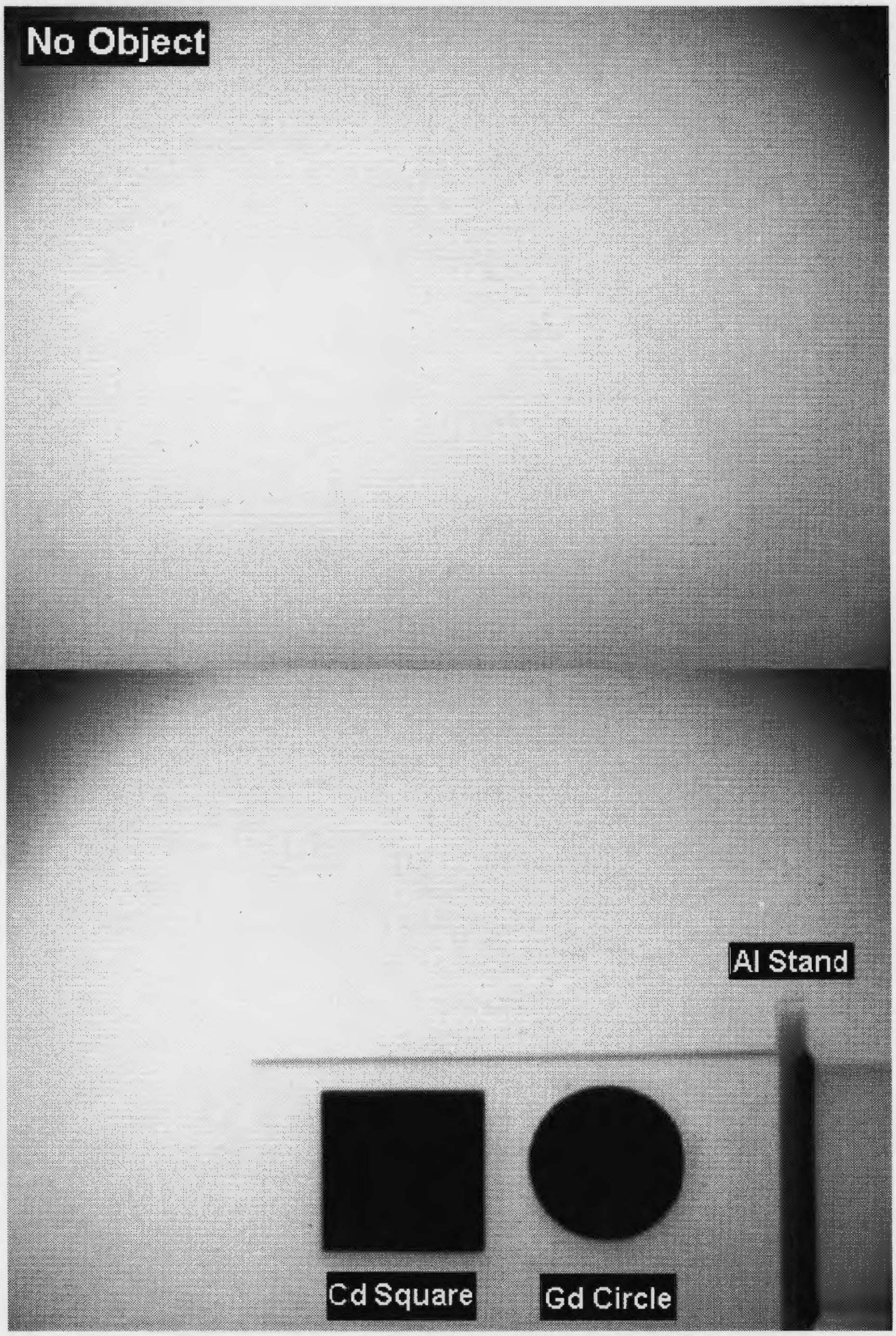

Figure 5.18. Neutron images of the beam with no object, a square cadmium foil and a circular gadolinium foil obtained by real-time neutron radiography system.

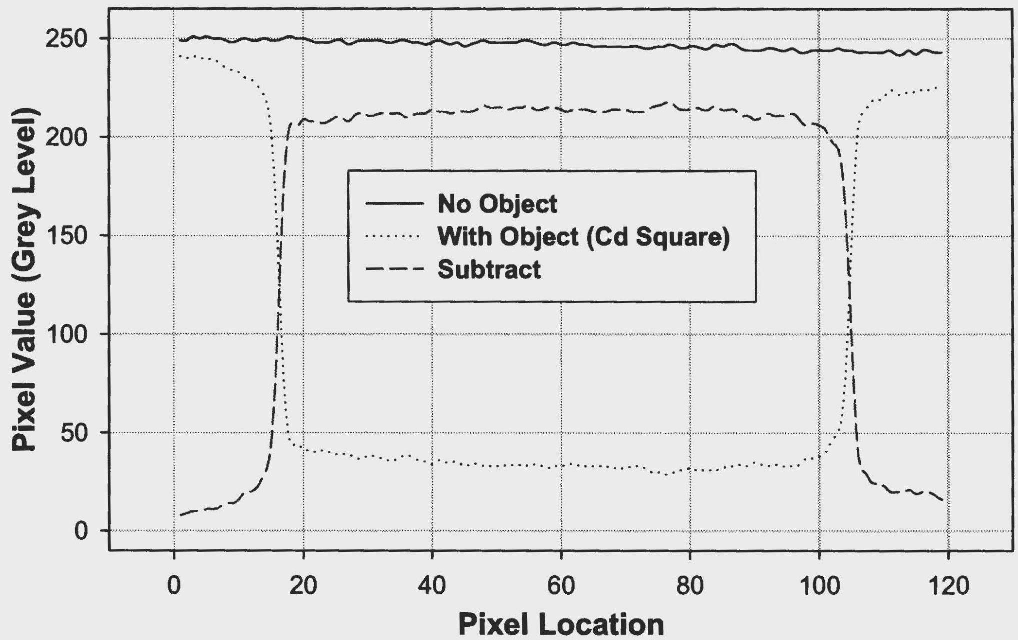

Figure 5.19. Image processing results for a line region-of-interest through the cadmium square neutron image.

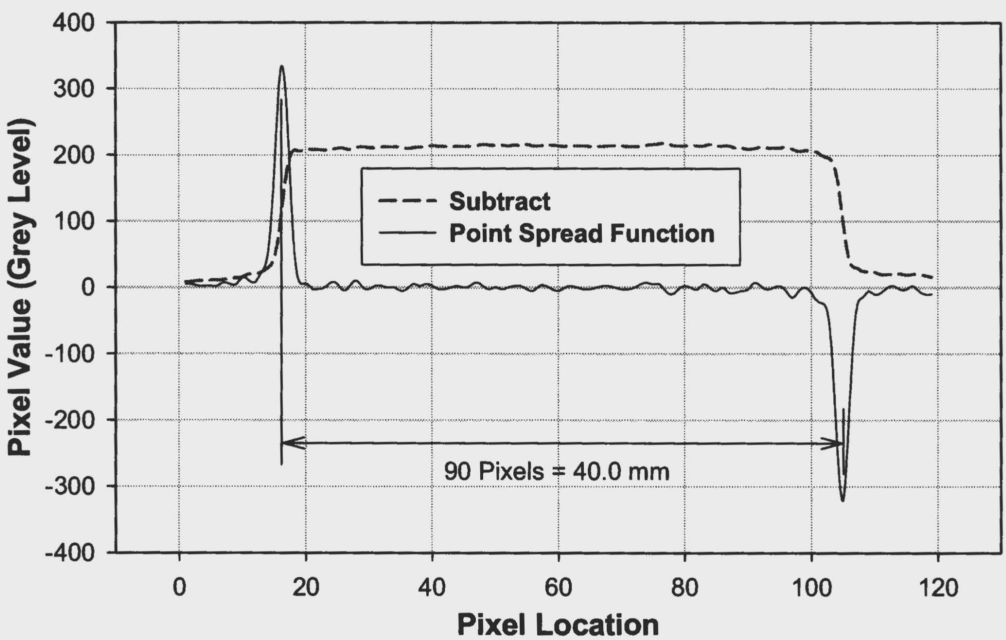

Figure 5.20. Point spread function of line profile through subtraction image from no object and cadmium square neutron images.

line profile obtained for a subtraction image and its Point Spread Function (PSF) obtained by differentiating the line profile. The PSF enhances the ability to determine the edges of the objects by providing quantitative information about the inversion points in the line profile (local maximum and minimum) representing the object edges. The spatial calibration shows that 90 ± 1 pixels are equivalent to 40.0 ± 0.5 mm of length, i.e., each pixel on the image is equivalent to 0.444 ± 0.007 mm.

5.3.2 Object Sensitivity / Thickness Resolution

When the brightness distribution of the neutron image is digitized by an image processor, a linear relation usually held between the visible light and the output signal (grey level), G, from the image processor:

$$G = G_o + Ce^{-\Sigma\delta} \tag{5.4}$$

where G_o is the offset or dark current grey level, and C is the gain or the sensitivity of the radiography system, and Σ is the macroscopic cross-section of the object material, δ is the object thickness. Hence, the no-object, the no-neutron (Cadmium) grey levels and system gain are given by:

$$G_{NoObject} = G_o + C \tag{5.5}$$

$$G_{Cd} = G_o$$

$$C = G_{NoObject} - G_{Cd} \tag{5.6}$$

the change in object thickness equivalent to one grey level (sensitivity) can be obtained by differentiating Equation 5.4;

$$\frac{\Delta G}{\Delta\delta} \approx \frac{\partial G}{\partial\delta} = -\Sigma \times Ce^{-\Sigma\delta}, \qquad \Delta G = 1 \tag{5.7}$$

$$\Delta\delta = \frac{1}{\Sigma \times Ce^{-\Sigma\delta}} = \frac{1}{\Sigma \times (G - G_o)} \tag{5.8}$$

Equation 5.8 shows that the sensitivity of the system depends not only on the system gain but also on the object thickness and object attenuation characteristics. Better sensitivity values are obtained for higher system gain values (i.e. lower offset or dark current value and finer grey level digitization). Also, as the object thickness increases the sensitivity gets worse regardless of its attenuation characteristics. The dependence of sensitivity on object attenuation characteristics is not monotonic. For a given object thickness, best sensitivity values will be obtained for materials with macroscopic cross-sections corresponding to 1.0 mean-free-path ($\Sigma\delta = 1.0$).

Based on neutron images at Figure 5.18 an average system gain of 205 grey levels is estimated for beam centre region (average no object and average no-neutron grey levels are 242 and 37 respectively). Table 5.2 lists some sensitivity analysis for light water, heavy water and aluminium according to the above-mentioned analysis.

5.3.3 Intensity Calibration and Response Linearity

Figure 5.21 shows two neutron images obtained with a 10.0 cm × 10.0 cm square gadolinium sheet and a 3.18 cm diameter aluminium rod. Figure 5.22 shows the image processing results, for a comparison of horizontal line profiles measured from the no object (Figure 5.18), No neutrons (Gd sheet) and aluminium rod neutron images for the

Table 5.2. RTNR system sensitivity values calculated for common materials.

	Light Water	Heavy Water	Aluminium
Macroscopic cross-section, Σ [cm^{-1}]	3.4652	0.45194	0.10362
One mean-free-path [cm]	0.2886	2.2127	9.6506
Minimum detectable thickness [cm]	0.0014	0.0108	0.0471
Sensitivity [cm] (at δ = 0.5 cm)	0.0080	0.0135	0.0496
Sensitivity [cm] (at δ = 1.0 cm)	0.0450	0.0170	0.0522
Sensitivity [cm] (at δ = 2.0 cm)	0.4640*	0.0267	0.0579
Sensitivity [cm] (at δ = 5.0 cm)	3.4639*	0.1034	0.079
Sensitivity [cm] (at δ = 10.0 cm)	8.4639*	0.9906	0.133

* Object is too thick. Sensitivity is calculated based on thickness reduction required to obtain first grey level above offset.

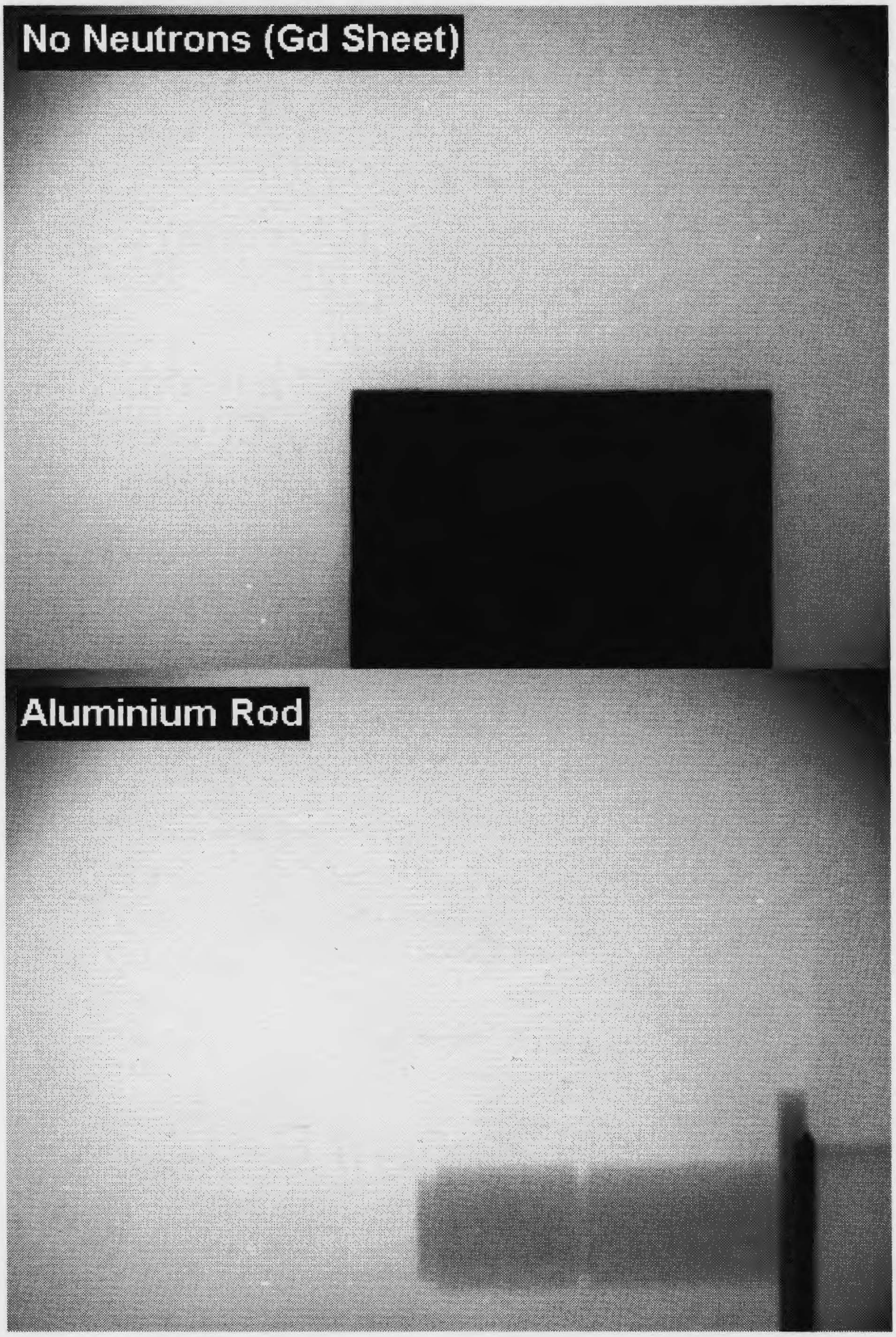

Figure 5.21. Neutron images of a square gadolinium sheet and a circular aluminium rod obtained by RTNR system.

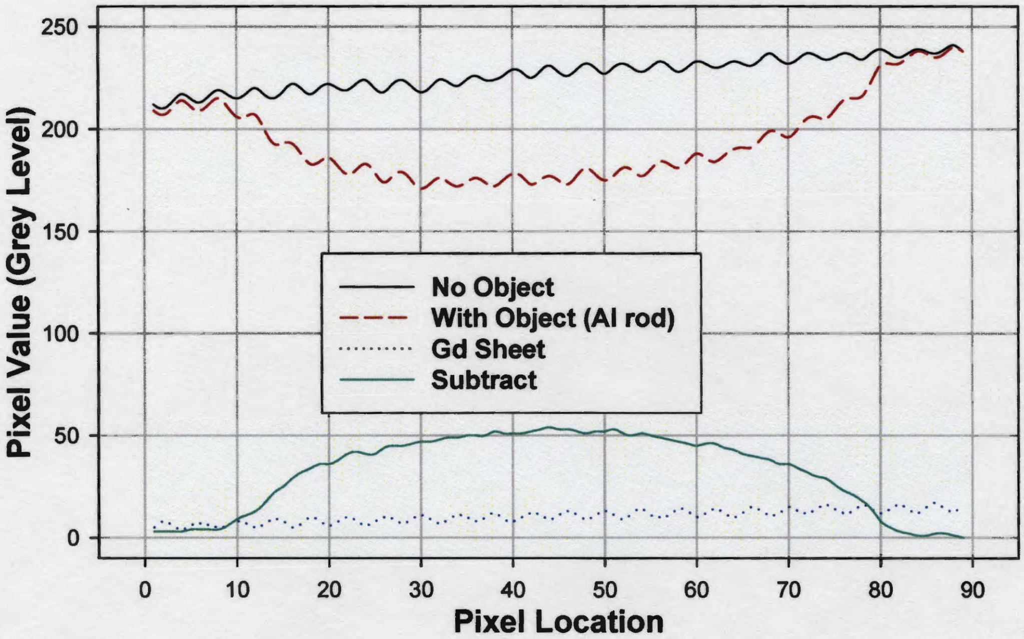

Figure 5.22. Intensity line profiles obtained by image processing for region-of-interest through no object and aluminium rod neutron images.

same region of interest. Figure 5.22 also shows the line profile obtained for a subtraction image. The fluctuations in the line profiles in Figure 5.22 are artifacts due to interlacing phenomena. Video is interlaced to achieve good visual quality within the limitations of a narrow bandwidth. The horizontal scan lines of each interlaced frame are numbered consecutively and partitioned into two fields: the odd field consisting of the odd-numbered lines and the even field consisting of the even-numbered lines.

The line profiles show that the aluminium rod (31.8 mm in diameter) is projected over 75 pixels, although calibration results obtained from cadmium foil neutron image would suggest 72 pixels only. These three pixels difference can be explained in terms of the image unsharpness caused by image processing (filtering). A 2D (3×3) filter was used and higher weight was assigned to the original pixel value. Although filtering reduces the noise level in the image, it reduces the sharpness of the object edges in the image as well.

Figure 5.23 shows the normalized pixel intensity versus attenuation length obtained from the neutron image of the aluminium rod. If the system response is linear, the Grey level is linearly proportional to the neutron intensity incident on the conversion screen. And the normalized pixel intensity, G^*, is related to the relative intensity of transmitted neutrons by:

$$G^* = \frac{G - G_o}{G_{NoObject} - G_o} = e^{-\Sigma\delta} \qquad (5.9)$$

where $G_{NoObject}$ is the grey level of the incident neutron beam with no object , G is the grey level of the transmitted neutron intensity, and G_o is the offset or dark current grey level, i.e., the pixel intensity when no neutron are incident to the neutron conversion screen.

Figure 5.23 shows that the normalized pixel intensity for attenuation lengths less than 1.2 cm of aluminium does not follow the exponential attenuation law and for attenuation lengths greater than 1.2 cm the normalized pixel intensity does follow exponential law with an attenuation coefficient similar the theoretical value but with an offset where the measured grey level intensity is greater than the expected theoretical value. This offset can be explained in terms of scattered neutrons, although aluminium has a relatively low neutron attenuation coefficient, it is mainly due to scattering interactions. Scattered neutrons produce distortions and blurring in neutron radiography images taken at small distances between the investigated object and the detector [101]. These scattered neutrons (neutron build-up) affect the measured object grey levels by increasing the intensity of transmitted neutrons. Contributions of scattered neutrons to the image disturb simple quantitative evaluation. Kardjilov et al. [102] has developed a correction method based on the iterative reconstruction of the measured image by overlapping point scatter functions determined by Monte-Carlo simulations.

5.4 Characteristics of The Neutron Scattering System

The neutron scattering system is described in Section 3.6. The key parameters of the system are the thermal neutrons detector operating voltage and its orientation with respect to the incident neutron beam.

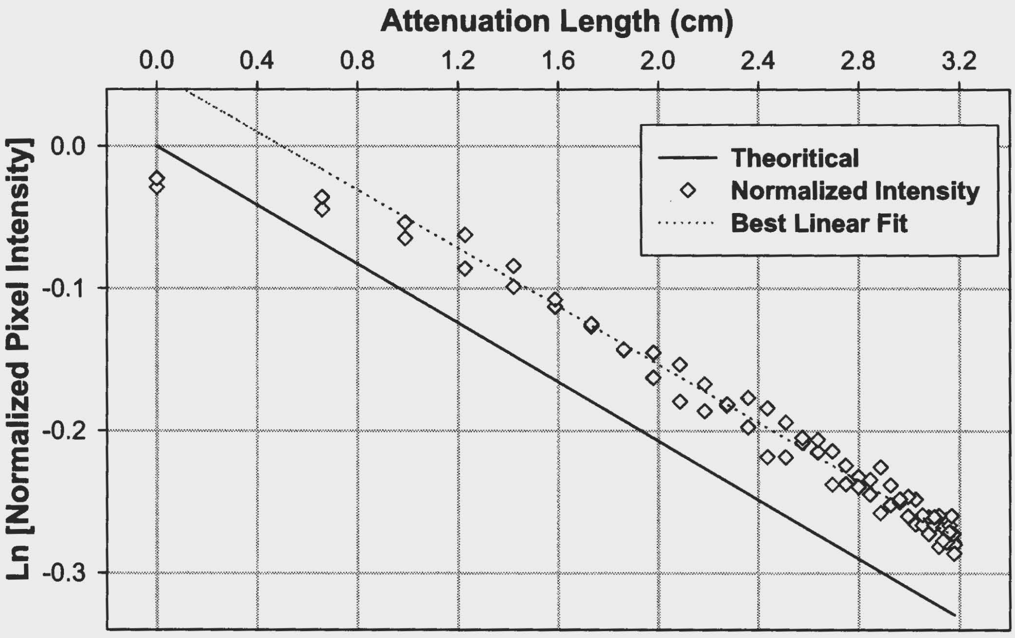

Figure 5.23. Neutron attenuation characteristics for aluminium rod image obtained by real-time neutron radiography system.

5.4.1 Detector Operating Voltage and Neutron Detection Efficiency

Detection efficiency is greatly affected by the detector operating voltage; low operating voltage will not provide enough amplification for the electrical signal created by the detection process to enhance discriminating noise through further signal processing. On the other hand, high operating voltages will increase noise level and load signal processing units with useless signals. Figure 5.24 shows typical Saint-Gobain BC-702 thermal neutron detector response spectra to the neutron beam at zero-power MNR operation at different detector operating voltages. At such a reactor power, the neutron intensity is at its minimum and the detector response will be mainly due to low energy events produced by interactions of the gamma rays that exist due to core radioactivity. Figure 5.25 shows typical Saint-Gobain BC-702 thermal neutron detector response spectra to a neutron beam at 10 kW MNR operation at different detector operating voltages with multichannel buffer dead-time correction. Based on the results represented by Figures 5.24 and 5.25 a detector operating voltage in the range of 550 – 600 Volts has been selected, since higher operating voltages increases the low level noise and lower operating voltages shows lower detection efficiency.

In order to evaluate the neutron detection efficiency for the three Saint-Gobain BC-702 thermal neutron detectors, the detectors has been placed in the neutron beam at different reactor powers with and without shield. The shield consists of a 0.5 mm thick gadolinium sheet followed by a 0.5 mm thick cadmium sheet. Typical detector responses are shown in Figure 5.26 for reactor operation of 600 watts.

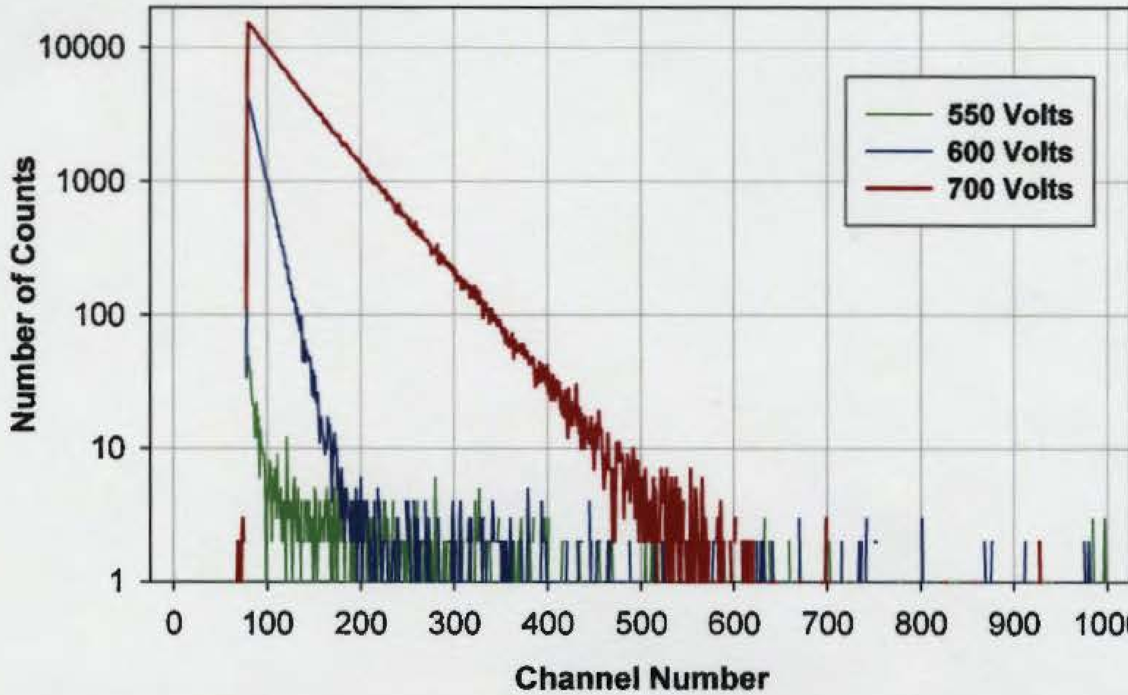

Figure 5.24. Typical BC-702 thermal neutron detector spectra for zero power MNR operation at different detector operating voltages.

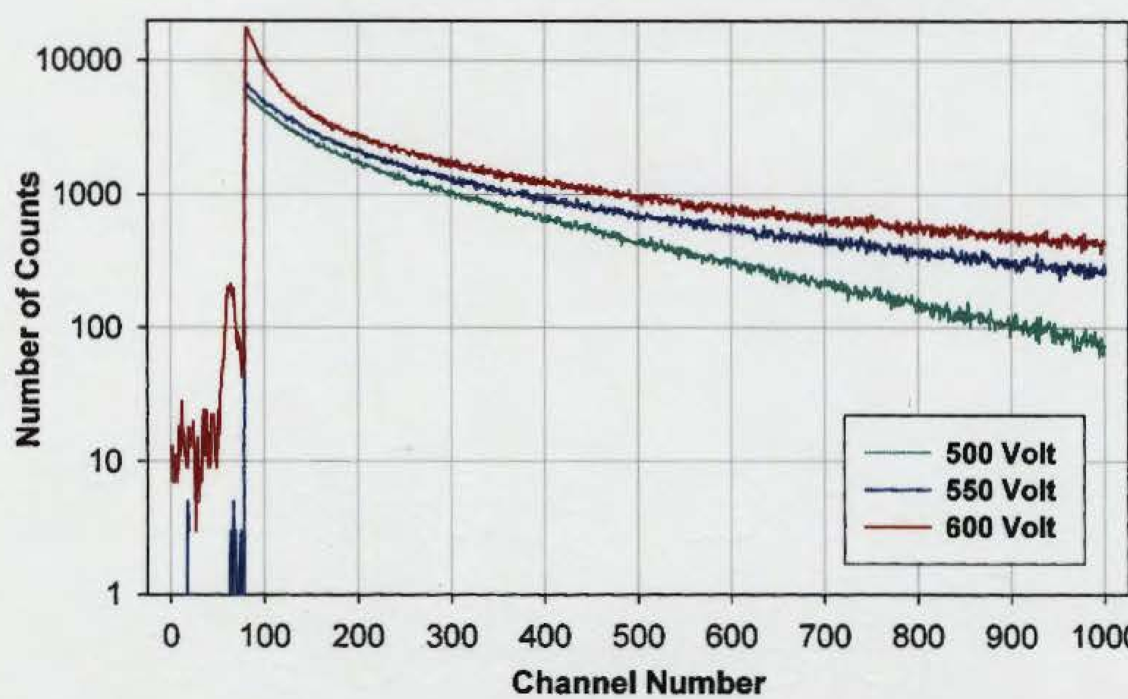

Figure 5.25. Typical BC-702 thermal neutron detector spectra for 10 kW MNR operation at different detector operating voltages.

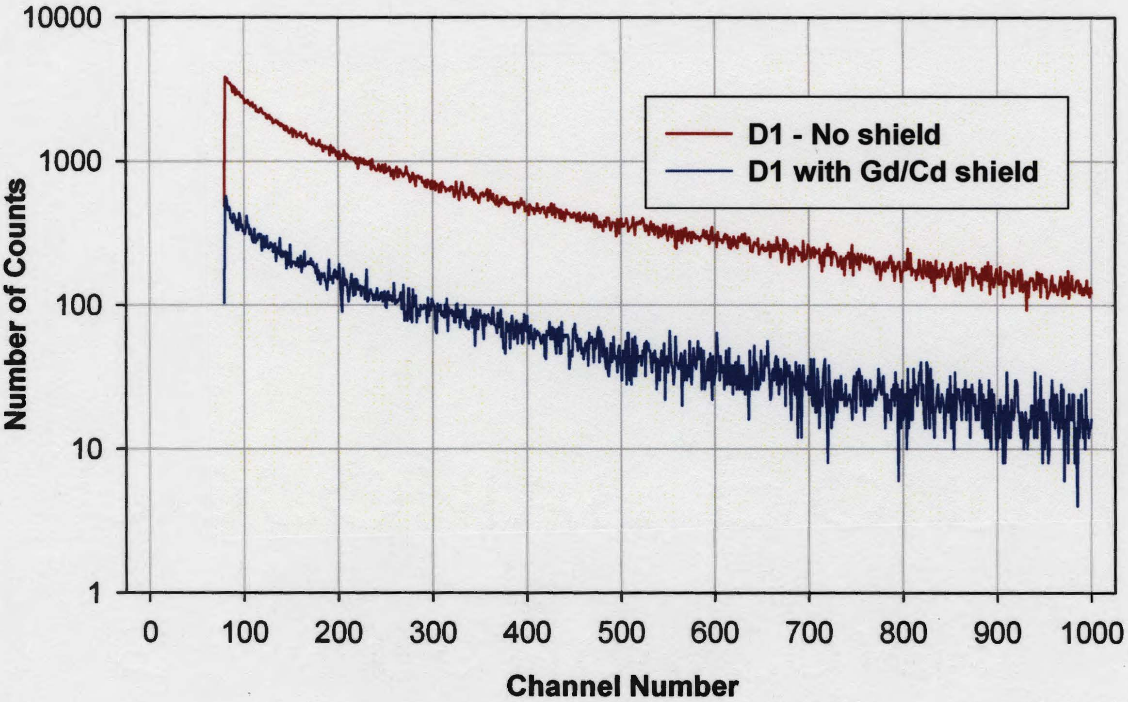

Figure 5.26. Typical BC-702 thermal neutron detector spectra for 600 watt MNR operation with and without shield.

Qualitative assessments show that the majority of detection events are due to thermal neutrons with low detector response to other radiations, fast neutrons and gamma ray, existing in the beam. The multichannel buffer, ORTEC Model 920E, has a fixed analog-to-digital conversion dead time of 15 μs. This dead time imposes a limit on the combined gross detection counts to be processed per unit time of 6.66×10^4 counts/s. As the combined gross count rate increases, the multichannel buffer dead time increases and the recorded count rate is much less than the true count rate. In addition another problem has arisen, as the combined gross count rate increases, the multichannel buffer dead time increases and the fraction of counts corresponding to each detector varies and as such the detection efficiency of each detector becomes dependent on the combined count rate. Figure 5.27 illustrates the dependence of gross count fraction for each detector as the gross count rate increases by increasing the reactor operating power.

To eliminate the dependence of detection efficiency on gross count rate, a region of interest (ROI) has been selected for each detector to reduce dead time fraction below 5% and to produce comparable gross count rates for each detector. Figure 5.28 shows the dependence of detection efficiency for each detector as function of reactor power.

5.4.2 Dependence of Scattering on Angular Direction

In order to select orientation angles for the thermal neutron detectors, measurements of typical detector response to neutrons scattered by a testing object are examined. The testing object with no water is placed in the neutron beam and the response of a thermal neutron detector is measured at different orientation angles ranged

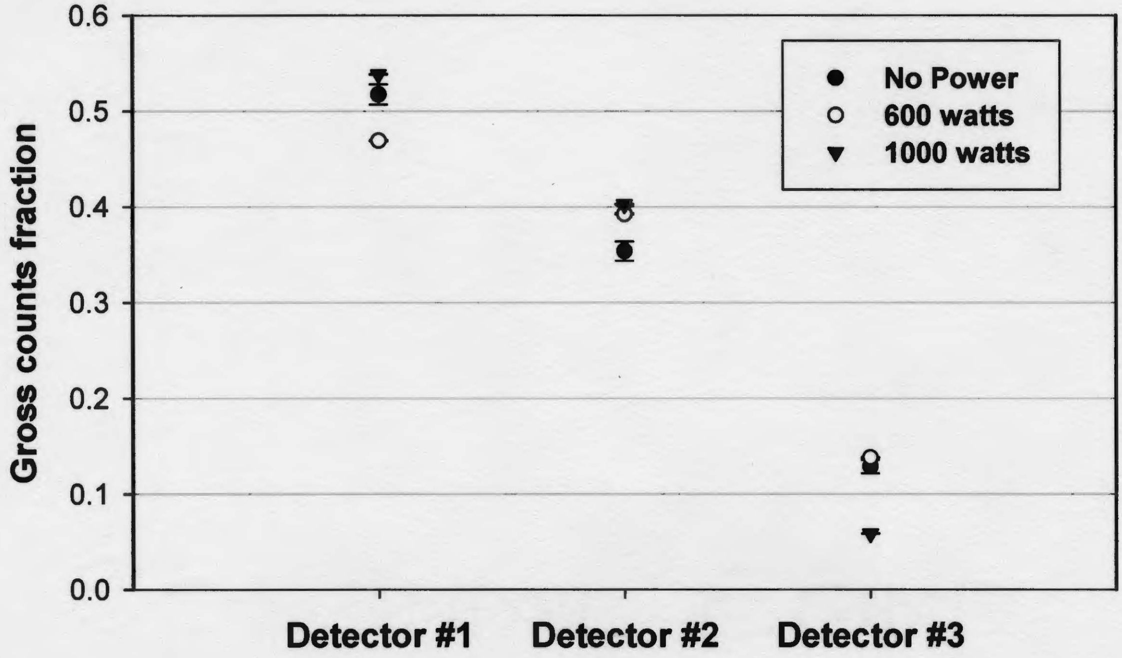

Figure 5.27. Changes in gross count fractions as a function of detector and reactor power.

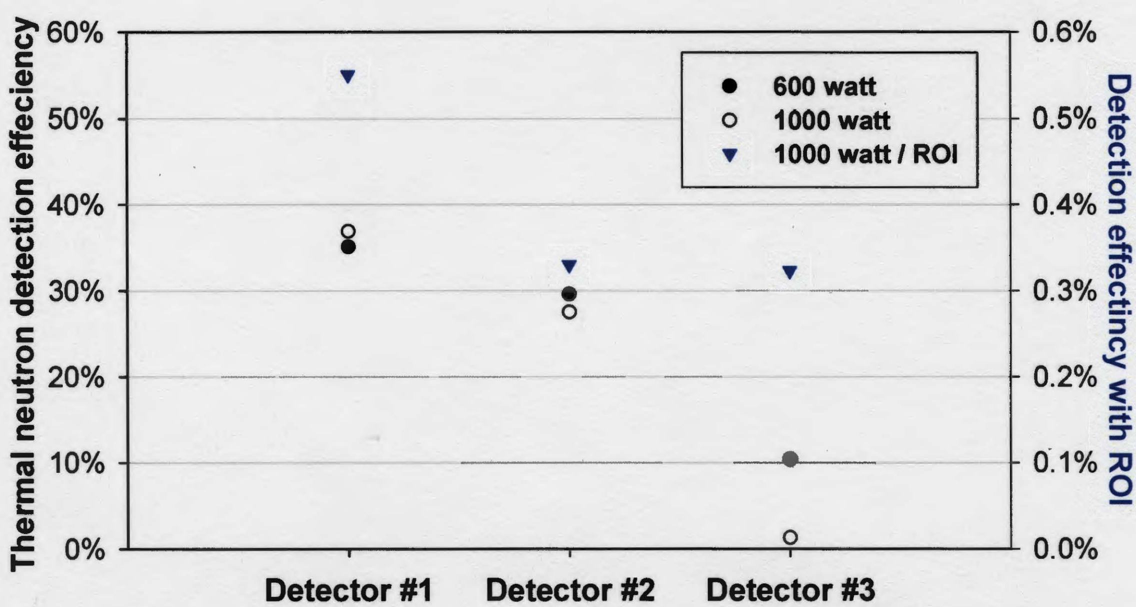

Figure 5.28. Thermal neutron detection efficiency dependence for each detector.

from 45 degrees to 135 degrees from the incident neutron beam direction. The measurements have been repeated with the test object filled with light water. Orientation angles smaller than 45 degrees and larger than 135 degrees have not been tested due to space limitation, and the detector will be exposed to the incident beam.

Figure 5.29 shows a typical detector response spectrum at an angular orientation of 90 degrees with different test object conditions. The detector shows a maximum response when the testing object is filled with water (Full water), while it shows a minimum response when the object is empty and the detector is shielded by cadmium and gadolinium sheets (No water with shield). The detector response when there is no object (No object) is slightly higher than a shielded detector response to an empty object, which implies the presence of some thermal neutron background due to scattering from the cave walls. The detector response when the testing object is empty (No water) is approximately the same as the shielded detector response to the object filled with water (Full water with shield), which can be related to fast neutron scattering.

Figure 5.30 shows gross counts detected by a thermal neutron detector as a function of orientation angle measured with the test object empty and filled with water. The detector response when the object is filled with water exhibits negligible fluctuations as a function of the detector orientation angle. The detector response to an empty object at lower orientation angles (45 and 60 degrees) is higher than the near steady response at larger angles, which can be explained in terms of neutron scattering from the walls of the opening in the shutter concrete brick wall.

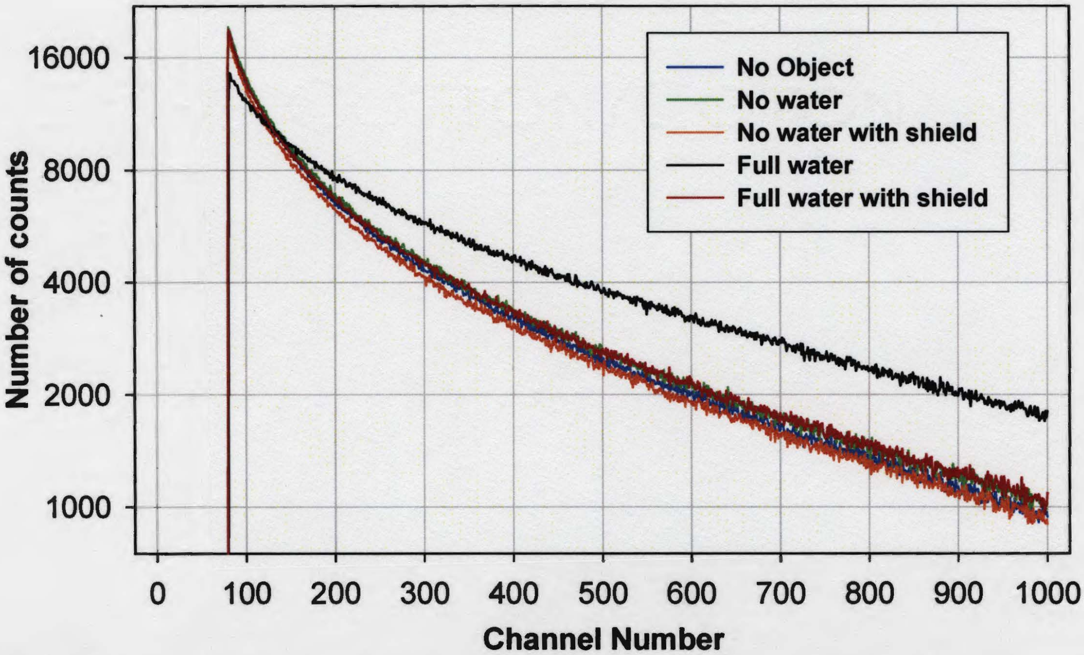

Figure 5.29. Typical BC-702 detector spectra at angular orientation of 90 degrees with different conditions.

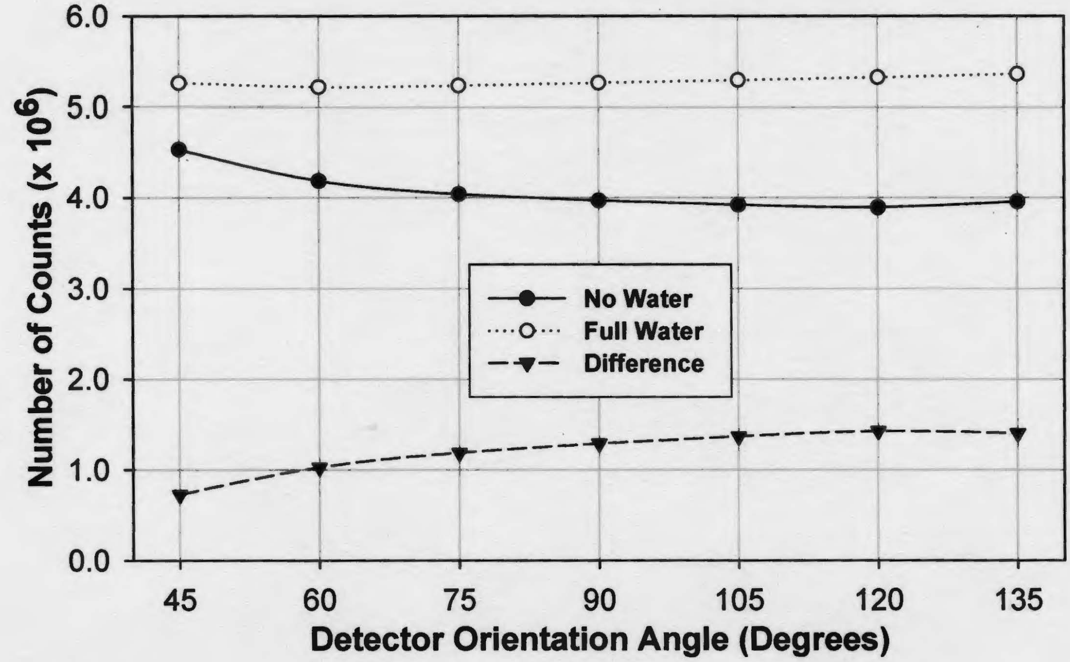

Figure 5.30. Gross counts detected by a thermal neutron detector as a function of orientation angle measured with the test object empty and water filled.

6 MULTI-DIMENSIONAL EXPERIMENTAL MEASUREMENTS

6.1 RTNR Two-Phase Flow Measurements

A two-phase air-water natural circulation loop is used to demonstrate the proof of principle for dynamic imaging. Such a loop allows for a simple yet straightforward test of dynamic imaging due to the motion of the gas and liquid phases. As water is an efficient neutron attenuator while gases are essentially transparent, then good contrast can be obtained.

A two-phase flow system refers to the simultaneous flow of two phases or two immiscible fluids, with a meniscus separation, within common boundaries. From a fundamental point of view, two-phase flow may be classified according to the phases involved into: gas-solid mixture, gas-liquid mixture, liquid-solid mixture, or two-immiscible-liquids mixture. Detailed understanding of two-phase flow heat-transfer and pressure-drop behaviour is of great importance for a wide range of engineering applications in the power generation, chemical, and oil industries.

Image processing is used to enhance the details of RTNR images for analysis and measurements of two-phase flow parameters. The experimental results are analyzed to determine the flow regime, void fraction distribution, cross-sectional average void distribution, bubble rise velocity and bubble diameter.

An enhancement of visualization using image-processing procedures is necessary to extract air-water interfaces and determine void fraction and bubble velocity using measured pixel intensity [39]. The capability of using the RTNR systems for measurement of void fraction [35,36], bubble velocity, and interfacial area [39] has been demonstrated as discussed in Chapter 2.

6.1.1 Natural Circulation Flow Loop

The natural circulation flow loop used in this work consists of a mixer section, a test section, a gas liquid separation tank, and a reservoir as shown in Figure 6.1. The test section is a 500 mm long vertical tube (stainless steel 316) with an inner diameter and outer diameter of 11.1 mm and 12.7 mm respectively. The working fluids are light water (H_2O) and compressed air. Air is injected into the lower mixer section of the test facility. The air rises to the separator causing the fluid to circulate naturally about the loop due to buoyancy effects. The air flow rate is measured by a rotameter and the induced liquid flow rate is measured by a turbine flowmeter in single-phase conditions.

6.1.2 Flow Visualization

Figures 6.2a to 6.2e are typical radiographic images obtained using the RTNR system where Figures 6.2a and 6.2b show images of 256-frames averaged empty and full water respectively, and Figures 6.2c to 6.2e show single frame images ($\Delta t \sim 33$ ms) captured during injection of different gas flow rates. Essentially, the dark regions of the image are liquid (light water) and the light regions are voids (Air). The images show lower resolution in the radial direction due to the small diameter of the test section (25 pixels only). Only flow regimes of bubbly flow and slug flow were observed since the

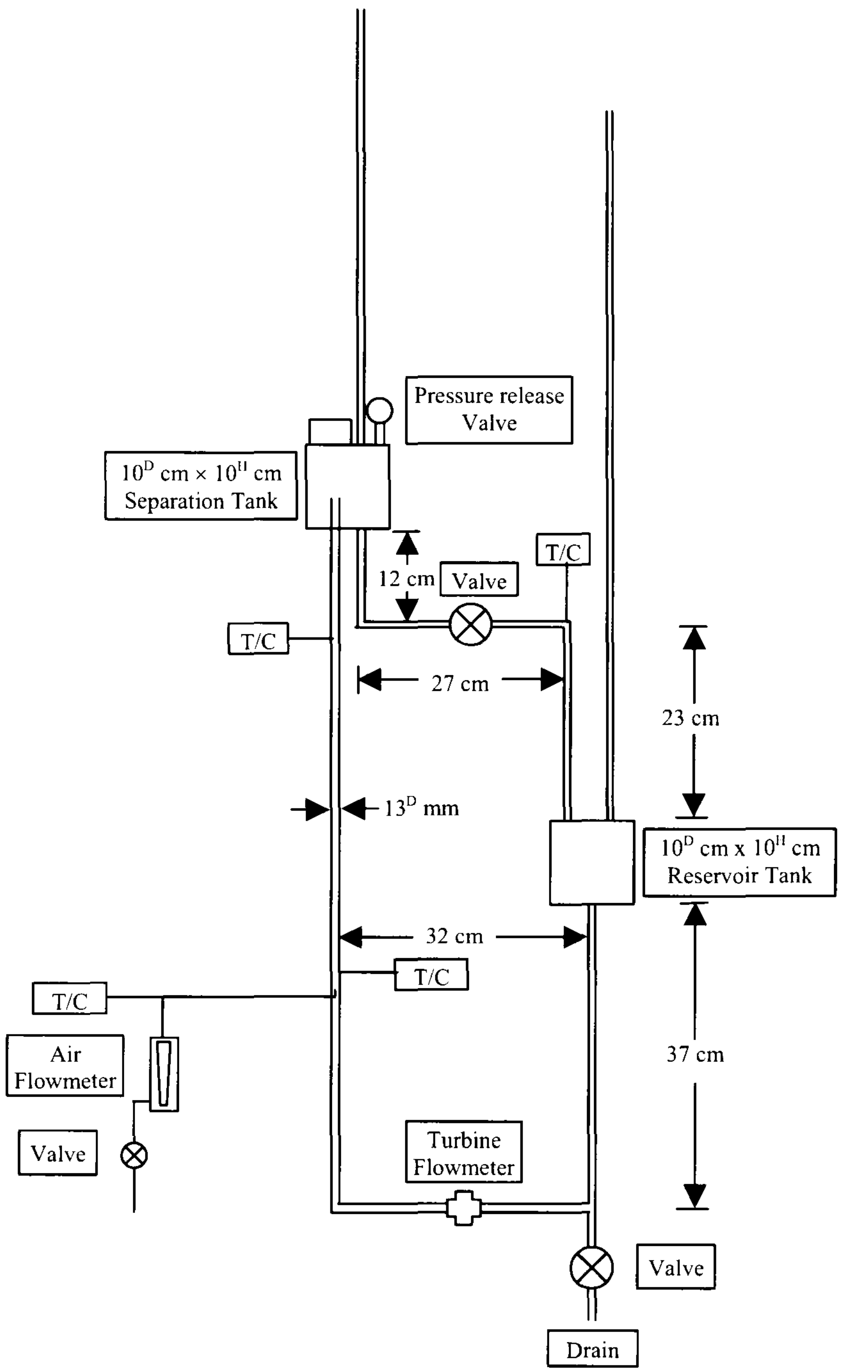

Figure 6.1. Schematic of the natural circulation loop.

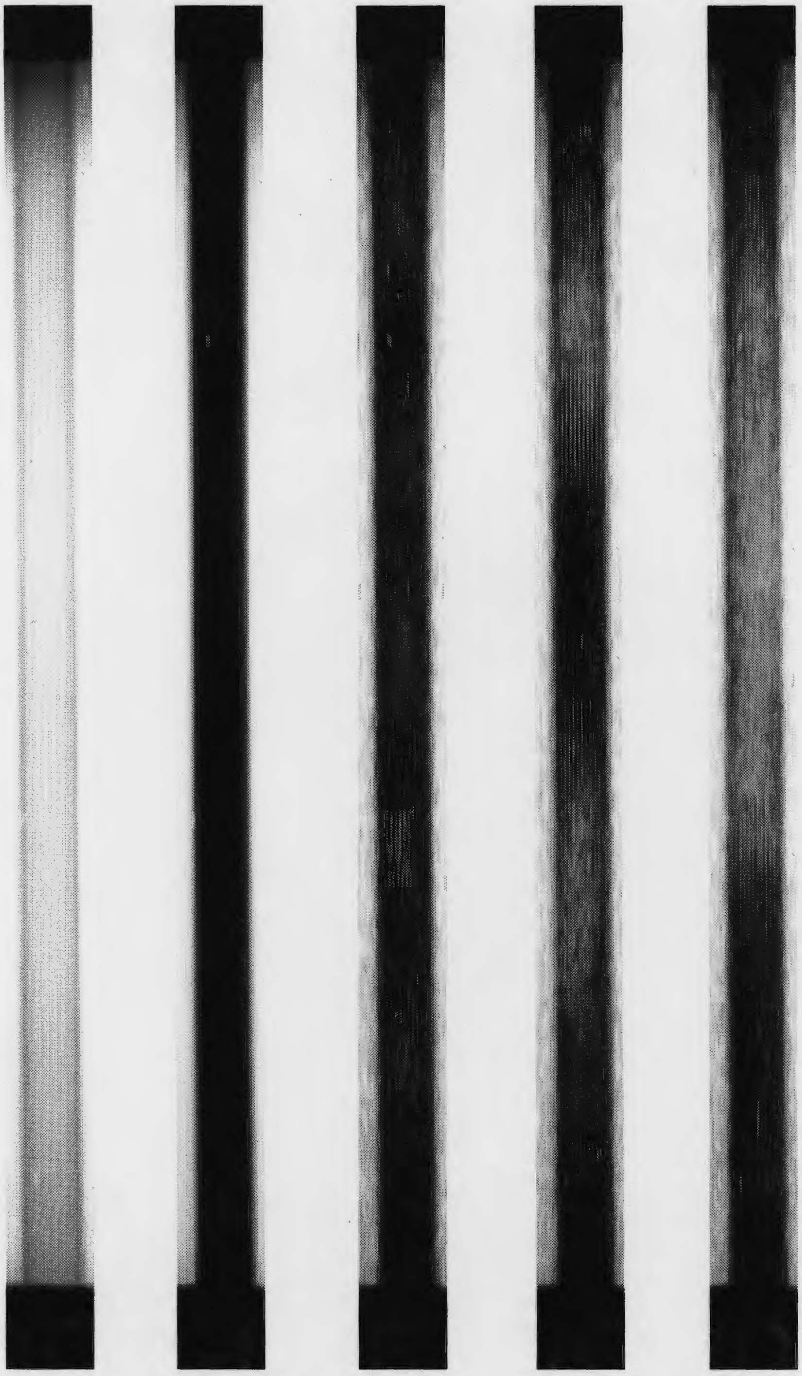

Figure 6.2. RTNR processed images of two-phase flow in natural circulation flow loop at different air flow rates. (a) No water – 256-frame average (b) Full water – 256-frame average (c) 1.0 lpm – single frame (d) 2.0 lpm – single frame (e) 3.0 lpm – single frame.

inlet air flow rates used are relatively small (<5.0 lpm). For small air flow rates (<1.5 lpm), small bubbles will be generated, and as the air flow rate is increased, the bubbles begin to coalesce and slug flow appears. Because of the mixer design and the small diameter of the tube, dispersed bubbly flow and annular flow have not been observed [103].

6.1.3 Void Fraction Measurements

The RTNR images need to be processed to reduce the camera thermal noise and the effect of background radiation in the beam. To remove the camera noise and background radiation effect, an averaged image of a 0.5 mm cadmium square (10.0 cm x 10.0 cm) is used to determine the non-thermal neutron related noises. Then the two-phase image is processed relative to single-phase empty and full water averaged images. Since the two-phase image consists of a single frame, the noise remaining in the subtracted image is still significant and a 1D (1×7) vertical filter was used [104] to reduce noise. A one-dimensional filter was chosen to average each of the two image fields separately. The following equations show the calculation of void fraction from different neutron images.

$$G = G_o + C \times e^{-(1-\alpha)(\Sigma L)_W} \times e^{-(\Sigma L)_{SS}} \tag{6.1}$$

$$G_{NW} = G_o + C \times e^{-(\Sigma L)_{SS}} \tag{6.2}$$

$$G_{FW} = G_o + C \times e^{-(\Sigma L)_W} \times e^{-(\Sigma L)_{SS}} \tag{6.3}$$

$$G_{Cd} = G_o \tag{6.4}$$

where G is the Grey level with void, G_{NW} is the Grey level with no water, G_{FW} is the

Grey level with full water, G_{Cd} is the Grey level with cadmium, G_o is the offset or dark current grey level, C is the gain or the sensitivity of the radiography system, α is the void fraction, $(\Sigma L)_W$ is the water mean-free paths when the tube is full, $(\Sigma L)_{SS}$ is the stainless steel mean-free paths of the tube wall. Two relative Grey levels are defined to eliminate the tube wall (stainless steel) contribution:

$$R_1 = \frac{G - G_{Cd}}{G_{FW} - G_{Cd}} = e^{\alpha(\Sigma L)_W} \tag{6.5}$$

$$R_2 = \frac{G_{NW} - G_{Cd}}{G_{FW} - G_{Cd}} = e^{(\Sigma L)_W} \tag{6.6}$$

then the void fraction is calculated using the following equation:

$$\alpha = \frac{\ln[R_1]}{\ln[R_2]} \tag{6.7}$$

Figures 6.3 to 6.5 show a set of enhanced 2D void distribution contour maps obtained by image processing of single frames shown in Figure 6.2. Higher void fraction is obviously present at higher gas flow rates and hence slug flow is obvious in the second and third images at 2.0 lpm and 3.0 lpm. At 1.0 lpm, there is a collection of small bubbles moving upwards and the void fraction is not large.

Figure 6.6 shows the cross-sectional averaged void fraction along the vertical axis for the same images shown in Figures 6.2c to 6.2e. At 1.0 lpm, the cross-sectional averaged void fraction ranges from 0.15 to 0.60 with a volume averaged void fraction of 0.33. The figure also, shows that the cross- sectional average void fraction at 1.0 lpm does not change significantly along the length. Hence, no large bubbles appear and no

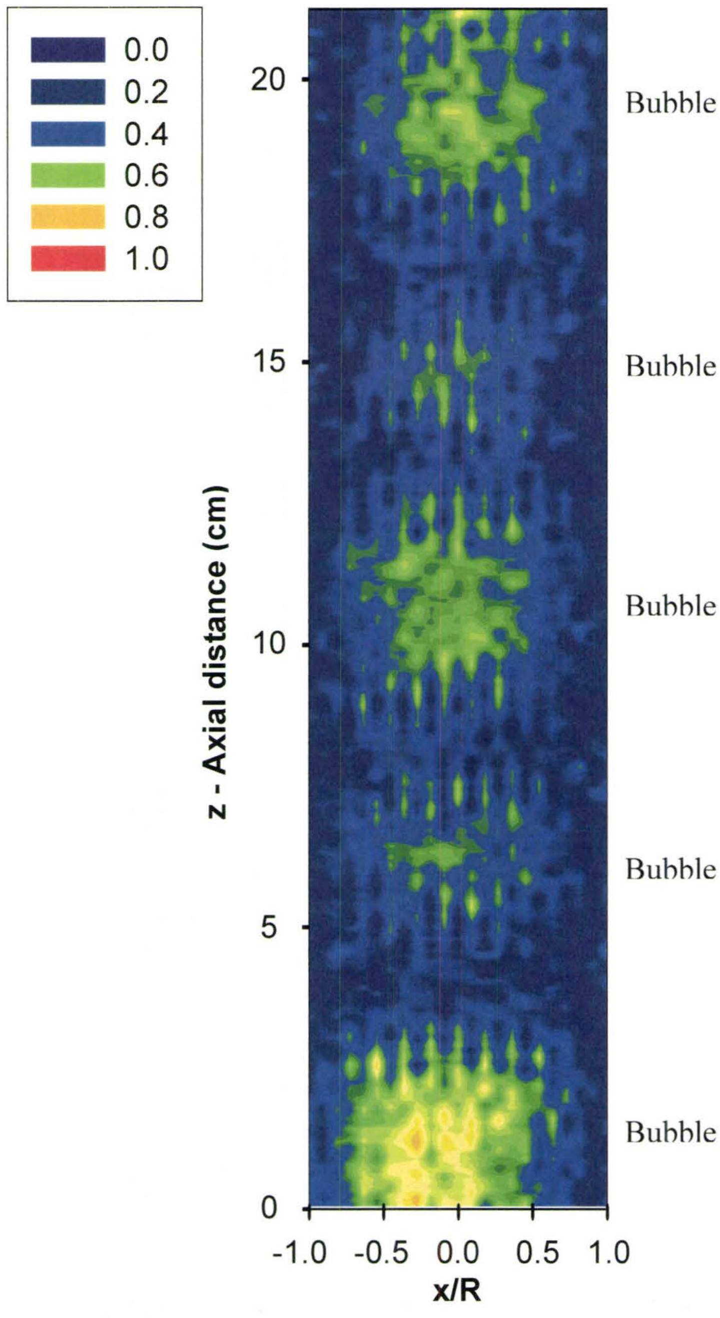

Figure 6.3. 2D void distribution contour map for image in Figure 6.2c – single frame captured at air flow rate of 1.0 lpm (induced water flow rate is 0.33 lpm).

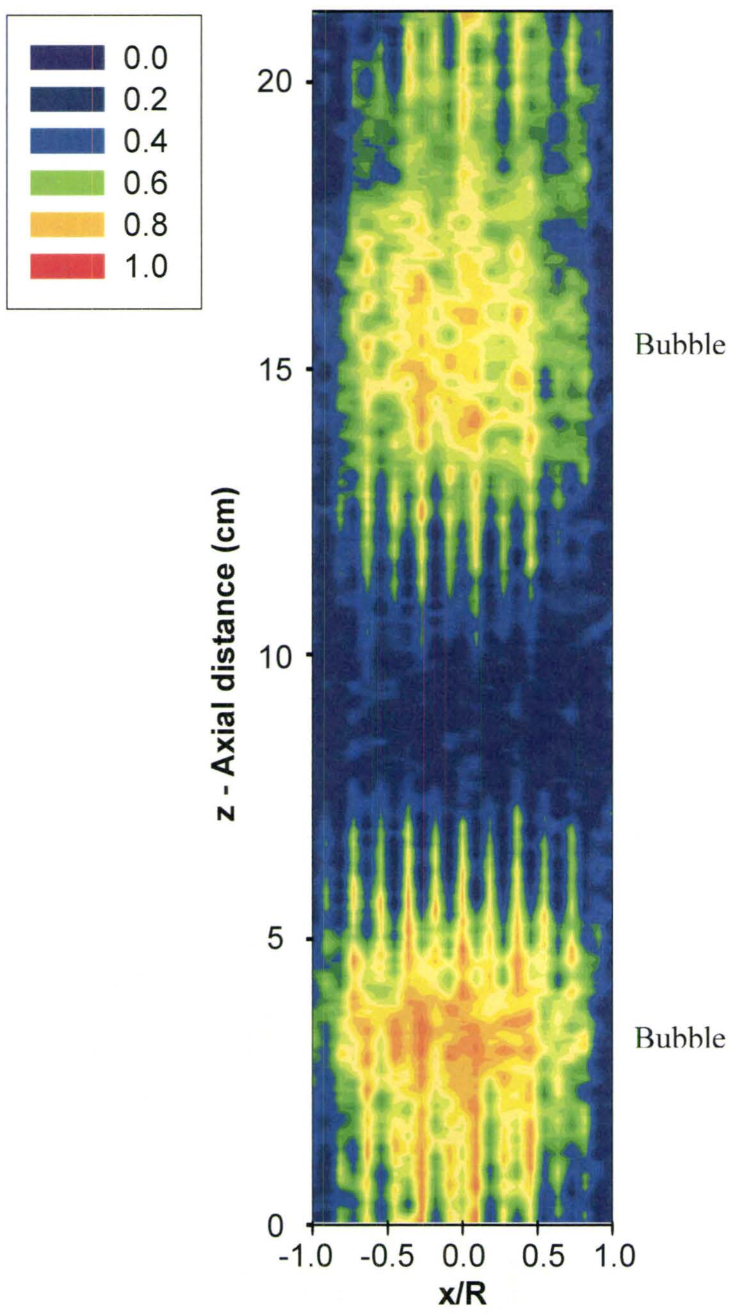

Figure 6.4. 2D void distribution contour map for image in Figure 6.2d – single frame captured at air flow rate of 2.0 lpm (induced water flow rate is 0.39 lpm).

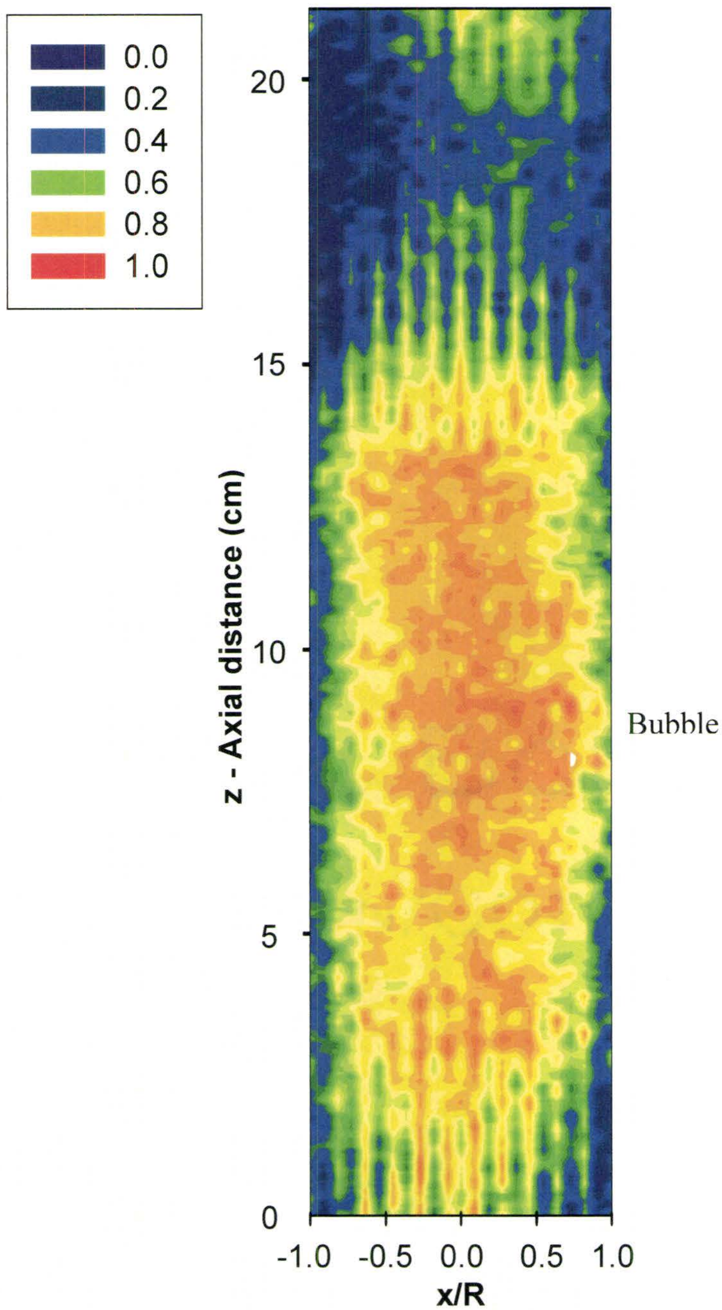

Figure 6.5. 2D void distribution contour map for image in Figure 6.2e – single frame captured at air flow rate of 3.0 lpm (induced water flow rate is 0.41 lpm).

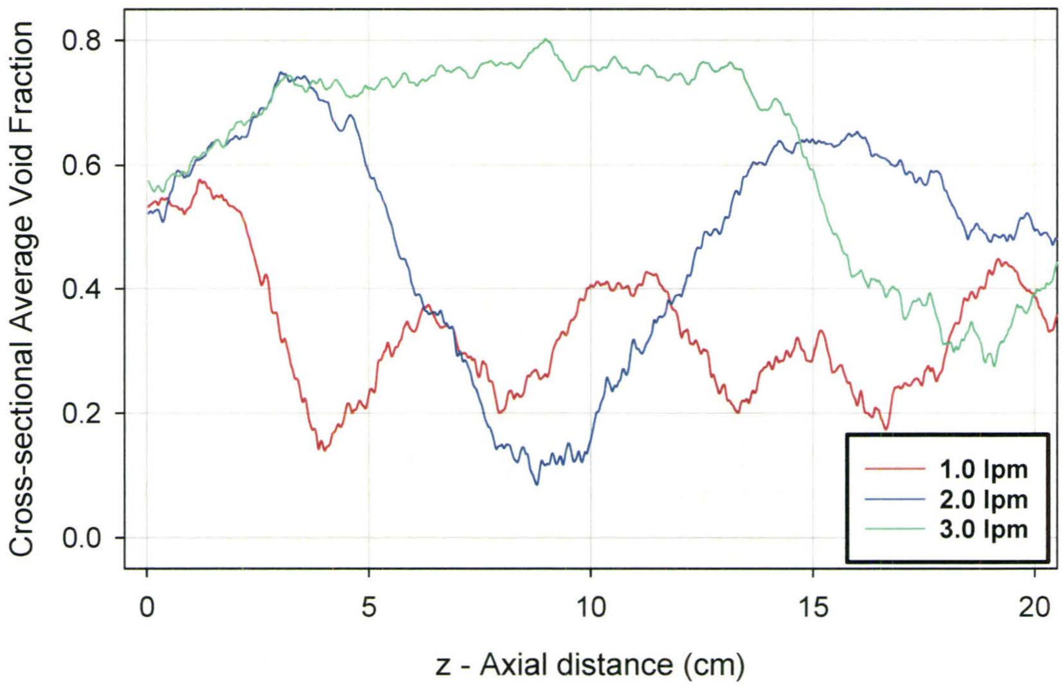

Figure 6.6. Cross-sectional averaged void fraction at various air flow rates corresponding to images shown in Figures 6.2c to 6.2e.

coalescing is observed. At 2.0 lpm, the cross-sectional averaged void fraction ranges from 0.15 to 0.70 with a volume averaged void fraction of 0.48. At 3.0 lpm, the cross-sectional averaged void fraction ranges from 0.30 to 0.80 with a volume averaged void fraction of 0.62. There is obviously a large bubble present in the system with a significant amount of entrainment. Due to the small diameter of the tube, the liquid film is still thick enough to ensure the void fraction stays below 0.80. The volume averaged void fraction can be obtained by integrating the cross-sectional averaged void fraction profile along the vertical axis.

6.1.4 Bubble Velocity Measurements

Figure 6.7 shows a sequence of enhanced frames captured approximately 33 ms (30 fps) apart for an injected air flow rate of 1.0 lpm. Similar sets of sequenced frames were obtained from RTNR images with injected air flow rates of 2.0 and 3.0 lpm and similar images to those shown in Figure 6.7 are obtained.

Figure 6.8 shows the change in vertical location of different bubbles with time, obtained from consecutive RTNR images for light water. These results are determined by tracking the centre (assumed to be at the peak of the grey level intensity across the bubble) of the bubble with time. For the most part, the bubbles move upwards at a constant speed. However, there are indications that the bubbles periodically accelerate or decelerate. Some bubbles have been observed to decelerate while a following bubble will accelerate and lead to coalescence forming a larger bubble.

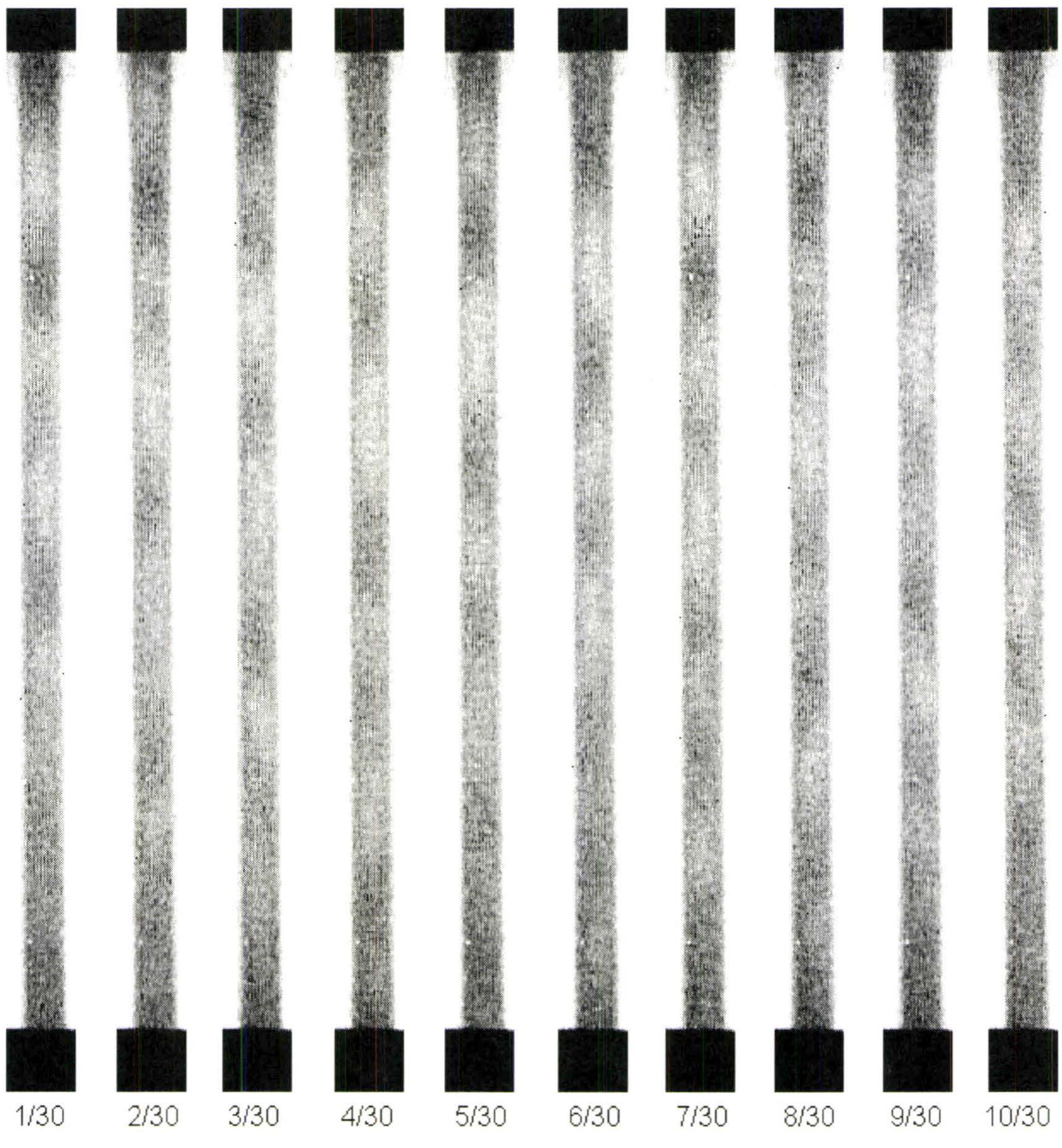

Figure 6.7. Sequence of successive enhanced RTNR frames approximately 33.0 ms apart (Air flow rate = 1.0 lpm).

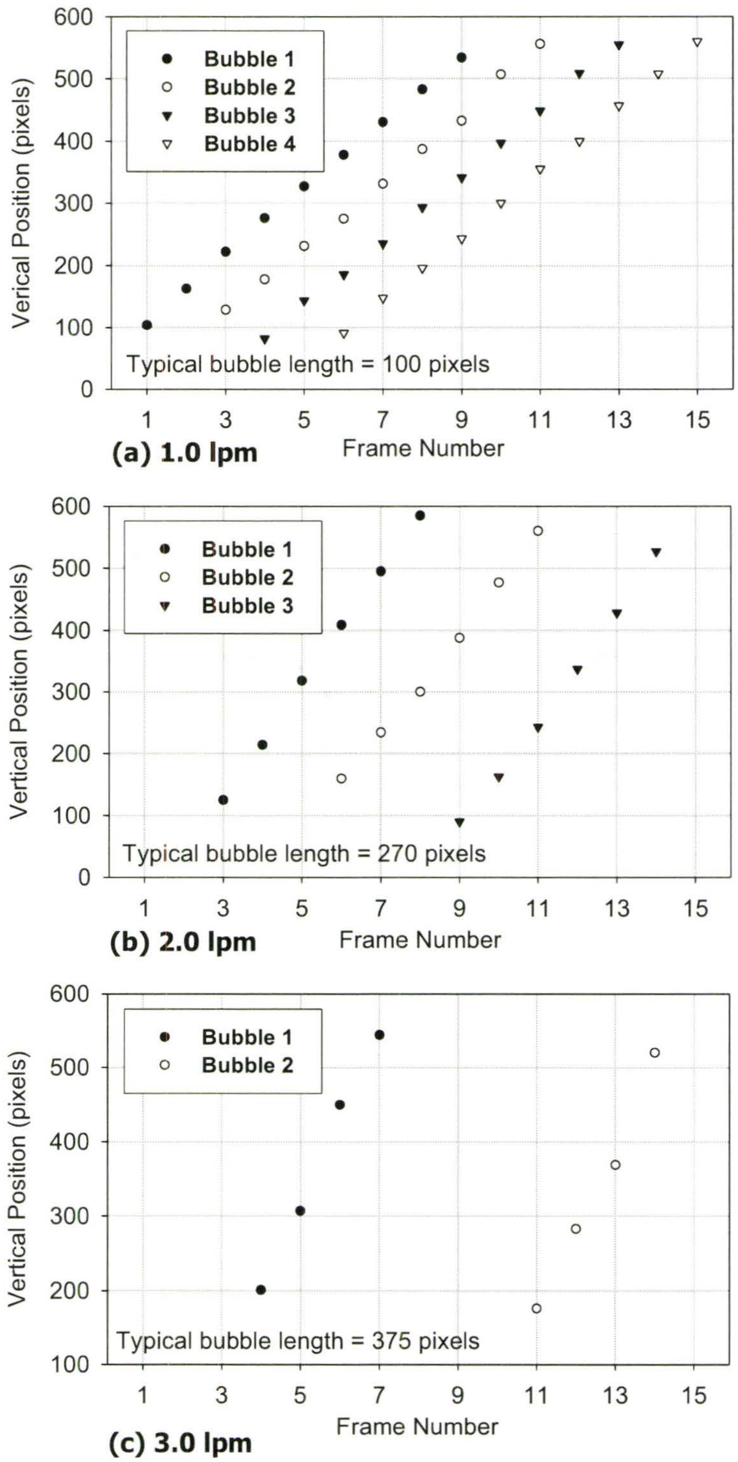

Figure 6.8. Change in vertical location of different bubble with time (30 frames = 1.0 sec).

Figure 6.9 shows average bubble rise velocities at different air flow rates calculated from the local frame-to-frame changes in vertical elevation of different bubbles represented in Figure 6.8. As expected the bubble rise velocity increases as the injected air flow rate is increased, but not in a linear manner as a result of the increasing two-phase friction multiplier due to the presence of higher void fraction values.

6.2 Three-Dimensional Neutron Imaging

6.2.1 Two-Phase Experimental Setup

The objective of the experimental measurements, presented in this section, is to examine the possibility of neutron scattering to complement neutron radiography and provide additional information to localize and discriminate between clusters of second phase, such as voids in liquid, having the same lateral position. The test object used in this work consists of two eccentric aluminium tubes, the outer tube is 38.1 mm in diameter and the inner tube is 19.0 mm in diameter both tubes have a wall thickness of 3.2 mm. The two tubes are mounted to an aluminium plate and the annulus between the tubes is filled with light water. In this manner, the inner tube represents a known void of air. The test object is placed on a computer controlled turn table that allows it to be rotated in the neutron beam. Since the annulus is eccentric, the void is moved through the third dimension. Figure 6.10 shows a top view and a front view of the test object used. The thermal neutrons scattered by the object are measured using three thermal neutron detectors (Saint-Gobain, Model BC-702 scintillator detectors) placed at the periphery of

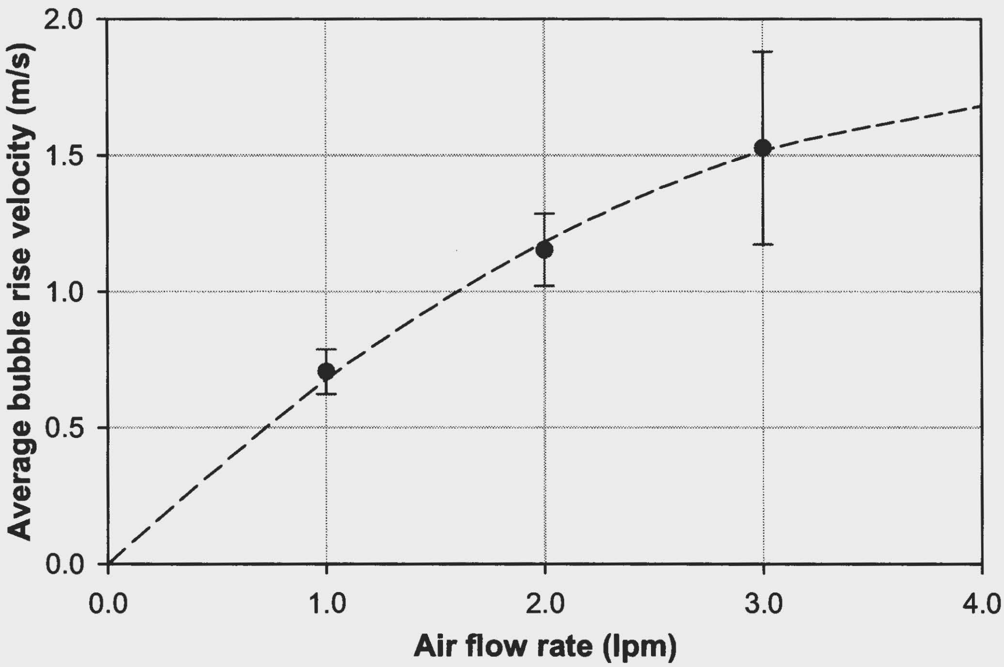

Figure 6.9. Average bubble rise velocity at different air flow rates.

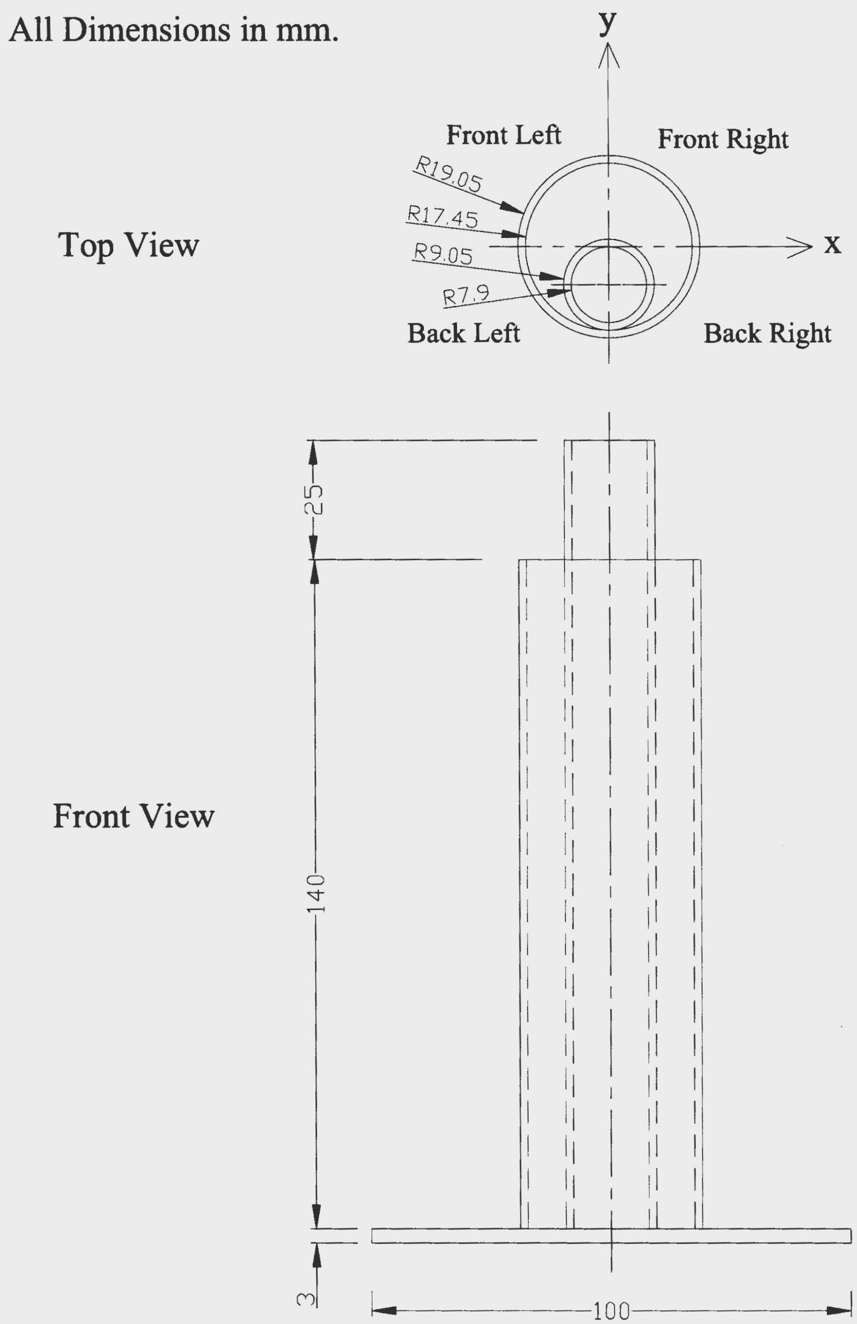

Figure 6.10. Schematic of test object used in neutron scattering measurements.

the neutron beam in a horizontal plane perpendicular to the test object. Each detector and its photo-multiplier tube (10.0 cm in length) are wrapped in 0.5-mm-thick cadmium sleeves (20.0 cm long) to provide collimation for neutrons scattered by the test object and to shield the detector from neutrons scattered by other components in the radiography facility.

Two different neutron scattering setups have been used, setup A with the three thermal neutron detectors located around the test object on one side relative to the neutron beam, and setup B where the three neutron detectors are located on both sides around the test object. Figures 6.11 and 6.12 show the top view schematic representations for setup A and setup B respectively.

6.2.2 Real-Time Neutron Radiography Results

Conventional neutron radiography produces a projected two-dimensional image, representing the attenuation information integrated along the neutron beam path. Due to this nature of neutron radiography, the grey level intensity of the produced images represents average attenuation characteristics of the test object and does not provide detailed information about the distribution of attenuating materials along the beam path. Figure 6.13 shows a set of 256-frame averaged neutron radiographic images obtained using RTNR for the test object at rotation different angles. Visual qualitative analysis shows no apparent difference between all images except for the two arcs above the water level. The RTNR images have few grey levels due to the large attenuation by the water. The human eye can discriminate about 32 grey levels over the range from white to black

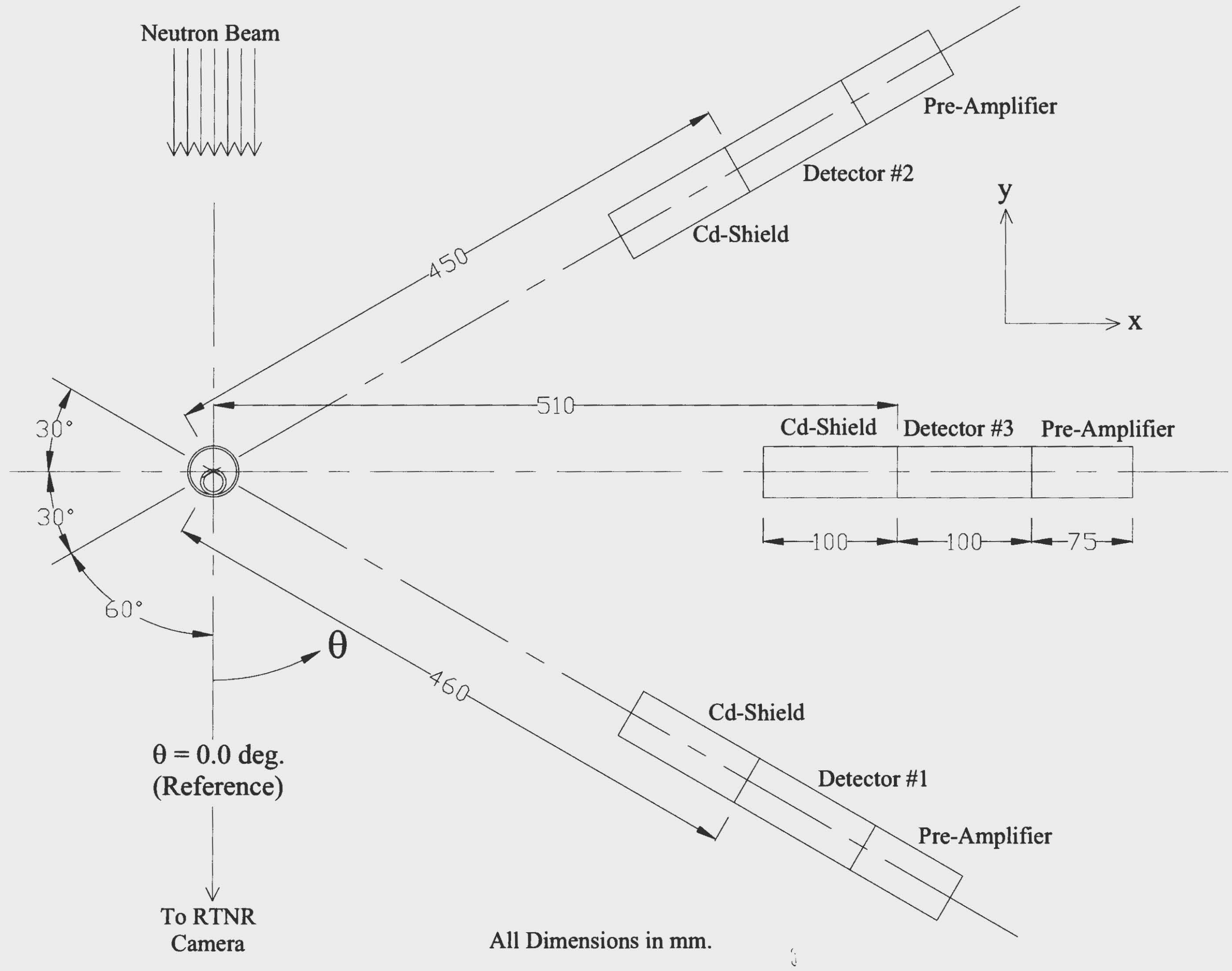

Figure 6.11. Top-view schematic of the geometrical representation for experimental scattering measurement - Setup A.

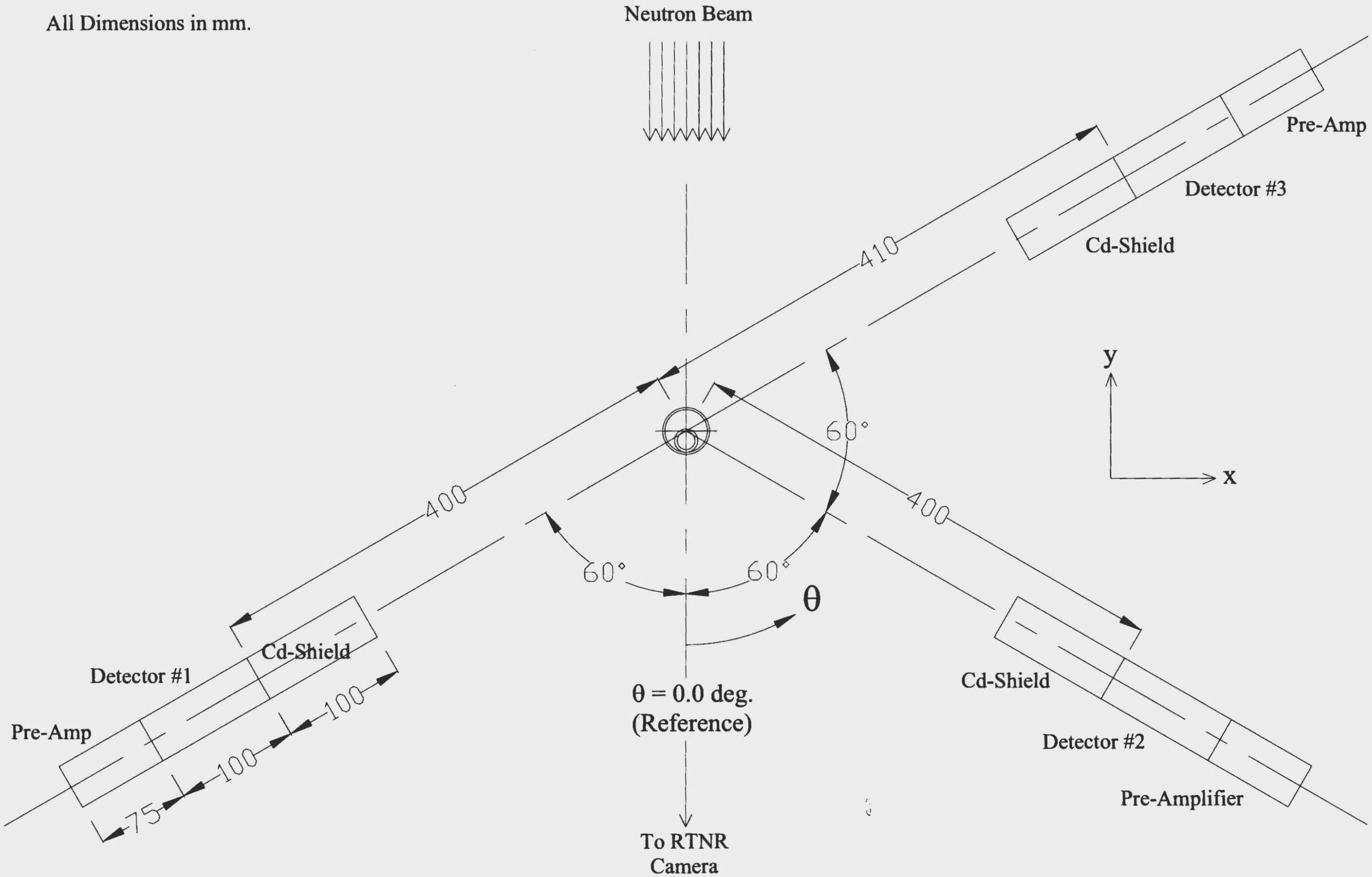

Figure 6.12. Top-view schematic of the geometrical representation for experimental scattering measurement - Setup B.

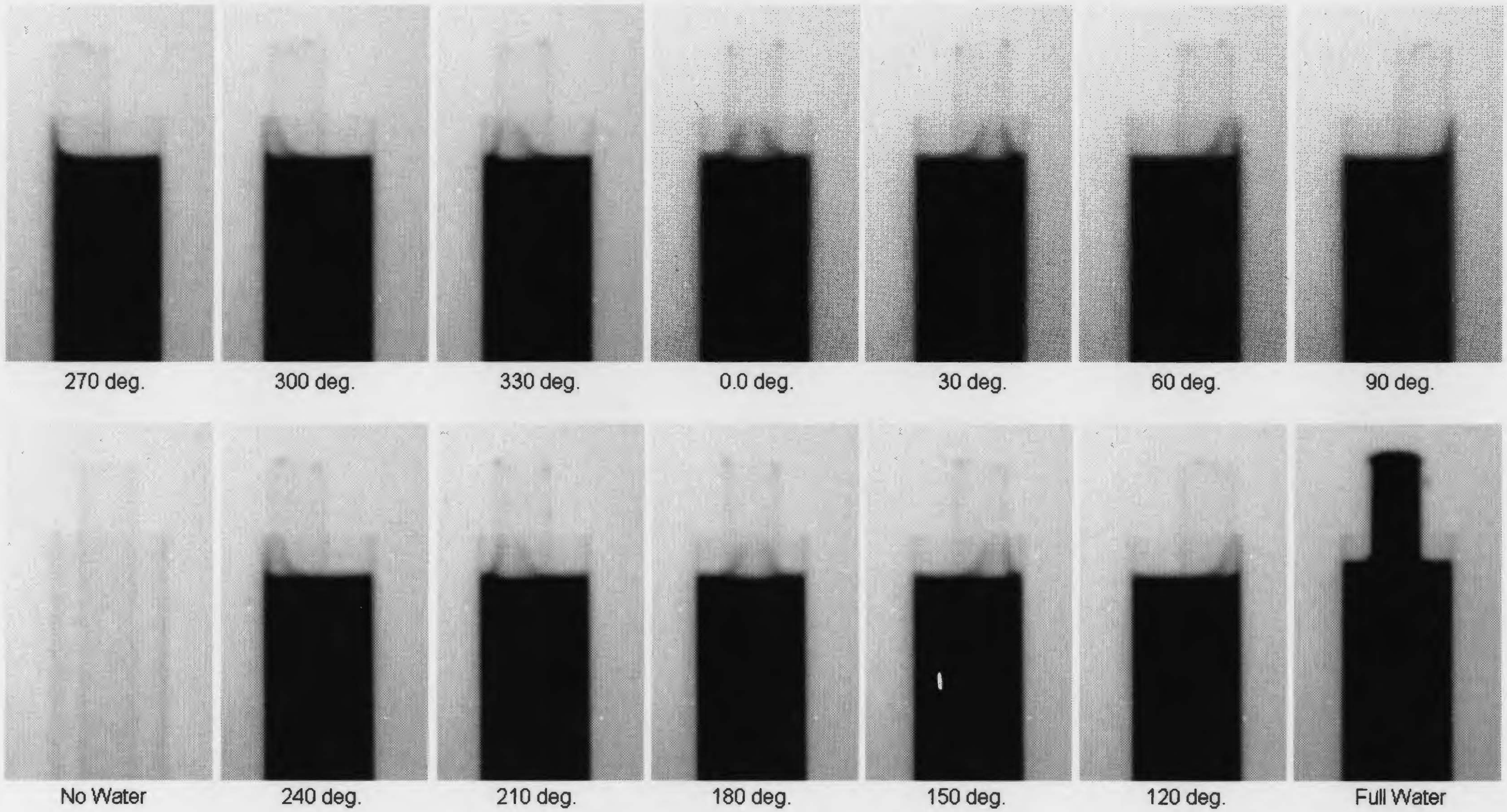

Figure 6.13. RTNR raw images of the scattering object obtained at different rotation angles.

and hence image processing is required to obtain quantitative grey level values. The presence of two small curved dark regions (arcs) above the water level, in the RTNR images shown in Figure 6.13, reflects the capillary phenomenon that occurs around the tangent line between the inner and outer tubes where the gap is narrow enough such that the surface tension forces drive the water above its bulk level.

Furthermore, the quantitative analysis of the grey level intensity, of images shown in Figure 6.13, shows insignificant differences that cannot represent a solid base to differentiate between voids with the same lateral position. Figures 6.14 to 6.18 show the grey level intensity (point spread function) across the test object for pairs of images that represent voids having the same lateral position. Figure 6.14 shows that for rotation angles 0.0 degrees and 180 degrees, where the test object has the same void fraction along the path length of the neutrons at the same transverse location but the location of that void is at opposite ends of the outer tube, the response of the neutron radiography system is comparable – as expected – since the void and the total path length is the same. The same effect can be seen in all of the other complementary angle pairs (i.e. 240 degrees and 300 degrees). Thus, while dynamic neutron radiography can be used to visualize void fraction and to obtain details such as the magnitude of the void and the axial and transverse location of the void, it cannot determine to which side (along the neutron path length) the void is located.

Figure 6.14 shows that the increase in grey level, in the cases where the void is present at a rotation angle of 0.0 degrees or 180 degrees, when compared to the full water case is very small. The large thickness of water before (0.0 degrees) or after (180 degrees)

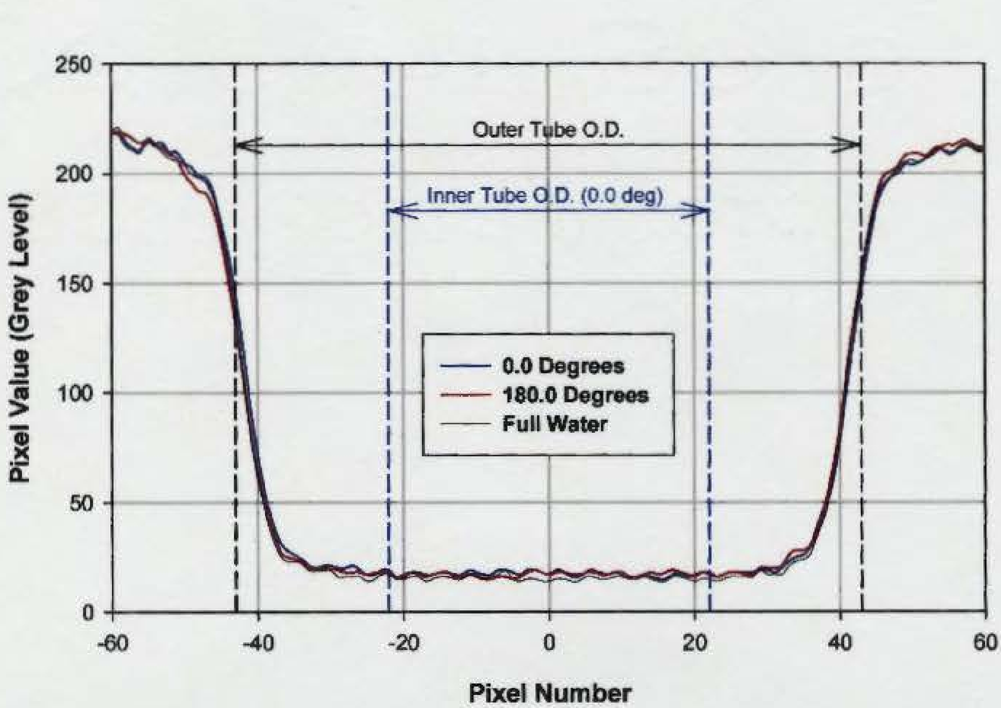

Figure 6.14. Pixel intensity profile across RTNR images in Figure 6.13 with rotation angles of 0.0 degrees and 180 degrees compared with full water case.

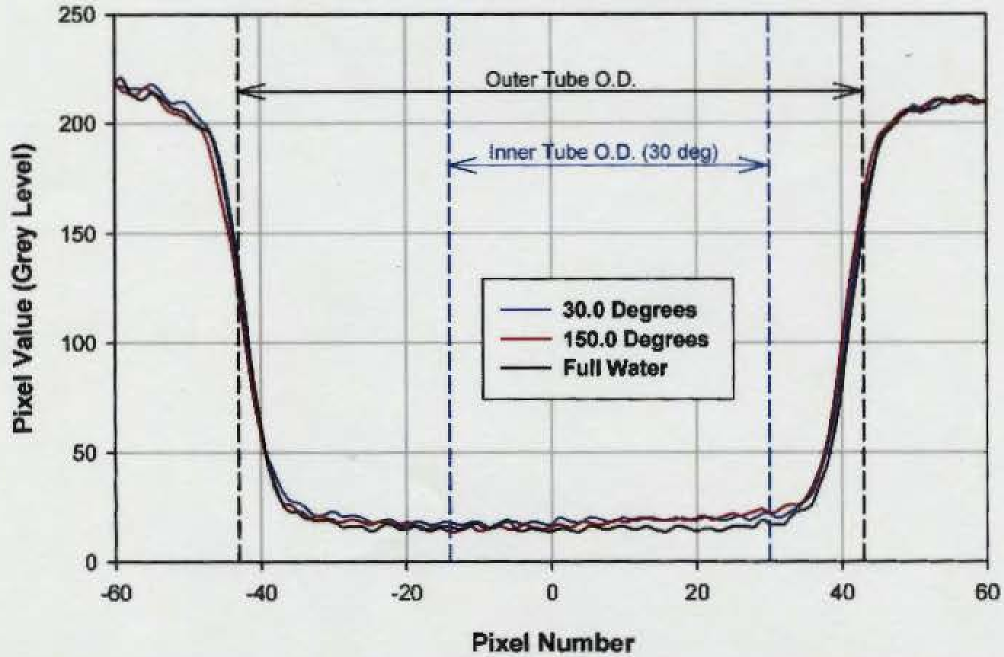

Figure 6.15. Pixel intensity profile across RTNR images in Figure 6.13 with rotation angles of 30 degrees and 150 degrees compared with full water case.

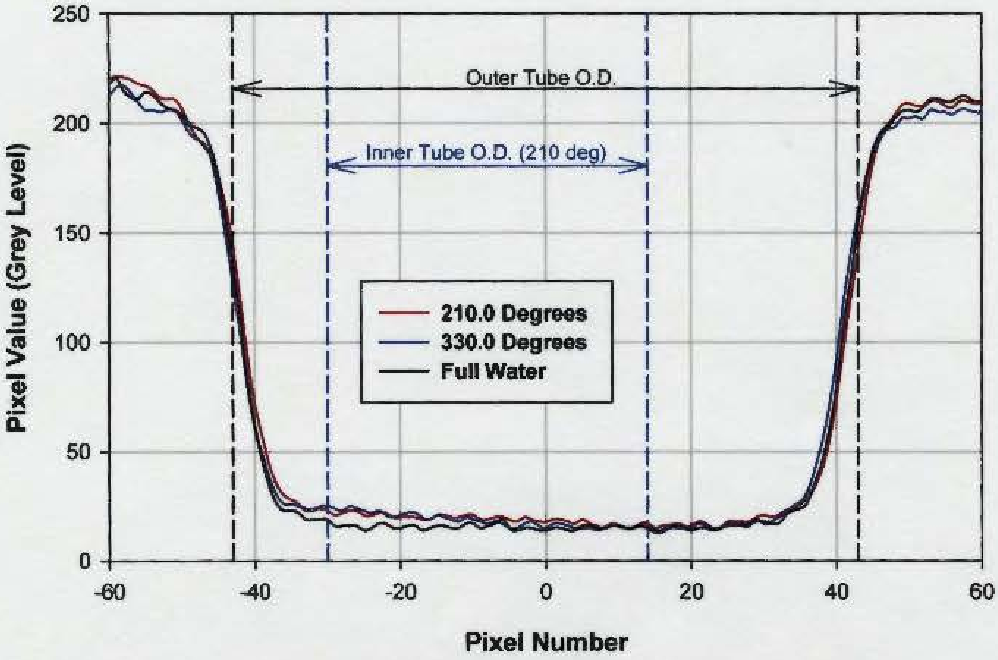

Figure 6.16. Pixel intensity profile across RTNR images in Figure 6.13 with rotation angles of 210 degrees and 330 degrees compared with full water case.

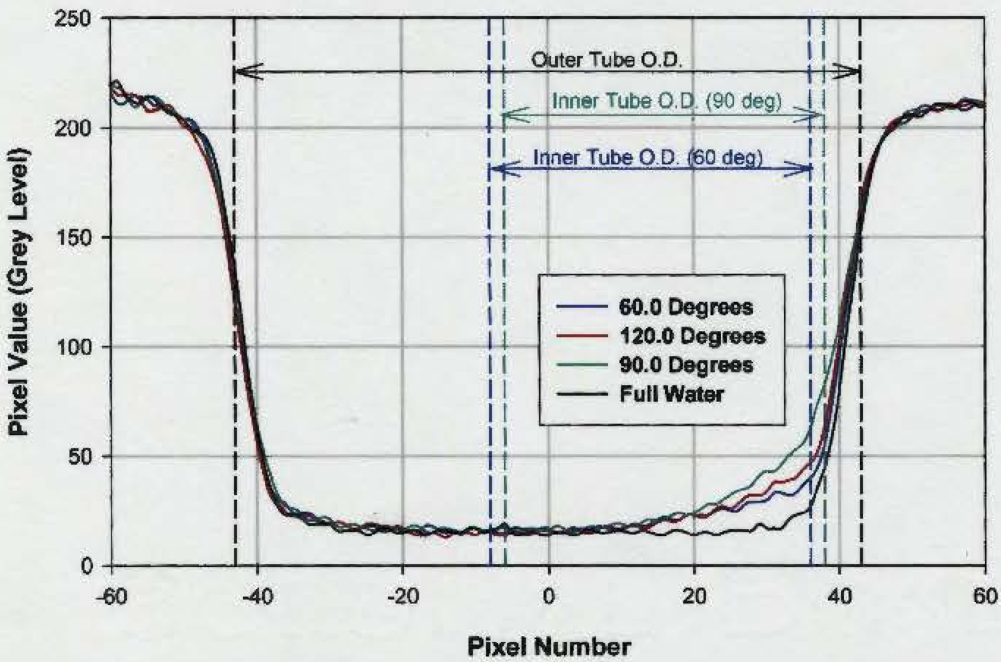

Figure 6.17. Pixel intensity profile across RTNR images in Figure 6.13 with rotation angles of 60 degrees, 90 degrees and 120 degrees compared with full water case.

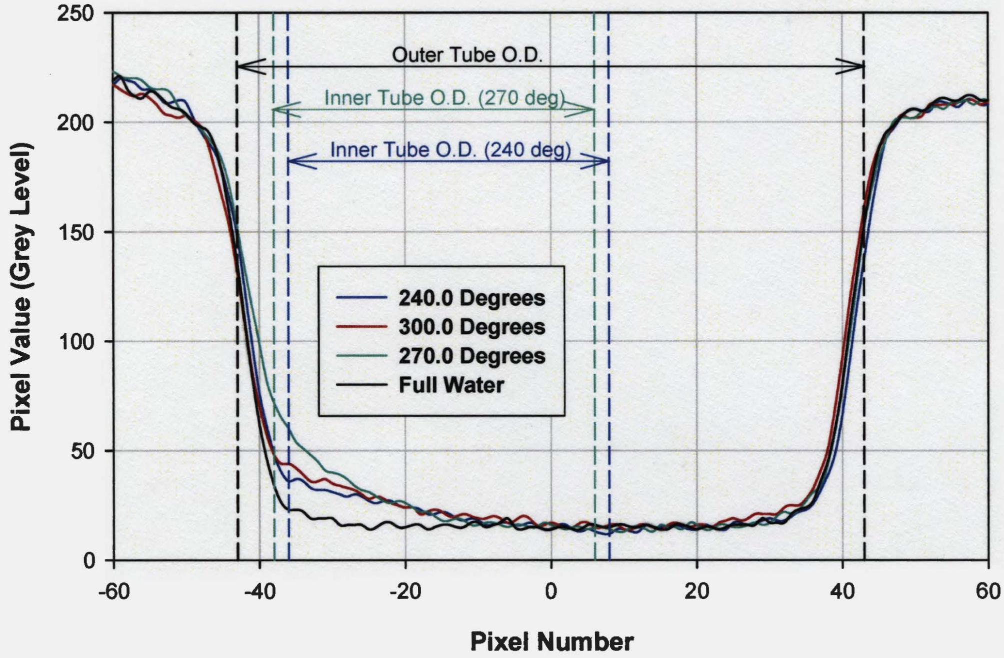

Figure 6.18. Pixel intensity profile across RTNR images in Figure 6.13 with rotation angles of 240 degrees, 270 degrees and 300 degrees compared with full water case.

the void is large enough to attenuate the neutron intensity to such a level where the sensitivity to the presence of a large void is greatly reduced.

Figure 6.14 shows also a small difference in the grey level values at the edge of the outer tube in different cases. These small discrepancies can be related to the misalignment of the test object on top of the turn table producing small shifts in angle and position. Although, these shift are very small, their effect is enhanced by the fact that the changes in water thickness at the edge of the outer tube with the lateral position (along the horizontal axis of the image) are relatively large. One pixel shift (0.045 mm) from the far edge of the outer tube will increase the neutron path length inside the tube wall from 0.0 to 3.4 mm (equivalent to 5% reduction in beam intensity and hence grey level). In other words, the RTNR imaging technique has a high sensitivity for changes in small thickness and hence small amounts of misalignments will lead to noticeable changes in grey levels around the edges of an object. Similar effect is shown in Figures 6.15 to 6.18. Figures 6.14 through 6.18 also show that the gradient in the grey level values is extended outside the physical dimensions of the outer tube. This effect is a result of the image unsharpness due to beam divergence (unparallelness) as discussed earlier in Chapter 1.

6.2.3 Thermal Neutron Scattering Results

As discussed in the previous section, although neutron radiography can provide details such as the magnitude of the void and the axial and transverse location of a void, it cannot determine its location along the neutron path and hence, it is not able to differentiate between voids with the same lateral position. A supplemental technique to obtain additional information about the spatial distribution of attenuating materials involves measuring neutrons scattered by the object.

The discussion in this section will be based on the test object described in Section 6.2.1 and hence, the main scattering species are hydrogen nuclei in the water molecules and aluminium nuclei of the object wall. The thermal neutron scattering cross-section for hydrogen is much higher than for aluminium. In addition, although thermal neutron scattering is isotropic in the centre-of-mass system (CMS) regardless of the mass number of the scattering nuclide, it has a forward scattering distribution in the lab system for hydrogen and a near isotropic distribution for aluminium. Based on these facts, it is expected that due to the presence of voids in the test object, the response of the neutron detectors will be a function of their angular location with respect to the main beam direction.

For detectors with angular location between 270 degrees and 90 degrees, the changes in their response will be mainly due to forward scattered neutrons, while for detectors with angular location between 90 degrees and 270 degrees, the changes in their response will be mainly due to backward scattered neutrons through multiple scattering (i.e., diffusion) with hydrogen.

Figure 6.19 represents the raw thermal neutron scattering signals (30 seconds gross counts) for the scattering measurement conducted with setup A (Figure 6.11) while Figure 6.20 represents the raw thermal neutron scattering signals (30 seconds gross counts) for the scattering measurement conducted with setup B (Figure 6.12).

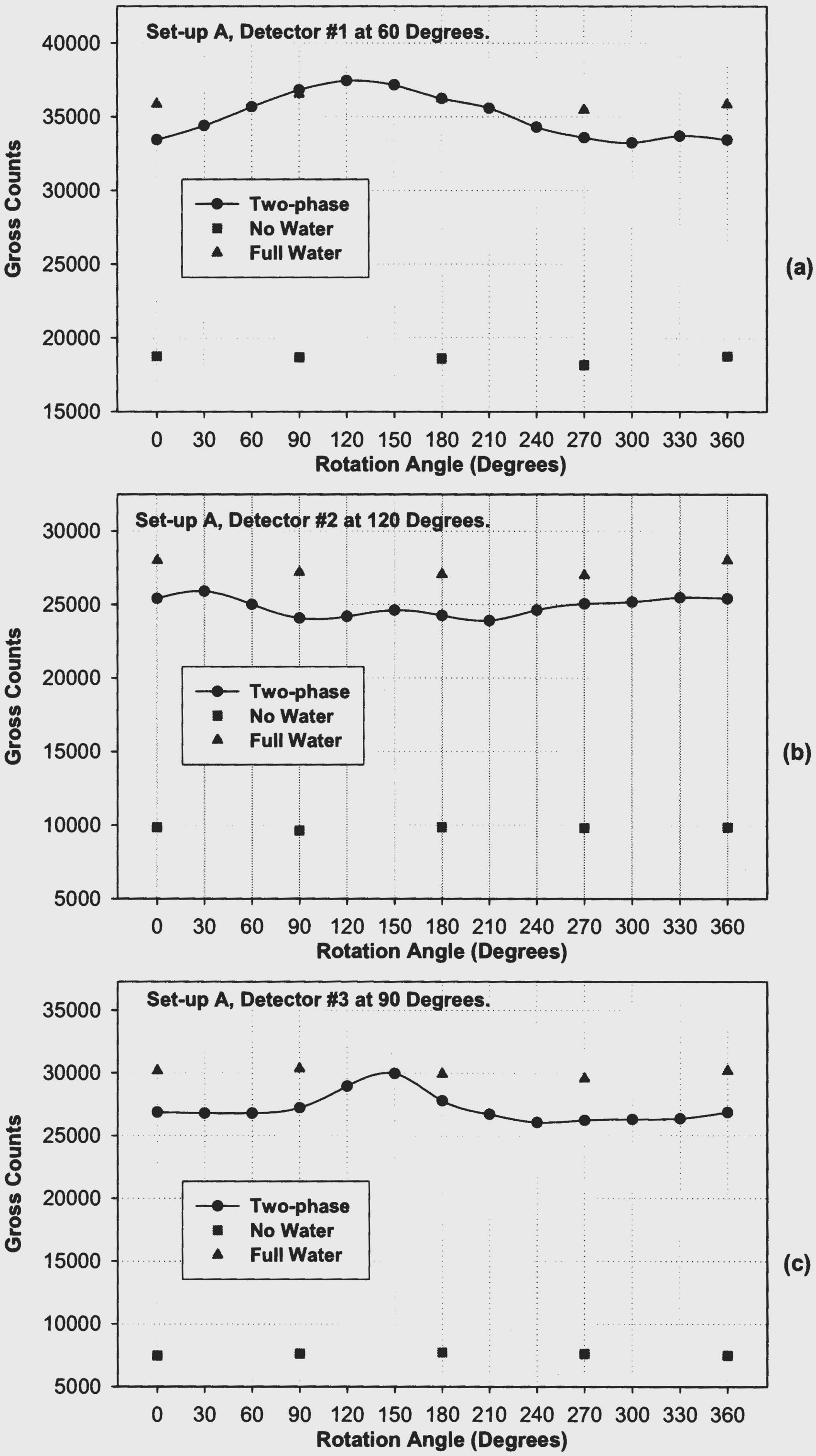

Figure 6.19. Scattering signal measured by detectors in setup A.

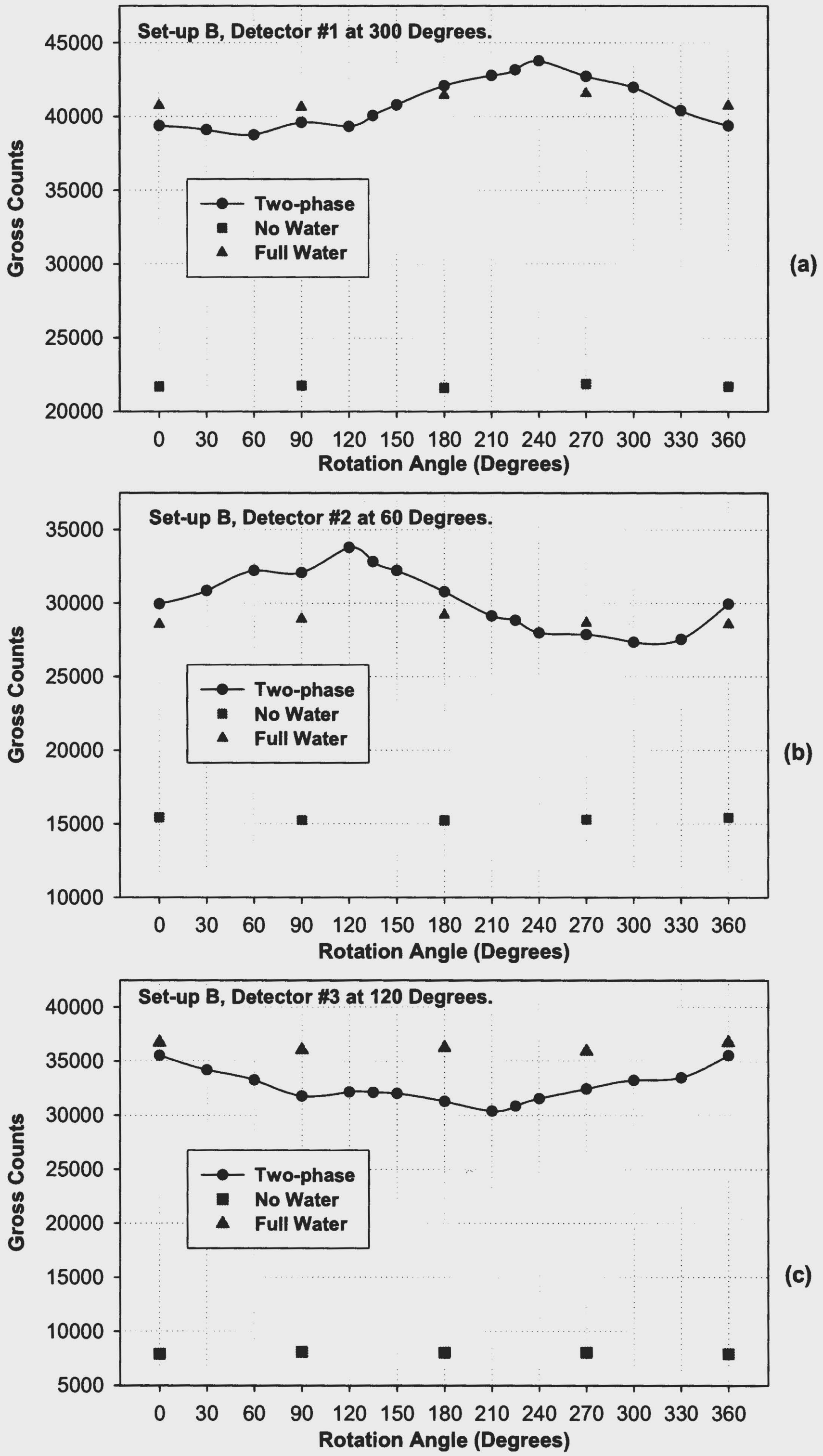

Figure 6.20. Scattering signal measured by detectors in setup B.

Figures 6.19 and 6.20 show that the response of each detector varies as a function of the rotation angle for the case when the test annulus (both tubes) is full of water and the case for the simulated void fraction (inner tube empty). The variance in gross counts when no water present is negligible as expected. The variance when both tubes are full is also small but not negligible. The variance with rotation angle for the case with inner tube empty is significant and thus it is possible to detect the void location by these detectors.

The examination of neutron scattering results shows that the response of the neutron detectors to the rotation angle of the object can be divided into four regions. Table 6.1 summarizes these regions and provides simple scattering source definition for each neutron detector according to its angular orientation. Figure 6.21 shows a schematic representation of the scattering object and the changes of the inner tube axis position at different rotation angles. The current analysis is valid for a single large bubble (void region) and further work is necessary before it can be generalized to multiple bubbles with the same lateral position. Although the combined RTNR and scattering information can predict the void distribution case, complete discrimination may have a void limit and bubble number limit.

The dimensionless thermal neutron scattering signals (counts) obtained by measurements conducted with setup A are shown in Figures 6.22 to 6.24. While, the dimensionless thermal neutron scattering signals (counts) obtained by measurements conducted with setup B are shown in Figures 6.25 to 6.27. The dimensionless neutron signal or counts is defined by [105]:

Table 6.1. Summary of scattering source location based on void region and detector orientation.

Region	Angle range (deg)	Detector at 300	Detector at 60	Detector at 90	Detector at 120
Back Left (BL)	270 to 0.0 (xc –ve, yc –ve)	Forward scattering from FL and BR regions.	Forward scattering from FR and BR regions.	Forward scattering from FR region and Backward scattering from BR region.	Backward scattering from FR, BR and FL regions.
Back Right (BR)	0.0 to 90 (xc +ve, yc -ve)	Forward scattering from FL and BL regions.	Forward scattering from FR and BL regions.	Forward scattering from FR region and Backward scattering from BL region.	Backward scattering from FR, FL and BL regions.
Front Right (FR)	90 to 180 (xc +ve, yc +ve)	Forward scattering from FL, BL and BR regions.	Forward scattering from BR and FL regions.	Forward scattering from FL region and Backward scattering from BR region.	Backward scattering from BR, FL and BL regions.
Front Left (FL)	180 to 270 (xc –ve, yc +ve)	Forward scattering from BL and FR regions.	Forward scattering from FR, BR and BL regions.	Forward scattering from FR region and Backward scattering from BR region.	Backward scattering from FR and BR regions.

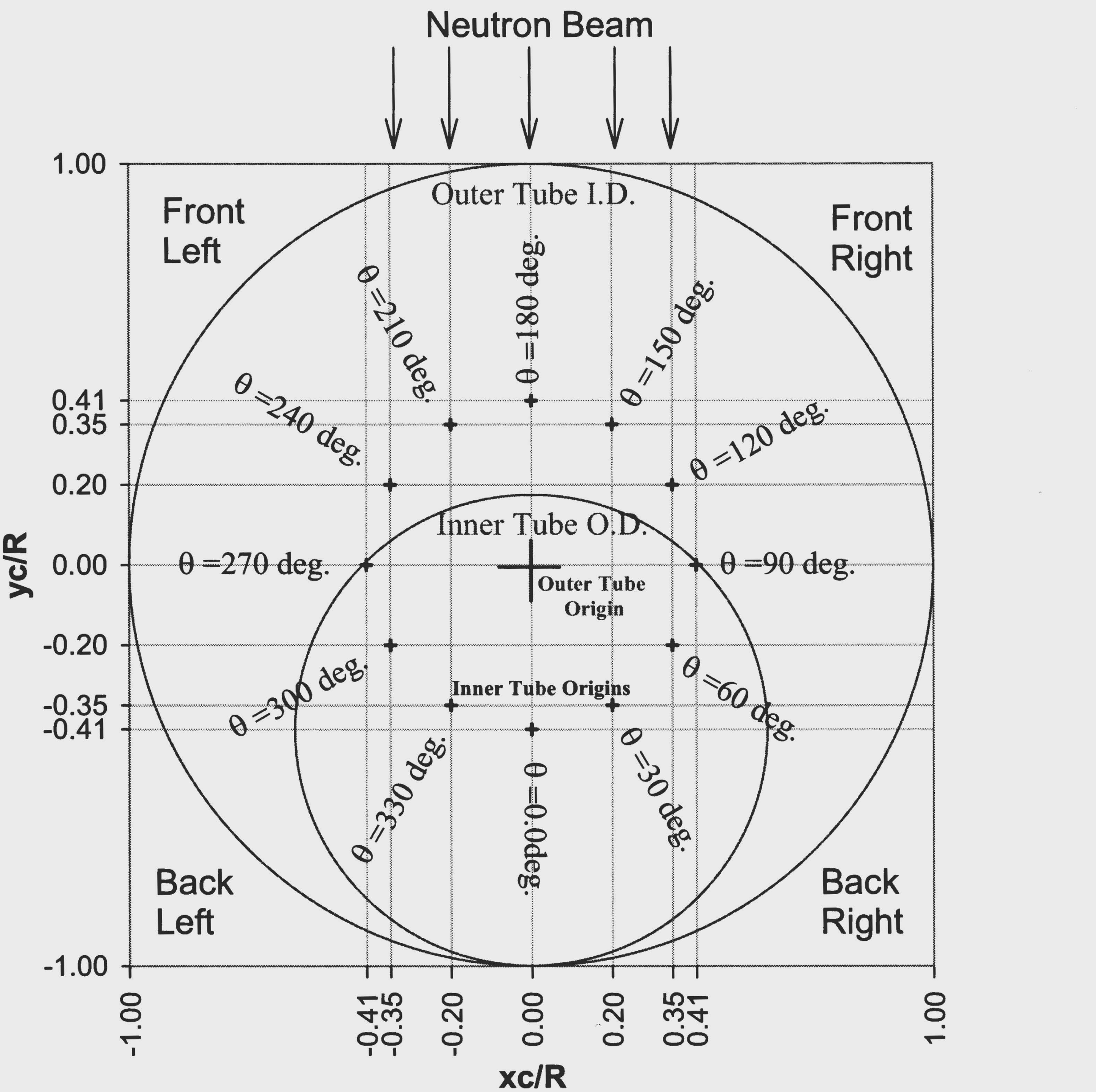

Figure 6.21. Schematic representation of inner tube axis position at different rotation angles.

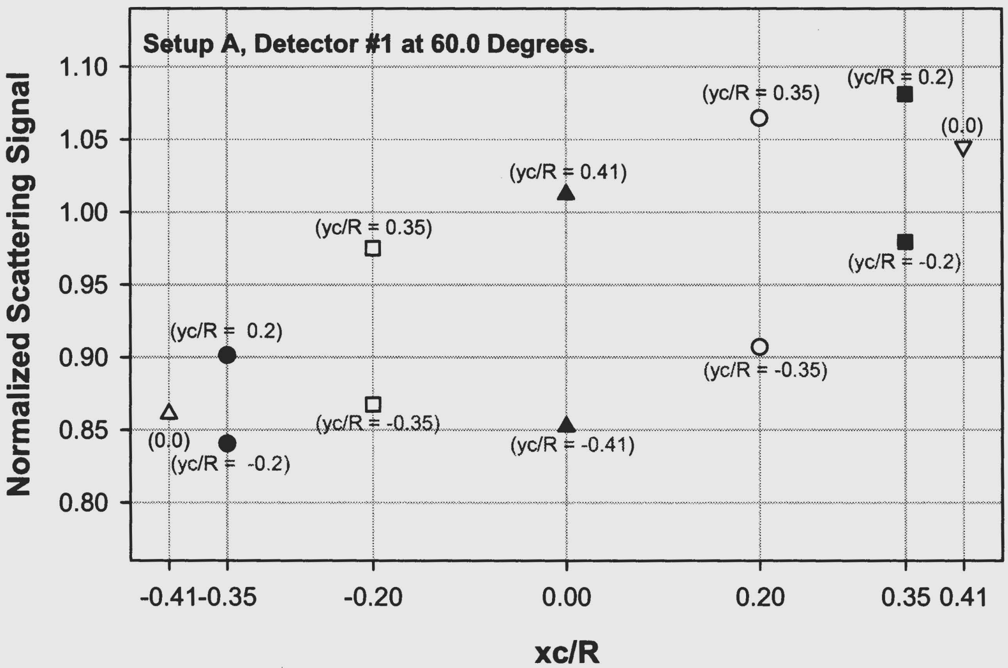

Figure 6.22. Normalized scattering signal measured by detector #1 (oriented at 60 degrees) in setup A. xc/R and yc/R represents the void centre coordinates relative to shell tube inner radius R.

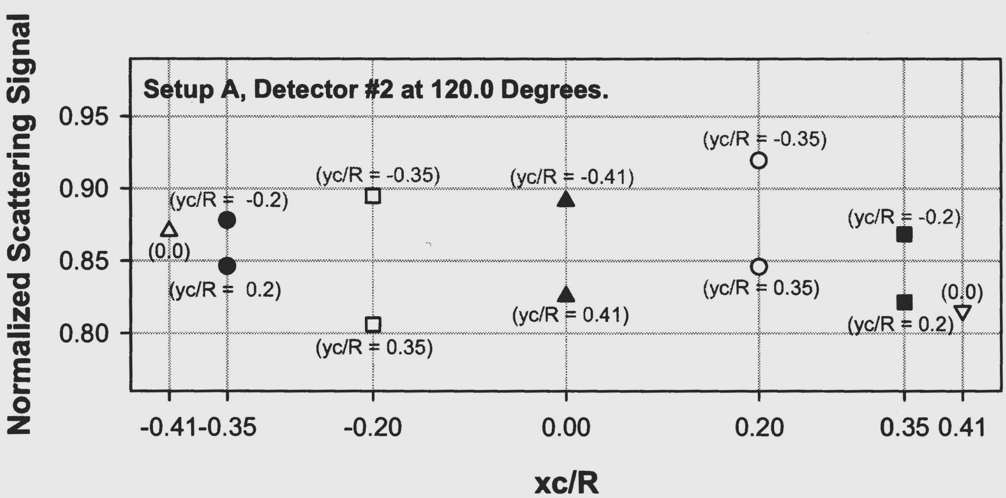

Figure 6.23. Normalized scattering signal measured by detector #2 (oriented at 120 degrees) in setup A. xc/R and yc/R represents the void centre coordinates relative to shell tube inner radius R.

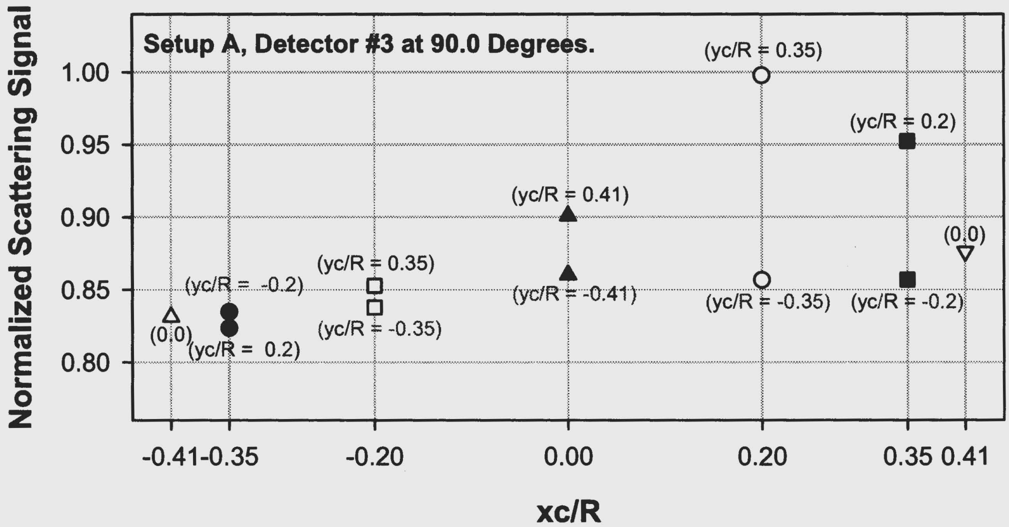

Figure 6.24. Normalized scattering signal measured by detector #3 (oriented at 90 degrees) in setup A. xc/R and yc/R represents the void centre coordinates relative to shell tube inner radius R.

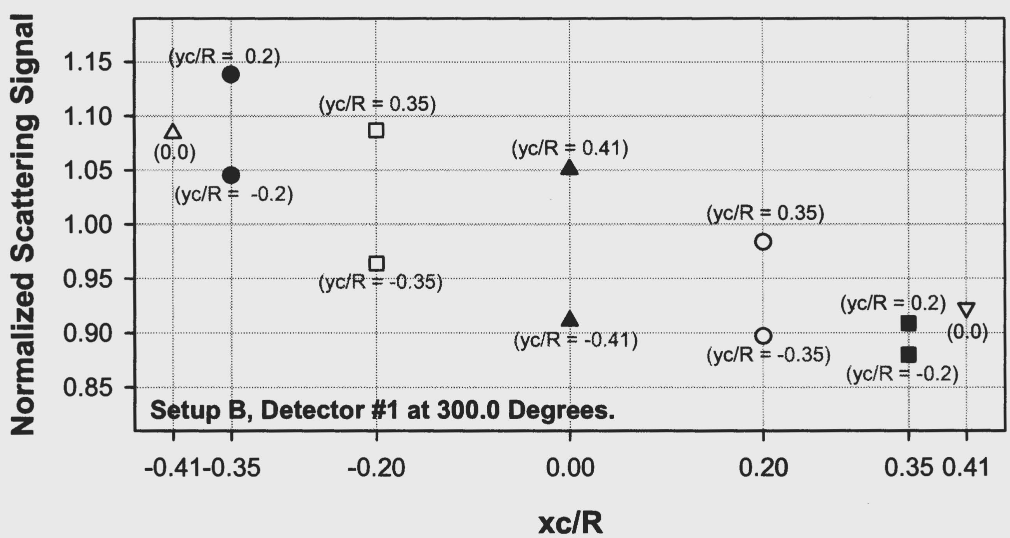

Figure 6.25. Normalized scattering signal measured by detector #1 (oriented at 300 degrees) in setup B. xc/R and yc/R represents the void centre coordinates relative to shell tube inner radius R.

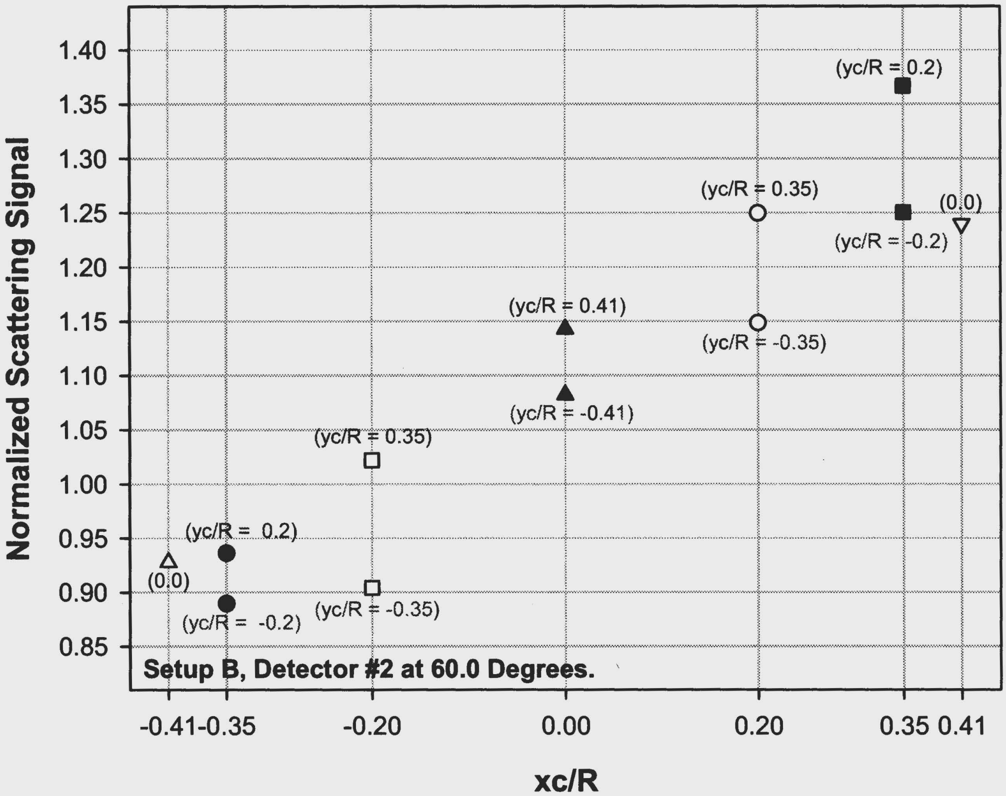

Figure 6.26. Normalized scattering signal measured by detector #2 (oriented at 60 degrees) in setup B. xc/R and yc/R represents the void centre coordinates relative to shell tube inner radius R.

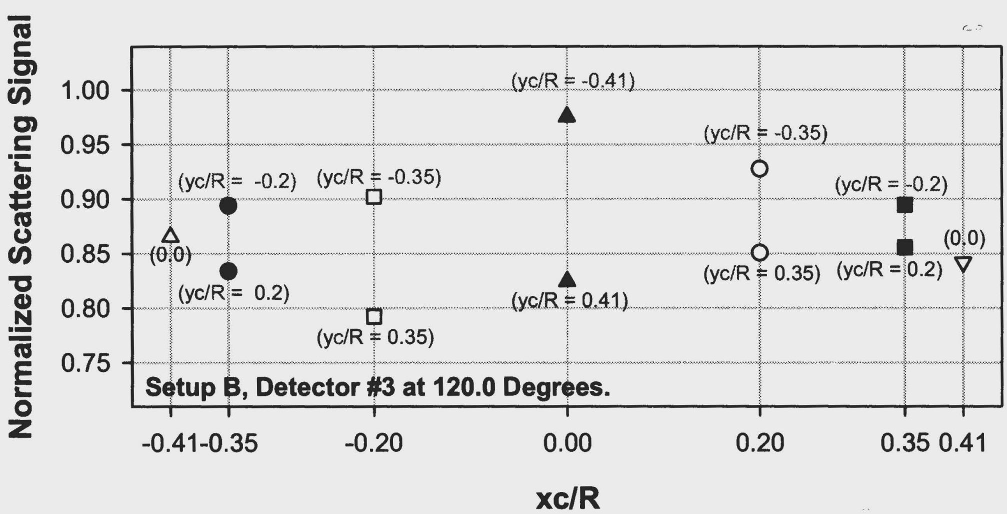

Figure 6.27. Normalized scattering signal measured by detector #3 (oriented at 120 degrees) in setup B. xc/R and yc/R represents the void centre coordinates relative to shell tube inner radius R.

$$\text{Dimensionless neutron signal} = \frac{\text{Neutron counts - No water counts}}{\text{Full water counts - No water counts}} \tag{6.8}$$

The dimensionless neutron signal depends on void fraction, but there are some effects of flow pattern [105, 106] or void distribution and the detector orientation. Figures 6.22 to 6.27 show that for all cases the dimensionless neutron signal is always greater than the existing void fraction (~0.75). Also, Figures 6.22 and 6.26 shows that in some cases the amount of neutrons scattered towards a detector located in front regions, can reach values higher than the full water case (void fraction = 0.0). Although it is expected that lower void fraction (higher water content) will scatter more neutrons, the void distribution changes the internal attenuation characteristics of the test object and hence scatter more neutrons. While a relationship can be developed, unfortunately, the relationship is not a simple and straightforward one and thus significant analysis effort may be required to produce an algorithm that can produce consistent results [107].

It is apparent that the use of two or three detectors is able to identify a unique variance between the scattered neutron signals and thus a relationship to the location of the void. Nevertheless, with a combination of an array of neutron detectors located at different elevations along the object and a 2D RTNR system, 3D dynamic neutron radiography can be achieved. Figure 6.28 shows a schematic representation of the proposed 3D dynamic neutron imaging system with a neutron detector array. Due to the limitations imposed by the multichannel buffer analog-to-digital conversion dead time (discussed in Section 5.4.1), testing of the proposed 3D dynamic neutron imaging concept was not applicable and a multichannel buffer with a faster conversion time is required.

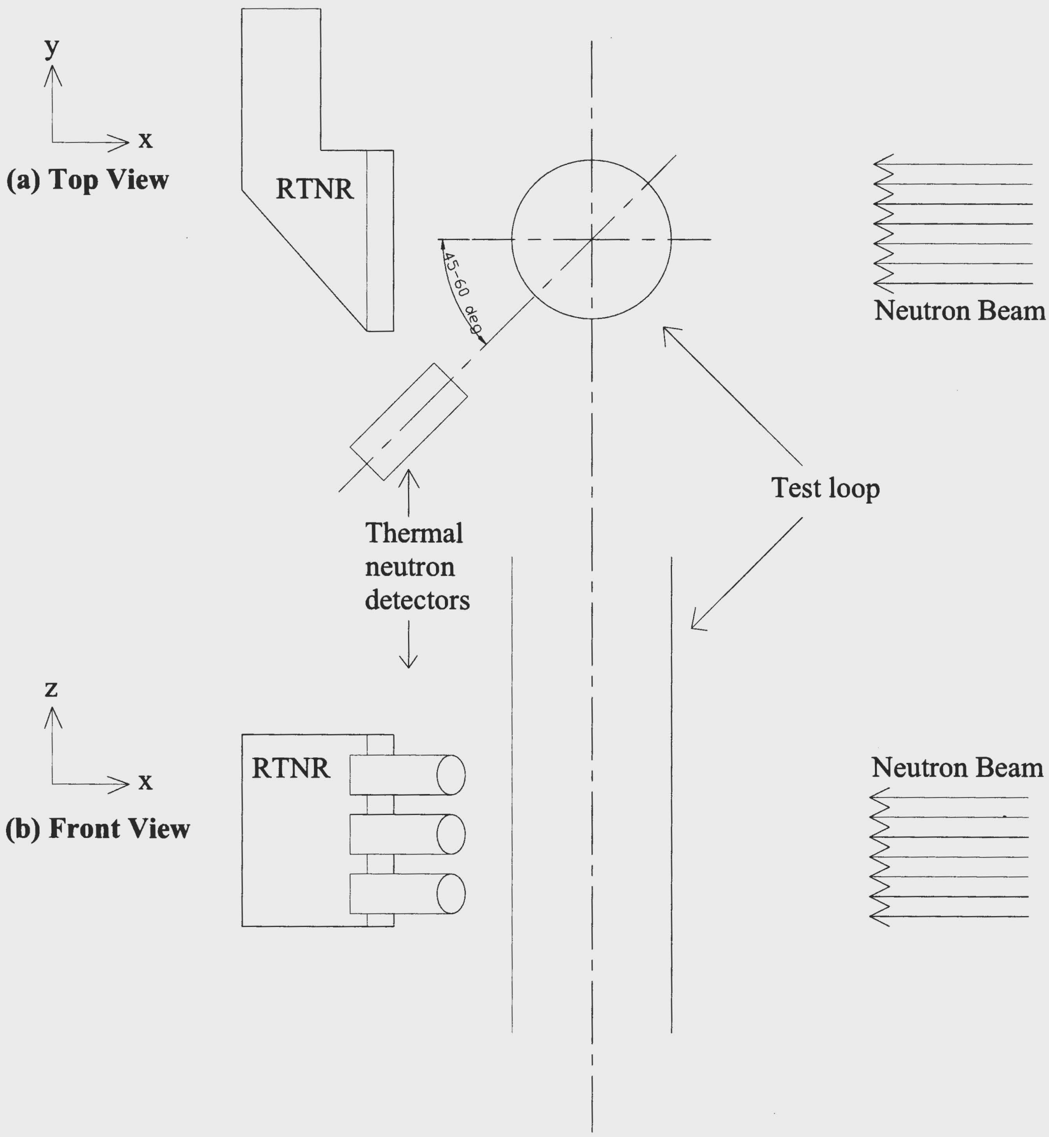

Figure 6.28. Schematic representation of the proposed 3D dynamic neutron imaging system.

7 CONCLUDING REMARKS

7.1 Conclusions

The optimization of a beam port based dynamic neutron radiography facility for the neutron source available from beam port #3 at the McMaster Nuclear Reactor (MNR) is the main focus of this work.

Neutron transport in dynamic neutron radiography has been investigated – theoretically and numerically – and successfully validated experimentally. The theoretical investigation was achieved analytically using closed-form solution technique based on the experimentally obtained neutron source intensity at the beam tube entrance. Monte-Carlo simulations (using MCNP code) were conducted to simulate the MNR advanced dynamic neutron radiography facility to confirm analytical model and predict beam characteristics at the imaging plane. The results show that there is a good agreement between numerical and analytical values for the thermal neutron flux at the imaging plane to within 5%. The presence of the back-wall shielding and the beam catcher has an insignificant effect on the thermal neutron flux at the image plan however, the epithermal and fast neutron fluxes have increased by 4-11% due to back scattering phenomena.

Neutron flux distributions at the imaging plane were mapped by irradiating copper foils and using the dynamic neutron imaging system. Thermal neutron flux is nearly uniform over an imaging area of 20.0-cm diameter. The thermal neutron flux ranges from 1.0×10^7 – 1.26×10^7 n/cm^2-s at 3.0 MW reactor operation. These values promote high-speed imaging with low neutron attenuation materials such as heavy water and real-time imaging with relatively high-attenuation materials such as light water.

The beam purity was determined experimentally. The measured values for the neutron-to-gamma ratio and the Cadmium-ratio were 6.0×10^5 n/cm^2-μSv and 1.22 respectively. These values promote dynamic neutron radiography with a minimal contrast degradation resulting for non-thermal neutron content of the beam.

A dynamic real-time neutron radiography (RTNR) system, using a low light level CCD camera and neutron-to-light scintillator conversion screen, has been developed and modified to obtain less neutron damage to the low-light level video camera. The RTNR system response linearity has been confirmed using an aluminium object. However, scattered neutrons have increased the measured grey levels. The system was able to contrast different materials and thicknesses although the presence of high noise level due to the nature of the neutron detection processes.

Dynamic neutron imaging was performed with the RTNR system using two-phase air-water mixture. Single frames of neutron images were captured with an image spatial resolution and temporal resolution of 0.44 mm and 33 ms respectively. The instantaneous, the cross-sectional averaged and the volume averaged void fraction profiles were obtained as well as bubble size and velocity.

A neutron scattering system using three thermal neutron detectors installed at the periphery of the neutron beam has been developed. The system was able to discriminate between regions of a second phase, such as voids in liquid, in the third dimension through extra information provided by thermal neutron scattered at different orientations. At least one thermal neutron detector must be in an orientation (45 – 60 degrees or 300 – 315 degrees relative to incident neutron beam) such that the majority of the neutrons being detected are forward scattered. The system was tested on a static object only due to the limitations imposed by the multichannel buffer analog-to-digital conversion dead time.

This work has generated the following contributions to knowledge:

- Development of a new dynamic neutron radiography facility producing a high quality neutron beam with intensity greater than 10^7 n/cm^2-s (at 3.0 MW operation) promoting high-speed radiography with low-attenuation materials such as heavy water and real-time radiography with relatively high-attenuation materials such as light water.
- Implementation of a Monte-Carlo technique (using commercial MCNP code) to simulate the neutron transport for optimization of the different facility components.
- Development of a neutron scattering system combined with the RTNR system to obtain 3D information and the demonstration of the system ability to locate single void in the third dimension of a simulated two-phase flow.

7.2 Recommendations for Future Work

The use of high sensitivity CCD (Charged Coupled Device) cameras in neutron radiography applications is limited because of the radiation damage in the silicon based CCD chip. A special cave design can reduce the radiation damage to the CCD chip where the Camera shield is part of the cave design. Cameras based on CMOS (Complementary

Metal-Oxide Semiconductor) chips have more radiation tolerance but are less sensitive. The development of cameras with large size CMOS chips can enhance its light sensitivity to produce low light images with comparable quality to CCD cameras. Also, implementing low light loss optical fibres will allow the development of a neutron radiography system where the camera is installed outside the biological shielding and hence reducing the radiation damage to negligible levels.

The quality of the neutron images obtained by the RTNR is reduced by the presence of high noise level due to the nature of the neutron detection processes, scattered neutrons, the neutron damage to the CCD chip and the nature of interlaced video capture. Further advanced image processing techniques are required to analyze neutron images and reverse these effects.

The relatively large dead time (processing time) for the Multichannel Buffer Ortec 920E Module imposed a limitation on the maximum combined gross count rate for all thermal neutron detectors and testing of dynamic 3D neutron imaging concept was not yet applicable. This upper limit value can be increased by using modules that incorporate separate analog-to-digital converter (ADC) for each signal or modules that have smaller dead time values. Further analysis is required to optimize thermal neutron scattering parameters such as; number of detectors, detector orientation, region of interest (ROI), etc. for develop dynamic scattering measurements to support dynamic 3D neutron imaging and to generalize the application of combined neutron radiography and scattering technique to locate multiple bubbles with the same lateral position.

REFERENCES

1- P. Von der Hardt and H.Rottger, "Neutron Radiography Handbook", 1981.

2- K. Mishima and T. Hibiki, "Quantitative limits of thermal and fluid phenomena measurements using the neutron attenuation characteristics of materials", Experimental Thermal and Fluid Science, Vol. 12, pp. 461-472, 1996.

3- G.D. Harvel, K. Hori, K. Kawanishi and J.S. Chang, "Cross-sectional void fraction distribution measurements in vertical annulus two-phase flow by high-speed X-ray computed tomography and real-time neutron radiography", Flow Measurement and Instrumentation, Vol. 10, pp. 259-266, 1999.

4- J.P. Barton, "Neutron radiography – an overview", in Practical Applications of Neutron Radiography and Gaging, ASTM STP 586, pp. 5-19, 1976.

5- L.E. Bryant and P. McIntire, Ed., "Nondestructive Testing Handbook", 2nd Edition, Volume 3, "Radiography and Radiation Testing", ASNT, 1985.

6- J.S. Chang and G.D. Harvel, "Determination of gas-liquid bubble column instantaneous interfacial area and void fraction by real-time neutron radiography method", Chemical Engineering Science, Vol. 47, pp. 3639-3646, 1992.

7- M. Matsubayashi, H. Kobayashi, T. Hibiki and K. Mishima, "Design and characteristics of the JRR-3M thermal neutron radiography facility and its imaging system", Nuclear Technology, Vol. 132, pp. 309-324, 2000.

8- D.C. Cutforth, "Neutron Sources for Radiography and Gaging", in Practical Applications of Neutron Radiography and Gaging, ASTM STP 586, pp. 20-34, 1976.

9- R.A. Quinn and C.C. Sigl, Ed., "Radiography in Modern Industry", Eastman Kodak Company, 1980.

10- B. Schillinger, W. Blumlhuber, A. Fent and M. Wegner, "3D neutron tomography: recent developments and first steps towards reverse engineering", Nuclear Instruments and Methods in Physics Research A, Vol. 424, pp 58-65, 1999.

11- J. Bordo, F. Mason and P. Zeisser, " Application of epithermal neutron radiography to performance tests on advanced LMFBR fuel", Proceeding of the 1st World Conference on Neutron Radiography, San Diego, USA, December 7-10, pp. 391-394, 1981.

12- M.R. Anderson and D.H.C. Harris, "Engineering applications of cold neutron radiography", Engineering, Vol 219, pp. 129-132, 1979.

13- M. Kamata, T. Esaka, K. Takami, S. Takai, S. Fujine, K. Yoneda and K. Kanda, "Studies on the Lithium ion conduction in $Ca_{0.95}Li_{0.10}WO_4$ using cold neutron radiography", Solid State Ionics, Vol. 91, pp. 303-306, 1996.

14- M. Kamata, T. Esaka, S. Fujine, K. Yoneda and K. Kanda, "Lithium batteries: Application of neutron radiography", Journal of Power Sources, Vol. 68, pp. 459-462, 1997.

15- N. Takenaka, H. Asano, T. Fujii, M. Mizubata and K. Yoshii, "Application of fast neutron radiography to three-dimensional visualization of steady two-phase flow in a rod bundle", Nuclear Instruments and Methods in Physics Research A, Vol. 424, pp. 73-76, 1999.

16- E. Lehmann, G. Frei, A. Nordlund and B. Dahl, "Neutron radiography with 14 MeV neutrons from a neutron generator", IEEE Transactions on Nuclear Science, Vol. 52, pp.

389-393, 2005.

17- R.A. Schrack, "Uranium-235 measurement in waste material by resonance neutron radiography", Nuclear Technology, Vol. 67, pp. 326-332, 1984.

18- J.C. Overley, "Element-sensitive computed tomography with fast neutron", Nuclear Instruments and Methods in Physics Research B, Vol. 24/25, pp. 1058-1062, 1987.

19- N.B. Edenborough, "Neutron radiography to detect residual core in investment cast turbine airfoils" in Practical Applications of Neutron Radiography and Gaging, ASTM STP 586, pp. 152-157, 1976.

20- J. Joseph, "Californium-based neutron radiography for corrosion detection in aircraft", in Practical Applications of Neutron Radiography and Gaging, ASTM STP 586, pp. 168-180, 1976.

21- J.P. Cassidy, "Use of a low-energy Van de Graff accelerator in neutron radiography of encased explosives", in Practical Applications of Neutron Radiography and Gaging, ASTM STP 586, pp. 117-124, 1976.

22- P.E. Underhill and R.L. Newacheck, "Miscellaneous applications of neutron radiography", in Practical Applications of Neutron Radiography and Gaging, ASTM STP 586, pp. 252-267, 1976.

23- B. Ismail, D. Ewing, J.S. Chang and J.C. Cotton, "Development of non-destructive neutron radiography technique to measure the three-dimensional soot deposition profiles in diesel engine exhaust system", Journal of Aerosol Science, Vol. 35, pp. 1275-1288, 2004.

24- E.H. Lehmann, P. Vontobel, G. Frei and C. Bronnimann, "Neutron imaging–detector options and practical results", Nuclear Instruments and Methods in Physics Research A, Vol. 531, pp. 228-237, 2004.

25- H. Berger, "Characteristics of a thermal neutron television imaging system", Materials Evaluation, Vol. 24, pp.475-481. 1966.

26- W.E. Dance and S.F. Carollo, "High sensitivity electronic imaging system for reactor or non-reactor neutron radiography", Proceeding of the 2nd World Conference on Neutron Radiography, Paris, France, June 16-20, pp.415-422, 1986.

27- H. Pleinert, E.H. Lehmann and S. Korner, "Design of a new CCD camera neutron radiography detector", Nuclear Instruments and Methods in Physics Research A, Vol. 399, pp. 382-390, 1997.

28- J.S. Brenizer, H. Berger, K.M. Gibbs, P. Mengers, C.T. stebbings, D. Polansky and D.J. Rogerson, "Development of a new electronic neutron imaging system", Nuclear Instruments and Methods in Physics Research A, Vol. 424, pp. 9-14, 1999.

29- D. Kramer, E. Lehmann, G. Frei , P. Vontobel, A. Wokaun and G.G. Scherer, "An on-line study of fuel cell behaviour by thermal neutrons", Nuclear Instruments and Methods in Physics Research A, Vol. 542, pp. 52-60, 2005.

30- J.J. Milczarek, A. Czachor, A.E.G. El Abd and Z. Wisniewski, "Dynamic neutron radiography observations of water migration in porous media", Nuclear Instruments and Methods in Physics Research A, Vol. 542, pp. 232-236, 2005.

31- F. Korosi, M. Balasko and E. Svab, "A distribution pattern of cadmium, gadolinium and samarium in phaseolus vulgaris (L) plants as assessed by dynamic neutron radiography", Nuclear Instruments and Methods in Physics Research A, Vol. 424, pp.

129-135, 1999.

32- M. Kamata, T. Esaka, S. Fujine, K. Yoneda and K. Kanda, "Application of NR for research in electrochemical systems", Nuclear Instruments and Methods in Physics Research A, Vol. 377, pp. 161-165, 1996.

33- E. Svab, M. Balasko and F. Korosi, "Dynamic neutron radiography in petrophysical applications", Physica B, Vol. 276-278, pp. 916-917, 2000.

34- J.M. Cimbala, D.E. Hughes, S.H. Levine and D. Sathianathan, "Application of neutron radiography for fluid flow visualization", Nuclear Technology, Vol. 81, pp. 435-445, 1988.

35- K. Mishima, T. Hibiki and H. Nishihara, "Some application of gas-liquid flow in narrow rectangular ducts", International Journal of Multiphase Flow, Vol. 19, pp. 115-124, 1993.

36- G.D. Harvel, J.S. Chang and V.S. Krishnan, "A two-phase flow regime map for a MAPLE-type nuclear research reactor fuel channel: Effect of hexagonal finned bundle", Nuclear Technology, Vol. 118, pp. 151-161, 1997.

37- N. Takenaka, H. Asano, T. Fujii, Y. Murata, K. Mochiki, A. Taguchi, M. Matsubayashi and A. Tsuruno, "Void fraction measurements in two-phase flow by real-time neutron radiography and real-time image processing", Nuclear Instruments and Methods in Physics Research A, Vol. 377, pp. 153-155, 1996.

38- S.S. Glickstein, W.H. Vance and H. Joo, "Void fraction measurements using neutron radiography", Nuclear Science and Engineering, Vol. 121, pp. 153-161, 1995.

39- K. Uchimura, G.D. Harvel, T. Matsumoto, M. Kanzaki and J.S. Chang, "An image processing approach for two-phase interfaces visualized by a real time neutron radiography technique", Flow Measurement and Instrumentation, Vol. 9, pp. 203-210, 1998.

40- T. Iwamura, H. Watanabe and Y. Murao, "Critical heat flux experiments under steady-state and transient conditions and visualization of CHF phenomenon with neutron radiography", Nuclear Engineering and Design, Vol. 149, pp. 195-206, 1994.

41- Y. Tsuji, S. Matsueda, M. Oda, M. Matsuda, T. Yagi, M. Tamaki, M. Matsubayashi and S. Fujine, "Visualization and correlation analysis of counter-current two-phase flow in a thermosyphon by neutron radiography", Nuclear Instruments and Methods in Physics Research A, Vol. 377, pp. 148-152, 1996.

42- J. Jasti and H. Fogler, "Application of neutron radiography to image flow phenomena in porous media", AIChE Journal, Vol 38, pp. 481-488, 1992.

43- T. Nemec, J. Rant, V. Apih and B. Glumac, "Study of building materials impregnation processes by quasi-real-time neutron radiography", Nuclear Instruments and Methods in Physics Research A, Vol. 424, pp. 242-247, 1999.

44- J. D. Jones, J.T. Lindsay, C.W. Kauffman, A. Vulpetti and B.D. Peters, "Real-time neutron imaging applied to internal combustion engine behaviour", SAE Technical Paper Series, 1985.

45- N. Takenaka, T. Kadowaki, Y. Kawabata, I.C. Lim and C.M Sim, "Visualization of cavitation phenomena in a Diesel engine fuel injection nozzle by neutron radiography", Nuclear Instruments and Methods in Physics Research A, Vol. 542, pp. 129-133, 2005.

46- H. Asano, N. Takenaka, T. Fuji, Y. Murata, K. Mochiki and A. Taguchi, "Application of neutron radiography to diagnosis of refrigerator", Nuclear Instruments and Methods in Physics Research A, Vol. 377, pp. 170-173, 1996.

47- H. Asano, N. Takenaka, T. Fuji, Y. Shibata, T. Ebisu and M. Matsubayashi, "Visualization and measurements of refrigerant flow in compression-type refrigerator by neutron radiography", Nuclear Instruments and Methods in Physics Research A, Vol. 424, pp. 98-103, 1999.

48- M. W. Weissenberger, A.J. Giacomin, J.A. Reuscher and C.M. Russel, "Real-time radiography of injection mold filling", International Polymer Processing, Vol. 8, pp. 360-364, 1993.

49- G.D. Harvel, J.S. Chang, J.C. Campeau, K. Uchimura, T. Matsumoto and M. Kanzaki, "Visualization of a gas-liquid metal two-phase natural circulation flow by a real-time neutron radiography technique", Proceedings of the 4th ASME/JSME International Conference on Nuclear Engineering, ICONE4, New Orleans, LA, USA, March 10-14 1996.

50- N. Takenaka, H. Asano, T. Fujii, Y. Motomura, A. Ono, M. Matsubayashi and A. Tsuruno, "Liquid metal flow visualization by neutron radiography", Nuclear Instruments and Methods in Physics Research A, Vol. 377, pp. 156-160, 1996.

51- R.H. Bossi and A.H. Robinson, "High-speed motion neutron radiography", Nuclear Technology, Vol. 59, pp. 363-374, 1982.

52- T. Hibiki and K. Mishima, "Feasibility of high frame-rate neutron radiography by using a steady thermal neutron beam with 10^6 n/(cm^2 s) flux", Nuclear Instruments and Methods in Physics Research A, Vol. 369, pp. 186-194, 1996.

53- T. Hibiki, K. Mishima and M. Matsubayashi, "Application of high-frame-rate neutron radiography with a steady thermal neutron beam to two-phase flow measurements in a metallic rectangular duct", Nuclear Technology, Vol. 110, pp. 422-435, 1995.

54- K. Mishima, T. Hibiki and H. Nishihara, "Visualization and measurements of two-phase flow by using neutron radiography", Nuclear Engineering and Design, Vol. 175, pp. 25-35, 1997.

55- Y. Saito, K. Mishima, T. Hibiki, A. Yamamoto, J. Sugimoto and K. Moriyama, "Application of high-frame-rate neutron radiography to steam explosion research", Nuclear Instruments and Methods in Physics Research A, Vol. 424, pp. 142-147, 1999.

56- K. Mishima, T. Hibiki, Y. Saito, J. Sugimoto and K. Moriyama, "Visualization study of molten metal-water interaction by using neutron radiography", Nuclear Engineering and Design, Vol. 189, pp. 391-403, 1999.

57- K. Mishima, T. Hibiki, Y. Saito, H. Nashihara, Y. Tobita, K. Konishi and M. Matsubayashi, "Visualization and measurement of gas-liquid metal two-phase flow with large density difference using thermal neutrons as microscopic probes", Nuclear Instruments and Methods in Physics Research A, Vol. 424, pp. 229-234, 1999.

58- Y. Saito, K. Mishima, Y. Tobita, T. Suzuki, M. Matsubayashi, I.C. Lim and J.E. Cha, "Application of high frame-rate neutron radiography to liquid-metal two-phase flow research", Nuclear Instruments and Methods in Physics Research A, Vol. 542, pp. 168-174, 2005.

59- M. Kureta, H. Akimoto, T. Hibiki and K. Mishima, "Void fraction measurement in subcooled-boiling flow using high-frame-rate neutron radiography", Nuclear Technology, Vol. 136, pp. 241-254, 2001.

60- M. Kureta, T. Hibiki, K. Mishima and H. Akimoto, "Study on point of net vapour generation by neutron radiography in subcooled boiling flow along narrow rectangular channels with short heated section", International Journal of Heat and Mass Transfer, Vol. 46, pp. 1171-1181, 2003.

61- G.M. Reynolds, "Neutron gaging systems", in Practical Applications of Neutron Radiography and Gaging, ASTM STP 586, pp. 58-73, 1976.

62- E.M.A. Hussein and E.J. Waller, "Review of one-side approaches to radiographic imaging for detection of explosives and narcotics", Radiation Measurements, Vol. 29, pp. 581-591, 1998.

63- D. de Soete, R. Gijbels and J. Hoste, "Neutron activation analysis", Wiley-Interscience, New York, USA, 1972.

64- W.T. Hancox, C.F. Forrest and A.A. Harms, "Void determination in two-phase systems employing neutron transmission", Proceedings of AIChE-ASME National Heat Transfer Conference, Paper No. 72-HT-2, Denver, Colorado, USA, August 6-9, 1972.

65- F.V. Frazzoli and A. Magrini, "Neutron gauge for measurement of high void fraction in water-steam mixtures", Nuclear Technology, Vol. 45, pp. 177-182, 1979.

66- J.W. Behrens, R.G. Johnson and R.A. Schrack, "Neutron resonance transmission analysis of reactor fuel samples", Nuclear Technology, Vol. 67, pp. 162-168, 1984.

67- J.C. Overley, "Determination of H, C, N, O content of bulk materials from neutron-attenuation measurements", International Journal of Applied Radiation and Isotopes, Vol. 36, pp. 185-191, 1985.

68- P.P. Glokhale and E.M.A. Hussein, “A ^{252}Cf neutron transmission technique for bulk detection of explosives”, Applied radiation and Isotopes, Vol. 48, pp. 973-979, 1997.

69- C.T. Oien, “Small angle neutron scattering: An NDE tool”, in Nondestructive methods for material property determination, pp. 59-68, Eds. C.O. Ruud and R. E. Green, Jr., Plenum Press, New York, 1984.

70- J. Schelten, “Small angle scattering complementing neutron radiography”, in Proceedings of the First World Conference on Neutron Radiography, pp. 953-959, Eds. J.P. Barton and P. von der Hardt, D. Reidel Puplishing Company, Dordrecht, Holland, 1983.

71- W.T. Sha and C.F. Bonilla, “Out-of-pile steam-fraction determination by neutron-beam attenuation”, Nuclear Applications, Vol. 1, pp. 69-75, 1965.

72- E.M.A. Hussein and E.J. Waller, “A neutron steam-quality meter for a fluidized bed plant”, Applied Radiation and Isotopes, Vol. 41, pp. 1049-1055, 1990.

73- P. Han, E.M.A. Hussein, P.J. Ingham and R.M. Henschell, “Nonintrusive measurement of transient flow boiling in rod-bundle channels using fast-neutron scattering”, Nuclear Instruments and Methods in Physics Research A, Vol. 353, pp. 695-698, 1994.

74- E.M.A. Hussein, “Modeling and design of a neutron scatterometer for void-fraction measurement”, Nuclear Engineering Design, Vol. 105, pp. 333-348, 1988.

75- W.J. Richards, M.R. Gibbons and K.C. Shields, “Neutron tomography developments and applications”, Applied Radiation and Isotopes, Vol. 61, pp. 551–559, 2004.

76- E.W. McFarland, R.C. Lanza and G.W. Poulosi "Multi-dimensional Neutron-computed tomography", IEEE Transactions on Nuclear Science, Vol. 38, pp. 612-622, 1991.

77- C.F. Barton, "Computerized axial tomography for neutron radiography of nuclear fuel", Transactions of American Nuclear Society, Vol. 28, pp. 212-213, 1977.

78- R.A. Koeppe, R.M. Brugger, G.A. Schdapper, G.N. Laren and R.J. Jost, "Neutron computed tomography", Journal of Computer Assisted Tomography, Vol. 5, pp. 79-88, 1981.

79- D.M. Tow, "Post irradiation examination using neutron tomography", in Proceedings of the First World Conference on Neutron Radiography, pp. 425-435, Eds. J.P. Barton and P. von der Hardt, D. Reidel Puplishing Company, Dordrecht, Holland, 1983.

80- S. Fujine, K. Yoneda and K. Kanda, "An application of the neutron television fluoroscopic system to neutron computed tomography", Nuclear Instruments and Methods in Physics Research, Vol. 226, pp. 475-481, 1984.

81- M. Dierick, J. Vlassenbroeck, B. Masschaele, V. Cnudde, L. Van Hoorebeke and A. Hillenbach, "High-speed neutron tomography of dynamic processes", Nuclear Instruments and Methods in Physics Research A, Vol. 542, pp. 296–301, 2005.

82- E.M.A. Hussein, D.A. Meneley and S. Banerjee, "Single-exposure neutron tomography of two-phase flow", International Journal of Multiphase Flow, Vol. 12, pp. 1-34, 1986.

83- N.F. Harrison, "Conceptual design of a high speed neutron radiography experimental facility", M. Eng. Thesis, Engineering Physics Department, McMaster University, Hamilton, Canada, 2003.

84- C.M. Lederer, and V.S. Shirley, Eds.; E. Browne, J.M. Dairiki, and R.E. Doebler (Principal Authors); A.A. Shihab-Eldin, L.J. Jardine, J.K. Tuli, and A.B. Buyrn, "Table of Isotopes", 7th Edition, John Wiely & Sons, 1978.

85- G. F. Knoll, "Radiation Detection and Measurement", 2nd Edition, John Wiely & Sons, 1989.

86- Reuter Stokes, Product Data Sheet, M-3.

87- S.F. Mughabghab, M. Divadeenam and N.E. Holden, "Neutron Cross Sections", Vol. 1 and 2, Academic Press, 1981.

88- D.R. Wyman, "Neutron transport in radiography", Ph.D. Thesis, Engineering Physics Department, McMaster University, Hamilton, Canada, 1984.

89- J.D. Parquet and G. Bayon, "Contribution of neutron radiography to the conservation of the environment", Neutron Radiography, Vol. 4, pp. 65-73, 1994.

90- A.R. Spowart, "Measurement of gamma sensitivity of granular and glass neutron scintillators and films", Nuclear Instruments and Methods in Physics Research, Vol. 82, p. 1-6, 1972.

91- McMaster Nuclear Reactor Radioactive Safety Program, Document No. HP-9000, McMaster University, Hamilton, Canada, December 2001.

92- John. R. Lamarsh, "Introduction to Nuclear Engineering", 2nd Ed., Addison-Wesley Publishing Company, 1983.

93- John. R. Lamarsh, "Introduction to Nuclear Reactor Theory", Addison-Wesley Publishing Company, 1966.

94- I.M. Sobol, “The Monte Carlo Method”, The University of Chicago Press, Chicago, 1974.

95- G.S. Fishman, “Monte Carlo: Concepts, Algorithms and Applications”, Springer, New York, 1996.

96- M.H. Kalos, “Monte Carlo Methods, Volume I: Basics”, John Wiley & Sons, New York, 1986.

97- J. Spanier and E.M. Gelbard, “Monte Carlo Principles and Neutron Transport Problems”, Addison-Wesley, Reading, 1969.

98- G. Ledanois, “Main features of the multipurpose Monte-Carlo linear transport code SICOMORE”, Proceedings of Monte-Carlo Methods and Applications in Neutronics, Photonics and Statistical Physics, Provence, France, April 22-26, pp. 26-32, 1985.

99- J. F. Briesmeister, “MCNP – A general Monte-Carlo N-Particle Transport Code, Version 4B” LA-13181, Los Alamos National Laboratory, August 1996.

100- S. Gerdung, P. “Pihet, J.E. Grindborg, H. Roos and U.J. Schuhmacher, “Operation and application of tissue-equivalent proportional counters”, Radiation Protection Dosimetry, Vol. 61, pp. 381-404, 1995.

101- H. Unesaki, T. Hibiki and K. Mishima, “”Evaluation of scattered neutron component in thermal neutron radiography image: Influence of scattered neutrons and unparallelness of incident neutron beam”, Nuclear Instruments and Methods in Physics Research A, Vol. 413, pp. 143-150, 1998.

102- N. Kardjilov, F. de Beer, R. Hassanein, E. Lehmann and P. Vontobel, “Scattering corrections in neutron radiography using point scattered functions”, Nuclear Instruments and Methods in Physics Research A, Vol. 542, pp. 336-341, 2005.

103- G.D. Harvel, J.S. Chang, J.C. Campeau, A. Khaial, V.S. Krishnan, K. Uchimura, T. Ishimoto, A. Furuya J. Su and J.L.H. Faccini, "Determination of two-phase natural circulation interfacial parameters by real-time neutron radiography", Proceedings of the 10th International Topical Meeting on Nuclear Reactor Thermal Hydraulics (NURETH-10), Seoul, Korea, October 5-9, 2003.

104- G.D. Harvel, "Determination of two-phase flow parameters for nuclear fuel channel using a real-time neutron radiography method", Ph.D. Thesis, Engineering Physics Department, McMaster University, Hamilton, Canada, 1995.

105- P.S.L Yuen, D.A. Meneley and S. Banerjee, "Measurement of void fraction by a neutron-scattering technique with portable sources: Effect of the incident energy spectrum", International Journal of Multiphase Flow, Vol. 14, pp. 401-412, 1988.

106- S. Banerjee, E. Hussein and D.A. Meneley, "Simulation of a scattering method for measuring void fraction in two-phase flow", Nuclear Engineering and Design, Vol. 53, pp. 393-405, 1979.

107- A.M. Khaial, G.D. Harvel and J.S. Chang, "Investigation of combined neutron scattering and neutron radiography techniques for measurements of gas-liquid two-phase flow", Proceedings of the 16th International Conference on Nuclear Engineering, ICONE16, Orlando, FL, USA, May 11-15, 2008.

Appendix A: Radiation Shielding Calculations

Background

The Canadian Nuclear Safety Commission (CNSC) regulations and limits, followed by the McMaster Nuclear Reactor [A1], state that the effective dose received by and committed to a Nuclear Energy Workers (NEW's) shall not exceed:

i- 100 mSv in a 5-year dosimetry period (equivalent to an average dose rate of 10 μSv/hr)

ii- 50 mSv in one-year dosimetry period (equivalent to an average dose rate of 25 μSv/hr)

The McMaster Nuclear Reactor Radioactive Safety Program [A1], divides radiation areas based on total effective dose rate into:

i- Generally Accessible Radiation Area (Dose rate < 25 μSv/hr),

ii- Designated Radiation Areas with Limited Access (25 μSv/hr < Dose rate <1000 μSv/hr) and,

iii- Restricted Radiation Area (Dose rate > 1000 μSv/hr).

As such there is no clear definition of required dose rate. As a factor of safety, the shielding calculation will assume a dose rate target of 10 μSv/hr.

Selection of Shielding Materials

In order to have a more efficient shutter with lowest achievable weight; a shutter design with composite materials is used. Each material is the most efficient attenuator for a certain type of radiation encountered in the beam tube: fast neutrons, thermal neutrons and gamma rays.

Paraffin wax is chosen as fast neutron attenuator as hydrogen is the most efficient fast neutron attenuator, paraffin has a lower density than water and higher hydrogen partial density (i.e., higher macroscopic cross section) and it is solid and is relatively easy to manipulate for construction purposes.

Boron carbide flexible sheets (boroflex) is chosen as the thermal neutron absorber (attenuator) since; it has a very high thermal neutron absorption cross-section, stable interaction products (Lithium and Helium.)

Lead is chosen as gamma ray attenuator since; Lead is the stable element with highest atomic number and is relatively easy to manipulate for construction purposes.

Table A-1 gives the attenuation characteristics of some common shielding materials. Table A-2 gives the attenuation factors for different materials at different thicknesses based on the exponential attenuation laws;

For fast neutron: $f_{fn} = \exp[-\Sigma_r X]$

For gamma rays: $f_\gamma = B(\mu X) \times \exp[-\mu X]$

Table A-1. Shielding Materials Attenuation Properties [A2-A5]

	Density g/cm^3	Thermal neutrons macroscopic cross-section (cm^{-1}) at 0.0253 eV			Fast neutrons	Gamma-rays Attenuation Coefficient μ (cm^{-1})		
		Σ_s	Σ_a	Σ_t	Σ_r (cm^{-1})	0.5 MeV	2.0 MeV	4.0 MeV
Bismuth	9.800	0.2541	0.932E-3	0.25503	0.0986	1.6141	0.4541	0.4135
Lead	11.34	0.3757	5.603E-3	0.3813	0.118	1.8319	0.52278	0.4764
Water (Ord)	1.000	3.443	0.0222	3.4652	0.103	0.09687	0.04942	0.03403
Heavy Water	1.105	0.4519	0.044E-3	0.45194	0.092	0.09687	0.04942	0.03403
Wax	0.952	NA	0.02665	NA	0.109	0.09251	0.0471	0.03203
Concrete (Ba)	3.500	NA	0.01975	NA	0.096	0.3118	0.1439	0.1135
B_4C	2.52	NA	83.382	NA	0.093	014847	0.08534	0.0516
Al	2.699	0.08976	0.01386	0.10362	0.079	0.09687	0.0471	0.03203

Table A-2. Attenuation Factors

Thickness [X]	Fast neutrons	Gamma Rays at 2.0 MeV		
	exp[-Σ_rX]	exp[-μX]	B[μX]	B[μX] × exp[-μX]
4.0 cm Bismuth	0.3605	0.1626	1.692	0.2751
7.5 cm Bismuth	0.4774	0.03318	2.275	0.0758
9.0 cm Bismuth	0.4117	0.01679	2.543	0.0427
12.0 cm Bismuth	0.3063	0.00430	3.046	0.0131
Water Tank (60 cm)	0.00207	0.05924	4.808	0.2848
7" Ba-Concrete	0.1809	0.07742	1.596	0.1236
14" Ba-Concrete	0.0330	0.00599	2.354	0.0141
21" Ba-Concrete	0.00598	0.00046	2.413	0.00111
2" Lead	0.54911	0.07025	2.004	0.14078
4" Lead	0.30153	0.00493	3.010	0.01484
6" Lead	0.1653	0.00035	3.971	0.00139
30 cm Lead	0.0290	0.1544×10^{-6}	7.144	1.1031×10^{-6}
4" Wax	0.3304	0.61969	1.382	0.8562
6" Wax	0.18992	0.48782	1.586	0.7735
8" Wax	0.10917	0.38402	1.796	0.6897
10" Wax	0.06275	0.30230	2.008	0.6072
12" Wax	0.03607	0.23797	2.228	0.5303
86 cm Wax	81.64×10^{-6}	0.01712	4.953	0.0848

Table A-3: Radiation fluxes Equivalent to 10 μSv/hr [A2]

Thermal neutrons	260 n/cm^2-s	650
Fast neutrons (E > 1MeV)	7 n/cm^2-s	17.5
2.0 MeV γ -rays	339 γ/cm^2-s	847.5

A-1 Shutter Design Calculations

A beam port shutter is required to reduce the radiation emerging from the beam port mouth to an acceptable safe level that allows safe access to experimental equipment inside the cave while the beam tube is not in use.

Assumptions

Reactor thermal power is 5.0 MW.

Fast neutron shielding based on removal attenuation method.

Gamma rays energy is 2.0 MeV.

Lead and Water build up tables are used for bismuth and wax respectively.

No thermal neutron build up.

Back-scattered radiation is not accounted.

Precautions

The shutter will fall close in the event of power loss

The shutter is interlocked with the door.

Extra shielding Dimensions

Radiation Levels

Based on flux measurement experiment (Section 3.1):

The average thermal neutron fluxes at the source are 6×10^{12} n/cm^2-s (at 2.0 MW)

The average fast neutron flux constant, C_F, is 2.566×10^{11} n/cm^2-s (at 2.0 MW)

The neutron-to-gamma ratio at the source = 8.724×10^{4} n/cm^2- μSv (From BP2 Design [A6],) Thus, the radiation content (at 5 MW) at the source is:

Thermal neutrons: $\phi_o = 1.5 \times 10^{13}$ n/cm^2-s

Fast neutrons (E>1.0 MeV): $F_o = 2.566\times10^{11} \times \ln(8) \times 5.0/2.0 = 1.334\times10^{12}$ n/cm^2-s (assuming 1/E flux extended u to 8.0 MeV)

Gamma rays: $H_o = 1.5 \times 10^{13} / (8.724 \times 10^5) \times 3600 = 6.19\times10^{11}$ μSv/hr

In terms of dose rates;

Thermal neutrons: $\phi_o = 5.769\times10^{11}$ μSv/hr

Fast neutrons: $F_o = 1.906\times10^{12}$ μSv/hr

Gamma rays: $H_o = 6.190\times10^{11}$ μSv/hr

Design and Calculations

1- Shielding Calculations

The total distance between the source and the end of the collimator, L_s, is 436 cm (beam tube length 286 cm). Recalling the geometrical design of the beam tube collimator, the apparent source diameter for both fast neutrons and gamma ray will be;

$$D_{eff} = \frac{L_S}{L_S - L_o} \times D_{C1} = \frac{436}{436-90} \times 5.5 = 6.93 \text{ cm}$$

and hence the geometric factor at the end of the shutter (L_S = 436 cm) is;

$$G = \frac{\pi}{4\cos 30} D_{eff}^2 / 4\pi L_S^2 = 1.824\times10^{-5}$$

where

L_o is the distance between the source and collimator start

D_{c1} is the diameter at the collimator start (core side)

(D_{c1} equals to 5.5 cm, the maximum diameter of the convergent part)

By introducing the attenuation due to Bismuth filter (4.0 cm) and the geometrical attenuation (1.824×10^{-5}); the radiation doses at the end of the shutter are:

Thermal neutrons: $\phi_s = 3.794\times10^6$ μSv/hr

Fast neutrons: $F_s = 2.343\times10^7$ μSv/hr

Gamma rays: $H_s = 3.066\times10^6$ μSv/hr

Using 100.0 cm of paraffin wax + 30.0 cm of Lead + 10.0 cm of Boroflex sheets will reduce theses doses into;

Thermal neutrons: ϕ_s <<< μSv/hr

Fast neutrons: $F_s = 4.18$ μSv/hr

Gamma rays: $H_s = 0.21$ μSv/hr

Total = 4.4 μSv/hr

Note: A test was performed on Boroflex sheets, and experimental thermal neutron absorption cross-section greater than 10.0 cm^{-1} had been encountered.

2- Geometrical Calculations

With the converging part of the collimator, the beam diameters at the beginning and the end of the shutter are $D_1 = 9.87$ cm and $D_2 = 14.53$ cm.

A shutter inner-diameter of 23 cm will cover the beam at all locations along the shutter. Having larger diameter at the beginning, where the radiations are more intense, will help in attenuating the scattered radiations resulting in more efficient performance.

3- Shutter Weight:

The shutter weight is given by;

$$W = A \times \sum \rho_i \times x_i = \frac{\pi \times 23^2}{4} \times (0.952 \times 100 + 11.34 \times 30 + 1.81 \times 10)$$

$$= 0.188 \times 10^6 \text{ g} = 188 \text{ kg (approximately)}$$

Note: Shutter weight does not include the container and supporting mechanism weights.

A-2 Biological Shielding Design

Assumptions

Reactor thermal power is 5.0 MW.

Fast neutron shielding based on removal attenuation method.

Gamma rays energy is 2.0 MeV.

No flux attenuation within the test object.

Fast neutron scattering cross-section equals to removal cross-section.

Lead and Water build up tables are used for bismuth and wax respectively.

No thermal neutron build up.

Back-scattered radiation is not accounted.

Attenuation characteristics of Barytes concrete (3.5 g/cm^3) are used for current concrete mix (3.55 g/cm^3.)

Shielding Calculations

1- Cave Walls (Scattering):

The radiation content (at 5 MW) at the source, in terms of dose rates, is;

Fast neutrons: $F_o = 1.906\times10^{12}$ μSv/hr

Gamma rays: $H_o = 6.190\times10^{11}$ μSv/hr

The total distance between the source and the test object, L_{Test}, is 540 cm. Recalling the geometrical design of the beam tube collimator, the apparent source diameter for both fast neutrons and gamma ray will be;

$$D_{eff} = \frac{L_{Test}}{L_{Test} - L_o} \times D_{C1} = \frac{540}{540-90} \times 5.5 = 6.60 \text{ cm}$$

and hence the geometric factor is;

$$G = \frac{\pi}{4\cos 30} D_{eff}^2 / 4\pi L_{Test}^2 = 1.078\times10^{-5}$$

Introducing the attenuation due to Bi-filter (4.0 cm) and the geometrical attenuation (1.078×10^{-5}); the radiation doses to be scattered by the test object are:

Fast neutrons: $F_s = 1.384\times10^7$ μSv/hr

Gamma rays: $H_s = 1.812\times10^6$ μSv/hr

The differential neutron scattering cross section for fast neutrons assuming isotropic scattering in the CMS (Center-of-Mass System) is given by

for Hydrogen [A7]:

$$\sigma(\theta) = \frac{\sigma}{\pi} Cos(\theta), \qquad 0 \le \theta \le \frac{\pi}{2}$$

for Deuterium [A7]:

$$\sigma(\theta) = \frac{\sigma}{9\pi(1-\alpha)} \frac{[\cos(\theta) + \sqrt{4-\sin^2(\theta)}]^2}{\sqrt{4-\sin^2(\theta)}}, \quad 0 \le \theta \le \pi$$

where

$\alpha = (A-1)^2/(A+1)^2$

While the differential Compton scattering coefficient for gamma rays is given by [A8]:

$$\sigma(\theta) = [\frac{r_o^2}{1+a(1-\cos(\theta))}]^2 [\frac{1+\cos^2(\theta)}{2}][1+\frac{a^2(1-\cos(\theta))^2}{(1+\cos^2(\theta))(1+a(1-\cos(\theta))}],$$

$$0 \le \theta \le \pi$$

where

r_o is the classical electron radius

$a = E_{\gamma o}/m_e c^2$

Thus, the scattered radiation dose rate at any location is given by:

$$H_p = \Sigma V \phi_o \times \frac{\sigma(\theta) \times d\Omega(\theta)}{\sigma \times dA} = \Sigma V H_o \times \frac{\sigma(\theta)}{\sigma \times R^2},$$

where

Σ is scattering macroscopic cross section of the test object

V is the scattering object volume subject to radiation

H_o is radiation dose at scattering object location

$d\Omega(\theta)$ differential solid angle around scattering direction

dA is differential element of area around shielding location

R is distance from scattering object to shielding location

θ is angle between scattering direction and beam direction

The scattering object is taken to be a 5.0 cm diameter pipe with 18.0 cm length (Beam diameter at object location.)

Back wall: The largest radiation scattering doses in μSv/hr are; 3013.7 and 181.5 for fast neutrons and gamma rays respectively. Using Table A-2; a 14" concrete wall plus 8" wax wall will reduce the total dose rate to:

$3013.7 \times 0.0195 \times 0.0775 + 181.5 \times 0.0141 \times 0.6897 = 6.32$ μSv/hr

(BP2/BP3) Side Wall: The largest radiation scattering doses in mrem/hr are; 414.2 and 26.8 for fast neutrons and gamma rays respectively. Using Table A-2; a 14" concrete wall will reduce the total dose rate to:

$414.2 \times 0.0195 + 26.8 \times 0.0141 = 8.45$ μSv/hr

Table A-4. Dose rates (μSv/hr) due to radiation scattering from 5.0 cm diameter test tube, at various locations.

i- Right hand side

Location			Fast Neutrons				Gamma Rays	
			Light Water		Heavy Water		E_o = 2.0 MeV	
θ	R	Wall	H_p	E`/E_o	H_p	E`/E_o	H_p	E`/E_o
15	176	Back	4676.5	0.933	2411.5	0.966	411.0	0.882
30	196	Back	3013.7	0.75	1709.3	0.873	181.5	0.656
45	240	Back	1269.7	0.5	912.2	0.738	66.8	0.466
60	302	BP2	283.5	0.25	414.2	0.589	26.8	0.338
75	271	BP2	--	0.067	334.6	0.449	24.2	0.256
90	262	BP2	--	0.0	205.9	0.333	20.9	0.204

ii- Left hand side

Location			Fast Neutrons				Gamma Rays	
			Light Water		Heavy Water		E_o = 2.0 MeV	
θ	R	Wall	H_p	E`/E_o	H_p	E`/E_o	H_p	E`/E_o
15	176	Back	4676.5	0.933	2411.5	0.966	411.0	0.882
30	196	Back	3013.7	0.75	1709.3	0.873	181.5	0.656
45	226	Door	1431.8	0.5	1028.7	0.738	75.3	0.466
60	185	Door	755.4	0.25	1109.7	0.589	71.3	0.338
75	166	Door	--	0.067	891.7	0.449	66.1	0.256
90	160	Door	--	0.0	552.1	0.333	56.0	0.204

iii- Vertical

Location			Fast Neutrons				Gamma Rays	
			Light Water		Heavy Water		E_o = 2.0 MeV	
θ	R	Wall	H_p	E`/E_o	H_p	E`/E_o	H_p	E`/E_o
15	176	Back	4676.5	0.933	2411.5	0.966	411.0	0.882
30	196	Back	3013.7	0.75	1709.3	0.873	181.5	0.656
45	207	Ceil	1706.8	0.5	1226.2	0.738	89.8	0.466
60	170	Ceil	894.6	0.25	1314.2	0.589	84.4	0.338
75	152	Ceil	--	0.067	1057.9	0.449	76.4	0.256
90	147	Ceil	--	0.0	650.5	0.333	66.0	0.204

Ceiling: The largest radiation scattering doses in μSv/hr are; 1706.8 and 89.8 for fast neutrons and gamma rays respectively. Using Table A-2; a 7" concrete plus 12" wax will reduce the total dose rate to

$1706.8 \times 0.1389 \times 0.0216 + 89.8 \times 0.1236 \times 0.5303 = 1.1$ μSv/hr

Door: The largest radiation scattering doses in μSv/hr are; 1431.8 and 75.3 for fast neutrons and gamma rays respectively. Using Table A-2; a 2" lead plus 14" wax will reduce the total dose rate to

$1431.8 \times 0.3326 \times 0.0042 + 75.3 \times 0.1408 \times 0.4601 = 6.88$ μSv/hr

2- Beam Catcher

The total distance between the source and the end of the cave back wall, L_{Back}, is 710 cm, and hence

$$D_{eff} = \frac{L_{Back}}{L_{Back} - L_o} \times D_{C1} = \frac{710}{710-90} \times 5.5 = 6.3 \text{ cm}$$

$$G = \frac{\pi}{4\cos 30} D_{eff}^2 / 4\pi L_{Back}^2 = 0.568 \times 10^{-5}$$

And the radiation doses to be shielded by the beam catcher (with Bi-Filter) are:

Fast neutrons: $F_s = 0.73 \times 10^7$ μSv/hr

Gamma rays: $H_s = 0.955 \times 10^6$ μSv/hr

The 14" concrete plus 8" wax back wall is enough to suppress the dose from scattered radiation, but the direct beam radiation will require extra shielding. In order to increase the cave workable space; an 18" movable wax wall, outside the concrete cave, in the beam catcher as a semi-permanent shield, i.e., it can be moved when necessary. Inside the cave 6" lead plus 6" wax will also used for beam catcher. The beam catcher will cover radiation scattered by the test object within 15^{o} around the beam centre-line. Using Table A-2, the total dose will be:

$$0.73\times10^{7} \times 0.033 \times 0.00685 \times 0.02073 \times 0.1653 + 0.955\times10^{6} \times 0.0141 \times 0.3391 \times 0.4601 \times 0.00139 = 8.58\ \mu Sv/hr$$

Thermal Neutrons:

Thermal neutrons are not considered in shielding wall calculations since:

1- Thermal neutron cross-sections are much larger than fast neutron cross-sections,

2- A thermal neutron flux of 260 n/cm^2-s is to produce the same dose effect (10 μSv/hr) that is produced by a fast neutron flux of 7 n/cm^2-s.

In order to account for thermal neutron diffusion, shielding walls are to be covered with a layer of borated rubber sheets.

A-3 Civil Calculations

The design mix used to produce concrete blocks is as follows:

Cement - Portland type 30	363 kg/m^3
Course Aggregate - High Density BRMT	1780 kg/m^3
Fine Aggregate - High Density BSPI	1335 kg/m^3
Water	166 kg/m^3

This mix provides a density of 3,550 kg/m^3 and a compressive strength of 34.0 MPa.

Concrete blocks are loaded with reinforcing steel bars to increase the fracture strength so that structural integrity during transportation and after installation is ensured. Two layers of re-enforcing steel bars loading are used.

Assumptions:

Density = 3,550 kg/m^3

External Load = 1,000 kg

Un-cracked Concrete

Un-factored Loads

Equations:

For Axial Stress:

$$\sigma_{Axial} = \frac{P}{A}$$

where;

P = The Total load

A = Cross-sectional Area

For Fracture Stress:

$$\sigma_{Fracture} = \frac{My}{I}$$

where;

The Moment, $M = \frac{wl^2}{8}$,

$$w = \rho ht + \frac{P_{External}}{l},$$

$$I = \frac{ht^3}{12}, \ y = \frac{t}{2}$$

where; l is the length, h is the width and t is the depth

For Reinforcement Area:

$$A_s = \frac{F}{\sigma_y}$$

$$F = \frac{M}{\Delta y}$$

where

F the Force

Δy the section depth

A_s Minimum required steel area

σ_y Steel yield strength

Calculations:

a- Axial Stress (Block W3)

P = 1/2 (Roof weight (R3) + Wax weight + External Load)

P = 0.5 x (3550x2.591x0.1778x1.42+950x2.591x0.305x1.42+1000)

P = 2194.2 kg

$$\sigma_{Axial} = \frac{P}{A} = \frac{2194.2}{1.295 \times 0.1778}$$ = 9,530 kg/m^2 = 0.0953 MPa = 13.8 psi

b- Fracture Strength (Block R3)

$$w = \rho h t + \frac{P_{Wax} + P_{External}}{l} = 3550 \times 1.42 \times 0.1778 + \frac{950 \times 1.42 \times 0.305 \times 2.591 + 1000}{2.591}$$

= 1693.7 kg/m

$$I = \frac{ht^3}{12} = \frac{1.42 \times 0.1778^3}{12} = 0.000665 \text{ m}^4$$

$$M = \frac{wl^2}{8} = \frac{1693.7 \times 2.591^2}{8} = 1421.3 \text{ kg/m}^2$$

$$\sigma_{Fracture} = \frac{My}{I} = \frac{14213 \times 0.1778/2}{0.000665}$$ =1.9x10^5 kg/m^2 = 1.9 MPa = 275.6 psi

c- Re-enforcement

i- Ceiling Blocks (R3)

$$F = \frac{M}{\Delta y} = \frac{1421.3}{0.13}$$ = 1.093x10^4 kg = 0.11x10^6 N

$$A_s = \frac{F}{\sigma_y} = \frac{0.11 \times 10^6}{400 \times 10^6}$$ = 0.000275 m^2 (for 1.42 m width)

Minimum Area Required; 1.94 cm^2 / meter width

ii- Vertical Walls (W3)

$w = \rho h t = 3550 \times 1.829 \times 0.3556$ =2308.9 kg/m

$$M = \frac{wl^2}{8} = \frac{2308.9 \times 2.337^2}{8} = 1576.3 \text{ kg/m}^2$$

$$F = \frac{M}{\Delta y} = \frac{1576.3}{0.3} = 5.254\text{x}10^3 \text{ kg} = 0.0526\text{x}10^6 \text{ N}$$

$$A_s = \frac{F}{\sigma_y} = \frac{0.0526 \times 10^6}{400 \times 10^6} = 0.000132 \text{ m}^2 \text{ (for 1.829 m width)}$$

Minimum Area Required; 0.72 cm^2 / meter width

Table A-5 gives the details of the reinforcement steel bars in each block parallel to length and parallel to width. The mat clearance (concrete cover) is 2.54 cm (1.0 inch) from top and bottom. The rods are 15 mm in diameter, and the yield strength in 400 MPa.

Concrete Blocks Specifications

Table A-6 gives the volume and weight of each concrete block, none is over 6.0 Ton in weight to provide safe and easy transportation and handling.

Table A-5

	Number of Reinforcement bars (15 mm ϕ, Grade 400w)			
	Top Mat		Bottom Mat	
Block	Length	Width	Length	Width
R1	79" at 4" cc	11" at 8" cc	79" at 4" cc	11" at 8" cc
R2	99" at 4" cc	60" at 5" cc	99" at 4" cc	53" at 5" cc
R3	99" at 4" cc	53" at 5" cc	99" at 4" cc	53" at 5" cc
R4	99" at 4" cc	37" at 10" cc	99" at 4" cc	30" at 10" cc
W1	96" at 8" cc	46" at 9" cc	89" at 8" cc	36" at 9" cc
W2	96" at 9" cc	51" at 9" cc	89" at 9" cc	51" at 9" cc
W3	96" at 9" cc	69" at 9" cc	89" at 9" cc	48" at 9" cc
W4	89" at 9" cc	31" at 9" cc	89" at 9" cc	26" at 9" cc
W5	89" at 7" cc	23" at 9" cc	89" at 7" cc	16" at 9" cc

Table A-6

Block	**Volume**		**Weight (Ton)**
	in^3	m^3	
W1	61,355	1.005	3.567
W2	72,198	1.183	4.200
W3	82,740	1.356	4.813
W4	41,538	0.681	2.416
W5	42,044	0.689	2.446
R1	7,840	0.128	0.456
R2	38,136	0.625	2.219
R3	39,984	0.655	2.326
R4	23,485	0.385	1.366
Total Concrete Weight			**23.809 Ton**

References

A1- McMaster Nuclear Reactor Radioactive Safety Program, Document No. HP-9000, McMaster University, Hamilton, Canada, December 2001.

A2- John. R. Lamarsh, "Introduction to Nuclear Engineering", 2nd Ed., Addison-Wesley Publishing Company, 1983.

A3- S.F. Mughabghab, M. Divadeenam and N.E. Holden, "Neutron Cross Sections", Vol. 1 and 2, Academic Press, 1981.

A4- E. P. Blizard and L. S. Abbott, Ed's., "Reactor Handbook, Vol III Part B Shielding", 2nd Ed., Interscince Publishers, 1962.

A5- Table of X-Ray Mass Attenuation Coefficients, NIST, Gaitherburg, April 1997 <http://physics.nist.gov/PhysRefData/XrayMassCoef/cover.html>

A6- D.R. Wyman, Neutron Transport in Radiography", Ph.D. Thesis, McMaster University, Hamilton, Canada, 1984.

A7- John. R. Lamarsh, "Introduction to Nuclear Reactor Theory", Addison-Wesley Publishing Company, 1966.

A8- G. F. Knoll, "Radiation Detection and Measurement", 2nd Ed., John Wiely & Sons, 1989.

Appendix B: MCNP Input

```
Beam Port 3 MCNP Simulation for HSNR Design
C Cell Cards
1 0 -2 5 -11 IMP:N=1 $ Beam tube - Before Filter
2 1 -9.81 -2 11 -12 IMP:N=1 $ Beam tube - Filter
3 0 -2 12 -13 IMP:N=1 $ Beam tube - After Filter
4 0 13 -14 -18 IMP:N=1 $ Beam tube - Conv. Coll. Hole
5 0 15 -16 -19 IMP:N=1 $ Beam tube - Div. Coll. Hole
6 7 -2.5 -2 13 -22 18 IMP:N=1 $ Beam tube - Boral Disk #1
7 2 -11.3 -2 22 -23 18 IMP:N=1 $ Beam tube - Part#1 - Lead
8 7 -2.5 -2 23 -24 18 IMP:N=1 $ Beam tube - Boral Disk #2
9 7 -2.5 -2 24 -25 18 IMP:N=1 $ Beam tube - Boral Disks #3,4,5
10 2 -11.3 -2 25 -14 18 IMP:N=1 $ Beam tube - Part#2 - Lead
11 7 -2.5 -2 15 -26 19 IMP:N=1 $ Beam tube - Boral Disk #6
12 2 -11.3 -2 26 -27 19 IMP:N=1 $ Beam tube - Part#3 - Lead
13 7 -2.5 -2 27 -28 19 IMP:N=1 $ Beam tube - Boral Disk #7
14 2 -11.3 -2 28 -29 19 IMP:N=1 $ Beam tube - Part#4 - Lead
15 7 -2.5 -2 29 -30 19 IMP:N=1 $ Beam tube - Boral Disk #8
16 2 -11.3 -2 30 -31 19 IMP:N=1 $ Beam tube - Part#5 - Lead
17 7 -2.5 -2 31 -32 19 IMP:N=1 $ Beam tube - Boral Disk #9
18 2 -11.3 -2 32 -33 19 IMP:N=1 $ Beam tube - Part#1 - Lead
19 7 -2.5 -2 33 -16 19 IMP:N=1 $ Beam tube - Boral Disk #10
20 4 -0.95 -3 16 -17 20 IMP:N=1 $ Beam tube - Wax Shield
21 0 16 -17 -20 IMP:N=1 $ Beam tube - Wax Shield Hole
22 0 -8 17 -3 IMP:N=1 $ BT - Gap btwn Wax and Lead Shields
23 2 -11.3 -4 8 -9 20 IMP:N=1 $ Beam tube - Lead Shield
24 0 8 -9 -20 IMP:N=1 $ Beam tube - Lead Shield Hole
26 0 -2 14 -15 20 IMP:N=1 $ Gap around Gd Aperture
27 3 -7.95 -20 14 -15 21 IMP:N=1 $ Gadolinium Aperture
28 0 -21 14 -15 IMP:N=1 $ Gadolinium Aperture Hole
29 0 7 -16 2 -3 IMP:N=1 $ Gap at Colli-Wax shield interface
30 5 -1.0 -1 5 -6 2 IMP:N=1 $ Water around Beam Tube
31 6 -3.35 -1 6 -7 2 IMP:N=1 $ Concrete around 6" Tube
32 6 -3.35 -1 7 -8 3 IMP:N=1 $ Concrete around 8" Tube
33 6 -3.35 -1 8 -9 4 IMP:N=1 $ Concrete around 12" Tube
40 0 9 -40 51 -52 58 -59 IMP:N=1 $ Clearance Gap before Shutter
41 8 -3.379 40 -41 -44 IMP:N=1 $ Shutter
42 0 40 -41 51 -52 58 -59 44 IMP:N=1 $ Around shutter
43 0 41 -42 51 -52 58 -59 IMP:N=1 $ Clearance Gap after Shutter
51 6 -3.35 9 -42 50 -51 58 -59 IMP:N=1 $ Right Concrete Wall -Old Cave
52 6 -3.35 9 -42 52 -53 58 -59 IMP:N=1 $ Left Concrete Wall -Old Cave
53 6 -3.35 9 -42 50 -53 59 -60 IMP:N=1 $ Roof
54 0 42 -43 54 -55 56 -57 IMP:N=1 $ Openeing in the Concrete Brick Wall
55 6 -3.35 42 -43 54 -55 58 -56 IMP:N=1 $ Brick Wall - Below Opening
56 6 -3.35 42 -43 54 -55 57 -60 IMP:N=1 $ Brick Wall - Above Opening
57 6 -3.35 42 -43 50 -54 58 -60 IMP:N=1 $ Concrete Brick Wall - Right
58 6 -3.35 42 -43 55 -53 58 -60 IMP:N=1 $ Concrete Brick Wall - Left
61 0 9 -43 -50 58 -1 IMP:N=1 $ Old Cave - Right side Gap
62 0 9 -43 53 58 -1 IMP:N=1 $ Old Cave - Left side Gap
63 0 9 -43 50 -53 60 -1 IMP:N=1 $ Old Cave - Gap above
65 0 43 -10 58 -1 IMP:N=1 $ Cave after shutter to image plane
```

```
66 0 900 -61 58 -1 IMP:N=1 $ Cave After Image Plane
67  6 -3.35 9 -999 -58 -1 IMP:N=1 $ Ground
71 7 -2.5 61 -62 -71 72 -73 74 IMP:N=1 $ First Boroflex
72 4 -0.95 62 -63  -71 72 -73 74 IMP:N=1 $ 6" Wax
73 7 -2.5 63 -64  -71 72 -73 74 IMP:N=1 $ Second Boroflex
74 2 -11.3 64 -65  -71 72 -73 74 IMP:N=1 $ 6" Lead
75 4 -0.95 65 -66 58 -1 IMP:N=1 $ 8" Wax Wall
76 6 -3.35 66 -67 58 -1 IMP:N=1 $ 14" Concrete Backwall
77 4 -0.95 67 -68 -75 76 -79 58 IMP:N=1 $ Movable shield - A
78 4 -0.95 68 -69 -77 78 -79 58 IMP:N=1 $ Movable shield - B
79 0 61 -65 71 58 -1 IMP:N=1 $ Right
80 0 61 -65 -72 58 -1 IMP:N=1 $ Left
81 0 61 -65 -71 72 73 -1 IMP:N=1 $ Above
82 0 61 -65 -71 72 -74 58 IMP:N=1 $ Below
83 0 67 -68 75 58 -1 IMP:N=1 $ Gap Right to Movable shield - A
84 0 67 -68 -76 58 -1 IMP:N=1 $ Gap Left to Movable shield - A
85 0 67 -68 -75 76 79 -1 IMP:N=1 $ Gap Above Movable shield - A
86 0 68 -69 77 58 -1 IMP:N=1 $ Gap Right to Movable shield - B
87 0 68 -69 -78 58 -1 IMP:N=1 $ Gap Left to Movable shield - B
88 0 68 -69 -77 78 79 -1 IMP:N=1 $ Gap Above Movable shield - B
C Tally Cells - at Imaging Plane
901 0 10 -900 -21 IMP:N=1 $ Tally Cell #1
902 0 10 -900 21 -901 IMP:N=1 $ Tally Cell #2
903 0 10 -900 901 -902 IMP:N=1 $ Tally Cell #3
904 0 10 -900 902 -903 IMP:N=1 $ Tally Cell #4
905 0 10 -900 903 -904 IMP:N=1 $ Tally Cell #5
906 0 10 -900 904 -905 IMP:N=1 $ Tally Cell #6
907 0 10 -900 905 58 -1  IMP:N=1 $ Outside Tally Cells
C Tally Cells - After Backwall
911 0 69 -999 -901 IMP:N=1 $ Tally Cell #7
912 0 69 -999 901 -902 IMP:N=1 $ Tally Cell #8
913 0 69 -999 902 -903 IMP:N=1 $ Tally Cell #9
914 0 69 -999 903 -904 IMP:N=1 $ Tally Cell #10
915 0 69 -999 904 -905 IMP:N=1 $ Tally Cell #11
916 0 69 -999 905 -906 IMP:N=1 $ Tally Cell #12
917 0 69 -999 906 58 -1  IMP:N=1 $ Outside Tally Cells
999 0 1:-5:999 IMP:N=0 $ Outside Problem World

C Surface Cards
1 KZ -100 0.16 $ World Edge Cone
2 CZ 8.35 $ 6 inches tube
3 CZ 10.25 $ 8 inches tube
4 CZ 16.2 $ 12 inches tube
5 P 1 0 1.732 0 $ Beam Tube Core-face
6 PZ 109.1 $ Pool Water/Concrete Interface
7 PZ 175.8 $ 6"/8" interface
8 PZ 261.5 $ 8"/12" interface
9 PZ 290.1 $ Beam Tube Cave-face
10 PZ 600 $ Image Plane
11 PZ 81 $ Filter Core-side Plane
12 PZ 85 $ Filter Cave-side Plane
13 PZ 90 $ Conv. Collimator Core-side Plane
14 PZ 120 $ Conv. Collimator Cave-side Plane
15 PZ 120.05 $ Div. Collimator Core-side Plane
```

```
16 PZ 180.05 $ Div. Collimator Cave-side Plane
17 PZ 256.25 $ Wax shield Cave-side Plane
18 KZ 200 0.000625 $ Collimator Convergent Cone
19 KZ 0.05 0.00027778 $ Collimator Divergent Cone
20 CZ 5.08 $ Wax Shield Hollow Cylinder
21 CZ 2.0 $ Aperture opening / Tally Ring #1
22 PZ 90.3 $ Boral disk #1 - Right face
23 PZ 104.7 $ Boral disk #2 - Left face
24 PZ 105 $ Boral disk #2 - Right face
25 PZ 105.9 $ Boral disks #3,4,5 - Right face
26 PZ 120.35 $ Boral disk #6 - Right face
27 PZ 135.05 $ Boral disk #7 - Left face
28 PZ 135.35 $ Boral disk #7 - Right face
29 PZ 150.05 $ Boral disk #8 - Left face
30 PZ 150.35 $ Boral disk #8 - Right face
31 PZ 165.05 $ Boral disk #9 - Left face
32 PZ 165.35 $ Boral disk #9 - Right face
33 PZ 179.75 $ Boral disk #10 - Left face
40 PZ 292.1 $ Shutter Left Face
41 PZ 436.1 $ Shutter Right Face
42 PZ 438.1 $ Brick wall Core Side Face
43 PZ 497.1 $ Brick wall Cave Side Face
44 C/Z 9.97 28.26 11.5 $ Shutter Cylinder - Open Position
50 PX -101.6 $ Old Cave Outer Edge - Right
51 PX -55.88 $ Old Cave Inner Edge - Right
52 PX 55.88 $ Old Cave Inner Edge - Left
53 PX 101.6 $ Old Cave Outer Edge - Left
54 PX -10.16 $ Brick Wall Opening - Right Face
55 PX 10.16 $ Brick Wall Opening - Left Face
56 PY -10.16 $ Brick Wall Opening - Bottom face
57 PY 10.16 $ Brick Wall Opening - Top Face
58 PY -100.0 $ Ground
59 PY 62.56 $ Roof Bottom
60 PY 115.9 $ Roof Top
61 PZ 622.37 $ Boroflex - Cave face
62 PZ 623.01 $ Boroflex - Wax interface
63 PZ 638.25 $ Wax - Boroflex interface
64 PZ 638.88 $ Boroflex - Lead interface
65 PZ 654.12 $ Lead - Wax interface
66 PZ 674.44 $ Wax - Concrete interface
67 PZ 710.00 $ Concrete - outer face
68 PZ 735.40 $ Movable shield middle plane
69 PZ 755.72 $ Movable shield outer face
71 PX 38.10  $
72 PX -38.10 $
73 PY 38.10  $
74 PY -38.10 $
75 PX 48.26  $
76 PX -48.26 $
77 PX 25.40  $
78 PX -25.40 $
79 PY 60.00  $
900 PZ 602 $ Image Plane - Tally End Plane
901 CZ 5.0 $ Tally Ring #2
```

```
902 CZ 10.0 $ Tally Ring #3
903 CZ 20.0 $ Tally Ring #4
904 CZ 30.0 $ Tally Ring #5
905 CZ 40.0 $ Tally Ring #6
906 CZ 60.0 $ Tally Ring #7
999 PZ 760.0 $ Back Wall - Tally End Plane

C
SDEF ERG D1  DIR D2  SUR 5 POS 0 0 0  RAD D3
C USE This Distribution for Thermal Neutrons E < 0.2 eV
C ***************************************************
SC1 Maxwellian at 0.026 ev (hardening effect) up to 0.2 ev (1/E Tail)
SI1 H 0 0.0000002
SP1 -5 0.000000026
C
C USE This Distribution for Epi-Thermal Neutrons 0.2 eV <E< 1.0 MeV
C **************************************************************
C SC1 1/E Slowing down flux starting at 0.2 eV up to 1.0 MeV
C SI1 H 2.0000E-7 3.0014E-7 4.5041E-7 6.7592E-7 1.0143E-6 1.5222E-6
C       2.2843E-6 3.4281E-6 5.1444E-6 7.7201E-6 1.1585E-5 1.7386E-5
C       2.6091E-5 3.9154E-5 5.8758E-5 8.8176E-5 1.3232E-4 1.9858E-4
C       2.9800E-4 4.4720E-4 6.7111E-4 1.0071E-3 1.5114E-3 2.2681E-3
C       3.4037E-3 5.1078E-3 7.6652E-3 1.1503E-2 1.7262E-2 2.5905E-2
C       3.8875E-2 5.8339E-2 8.7549E-2 1.3138E-1 1.9716E-1 2.9588E-1
C       4.4402E-1 6.6633E-1 1.0000000
C SP1   0.0 1.0 1.0 1.0 1.0 1.0 1.0 1.0 1.0 1.0 1.0 1.0 1.0
C       1.0 1.0 1.0 1.0 1.0 1.0 1.0 1.0 1.0 1.0 1.0 1.0 1.0
C       1.0 1.0 1.0 1.0 1.0 1.0 1.0 1.0 1.0 1.0 1.0 1.0 1.0
C
C USE This Distribution for Fast Neutrons 1.0 MeV < E < 8.0 MeV
C **********************************************************
C SC1 1/E Slowing down flux starting at 1.0 MeV up to 8.0 MeV
C SI1 H 1.0000 1.1000 1.2100 1.3310 1.4641 1.6105 1.7716 1.9487 2.1434
C       2.3579 2.5937 2.8531 3.1384 3.4523 3.7975 4.1772 4.5950 5.0545
C       5.5600 6.1160 6.7275 7.4002 8.0000
C SP1   0.0 1.0 1.0 1.0 1.0 1.0 1.0 1.0 1.0 1.0 1.0 1.0
C       1.0 1.0 1.0 1.0 1.0 1.0 1.0 1.0 1.0 1.0 0.8177
SC2 Isotropic angular distribution (Backward ones are not considered)
SI2 H 0 1
SP2 -31 0
SC3 Uniform area sampling - number of neutrons linear with radius
SI3 H 0 15
SP3 -21 1
C
C Material Cards
M1 83209.60c 1 $ Bismuth
M2 82000.35c 1 $ Lead
M3 64000.35c 1 $ Gadolinium
M4 1001.60c 0.674 6000.60c 0.326 $ Wax
M5 1001.60c 0.6667 8016.60c 0.3333 $ Water
M6 1001.60c -0.003585 8016.60c -0.311622 12000.60c -0.001195 13027.60c
     -0.004183 14000.60c -0.010457 16000.60c -0.107858 20000.60c
     -0.050194 26000.35c -0.047505 56138.60c -0.4634 $ Barytes Concrete
M7 5010.60c 0.16 5011.60c 0.64 6000.60c 0.2 $ Boron Carbide
```

```
M8 1001.60c -0.02886 5010.60c -0.00896 5011.60c -0.03940 6000.60c
     -0.17978 82000.35c -0.74300 $ Shutter (Lead Wax and Boron Carbide)
C
C Energy Card
PHYS:N 8.0 0.001
C
C Tally Definition
FC4 average flux of cells at imaging plane and after back wall
F4:N 901 902 903 904 905 906 911 912 913 914 915 916
E4: 2E-7 5E-7 0.01 1.0 8.0
C Uncomment the following lines to obtain dose tallies
C Fluence to Dose Equiv. conversion in [uSvcm^2] from ICRP 74
C DE4  1.0e-9 1.0e-8 2.53e-8 1.0e-7 2.0e-7 5.0e-7 1.0e-6 2.0e-6 5.0e-6
C      1.0e-5 2.0e-5 5.0e-5 1.0e-4 2.0e-4 5.0e-4 1.0e-3 2.0e-3 5.0e-3
C      0.01 0.02 0.03 0.05 0.07 0.1 0.15 0.2 0.3 0.5 0.7 0.9 1.
C      1.2 2. 3. 4. 5. 6. 7. 8. 9. 10. 12. 14. 15. 16. 18. 20.
C DF4  6.6e-6 9.0e-6 1.06e-5 1.29e-5 1.35e-5 1.36e-5 1.33e-5 1.29e-5
C      1.2e-5 1.13e-5 1.06e-5 9.9e-6 9.4e-6 8.9e-6 8.3e-6 7.9e-6 7.7e-6
C      8.0e-6 1.05e-5 1.66e-5 2.37e-5 4.11e-5 6.0e-5 8.8e-5 1.32e-4
C      1.7e-4 2.33e-4 3.22e-4 3.75e-4 4.0e-4 4.16e-4 4.25e-4 4.2e-4
C      4.12e-4 4.08e-4 4.05e-4 4.0e-4 4.05e-4 4.09e-4 4.2e-4 4.4e-4
C      4.8e-4 5.2e-4 5.4e-4 5.55e-4 5.7e-4 6.0e-4
C
CUT:N
NPS 5E8
PRINT 10 30
PRDMP 2E7 2E7 -1 1
```

Appendix C: Radiation Dose Surveys

C-1 Closed Shutter Radiation Dose Surveys

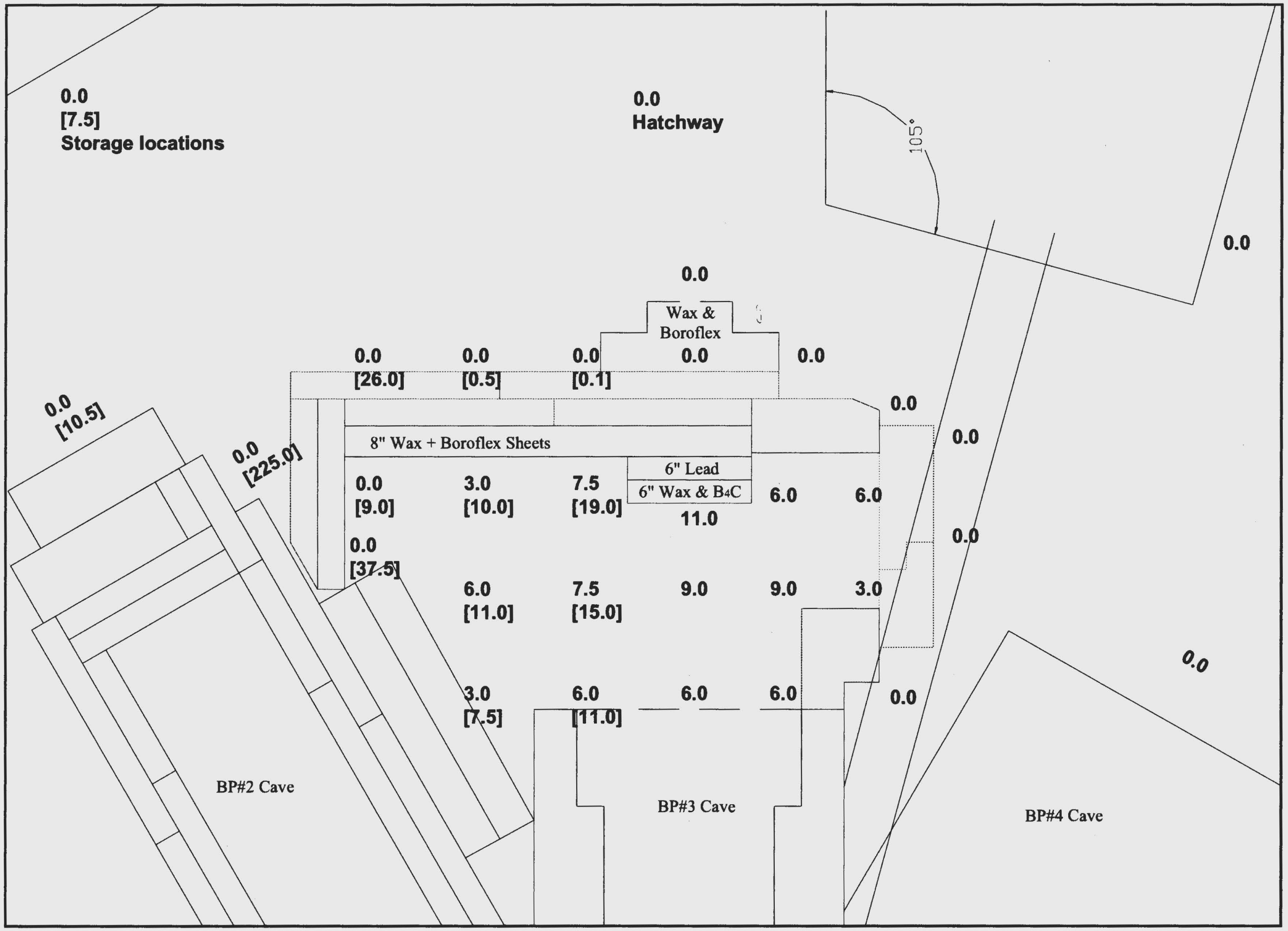

Figure C.1. Closed Shutter Survey – Neutron dose rate (μSv/hr) at 0.25 m from ground level. Scaled to 3.0 MW reactor power.

[Values in square brackets are measured with BP#2 shutter open].

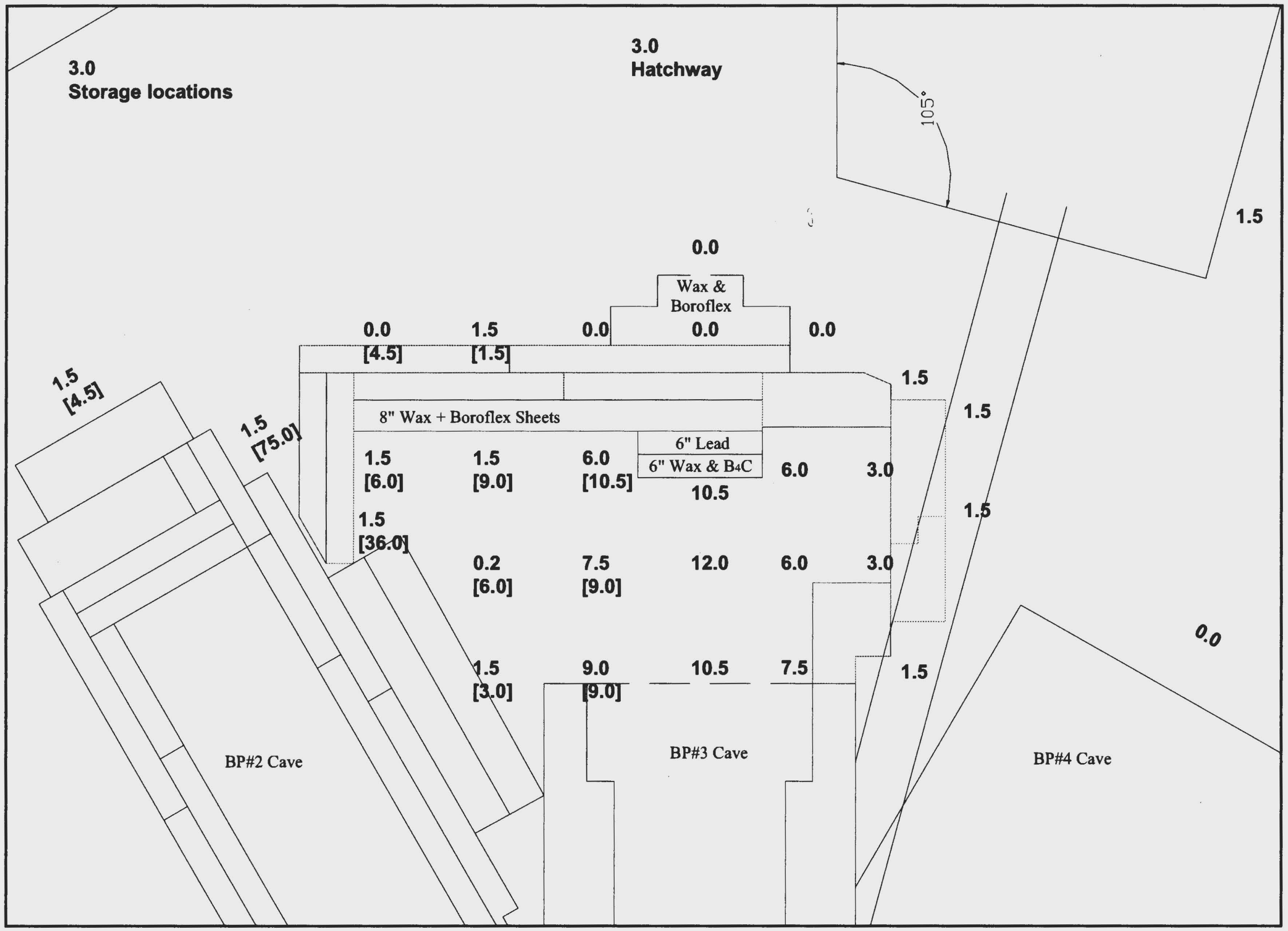

Figure C.2. Closed Shutter Survey – Gamma dose rate (μSv/hr) at 0.25 m from ground level. Scaled to 3.0 MW reactor power.

[Values in square brackets are measured with BP#2 shutter open].

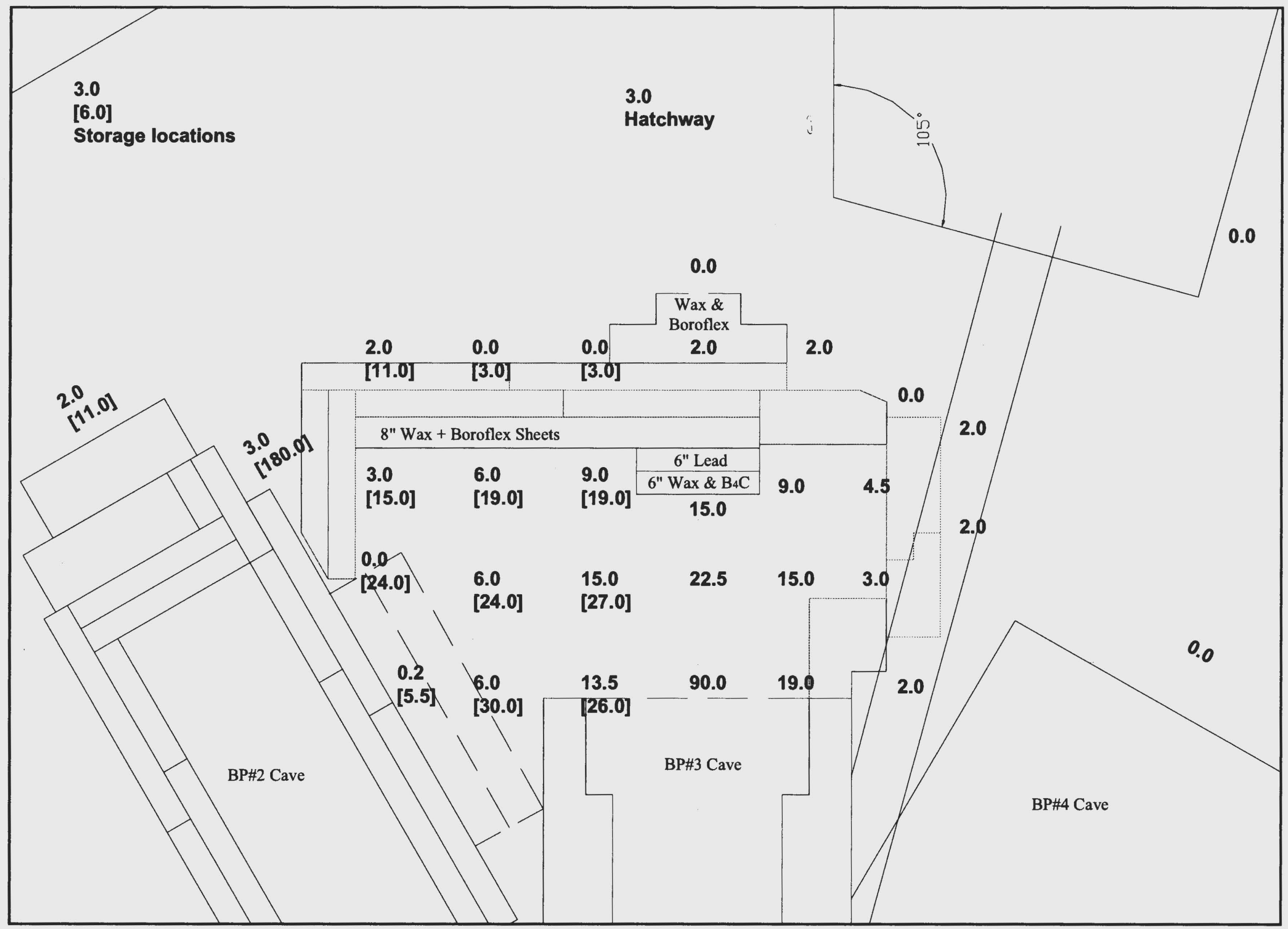

Figure C.3. Closed Shutter Survey – Neutron dose rate (μSv/hr) at 2.0 m from ground level. Scaled to 3.0 MW reactor power.

[Values in square brackets are measured with BP#2 shutter open].

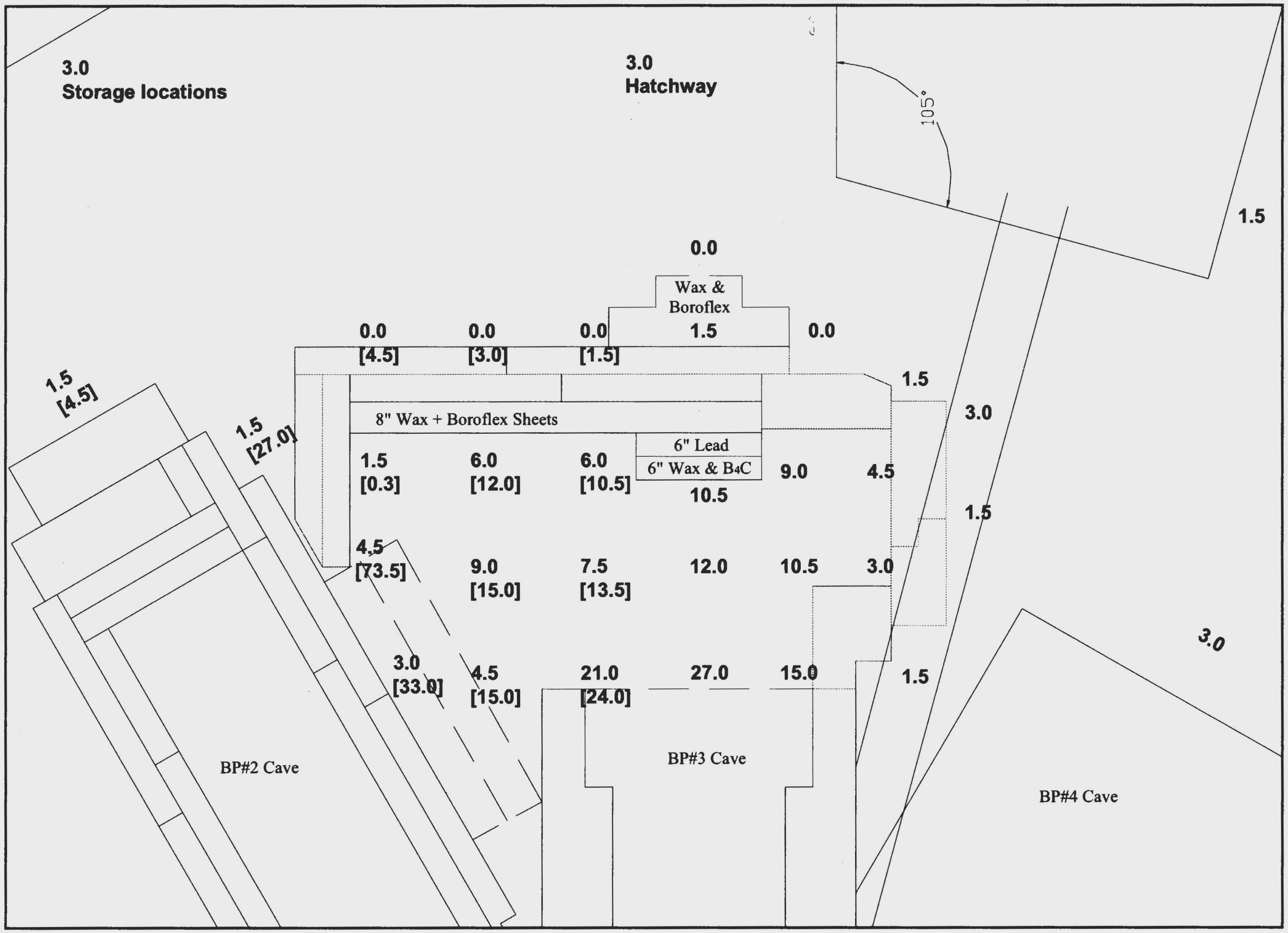

Figure C.4. Closed Shutter Survey – Gamma dose rate (μSv/hr) at 2.0 m from ground level. Scaled to 3.0 MW reactor power.

[Values in square brackets are measured with BP#2 shutter open].

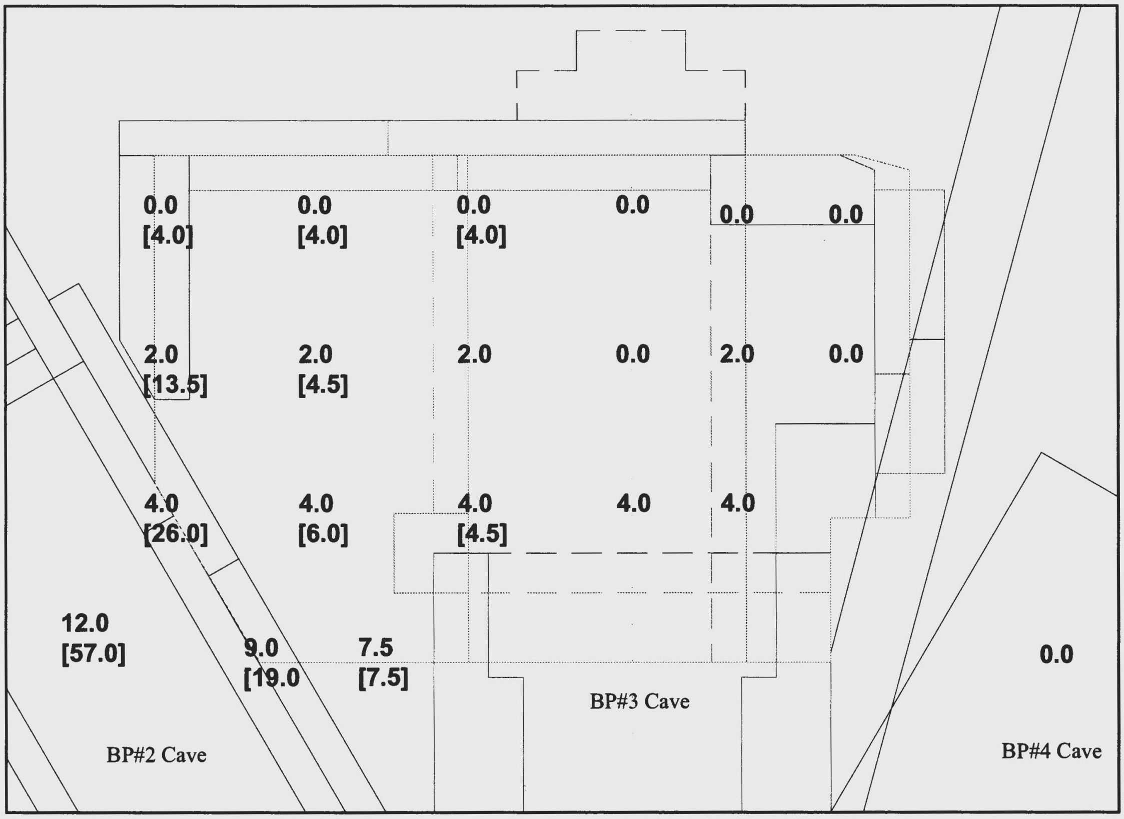

Figure C.5. Closed Shutter Survey – Neutron dose rate (μSv/hr) above Cave Ceiling.

Scaled to 3.0 MW reactor power.

[Values in square brackets are measured with BP#2 shutter open].

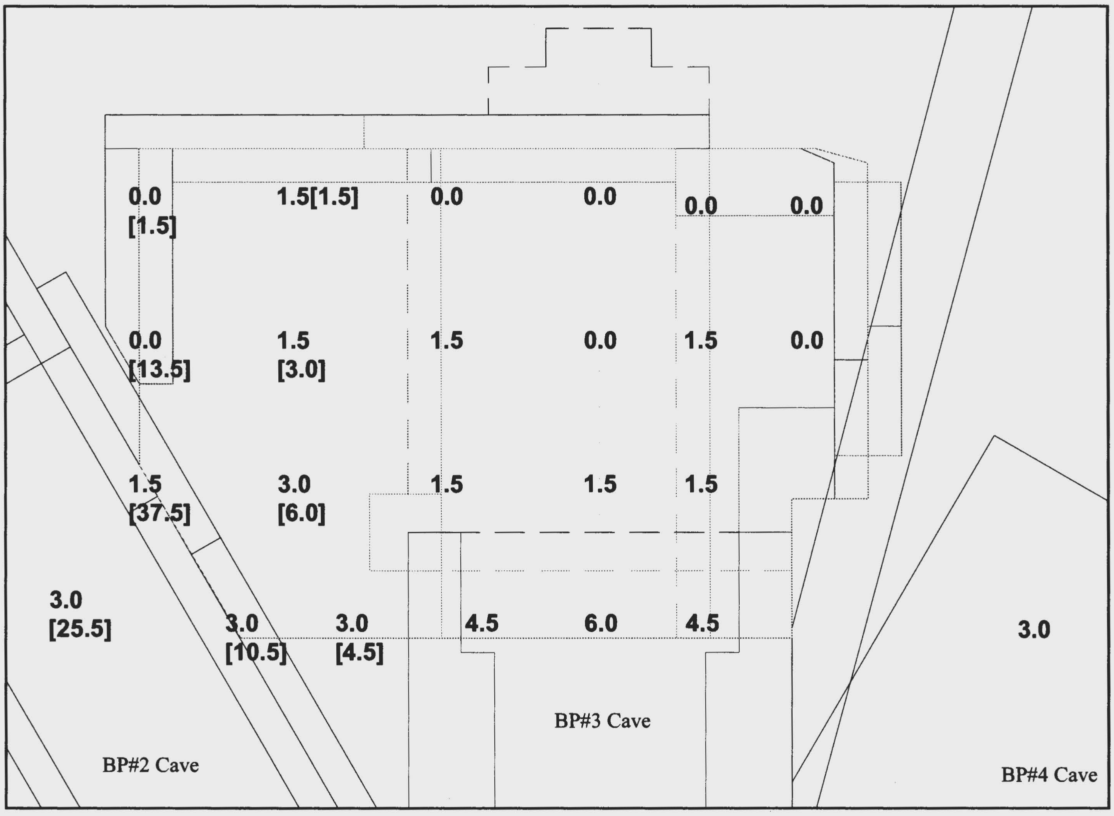

Figure C.6. Closed Shutter Survey – Gamma dose rate (μSv/hr) above Cave Ceiling. Scaled to 3.0 MW reactor power.

[Values in square brackets are measured with BP#2 shutter open].

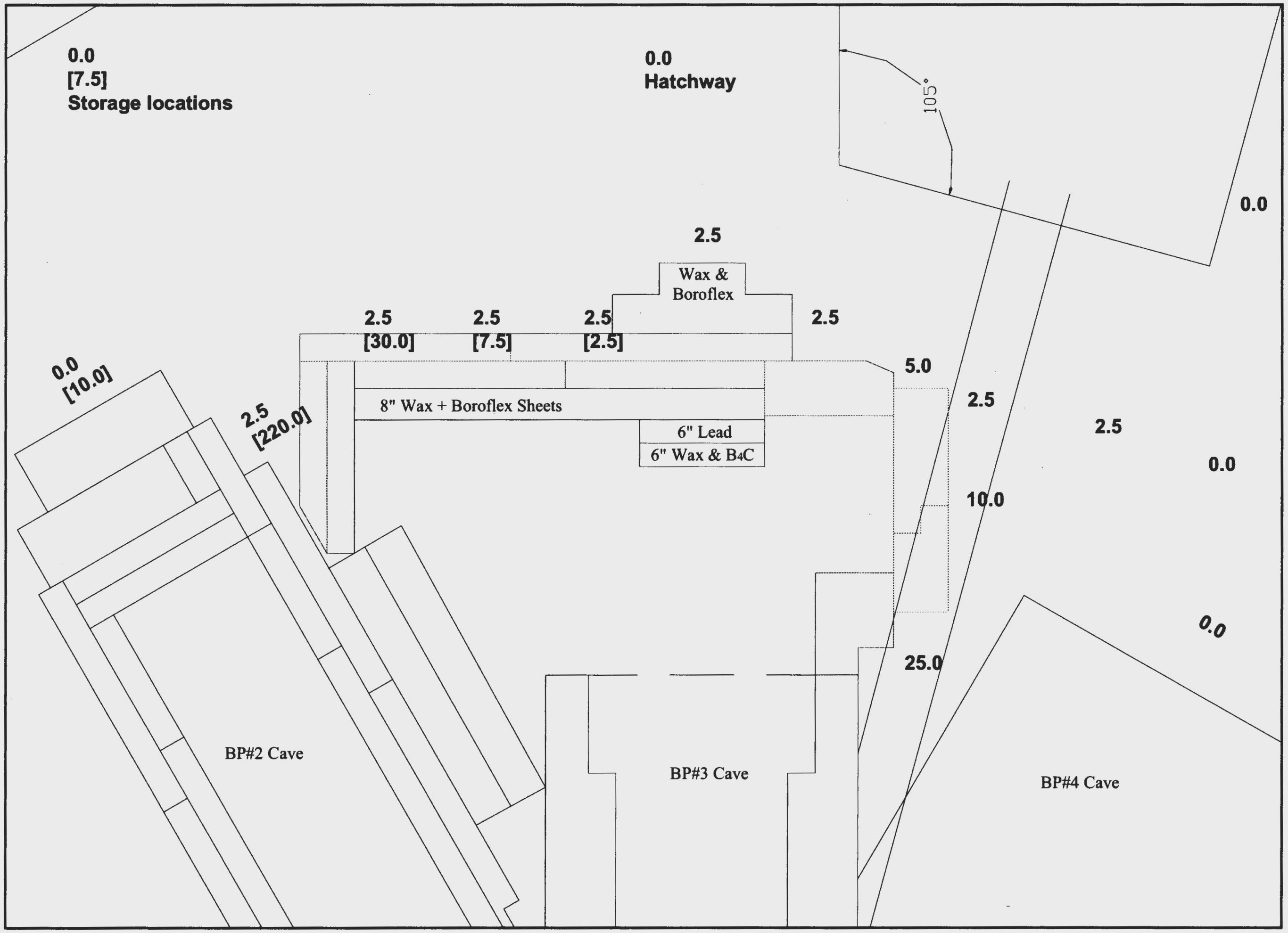

Figure C.7. Open Shutter Survey – Neutron dose rate (μSv/hr) at 0.25 m from ground level. Measured at 3.0 MW reactor power.

[Values in square brackets are measured with BP#2 shutter open].

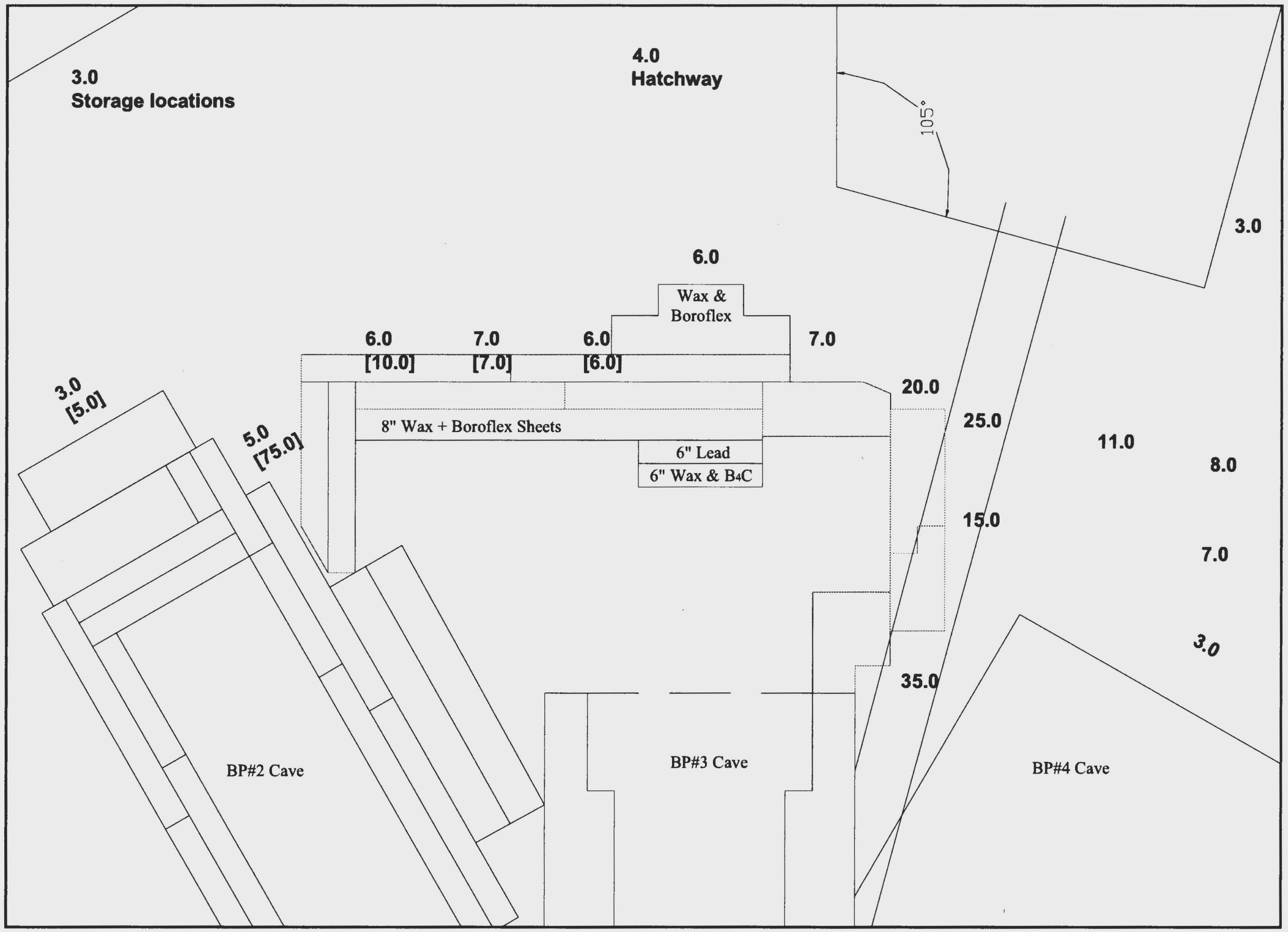

Figure C.8. Open Shutter Survey – Gamma dose rate (μSv/hr) at 0.25 m from ground level. Measured at 3.0 MW reactor power.

[Values in square brackets are measured with BP#2 shutter open].

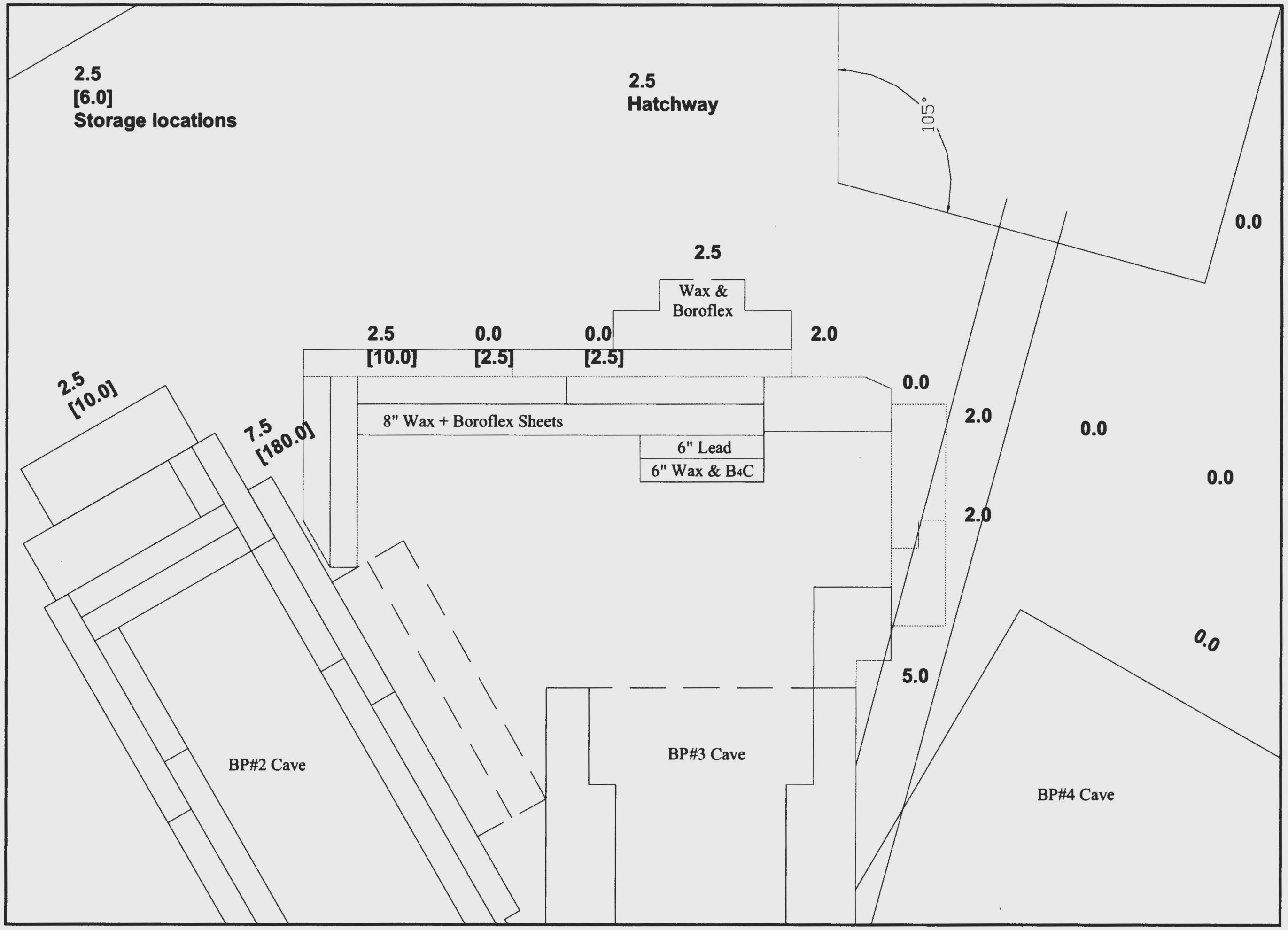

Figure C.9. Open Shutter Survey – Neutron dose rate (μSv/hr) at 2.0 m from ground level. Measured at 3.0 MW reactor power.

[Values in square brackets are measured with BP#2 shutter open].

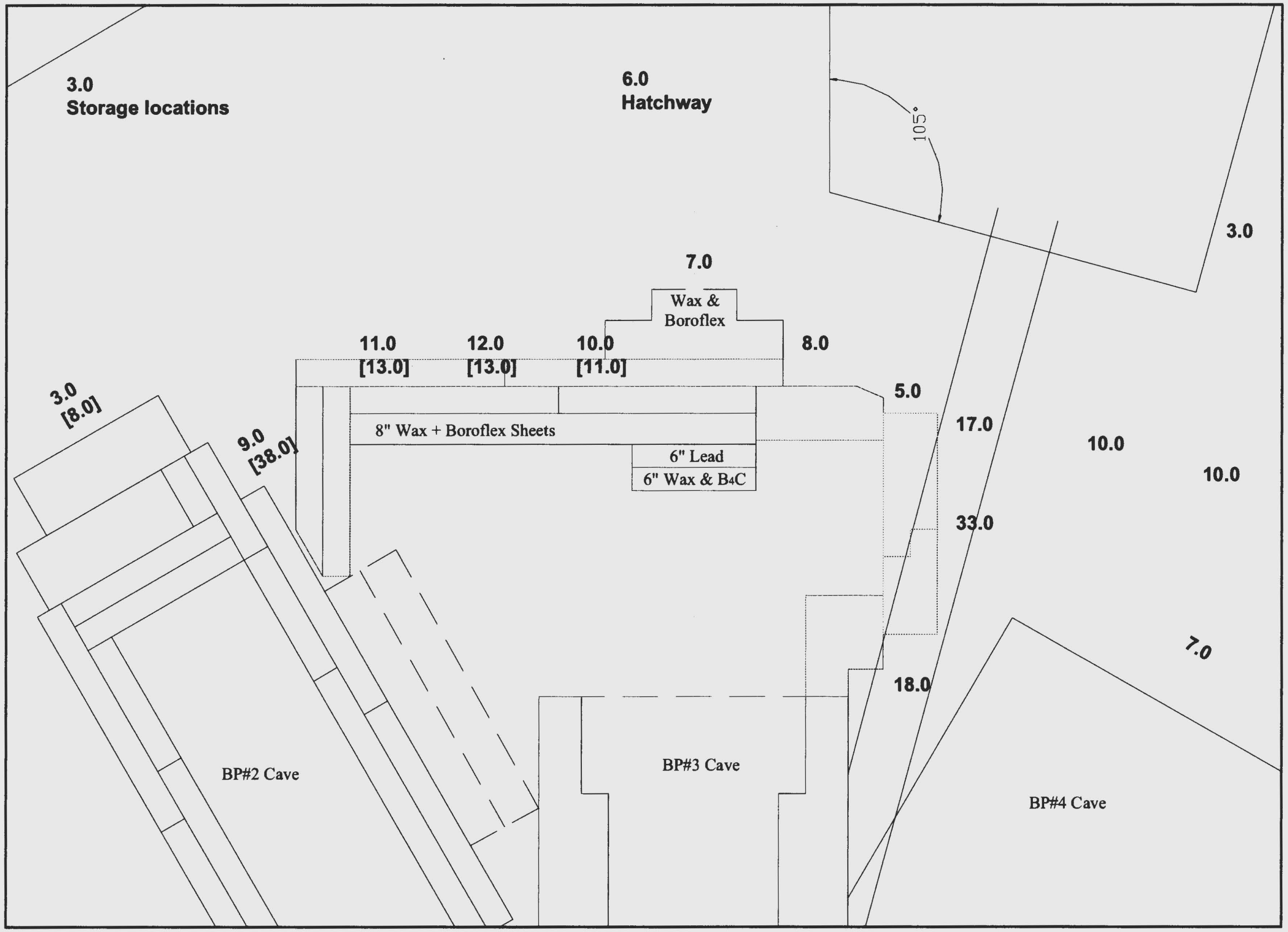

Figure C.10. Open Shutter Survey – Gamma dose rate (μSv/hr) at 2.0 m from ground level. Measured at 3.0 MW reactor power.

[Values in square brackets are measured with BP#2 shutter open].

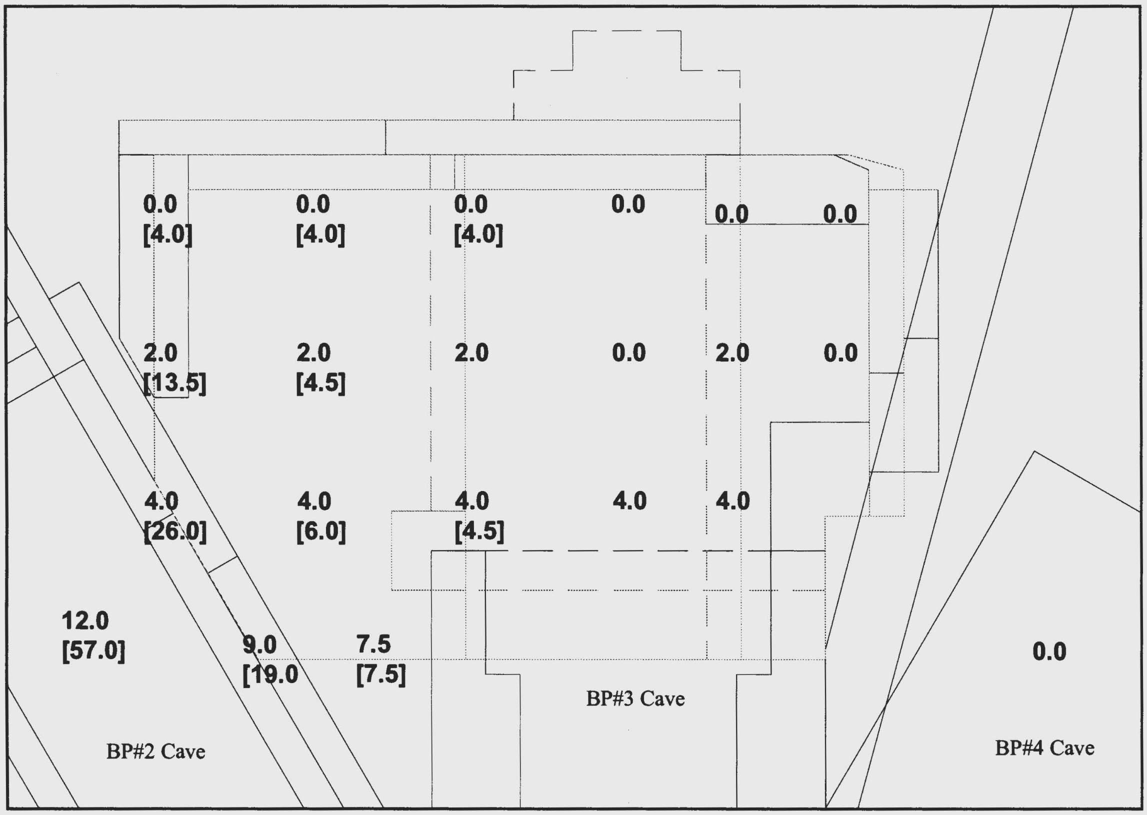

Figure C.11. Open Shutter Survey – Neutron dose rate (μSv/hr) above Cave Ceiling. Measured at 3.0 MW reactor power. [Values in square brackets are measured with BP#2 shutter open].

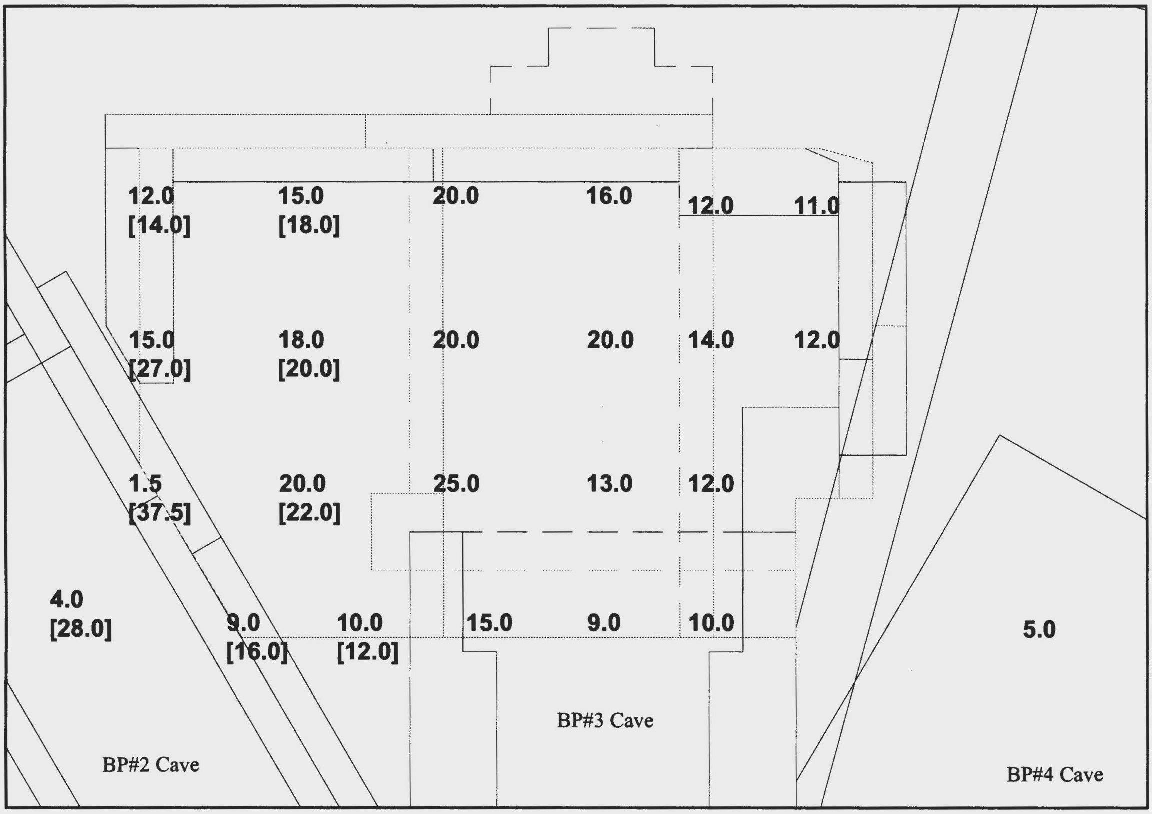

Figure C.12. Open Shutter Survey – Gamma dose rate (μSv/hr) above Cave Ceiling. Measured at 3.0 MW reactor power.

[Values in square brackets are measured with BP#2 shutter open].

Appendix D: Characterization of Different Scintillator Screens.

The neutron conversion screen is a critical component in the dynamic neutron radiography system. A neutron converter should have a relatively short light-decay time, in addition to high neutron sensitivity (or light yield) and high spatial resolution.

Three different scintillator-type neutron conversion screens are available for experimental use in addition to the screen originally available from the LTV RTNR system:

1- Applied Scintillator Technologies, ND screen

2- Applied Scintillator Technologies, NDG screen

3- Saint-Gobain, BC 704

Figure D-1 shows four processed (filtered) neutron images of the beam with no object recorded using real-time neutron radiography system; the images are an average of 256 frames captured by the frame grabber. Figure D-2 shows vertical line profiles obtained from neutron images in Figure D-1 along beam centre-line.

Figure D-1 shows that the Saint-Gobain BC 704 scintillator has some non-uniformities. While the screen from the LTV system has the lowest light yield. Table D-1 provide some quantitative Grey level analysis for line profiles show in Figure D-2.

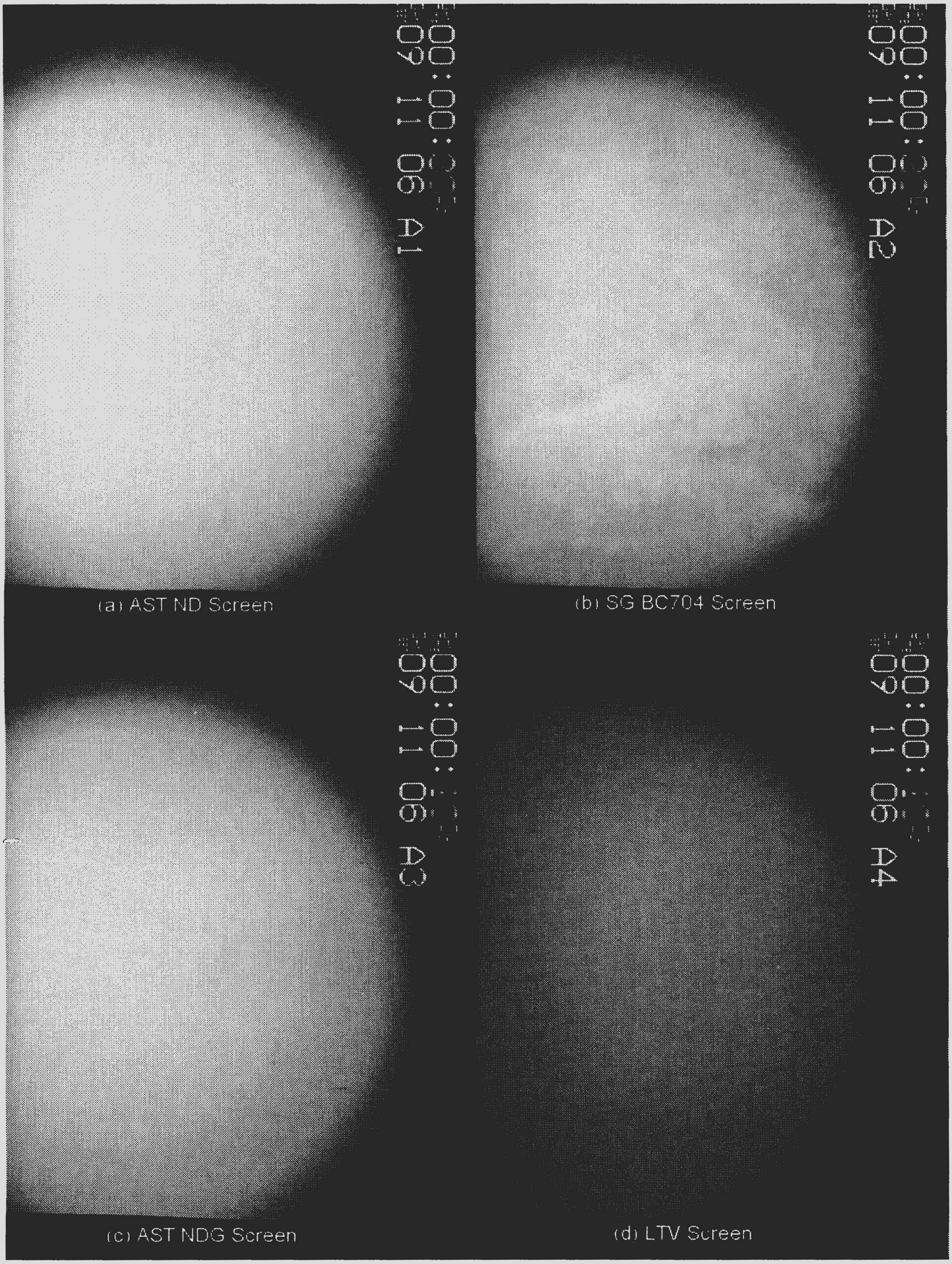

Figure D-1. 256-frame-average processed neutron images of the beam with no object recorded using different scintillator screens.

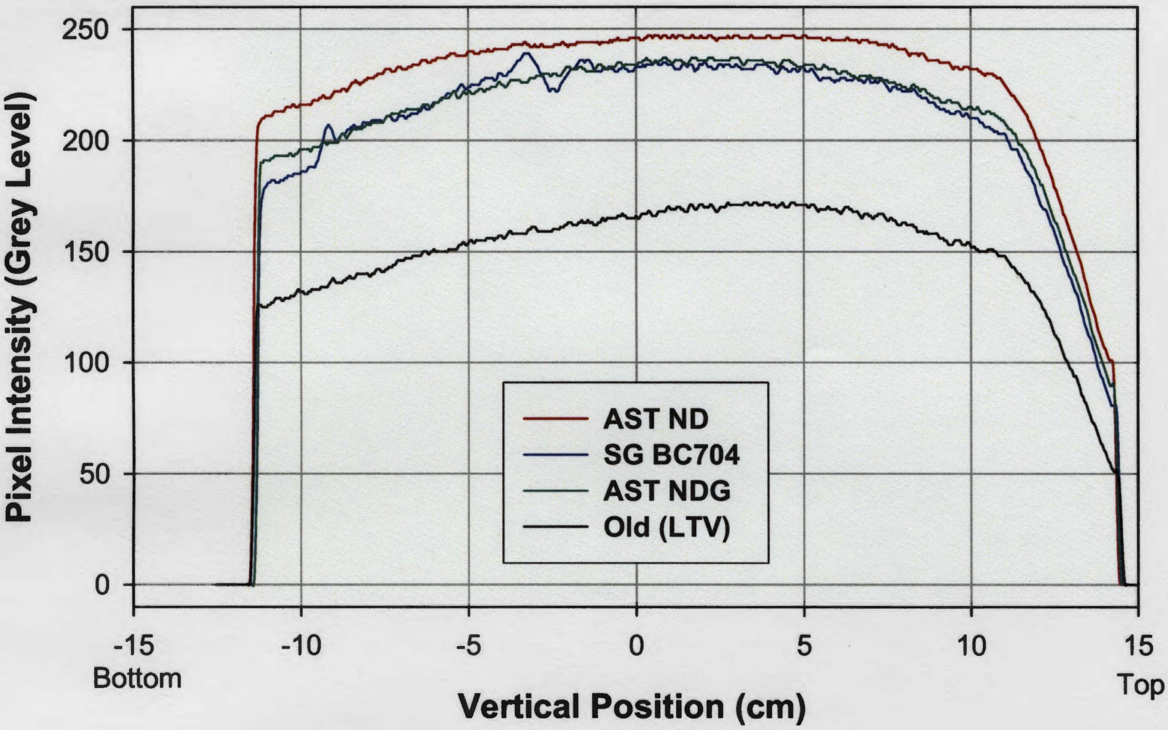

Figure D-2. Vertical line profiles obtained from neutron images in Figure D-1 along beam centre-line

Table D-1. Grey level analysis along beam vertical axis for different screens.

	Max	Min	Average	Min/Max	Average/Max
AST ND	247	216	239.8	87.45%	9708%
SG BC704	239	186	223.7	77.82%	93.60%
AST NDG	237	195	224.75	82.28%	94.83%
Old (LTV)	172	131	159.07	76.16%	92.48%